

THÈSE DE DOCTORAT D'ÉTAT ÈS SCIENCES PHYSIQUES

présentée à la

Faculté des Sciences de Paris
Université de Paris 7

par

Jean-Claude VIAL

pour obtenir le grade de

DOCTEUR ÈS SCIENCES

Sujet

**Contribution à l'étude des protubérances solaires,
à partir des observations effectuées sur l'instrument
du LPSP à bord du satellite OSO-8**

Soutenue le 30 avril 1981 devant la commission d'examen

J. HEYVAERTS Président

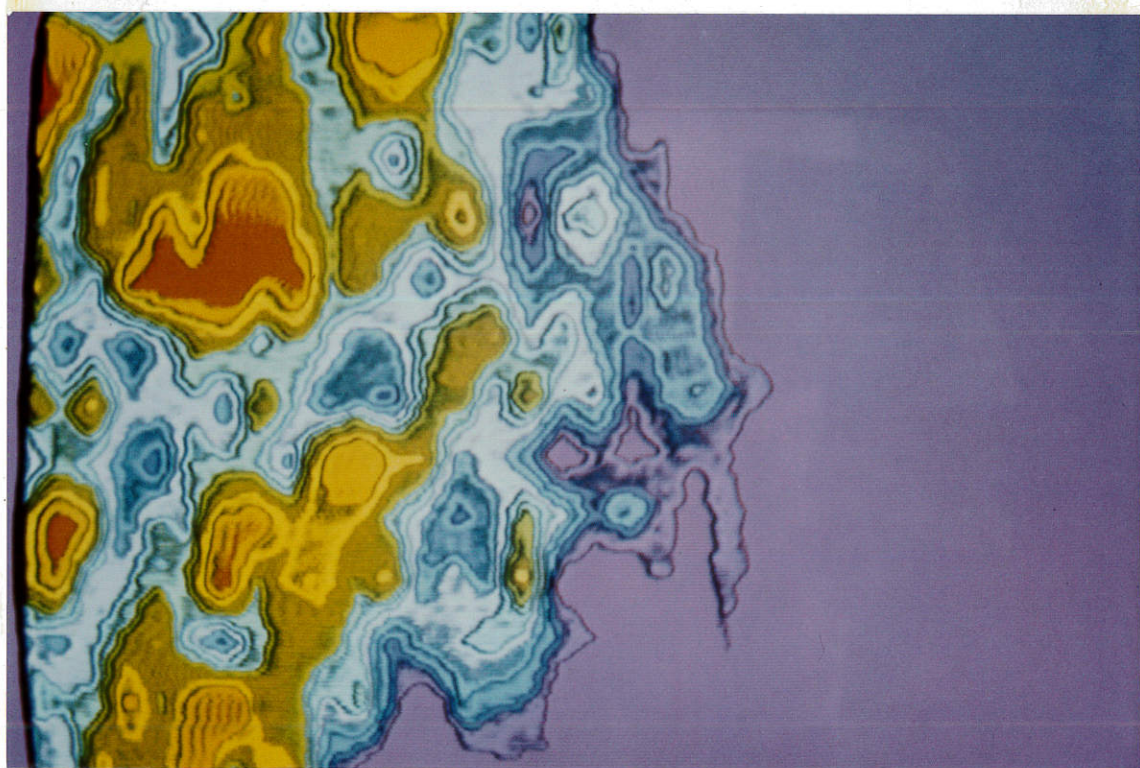
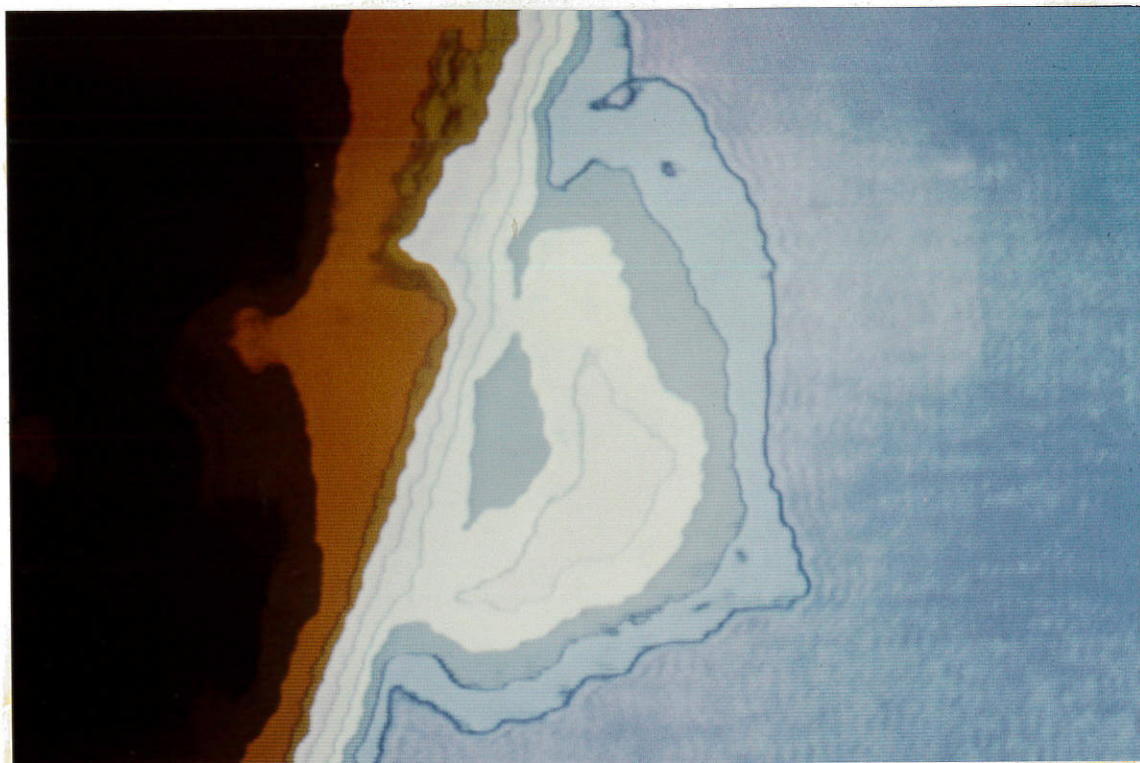
D. MIHALAS

J. C. PECKER

R. M. BONNET

P. LANTOS

P. LENA



Spectrohéliogrammes d'une protubérance quiescente, obtenus (en mode raster) par le spectromètre du LPSP embarqué sur le satellite OSO-8.

La taille de l'image est 2,5 minutes d'arc environ ; le disque solaire est à gauche.

En haut : raie K3 du calcium ionisé.

En bas : raie L α de l'hydrogène

(codage couleur par le VIT de l'IAP)

"Car il devenait de plus en plus urgent qu'une nécessité extérieure inexorable me contraignit à faire appel à toutes les ressources de mon esprit et que je cessasse de reculer devant la lourdeur du fardeau à l'égal de la bête d'Horace, *iniquae mentis asellus*".

P-E Littré, 1880, Comment j'ai fait mon dictionnaire de la langue française.

"Pour se donner l'existence, il faut agir".

Diderot, 1749, Lettre à Voltaire.

REMERCIEMENTS

Je voudrais exprimer ici ma profonde reconnaissance à R.M. Bonnet sous la direction de qui l'aventure OSO-8 a pu avoir lieu. Il a fallu son soutien énergique et constant à l'équipe et à mon travail personnel pour aboutir au succès.

Je remercie très sincèrement P. Lemaire qui a joué un rôle décisif à bien des étapes du projet, et dont les patients conseils ont permis d'obtenir des résultats qui sont, je l'espère, nouveaux et peu critiquables.

Je remercie également mes amis de travail, G. Artzner, P. Gouttebroze et J. Leibacher tous trois engagés, à des titres divers, dans la même aventure et qui m'ont apporté une aide précieuse.

Je n'oublie pas bien sûr D. Mihalas qui m'a donné accès à son programme de calcul, J.C. Pecker pour l'appui apporté à l'équipe et moi-même, et A. Skumanich, avec qui les observations et les discussions menées pendant un an à Boulder ont été enrichissantes.

Mes remerciements s'étendent à tous les "Guest Observers" d'OSO-8 (Observateurs Invités : Simone Dumont, Guy Simon, et tous les autres) ainsi qu'à J.L. Leroy, Madame Martres, P. Mein, S. Koutchmy qui n'ont pas mesuré leur temps pour discuter de mes résultats.

Rien n'aurait été obtenu, bien sûr, sans le travail et le dévouement de toutes les équipes techniques du LPSP (bureau d'études, atelier, laboratoires d'étalonnages de Chalais-Meudon et Verrières, laboratoires d'électronique et asservissements etc...) équipes coordonnées par M. Vite. La même remarque s'applique à tous ceux qui ont contribué aux observations (A. Jouchoux, M. Choucq) aux dépouillements des résultats (J. Salm) ou aux deux (N. Lizambert).

Je remercie tous les informaticiens de Verrières et en particulier F. Bougnet, qui ont bien voulu examiner les (nombreux) messages d'erreurs issus de mes programmes. Il faut souligner ici le travail considérable effectué au Centre de Calcul du CNES à Toulouse, notamment par M. Perthuis (II) et l'équipe du CDC 7600.

Cette thèse est aussi le produit de longues patiences : celle de F. Marchand qui m'a fourni toute l'aide bibliographique que je demandais, Madame Peyroux qui a assuré le tirage, de R. Olombel qui a assuré toute l'illustration, et enfin celles de Mmes A. Talbot, M. Noël-Giraud et M. Orine qui ont dactylographié les diverses parties de ce volume.

Mes remerciements vont enfin à tous ceux qui, au LPSP et ailleurs, m'ont permis de mener à bien, dans des conditions pas toujours faciles, ce travail de longue haleine.

TABLE DES MATIERES

	Pages
INTRODUCTION	1
I - <u>L'INSTRUMENT LPSP SUR OSO-8</u>	3
Article I	6
Article II	38
II - <u>OBSERVATIONS DES PROTUBERANCES SOLAIRES</u>	69
Protubérances actives	78
Article III	79
Article IV	101
Protubérances quiescentes	122
Article V	124
Article VI	135
III - <u>CALCUL DU TRANSFERT (à deux dimensions et hors e.t.l.) DANS LES CINQ RAIES DE RESONANCE (H L_{α}, Mg II h et k, Ca II H et K). COMPARAISON AVEC LES OBSERVATIONS OSO-8</u>	195
CONCLUSION	232
REFERENCES GENERALES	235
ARTICLES OSO-8 non mentionnés dans la Thèse	237

INTRODUCTION

La proposition d'expérience à bord du satellite OSO-I de la NASA ("Study of the chromosphere fine structure by means of simultaneous high resolution observations of the profile of the $L\alpha$, $L\beta$, $Mg II$, $Ca II$ H and K lines" by P. Lemaire, R.M. Bonnet, J.C. Vial, A. Vidal-Madjar) a été faite en Juin 1969 et acceptée par la NASA le 22 Décembre 1969.

A cette date, le dernier modèle moyen de la photosphère et chromosphère solaire (le "Bilderberg Continuum Atmosphère") connaissait un certain succès puisqu'il était en accord avec les observations des continus infra-rouge et ultra-violet. Des raffinements étaient en cours d'élaboration (le Harvard Smithsonian Reference Atmosphere) pour intégrer les observations de raies chromosphériques ($L\alpha$ de H I, h et k de $Mg II$, H et K de $Ca II$). Dès cet époque pourtant (et même avant), les physiciens solaires insistaient sur la nécessité d'observations à haute résolution dans des raies u.v. assez intenses. Par haute résolution, nous entendons haute résolution spatiale (permettant une étude fine dans un plan solaire horizontal, à $\mu = 1$) et spectrale (permettant une étude fine selon la verticale à $\mu = 1$). L'instrument proposé par le LPSP sur OSO-I (devenu OSO-8 au lancement) non seulement satisfaisait à ces 2 propriétés (1 à 2 "de résolution spatiale", 20 mÅ de résolution spectrale) mais permettait l'étude simultanée de différentes raies (pour la plupart de résonance) formées à des altitudes différentes (mais avec de grandes régions communes). La présence des raies du doublet de $Ca II$ permettait en outre une bonne localisation "à bord" des structures visées, et un moyen de recalage avec les observations au sol. Ces observations devaient, en principe, aboutir à l'établissement de modèles (densités, températures, turbulence, vitesses,...) pour chaque structure caractérisée du soleil (réseau chromosphérique, cellule de supergranulation etc...). Force est de constater que si des observations tout à fait nouvelles ont été obtenues par OSO-8 (ainsi que Skylab et SMM), les progrès dans la modélisation fine ont été moins rapides et aujourd'hui encore, aucun modèle moyen dérivé du VAL (Vernazza et al., 1973, 1976) ne rend compte de toutes les observations.

Cela est vrai, en particulier des protubérances solaires. Ces "amas de matière lumineuse ayant une grande vivacité et possédant une activité photogénique très remarquable" (Secchi "Le soleil", 1877, I. 385) sont étudiés systématiquement depuis 1868 (Secchi écrit (II.1) : "L'éclipse de 1868 sera une date mémorable dans l'histoire de l'Astronomie car c'est alors que M. Janssen apprit aux savants à étudier en tous temps les protubérances"). L'observation de la raie D3 aboutit à la découverte de l'hélium. Beaucoup d'études morphologiques, dynamiques, statistiques ont été réalisées sur les filaments (D'Azambuja et D'Azambuja, 1948) ou sur les protubérances (grâce au coronographe). Il est impossible de résumer ici les plus récents travaux d'observations ; on se reportera à "Solar Prominences" (Tandberg-Hanssen, 1974) et aux proceedings du Colloque d'Oslo ("Physics of Solar Prominences" IAU Colloquium 44. 1978). Les travaux théoriques ont été, à notre avis, moins nombreux et se classent sommairement selon 2 thèmes :

a) Etude de la stabilité (et de la formation) des protubérances : quelques modèles nouveaux ont été proposés depuis le Kippenhahn-Schlüter (1957) : par Pikelner (1971), Kuperus and Tandberg-Hanssen (1967), etc...

b) Etude des conditions thermodynamiques (T, p...) dans les protubérances. Depuis que l'on a compris l'importance du rayonnement u.v. incident (voir par exemple Hirayama (1963)), on sait que la température (électronique, ionique...) est bien plus basse que la température d'excitation mesurée. Les premiers (et les seuls) modèles bâtis à ce jour sont les modèles construits à partir de calculs de transfert hors e.t.l. par Poland et al. (1971) Heasley and Mihalas (1976) et Heasley and Milkey (1978).

Il est important de remarquer que ces travaux ont impérativement besoin de bonnes observations u.v. : les premiers (a) afin d'inclure les pertes radiatives dans l'équation d'énergie, les seconds (b) car ils reposent sur la comparaison avec les intensités observées.

Comment se situent les possibilités d'OSO-8 dans ce contexte ? Les plus récentes observations u.v. remontent à Skylab : à partir de raies très chaudes ($T \approx 10^5$ K) Orrall et Schmahl (1976) ont défini le concept d'interface entre la protubérance et la couronne et mis en évidence que cette région était assez peu différente de la zone de transition chromosphère-couronne. Au sol, la masse d'observations opérées dans plusieurs raies, une bonne calibration absolue, ont permis au groupe d'Hawaï de tester les différents modèles proposés (au moins leur région interne) et l'ont amené à conclure à l'existence de 2 régions de température (Landman et al., 1977).

Les observations effectuées avec l'instrument LPSP à bord d'OSO-8 apportent, avec une résolution spatiale comparable à celle des observations mentionnées (quelquefois meilleure) des informations complémentaires : les raies observées se forment depuis le noyau froid jusqu'à l'interface avec la couronne. Des informations originales : par le fait que des raies différentes sont mesurées simultanément en un même "point". Des informations entièrement nouvelles : par la mesure d'intensités absolues de $L \alpha$, $L \beta$ et $Mg II$ et des profils de ces raies.

Nous présentons ci-dessous le travail entrepris depuis la conception de l'expérience jusqu'au traitement des données et leur interprétation en précisant, si nécessaire, ma contribution personnelle à une aventure qui n'a pu aboutir que par les efforts conjugués des équipes scientifiques et techniques du LPSP, du LASP, de la NASA et du CNES.

I. L'Instrument LPSP sur OSO-8.

ARTICLES I et II.Papier I.

La proposition d'expérience définissait schématiquement les objectifs scientifiques, l'instrument et les modes d'observation. La proposition acceptée, il a fallu constamment itérer entre la satisfaction des objectifs scientifiques (ou la définition de nouveaux objectifs), la définition de l'instrument (y compris des modifications compte tenu des contraintes imposées par le satellite, ou des nouveaux objectifs) et la mise au point des modes correspondants d'observation. J'ai particulièrement travaillé sur le spectromètre de l'expérience (cf. 3.2. et 6.2.) instrument particulièrement complexe avec 6 canaux, 16 fentes, 6 polariseurs ou atténuateurs, etc... Les parties pointées des précédents OSO satellites étaient constituées de 2 boîtes identiques disposées verticalement. Une telle configuration nous aurait obligé à adopter un montage "vertical" du spectromètre. Le calcul m'a montré que les aberrations étaient d'un ordre de magnitude supérieures aux aberrations du montage "horizontal", et donc incompatibles avec la résolution spectrale visée (20 mÅ). L'instrument associé du LASP (USA) étant soumis aux mêmes contraintes, la NASA a accepté de découper la partie pointée, horizontalement et non verticalement. Le calcul par tracés de rayons nous a permis d'abandonner le montage Czerny-Turner pour un montage à miroirs paraboliques, de préciser les tolérances etc... Parallèlement, le calcul de la dispersion permettait de déterminer l'intervalle spectral possible et donc les raies observables (0 VI à 1032 Å par exemple). Fentes, filtres, détecteurs, revêtement de surfaces (du LiF) ont été choisis. D'autres améliorations ont été apportées ensuite : lame correctrice sur la voie Mg II (calculée par Godell et Muffoletto) et minispectromètre derrière la fente de sortie L α (calculé par P. Lemaire). J'ai vérifié le principe général du spectro sur une maquette travaillant sur des raies fines (laser, cathode creuse) dans des ordres équivalents.

Les calibrations photométriques (cf. 6.3) ont nécessité depuis leur définition même jusqu'à leur mise en oeuvre, un travail très lourd (trop brièvement résumé dans la table X. On trouvera plus de renseignements sur la philosophie adoptée dans "Etalonnages de l'expérience OSO-I" rapport interne LPSP.TS.52009048. J'ai plus spécialement travaillé sur la définition et la calibration des sous-ensembles conçus à cet effet (mécanisme de "contrôle de flux", périscope, collimateur etc...) (voir pages 42 à 62). La méthode de calibration sous vide adoptée a consisté à étalonner séparément le télescope et le spectromètre. Une carte de transmission du télescope (correspondant à une mesure à 1200 Å) est donnée dans la figure I.1. Les résultats obtenus se sont révélés cohérents entre eux et en bon accord avec les mesures "corps noir" faites à l'air pour les raies Ca II (et Mg II).

Pour la raie Lyman α , le résultat obtenu mettait déjà en évidence une dégradation de la transmission par rapport aux mesures des éléments séparés (faites entre 1971 et 1974). Cette dégradation allait être encore plus brutale aux cours des premiers mois d'observations. (Cf. Papier II).

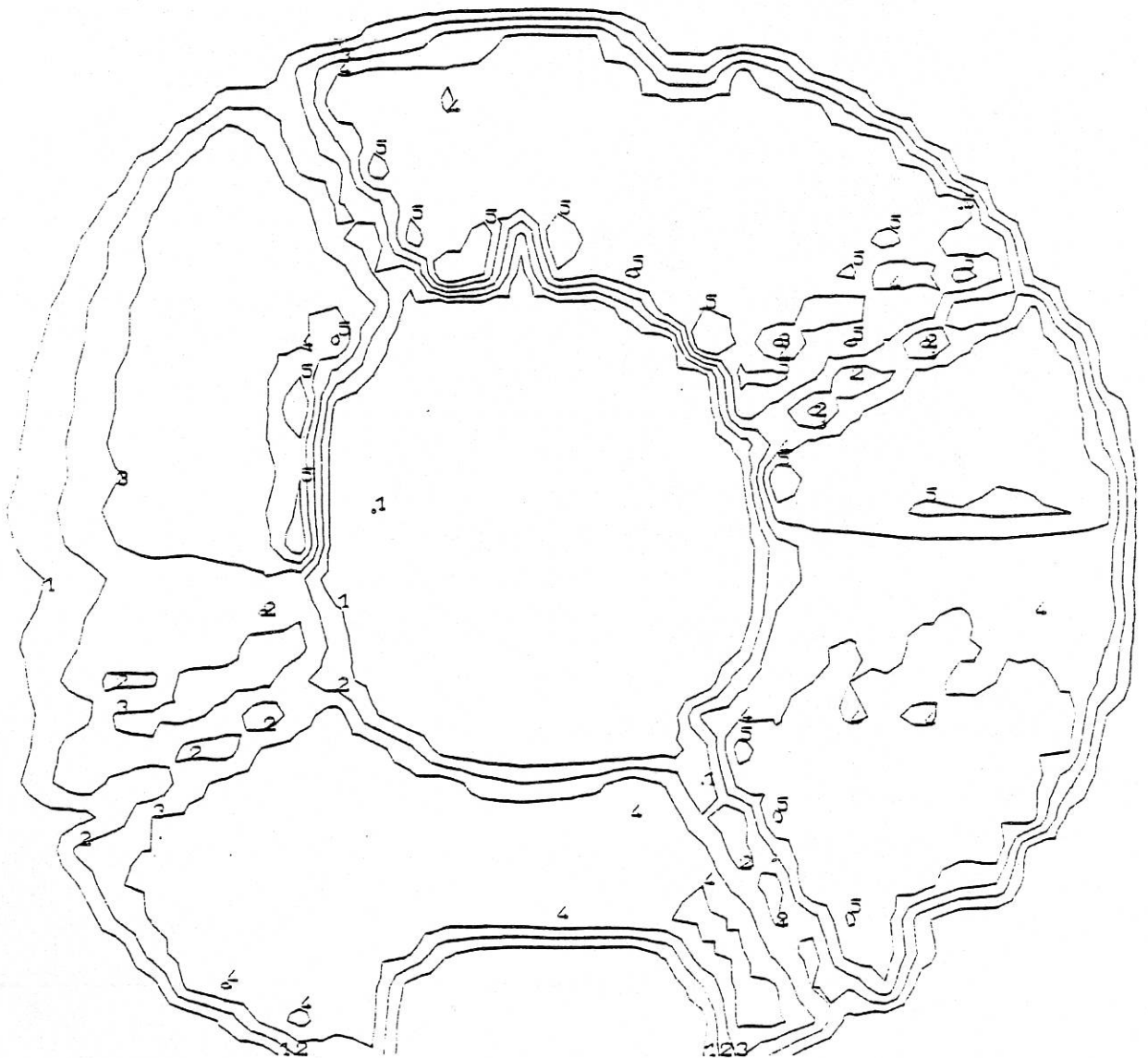


FIG. I.1. : Carte de la transmission du télescope OSO-8 à $\lambda = 1200 \text{ \AA}$.

On remarque les 4 supports du miroir secondaire et, en bas, l'obstruction due au capteur solaire installé sur le télescope.

Papier II

L'instrument allait d'ailleurs subir une dégradation rapide dans toutes les voies (cf. Figure 4) dont la surveillance constante a nécessité des mesures fréquentes d'un rayonnement de référence ("le Soleil calme"). D'autres problèmes sont également apparus : la perte du pointeur solaire installé sur le télescope LPSP, les dérives (horizontale et verticale) de l'autre pointeur, des variations importantes de température (en début de mission) etc...

Ces problèmes n'ont pu être détectés et surmontés que par un système très performant d'envoi de commandes et réception des données installé à Boulder (Colorado). Ceci est illustré par la Figure 6 pour le pointage sur un objet déterminé sur le soleil. Quant aux multiples objectifs scientifiques, ils ont été définis au LPSP et élargis aux "Guest Observers" dans le cadre d'un programme d'"observateurs invités" mis sur pied près de 3 ans avant le tir. Les modes d'observations correspondants ont donc été définis puis générés et enfin exécutés pendant plus de 3 ans de l'activation de l'expérience (plus d'un an pour ce qui me concerne).

Il n'est pas exagéré de dire que les résultats obtenus touchent à beaucoup de domaines de la physique solaire (cf. liste complète des publications).

Article I

THE LPSP EXPERIMENT ON OSO-8

I : Instrumentation, Description of Operations, Laboratory Calibrations and
Pre-Launch Performances

G. ARTZNER, R.M. BONNET, P. LEMAIRE, J.C. VIAL, A. JOUCHOUX
J. LEIBACHER, A. VIDAL-MADJAR, and M.VITE

THE LPSP EXPERIMENT ON OSO-8

I: Instrumentation, Description of Operations, Laboratory Calibrations and Pre-Launch Performances

G. ARTZNER, R. M. BONNET, P. LEMAIRE*, J. C. VIAL, A. JOUCHOUX,
J. LEIBACHER**, A. VIDAL-MADJAR, and M. VITE

Laboratoire de Physique Stellaire et Planétaire, BP No. 10, 91370 Verrières le Buisson, France

(Received 3 February; in revised form 22 July, 1976)

1. Introduction

The LPSP instrument on OSO-8 is designed to study the solar atmosphere with high spatial, spectral and temporal resolution.

The scientific objectives of the LPSP experiment concern the investigation of the dynamics of the upper atmosphere of the Sun and the fine structure of the quiet and active chromosphere. Observations are made simultaneously at six wavelengths corresponding to six strong spectral lines, originating at different altitudes in the chromosphere. Their number was limited only by the volume and weight available on the spacecraft for this instrument. They are listed in Table I. In addition, several other chromospheric and transition-region lines can be observed in the two UV channels, nearly simultaneously with the six principal lines, with the use of a fast spectrum scanner.

TABLE I
Lines studied in the experiment, orders of diffraction and spectral ranges investigated

Channel	Order	$\lambda_0(\text{\AA})$	Angle of incidence	Spectral ranges (\AA)
$L\beta H\gamma$	14	1025.76	53° 389	1016.860–1032.218
$L\alpha H\gamma$	12	1215.67	56° 105	1205.689–1222.908
Mg h	5	2803.52	49° 606	2777.396–2822.639
Mg k	5	2796.34	49° 227	2770.051–2815.512
Ca K	4	3934.22	75° 509	3914.445–3949.427
Ca H	4	3969.58	80° 029	3951.643–3982.443

*Presently visiting HAO/NCAR, Boulder, Colorado. (The National Center for Atmospheric Research sponsored by the National Science Foundation.)

**Presently at Lockheed Research Laboratory, Palo Alto, Calif.

This instrument can also be operated during orbit nights and sunsets and sunrises. Hence, good data can be obtained on the distribution of several constituents of the Earth's atmosphere, particularly ozone.

In this paper, we describe the instrument and present its optical, electrical and photometric performances as measured on the ground before the launch. OSO-8 was launched on June 21, 1975 from the Kennedy Space Center. LPSP scientists and their Guest Investigators are accumulating excellent scientific data which will be presented in subsequent papers.

2. The OSO-8 Spacecraft

OSO-8 is the last spacecraft of the OSO series. It was built by the Hughes Aircraft Company, under contract to the Goddard Space Flight Center. Like its predecessors, it consists of a rotating wheel and a solar pointed instrument assembly (PIA). However, its capabilities are considerably improved. The total weight of the pointed instruments is greater than 250 pounds. The design pointing stability is $\pm 1''$ at Sun center over 5 min of time. The telemetry rate is 6400 bits s^{-1} , of which 600 are available for this instrument. In addition, the use of a Stored Command Processor allows the preprogramming of different observing sequences, ensuring optimal use of the instruments onboard.

As shown on Figure 1, the LPSP shares the pointed section with the University of Colorado which has a high resolution UV spectrometer, operating in the range 1050–2300 Å. The wheel contains six instruments prepared by Columbia University, the University of Wisconsin, the Lockheed Palo Alto Research Laboratory, the Naval Research Laboratory and two instruments prepared by the Goddard Space Flight Center.

High pointing stability is achieved by a new type of sensor (SEAS) which brings into close alignment, the solar direction and the optical axis of the two pointed instruments; one sensor is mounted on each experiment for pointing control. At any time the sensor from only one experiment is selected by ground control.

The PIA can be commanded to any point of an offset pointing grid within a rectangular pattern of $44' \times 40'$, centered on the Sun. The grid consists of increments of $1.29''$ in azimuth and $2.35''$ in elevation. The spacecraft can generate two raster patterns: a large one of $44' \times 40'$ and a small one of $2.75' \times 2.3'$ positioned on any point of the offset grid. The combination of selectable scanning rates and line separation leads to eight different raster patterns whose characteristics are given in Table II.

During orbit nights, a PIA azimuth scan of $2 \text{ deg s}^{-1} \pm 20\%$ can be provided, with an elevation angle for the PIA of $+3, 0$ or -3 deg . The PIA can also maintain azimuth pointing in any direction in any one of these three planes of observation. The design azimuth pointing drift is less than 0.2 deg h^{-1} .

Commands can be sent in real time from the ground stations or from the Stored Command Processor which analyzes and dispatches 1360 stored commands which

THE LPSP EXPERIMENT ON OSO-8, I

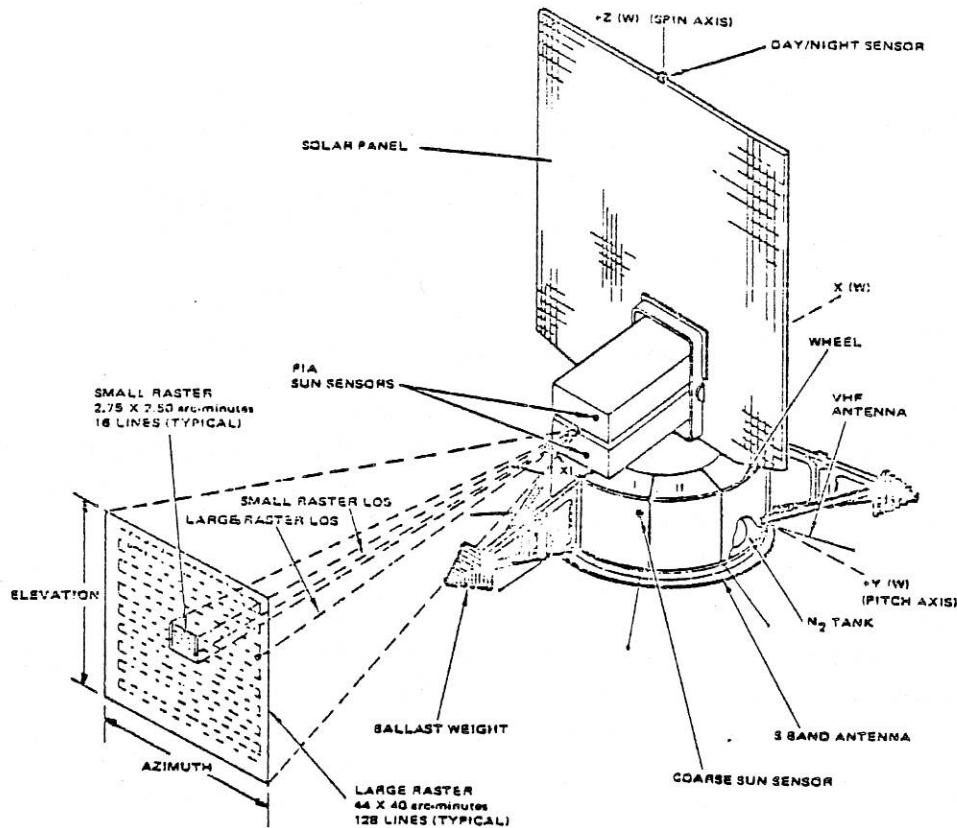


Fig. 1. The NASA spacecraft OSO-8 with its pointed and spinning instruments. Shown also on this figure are the spacecraft rasters of $44' \times 40'$ and $2.75' \times 2.3'$.

TABLE II
Sizes and characteristics of the OSO-8 rasters

Type of raster	Large rasters				Small rasters			
Number of lines	64	128			8	16		
Line length (arc min)	44	44			2.75	2.75		
Line separation (arc sec)	37.5	18.8			18.8	9.38		
Frame height (arc min)	39.41	39.73			2.19	2.34		
Line period (s)	5.12	20.48	5.12	20.48	5.12	20.48	5.12	20.48
Duration of raster (min)	5.46	21.85	10.9	43.69	40.96	2.73	1.36	5.46
					(sec)			

G. ARTZNER ET AL.

may be absolute time commands, relative time commands or event generated commands.

Digital and analog data can be sent to the ground stations in real time or can be stored on two redundant on-board tape recorders, each of which can store up to two orbits.

3. Description of the Instrument

The LPSP instrument is schematized on the optical layout of Figure 2. It consists of two separate subassemblies: the telescope and the spectrometer. It was originally designed to achieve a spatial resolution of one to two arc seconds and a spectral resolution of 0.03 \AA at all wavelengths except Lyman beta where it was 0.06 \AA . We later aimed at a resolution of 0.02 \AA except at $L\beta$ (Lyman beta).

3.1. THE TELESCOPE

The telescope is a Cassegrainian. This choice was dictated by the need for a long focal length and the constraint of a limited space. Table III gives the main characteristics of the telescope.

The best separation between two lines of the satellite rasters is $10''$. This is much larger than the diffraction pattern of a 160 mm diam telescope which varies between $0.3''$ and $1.2''$ for wavelengths 1000 \AA and 4000 \AA . In order to take advantage of this high resolution, we have designed an internal raster device which allows the exploration of a field of view of $64'' \times 64''$ by steps of $1''$.

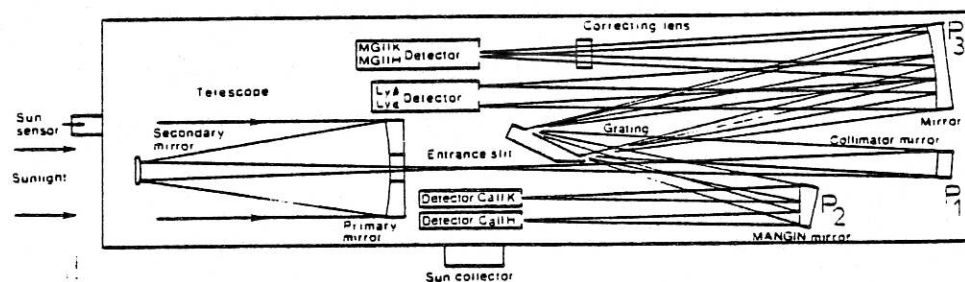


Fig. 2. Optical lay-out of the instrument.

TABLE III
Main optical characteristics of the telescope

Type	Cassegrainian
Diameter of primary mirror	160 mm
Diameter of central obscuration	62 mm
Equivalent focal length	3000 mm
Spacing between mirrors	408 mm
Focal ratio	1/18.8

THE LPSP EXPERIMENT ON OSO-8, I

The scanning element is the secondary mirror of the telescope, which is supported by a flexible rod. An angular rotation of $3'$ around a center of rotation located 35 mm away from the vertex of this mirror induces a 1 arc min rotation of the telescope's optical axis. The mounting and the servo-loop are described by Labeque [1]. The smallest controlled displacement step is 0.3μ and the time to move from any point to any other point inside a $64''$ grid and stabilize is less than 30 ms. Ray-tracings show that the final image degradation due to rotation of the secondary mirror is negligible.

The primary mirror is fixed at three equidistant points. The focus is adjusted before flight, with no provision for adjustment in orbit. Three cervit rods are used to keep a fixed spacing between the mirrors.

At the focus, 8 different size areas can be selected by commands. They are defined by the intersection of a fixed slit with a rotating disk in front of the fixed slit. The 8 possible positions are:

- (1) $1'' \times 1''$ for high spatial resolution work
- (2) $1'' \times 1''$ (spare slit)
- (3) $1'' \times 3''$ for medium resolution
- (4) $1'' \times 10''$ equal to the line spacing of the 16 line small satellite raster
- (5) $1'' \times 20''$ equal to the line spacing of the 8 line small satellite raster and to the 128 line large satellite raster
- (6) $1'' \times 40''$ equal to the line spacing of the 64 line large satellite raster
- (7) $6' \times 6''$ for nighttime observations
- (8) $6' \times 6'$ for nighttime observations

The telescope tube is machined out of a solid piece of titanium. This metal was selected for thermal reasons as described in more detail below. Figure 3 shows the flight model of the telescope tube.

3.2. THE SPECTROMETER

The spectrometer is a modified Czerny-Turner design.

3.2.1. Principle

As shown on Figure 2, the grating is illuminated by the light reflected by collimator P1 whose focus is at the entrance slit. The entrance slit is imaged on an exit slit plane after reflection by mirrors P2 and P3. Appropriate filters and detectors isolate the desired wavelength. The rotation of the grating scans each line around the nominal wavelength. The grating is locked during the launch and is actuated, after unlocking, by a torque motor. Its position is controlled by a differential transformer whose coil is fixed on the structure and used as a fixed reference [2]. A digital to analog converter allows the system to be driven step by step. The number of magnitude commands available set an upper limit of 2048 steps. Each step corresponds to a $2.63''$ increment. The angular range scanned by the grating is $+40'$ to $-50'$.

The choice of this system as opposed to a mechanically driven one was mostly dictated from volume and weight saving considerations. It was also found very

G. ARTZNER ET AL.

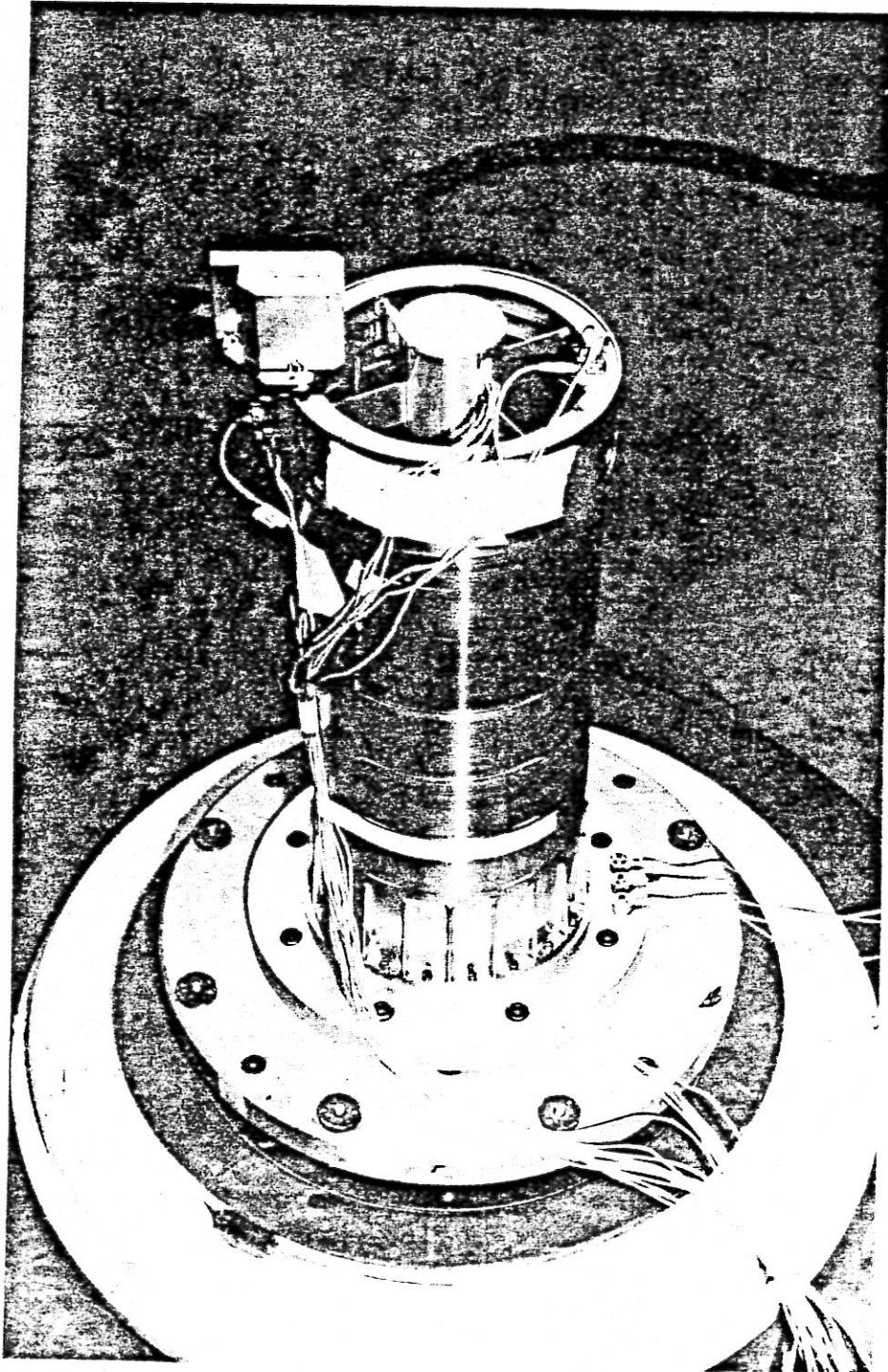


Fig. 3. Engineering model of the telescope tube machined out of a solid block of titanium.

THE LPSP EXPERIMENT ON OSO-3, 4

powerful in terms of rapidity: it takes only 30 msec to go from one position to any other one within the grating range.

A visible reference signal is given on the $L\beta$ channel by a small plane mirror attached to the grating and reflecting the light onto the P3 mirror and the $L\beta$ detector. The amplitude of the scan in Å, the order of diffraction, and the angles of incidence are given in Table I for each channel. Table IV gives the main characteristics of each optical element in the spectrometer. As for the telescope, all optical parts are adjusted before launch with no provision for in-flight focusing.

TABLE IV
Main optical characteristics of the spectrometer

Collimating mirror	Cervit, Parabolic off-axis (4.4°)	$\varnothing = 55$ mm	$f = 678.65$ mm
Focusing mirror (Ca II H, K)	Silica, Mangin off-axis H: 3° K: -1°6	48 × 78 mm	$f^* = 489$ mm
Focusing mirror (Mg II, $L\alpha$, $L\beta$)	Cervit, Parabolic on-axis, $L\alpha$ off-axis $L\beta$: 2°7 off-axis Mg II: 6°7	50 × 131 mm	$f = 668.5$ mm
Grating 1200 gr mm ⁻¹	Cervit, Plane, blaze angle: 57°22	50 × 110 mm	

Manufactured by Muffoletto Optical Company.

Manufactured by Bausch and Lomb.

2. Correction of Aberrations

The use of off-axis optics introduces strong aberrations which must be corrected for. This is done individually for each channel.

— Ca II H and K:

Coma is corrected by the use of a Mangin mirror which is coated on its back face. This principle concept is equivalent to a mirror plus a corrector.

— $L\alpha$, $L\beta$:

For $L\alpha$ all aberrations are minimized by the use of on-axis optics and no correction is necessary. For $L\beta$, aberrations are tolerable and put the final image of the entrance well within the exit slits, thereby eliminating the need for correction.

— Mg II:

The Mg II lines pose a more severe problem. The Mg II exit slits being 6°50 and 6°88 off-axis, coma and astigmatism must be reduced. This is done by a three lens corrector (computed by J. Godell and V. Muffoletto) which cancels coma and reduces astigmatism.

G. ARTZNER ET AL.

3.2.3. Variable Spectral Resolution and Line Centering

The spectral resolution depends upon residual aberrations, the widths of the slits and the stepping of the grating. Two exit slits can be selected: one for day mode, and one for the night or special day mode. Table V indicates the various possible spectral resolutions.

TABLE V
Theoretical spectral resolution of the instrument

Channel	Narrow slits (Å)	Wide slits (Å)
<i>Lα</i>	0.02	0.2
<i>Lβ</i>	0.06	1
Mg h	0.02	1
Mg k	0.02	0.2
Ca H	0.02	1
Ca K	0.02	0.2

Simultaneity of measurements is critical for the study of rapidly fluctuating phenomena on the Sun. This is ensured through a careful adjustment of the optics and of the positioning of each exit slit in the laboratory. When using the wide exit slits, the simultaneity of measurements is lost.

3.2.4. Elimination of Stray Light and Low Orders of Diffraction

Special care was given to the elimination of stray light in the spectrometer, through baffling and use of appropriate filters. A very well designed baffle isolates all channels inside the spectrometer and blocks out the light from the outside which may fall on the detectors. It is a removable, black unit, internally bolted to the rest of the structure.

The use of high orders of diffraction requires that we eliminate the light diffracted in lower ones. This is done with 3 narrow band interference filters in Ca II K and H and in Mg II. At *Lα*, we use a small dispersing optical device schematized in Figure 4, which is composed of a flat holographic grating (3600 l mm^{-1} , $9 \times 25 \text{ mm}$) which diffracts the divergent beam to a spherical mirror ($R = 600 \text{ mm}$) that focuses the light on the detector, located 45 mm above the dispersion plane. At *Lβ*, the combined transmission of the optics and of the detector defines a 200 Å bandpass at half maximum (Figure 5) which includes light from the 13th, 12th and 11th orders. After checking the solar features in this bandpass, we found it more useful to let these orders pass. This allowed us to increase substantially the number of lines we could observe – e.g. O I 1303.2, 1304.8, 1306.0 and N I 1200.2 Å. Si II 1193.2, Si III 1298.9, 1300.9, 1303.26. If necessary, plates of either LiF, or MgF_2 or CaF_2

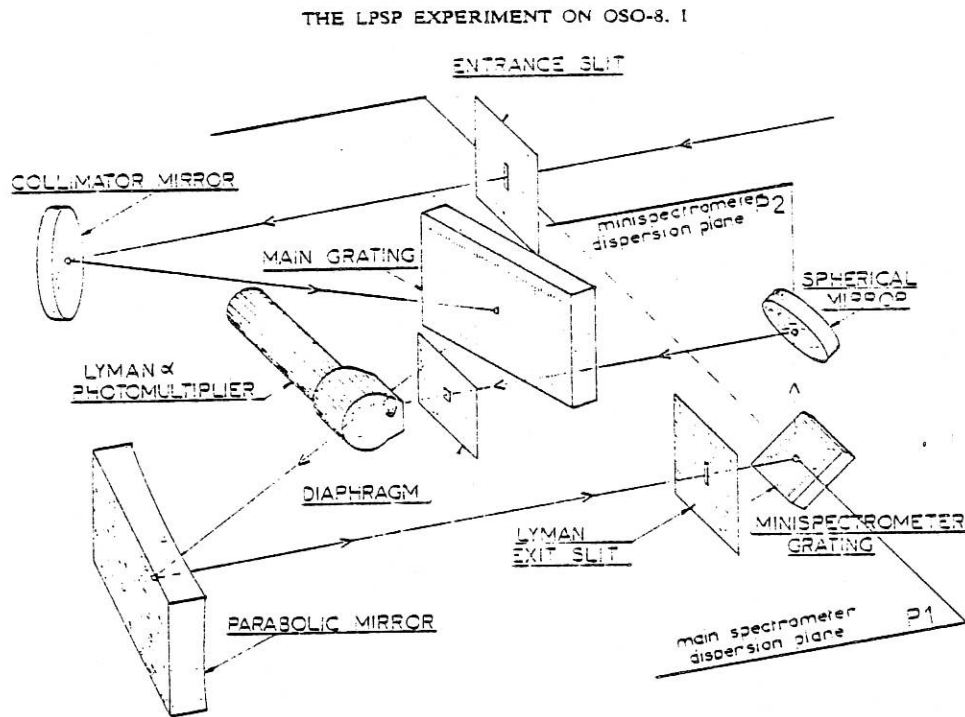


Fig. 4. The mini-spectrometer used for the rejection of the low orders of diffraction in the $L\alpha$ channel.

may be inserted into the beam by an 8 position filter wheel, located 10.5 mm from the spectrometer slit, allowing discrimination between the different orders, by subtraction.

3.2.5. Polarization Properties

Calibration of the grating in polarized light has shown that it presents polarizing properties as indicated on Table VI. It was therefore suggested by J. Beckers and J. O. Stenflo that the grating could be used as an analyzer of polarized light. Two $\lambda/2$ and $\lambda/4$ plates of MgF_2 have consequently been implemented in an attempt to measure linear and circular polarization. These plates have been sliced so that the $\lambda/2$ plates for $L\alpha$ are $\lambda/4$ plates for Mg II and conversely. They are mounted on the 8 position filter wheel. Table VII gives the configuration of the filter wheel.

3.2.6. Detectors

In Table VIII a description of each of the 5 detectors is given. The proximity of the two Mg II lines (8 mm along the dispersion plane) constrained us to use a single phototube. The separation between the lines is given by a split photocathode. The spiraltron of the $L\beta$ channel was covered with a grid at +12 volts in order to eliminate low energy electrons in space. The basic counting gate is one minor frame of the telemetry format; i.e. 0.160 s of which 0.130 s is assigned to the counting time

G. ARTZNER ET AL.

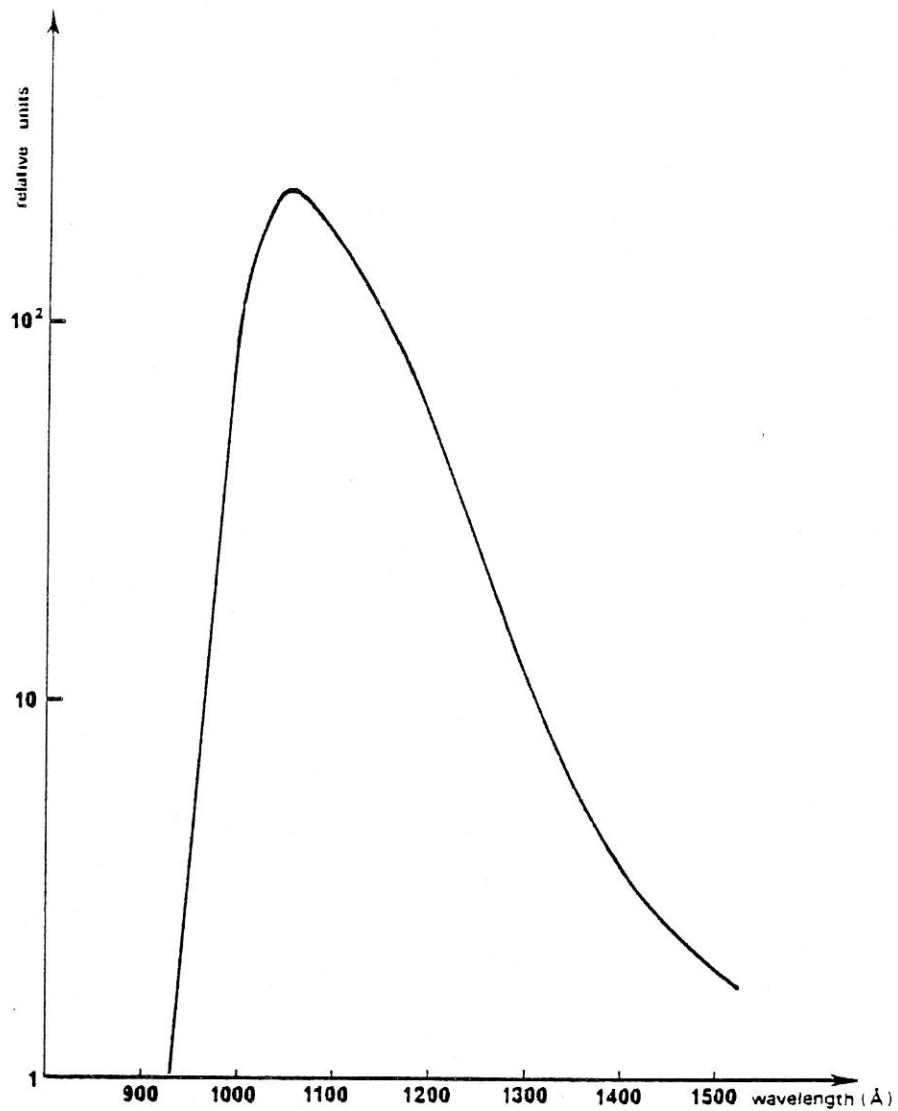


Fig. 5. The spectral response of the $L\beta$ channel. The cut-off at short wavelengths is given by the Al + LiF coating of the 5 reflecting surfaces. At long wavelengths the cut-off is that of the spiraltron.

TABLE VI
Polarization properties of the grating

λ (Å)	1216	2800	3930
$\epsilon_{\parallel}/\epsilon_{\perp}$	0.3	1.4	1.1

THE LPSP EXPERIMENT ON OSO-8, I

TABLE VII
The configuration of the 8 different positions of the filter wheel

Position	Description	Purpose
1	MgF2 small attenuator with $\lambda/4$ plate for $L\alpha$ and $\lambda/2$ plate for Mg II	Circular polarization axes are $\pm 45^\circ$ to the grooves of the grating
2	MgF2 large	
3	Day aperture	Detection of low orders longward of $L\beta$
4	LiF filter	
5	MgF2 polarizer A. $\lambda/2$ plate for $L\alpha$ and $\lambda/4$ for Mg II	Axes are at 45° and 22.5° to the grooves
6	MgF2 polarizer B. $\lambda/2$ for $L\alpha$ and $\lambda/4$ for Mg II	
7	CaF2 filter	Discrimination of low orders
8	Night aperture	

TABLE VIII
List of detectors used in the instrument

Channel	Type	Quantum efficiency	Measured dark counts	Window	Voltage (Volts)
Ca H	EMR 531 m	24%	6 s^{-1}	Front window	2205
Ca K	EMR 531 m	20%	6 s^{-1}	Front window	2210
Mg II	RTC 403 FUH	14%	2 s^{-1}	Split photocathode	2344
$L\alpha$	EMR 641 J	13%	0.25 s^{-1}	Side window	2612
$L\beta$	4219 Bendix spiraltron	7%	0.1 s^{-1}	Open detector	3215

and 0.030 s to count storage, and mechanism set-up. The high voltage is fixed and is not adjusted in flight.

A shutter located just behind the filter wheel and actuated by a stepping motor, locked open in case of power failure, blocks the optical path to the spectrometer and permits dark count measurements.

3.3. THERMAL DESIGN

The tolerances in the positioning of most optical parts are extremely severe, as shown in Table IX. These severe constraints led us to select titanium as the basic metal for the structure of the instrument. Titanium presents also the advantage of lightness,

G. ARTZNER ET AL.

TABLE IX

Allowable dimensional and temperature changes in the instrument

<i>Telescope</i>	Primary to secondary mirror spacing	$\pm 3 \mu (\pm 1.2 \times 10^{-4} \text{m})$
Average $T: 20 \pm 6^\circ\text{C}$	Secondary mirror decentration:	$\pm 2 \mu (\pm 7.9 \times 10^{-5} \text{m})$
ΔT of $\pm 0.3^\circ\text{C}$	Secondary mirror tilt:	$\pm 5''$
<i>Spectrometer</i>	Axial displacement of mirrors from slit:	$\pm 50 \mu (\pm 2 \times 10^{-3} \text{m})$
$T: 20^\circ\text{C} \pm 7^\circ\text{C}$	Centering of mirrors:	$\pm 50 \mu (\pm 2 \times 10^{-3} \text{m})$
	Tilt of mirrors:	$\pm 20''$
ΔT top to bottom: $\pm 1^\circ\text{C}$	Axial displacement of exit slits to entrance slit:	$\pm 30 \mu (\pm 1.2 \times 10^{-3} \text{m})$

although it is extremely difficult to machine. Figure 6 shows the structure of the spectrometer during mechanical set-up. The basic thermal strategy consists of thermally isolating the internal structure of the instrument from the spacecraft and from the other pointed instrument. An aluminum thermal cover surrounds the interior of the instrument and shields it from the environment. Fiber glass bushings are used to fix it to the titanium structure. The thermal time-constant is maximized, resulting in lower orbital temperature level fluctuations.

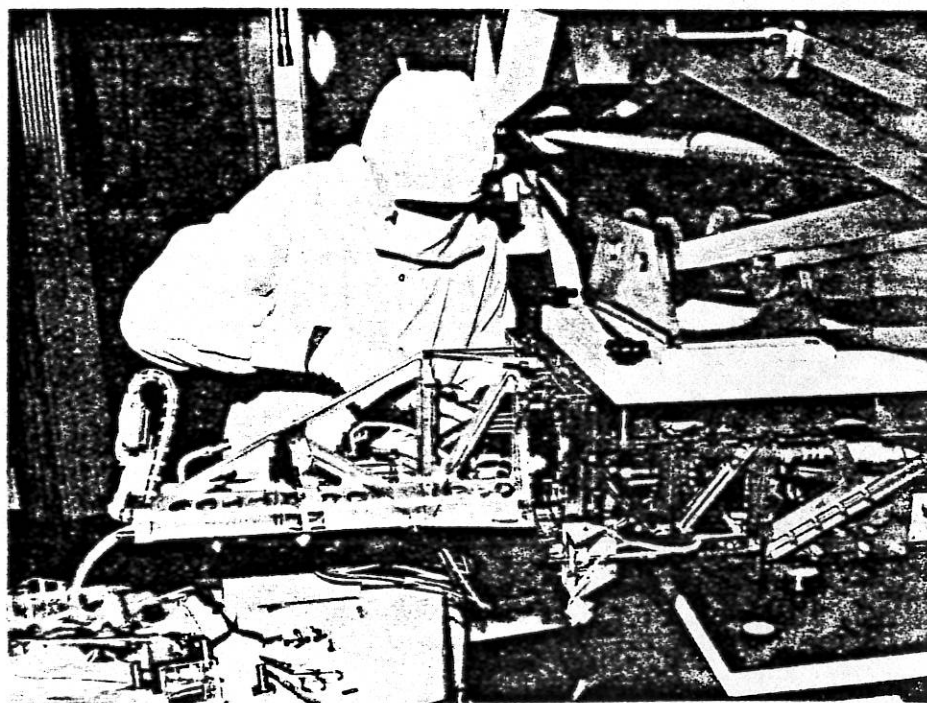


Fig. 6. The structure of the spectrometer during mechanical assembly.

THE LPSP EXPERIMENT ON OSO-8. I

The main guidelines followed in the thermal design are the following:

- Isolate the structure and the telescope tube from localized heat inputs.
- Minimize solar heat inputs to elements located within the interior.
- Dissipate solar inputs and electronics heat directly to the thermal cover.
- Control temperature levels of the structure and critical elements by selection of surface properties on the cover and where necessary by use of heaters.

The surface coatings on the thermal cover have been chosen to maintain a relatively isothermal environment for the structure at an average of 20 °C.

Particularly difficult was the design of the telescope which is directly illuminated by solar light. The unused solar flux is rejected out of the instrument without striking

- the back of the primary mirror,
- the secondary mirror assembly and spider,
- the Sun sensor, located within the aperture of the telescope.

These conditions are fulfilled with a four lobe heat rejection mirror, coated with silver and silica, located in front of the entrance slit mechanism. This mirror focuses 4 images of the primary between the four vanes which support the secondary, independent of the angle of incidence. The secondary mirror and its actuator are the hottest spots in the instrument as a consequence of the concentration of ~20 solar constants and of the dissipation of 4 W from the 4 magnetic coils of the internal raster mechanism. The heat is conducted to an external tube protecting the secondary mirror and the actuator, and then radiated to external space. The thermal design and thermal tests have been conducted under contract to Arthur D. Little Company.

4. Modes of Operation

The relatively large number of mechanisms (internal raster, grating mechanism, slit and filter wheels, shutter, exit slits) and the allocation of four 16-bit words of magnitude commands considerably enlarges the possibilities of observation as compared to those of pointed instruments on previous OSO's.

Commands can be sent manually to each individual mechanism, in a group, or sequentially through the use of pre-wired automatic modes. They can be sent either in real time or through the Stored Command Processor of the spacecraft. The instrument logic allows for a variable exposure time, ranging from 0.16 s minimum (except for the slit and filter wheels for which it is 0.64 s) up to 138 s maximum.

4.1. THE IMAGE SCANNER

Images are formed step by step and line by line as in a television raster but with the possibility of changing

- the size of the horizontal dimension from 1" to 64" by successive powers of 2,
- the size of the vertical dimension from 1" to 64",
- the location of the starting point of the rectangular image (upper left corner), anywhere in a 64" × 64" region,
- the orientation of the linear scans, horizontal or vertical,
- the separation between two consecutive steps or lines, 1" or 0.5".

4.2. THE GRATING MECHANISM

The mechanism behaves as a one dimensional image scanner insofar as the command possibilities are concerned. The following parameters may be defined:

- length of the spectral scan from 1 to 2048 steps (2^N discrete values),
- starting point of the spectral scan anywhere within the 2048 steps,
- separation between two consecutive positions may be 1, 4, 8 or 16 steps.

4.3. THE SLIT AND FILTER WHEELS, AND SHUTTER MECHANISMS

These mechanisms may be commanded either by defining one of the eight possible positions or by selecting an automatic mode which changes in sequence any slit or filter to the next one at a given rate. For safety reasons, the two 'night slits' ($6'' \times 6'$ and $6' \times 6'$) cannot be operated during day time, in 'normal' operations. When a 'night slit' comes into position in day time, the shutter is kept closed and the mechanism is activated until the next day slit is encountered. This security can be overridden, however, in case one wants to use one of the two night slits at day.

The shutter is also closed periodically, every 3 or 15 min, for dark current measurements.

4.4. EXIT SLITS

In the case of the Mg II and Ca II channels, there are two different exit slits which can be uncovered by a mask. In the high resolution mode (0.02 \AA) the wide slits are masked, while in the low resolution mode both slits are uncovered. Hence, the low resolution spectra are in fact the addition of two spectra. This 'defect' can be corrected for, if necessary, through data reduction, by subtracting one spectrum from the other. In most cases used so far, this did not prove to be necessary. The command of this mechanism for these two channels is only manual, through pulse commands.

For the $L\alpha$ and $L\beta$ channels, the slits are on the same plate (3 day-slits and one night slit for each wavelength); the selection is made by a stepping motor translating the plate in front of an opening uncovering the detectors. The use of the 3 day positions is made necessary by the difference in spectral dispersion between the L and the Mg and Ca channels. Coincidence between the K3 cores of all lines or the K2 peaks (blue and red) is ensured by this mechanism. Each of the four positions may be selected manually. There is also an automatic mode in which the three high resolution slits are positioned sequentially.

4.5. PRE-WIRED PROGRAMS

In order to reduce the number of commands and save space in the command memory, we have defined 6 pre-wired programs which make use of the internal raster and grating mechanism and either none, or any other one, of the remaining mechanisms (except the shutter). These programs use each mechanism sequentially.

THE LPSP EXPERIMENT ON OSO-8. I

The 6 pre-wired programs are:

- (1) Spectrum - image - mechanism
- (2) Spectrum - mechanism - image
- (3) Image - spectrum - mechanism
- (4) Image - mechanism - spectrum
- (5) Mechanism - image - spectrum
- (6) Mechanism - spectrum - image

For instance, program 3 generates successive images for each point of a spectral scan whose characteristics are adjusted by other commands: if the spectral scan has 4 steps, then we obtain 4 successive monochromatic images. At the end of this sequence, the mechanism is commanded automatically to step to its next position and the sequence starts again for the new position of the mechanism. In program 1, we make line profiles for every point of an image, etc.

5. Observation Planning and Data Acquisition

The first step in planning the observations consisted in establishing the LPSP observing program and in selecting Guest Investigators, several years before the launch.

5.1. THE LPSP OBSERVING PROGRAM

In its entirety, the LPSP observing program represents ≈ 2000 orbits of complete control of the pointing, covering observations for at least six main topics of interest:

- (1) study of the dynamical structure of the quiet and active chromosphere (oscillations, shocks, etc.)
- (2) three dimensional study of the inhomogeneous physical structure of the quiet and active chromosphere (chromospheric network, plages, spots, coronal holes, spicules, etc.)
- (3) study of prominences
- (4) study of flares
- (5) determination of seasonal variation of H, O₂, N₂, O₃ and OH in the Earth atmosphere
- (6) aeronomy and nighttime observations.

5.2. THE GUEST INVESTIGATOR PROGRAM

A total of 24 Guest Investigators were selected between April 1971 and July 1973. To become a Guest Investigator, one had to submit a proposal for an observing program, which was then analyzed by a selection committee. Selecting Guest Observers several years before launch proved very useful not only for taking full advantage of the observing capabilities of the instrument but also, in some cases, for modifying its final design.

G. ARTZNER ET AL.

5.3. DAILY PLANNING

The daily planning is done from the Experiment Control Center located in the Laboratory for Atmospheric and Space Physics (LASP) on the campus of the University of Colorado in Boulder, from which the observations, planned with both pointed experiments, are coordinated on a daily basis.

5.4. THE QUICK-LOOK FACILITIES

Play-back and real-time data from the instrument are received at ground stations and then sent to Goddard Space Flight Center. A telephone line between GSFC and Boulder permits the recording of the LPSP and LASP data approximately 30 min after they have been transmitted from the spacecraft to the ground station. Both LPSP and LASP have PDP-11/20 computers which are time-shared to support data acquisition and analysis simultaneously. The scientists can have access to their data through two consoles connected to the PDP-11 computer. They can get hard copies of profiles and pictures of rasters ≈ 1 h after they have been taken by the instrument. The PDP-11 has limited capabilities and is used only for quick-look observations and command generation. Production tapes, for the LPSP experiment are analyzed by the Centre National d'Études Spatiales in Toulouse, France, for both the LPSP Scientists and their Guest Investigators.

6. Prelaunch Performances – Tests and Qualification

We describe here the performance of the instrument as measured before launch: spatial and spectral resolution, line centering and photometric sensitivity, including stray light and dark current. Pre-launch performance was evaluated during two series of tests: the first, conducted at LPSP prior to delivery to the spacecraft contractor in May 1974 and the second conducted at the spacecraft contractor's facilities during the 9 months preceding the launch. We verified that the performances were maintained after the qualification tests, conducted according to NASA specifications at both the experiment and the spacecraft level.

6.1. TELESCOPE FOCUSING AND SPATIAL RESOLUTION

The telescope was adjusted separately from the rest of the instrument before coupling with the spectrometer. The primary mirror is fixed, therefore the focus is adjusted by moving the secondary. The search for the right position is done by photographing the image of a point source given by a 3 m collimator. During these tests, power was applied to the internal raster in order to balance the secondary mirror against gravity. The fixture of the primary proved to be the most critical part of the telescope and several iterations were necessary to qualify it to the vibration levels required by NASA.

Before coupling the telescope to the spectrometer, the performances of the raster mechanism were also measured. They afford a second test of the image quality. The

THE LPSP EXPERIMENT ON OSO-3. I

linearity and repeatability were measured photographically by commanding a $64'' \times 64''$ image of a point source at the focus of the 3 m collimator. The resulting picture is composed of 4096 pixels. By repeating this operation several times, we were able to check that the repeatability of the mechanism was better than $0.3''$ over the 30 min of the test, in agreement with the error signals issued by the position sensor. The linearity and orthogonality of lines and columns of the raster pattern were found to be better than $0.5''$ over the field of $64'' \times 64''$.

The telescope performance was also checked photoelectrically after coupling with the spectrometer using either the detectors of the instrument or a special test detector inserted behind the entrance slit, through a hole in the structure.

Figure 7 compares the theoretical and measured instrumental profiles at $L\alpha$ measured by scanning the image of a $3''$ slit. It shows that some residual aberration is still apparent in the wings probably due to stresses of the primary. However, there is a good general agreement which shows that we are very close to the theoretical

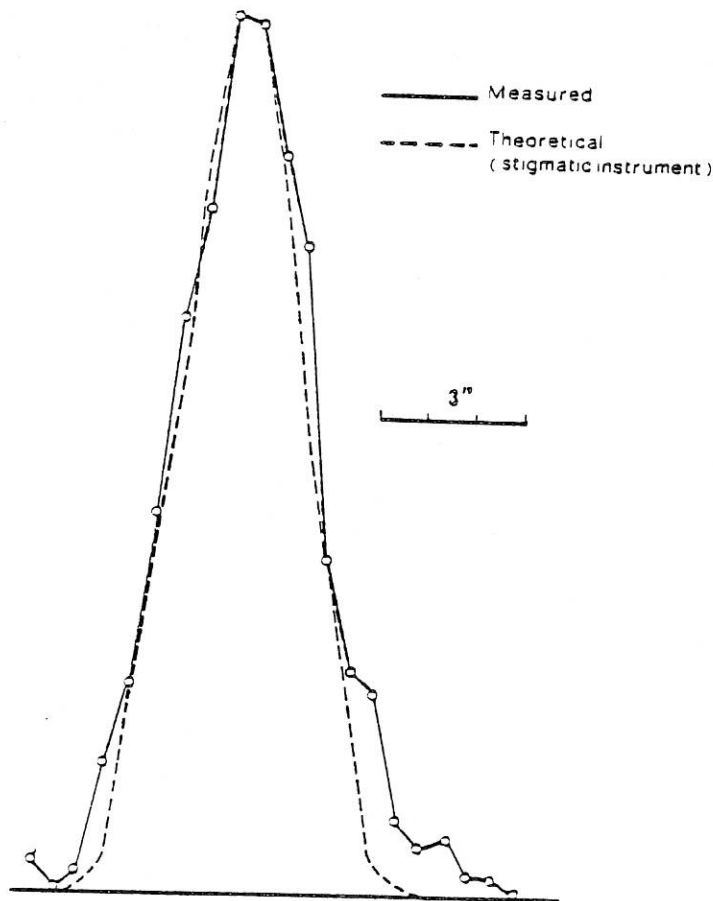


Fig. 7. Comparison between the theoretical and observed telescope instrumental profiles for a $3''$ slit scanning across the slit width at the wavelength of $L\alpha$.

G. ARTZNER ET AL.

resolution. Figure 8 shows the distribution of intensity far in the wings for a $190\ \mu$ slit, which defines the instrumental profile, as measured 6 weeks before the launch, at the spacecraft contractor's facilities. It shows good image quality and indicates increased scattering towards shorter wavelengths. We were also able to check that

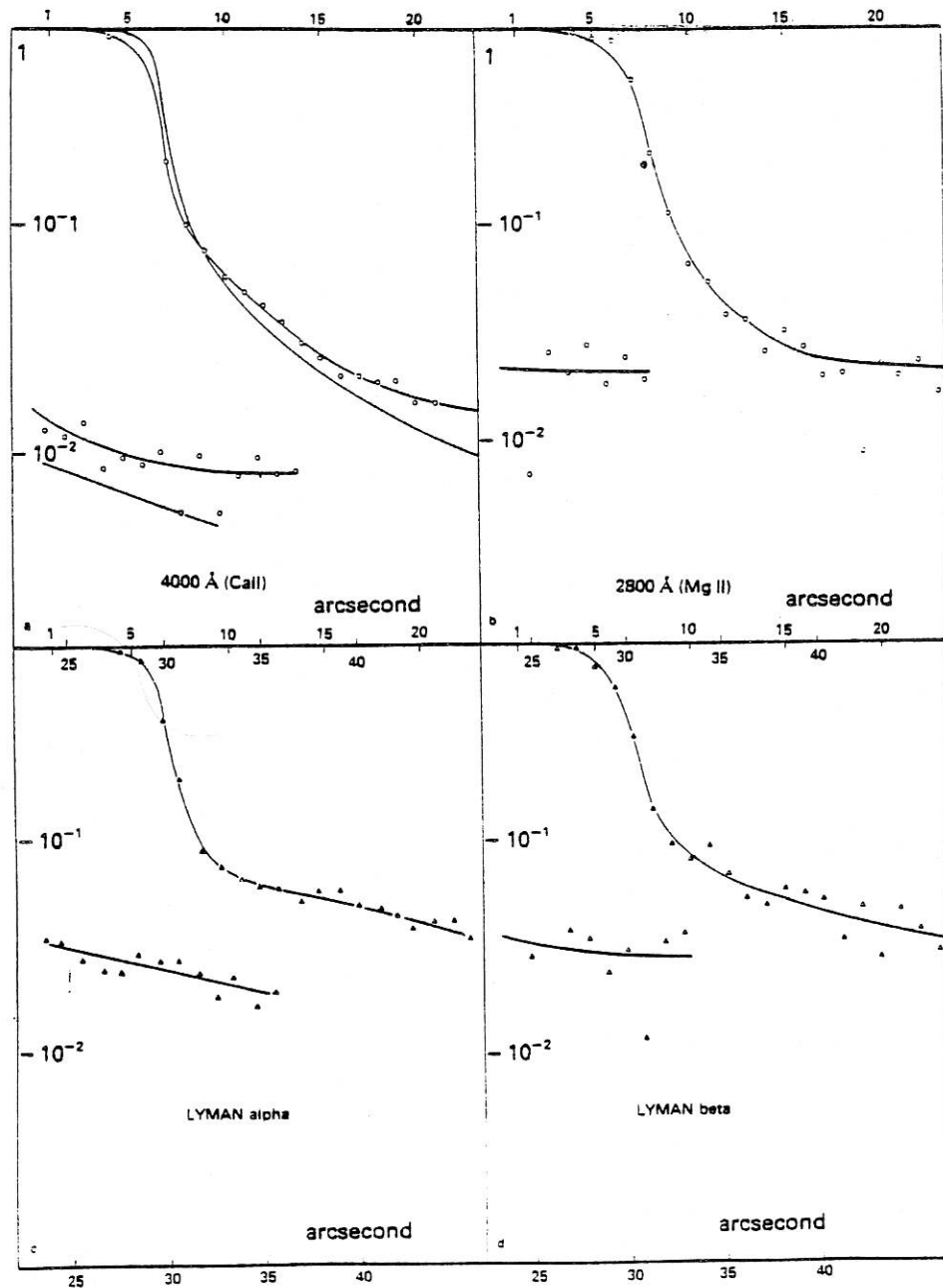


Fig. 8. Distribution of intensity at all wavelengths in the wings of the image of a slit of $190\ \mu$ width ($\approx 10''$) using the $1''$ slit. At $4000\ \text{\AA}$ we compare the results to the values expected from theory.

the raster mechanism did not induce any vignetting and that the intensity of a uniform field of view was constant within ± 0.003 .

The dependence of spatial resolution on temperature was checked in the LPSP vacuum chamber which can also provide a thermal vacuum. The equipment used in this test includes a collimator placed in the chamber in front of the instrument, and it is not possible in fact to separate the effect of the temperature on the instrument from that of the collimator: since the design of both the collimator and the telescope are very similar, we assess that any observed variation in focus corresponds to twice that of the telescope alone. Under this assumption, we were able to confirm that there were no major changes of the image quality in the temperature range from $+12^\circ\text{C}$ to $+35^\circ\text{C}$.

At completion of these tests, we could say that the spatial resolution of our instrument varied between 1.5" and 2.0", in agreement with our objectives.

6.2. SPECTRAL RESOLUTION AND LINE CENTERING

The designed spectral resolution ($30\text{ m}\text{\AA}$) and the simultaneous positioning of 6 exit slits at 6 wavelengths require a very precise adjustment.

6.2.1. Settings

The grating was first simulated by a plane mirror (G.S.) the position of which could be set with a theodolite. P1 was adjusted by autocollimation on the G.S. Then the $L\alpha$ slit was mechanically positioned and P3 adjusted by the same autocollimating process. The position of the $L\alpha$ slit at the focus of P3 was checked through the set (entrance slit + P1 + G.S. + P3). The other slits and the corrector were positioned in the same manner. The optical properties were checked in air for the Mg and the Ca channels. The simultaneous centering for all wavelengths was obtained by iterations on these 4 channels in vacuum, because of the variation of the index of refraction of air, particularly important in the Mg and Ca channels.

6.2.2. Spectral Resolution

The method used to determine spectral resolution differed for the Ca and Mg channels, and the Lyman channels. Hollow cathode light sources, which emit very narrow lines of Ca II and Mg II, were used to determine the spectral resolution nearly directly. Figure 9 compares the measured profiles with a synthesized profile obtained through the convolution of the line shape assumed to have a width at half maximum of $5\text{ m}\text{\AA}$, with the theoretical instrumental profile of 0.02 \AA FWHM. The theoretical resolution seems to be reached for Ca II except in the far wings. For the Mg II lines, the observed profile is nearly 0.01 \AA broader than the theoretical one, making the spectral resolution at this wavelength close to 0.03 \AA . We probably see here the effect of the strong aberrations in this channel, that could not be eliminated totally by the corrector.

For the $L\alpha$ channel, it was not possible to find any light source with lines narrow enough to use the same procedure. However, as shown on Figure 10a, the $L\alpha$ line of

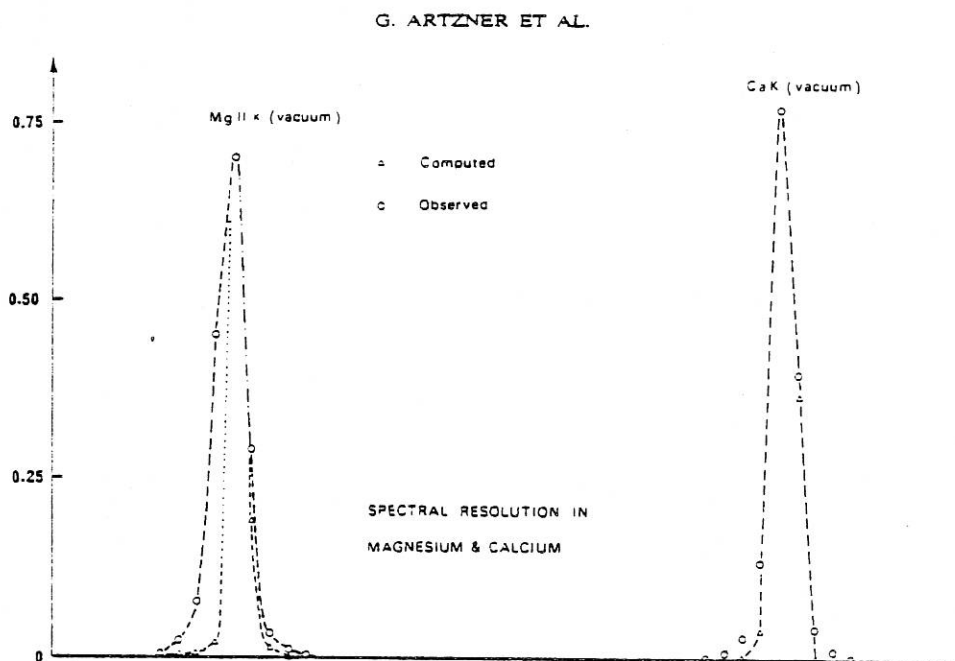


Fig. 9. Comparison between the theoretical and observed spectrometer instrumental profiles. The computation of the theoretical profile assumes that the width of the lines emitted by the hollow cathode light source is $5 \text{ m}\text{\AA}$.

both atomic hydrogen and deuterium is strongly self-reversed and spectral resolution can be determined by measuring the width of either the reversed core or of the two narrow lateral emission peaks. Both methods showed that it was better than $21 \text{ m}\text{\AA}$.

The source used at Lyman alpha emits narrow Lyman beta lines of D_1 and H_1 that are single peaked if the gas in the lamp is at low pressure (Figure 10b). The D_1 1025 \AA line was used and it was found that the spectral resolution of the $L\beta$ channel was equal to its theoretical value of $60 \text{ m}\text{\AA}$.

The presence of 'ghosts' is easily noticeable in all channels, in the wings of the lines (Figure 11). The separation between successive ghosts obeys the theory for Rowland ghosts. However, their intensity does not decrease as rapidly as expected for Rowland ghosts. The ghosts were measured carefully up to 2 \AA from the core of the lines and their effect on the resulting instrumental profile has been taken into account, so that it is possible through deconvolution techniques to restore the original line profile.

No changes in spectral resolution could be detected after vibration and shock tests. However, during thermal vacuum below 0°C , we noticed the appearance of coma aberration in the Mg II channel. We interpreted this to be the result of thermal deformation of the aluminium casting of the corrector. This effect was nevertheless negligible in the range of normal operating temperatures. No thermal effects were observed in the other channels.

THE LPSP EXPERIMENT ON OSO-8. I

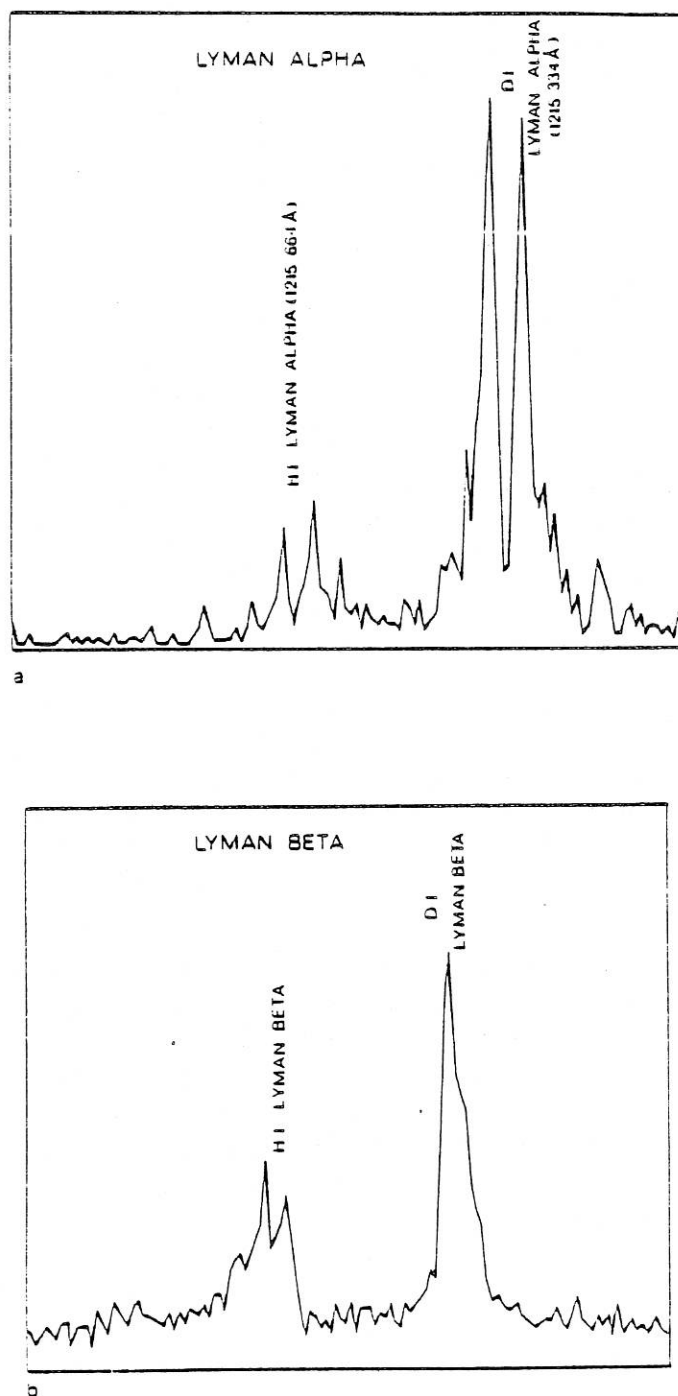


Fig. 10. Profiles of the $L\alpha$ and $L\beta$ lines of hydrogen and deuterium emitted by a low pressure discharge lamp, measured with the instrument. The separation between two points of measurement corresponds to one grating step, i.e.: 0.0084 \AA for $L\alpha$, 0.0074 \AA for $L\beta$.

G. ARTZNER ET AL.

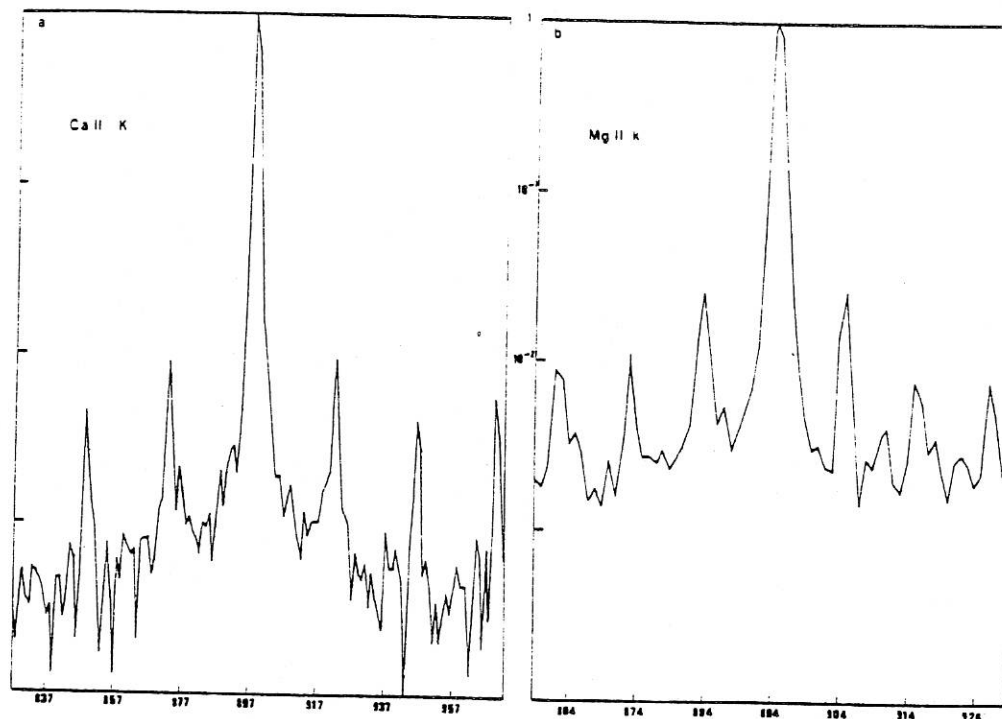


Fig. 11. The spectrometer instrumental profile at the wavelengths of the Mg II k and Ca II K lines on a logarithmic scale showing the successive 'ghosts' in the wings of the central line. Hollow cathode light sources were used for this measurement. The abscissa is grating step number.

6.2.3. Line Centering

Centering was performed in vacuum through several iterations. The cores of the six main lines could be adjusted to within four grating steps. Temperature variations have no effect on the centering; however, we noticed changes in the absolute position of the lines, for temperatures ranging from -2°C to $+35^{\circ}\text{C}$. These positions vary by no more than 6 grating steps. A global change of 20 steps was noticed in the centering after vibrations at Hughes Aircraft. This was probably due to a change in the relative positions of the core and coils of the differential transformer. No measurable change occurred in the position of lines following launch.

6.2.4. Scanner Linearity and Dispersion Law

Scanner linearity and dispersion law were measured by the use of narrow spectral lines. Throughout different scans obtained in different conditions, the grating scanner was observed to be linear to better than 3%. The repeatability is better than 0.25 step.

6.3. PHOTOMETRIC CALIBRATIONS

The sensitivity of an instrument like ours may change rapidly and strongly once in orbit. Changes in sensitivity have already been observed in other instruments [3].

THE LPSP EXPERIMENT ON OSO-8, I

The use of LiF coated optics makes these changes more likely. This is why several calibration rockets have been scheduled to be launched during the lifetime of OSO-8 to calibrate in orbit. The knowledge of the instrument efficiency before launch is necessary in order to know the relationship between the incident solar flux and the number of counts measured on board during the orbits preceding the first calibration rocket.

The instrument efficiency is the product of the efficiency of each optical element times that of the detectors. When necessary, the effect of the non-linearity of the detectors must be taken into account. Since we were supposed to work at moderate or low counting rates, this effect was absolutely negligible and was taken to be unity for the range of utilization. The efficiency can be measured element by element or globally. Both methods have been used here.

Photometric calibrations have been conducted at LPSP in May 1974, more than one year before the launch, and in April 1975 at the Hughes Aircraft Company.

The use of an Al + LiF coating maximizes the efficiency at $L\beta$ [4]. However, it is a fragile coating which deserves particular attention. This is why we have designed and built at LPSP a special laboratory which we briefly describe here:

6.3.1. *The LPSP Integration and Calibration Laboratory*

This laboratory is located in Chalais-Meudon (Figure 12), on the grounds of the Office National d'Études et de Recherches Aeronautiques (ONERA) which kindly lent the space to us. It was specially designed for OSO-8. It is located inside a pressurized tent. These facilities include:

- (a) a 15 m³ vacuum chamber with cryogenic and turbo-molecular pumping. The use of a 1.25 m aperture valve allows a fast turn around, and it takes only 45 min to go from atmospheric pressure down to 5×10^{-7} torr. The vacuum chamber has thermal vacuum capabilities and can go from -30°C to $+70^\circ\text{C}$. Inside the chamber is an optical bench, isolated against vibrations by air cushions servo controlled in position to better than $30\ \mu$.
- (b) a normal incidence MacPherson 225 monochromator, coupled to the optical bench,
- (c) a clean room (class 1000, with class 100 areas over the optical benches), equipped with two granite optical benches isolated against vibrations. The opening of the vacuum chamber is into the clean room area.
- (d) special clean working areas for mechanical and electrical assembly,
- (e) storage areas,
- (f) a PDP-11/20 computer.

Temperature and humidity are controlled everywhere in the clean room area and are maintained at $20^\circ\text{C} \pm 1^\circ\text{C}$ and lower than 30% respectively, throughout the year.

G. ARTZNER ET AL.

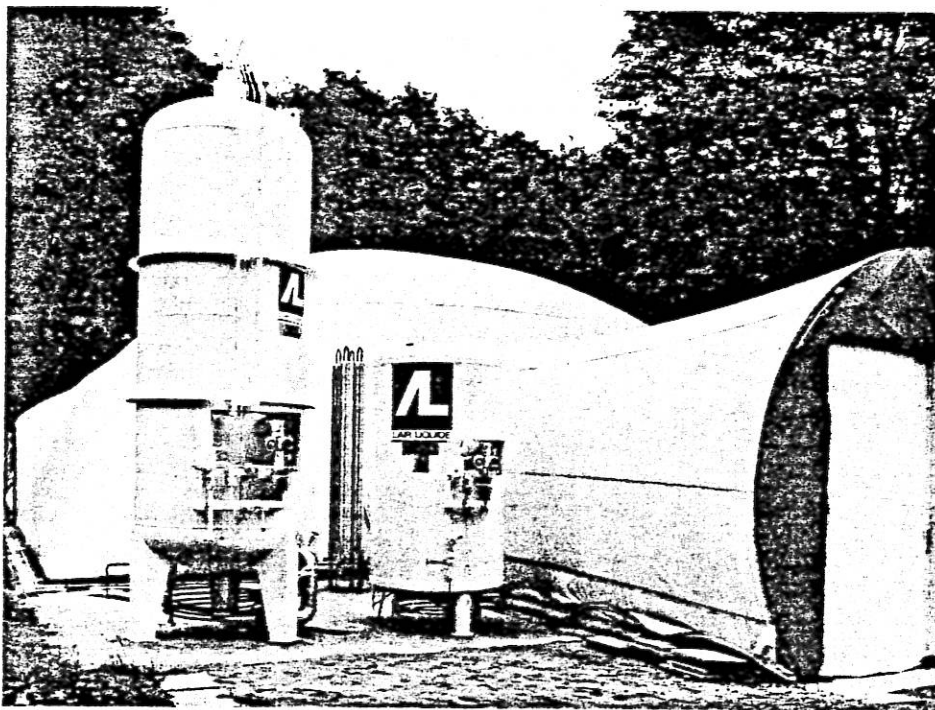


Fig. 12. The LPSP integration and calibration facilities at the Office National d'Études et de Recherches Aeronautiques in Chalais-Meudon.

6.3.2. Mirror and Grating Efficiency

The grating and the mirrors have been coated at the Goddard Space Flight Center with Al+LiF. All optical parts have been shipped in pressurized containers filled with dry nitrogen. They were stored at Chalais-Meudon in special containers, periodically purged with dry nitrogen. The instrument contained two monitor mirrors whose efficiency was frequently measured from the time of coating up to launch. At Hughes Aircraft, the experiment was continuously purged with dry nitrogen.

On Figure 13 we show the variation of efficiency with time of one monitor mirror at $L\alpha$ and $L\beta$. No detectable variations were observed.

6.3.3. Photometric Calibrations at Chalais-Meudon

We have evaluated the absolute efficiency using three methods:

(a) Calibration of each individual element:

Prior to the assembly of the experiment, the efficiency of each component was measured. Relative efficiency of the mirrors, grating and filters was determined using a stable source and a detector (a photomultiplier from 1150 Å to the visible, and a spiraltron below 1150 Å). The absolute sensitivity of the detectors was obtained by comparison with a NBS type 543P09 photodiode. The results of these measurements are given in the first line of Table X.

THE LPSP EXPERIMENT ON OSO-3. I

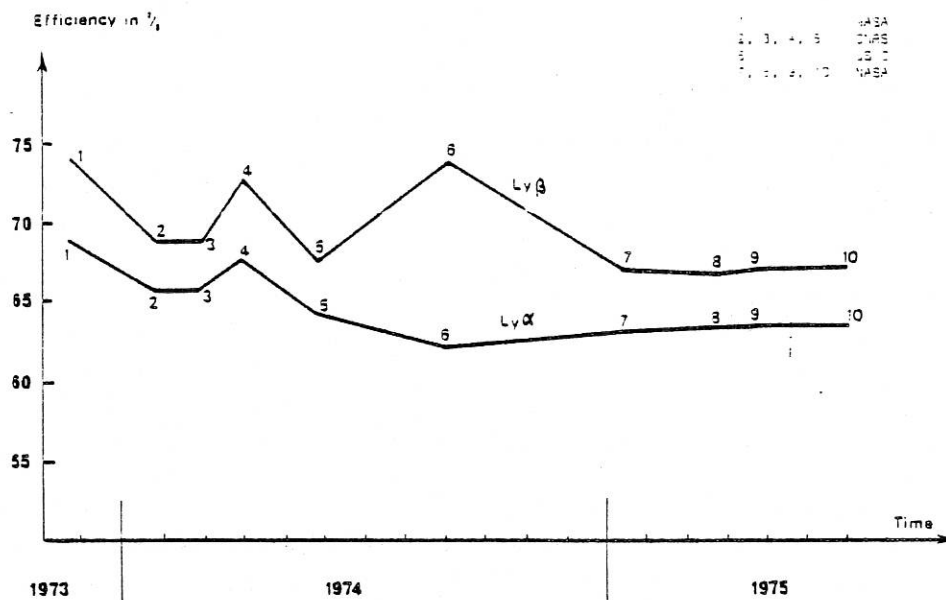


Fig. 13. The variation with time of the monitor mirror efficiency. The mirror was located aft of the spectrometer. The coating is Al + LiF.

(b) Calibration in Ca II and Mg II using a black body:

We made a calibration in the near ultraviolet (Ca II and Mg II channels) using a black body provided by R. Peyturaux of the Institut d'Astrophysique de Paris. A pyrometer measured the black body temperature, at 6000 Å, with an accuracy of 1 °C, and a servo-loop controlled the power supply to maintain the temperature within 1 °C. During calibration, the internal raster mechanism was commanded to measure the homogeneity of the area of the arc intercepted by the entrance slit. We could verify that the uniformity was better than 20%. We made a wavelength scan for several temperatures and several entrance slits and were able to measure the sensitivity as a function of wavelength. These measurements were made at atmospheric pressure and were corrected for residual atmospheric absorption later. They are given in the second line of Table X.

(c) Vacuum UV calibrations:

We measured the sensitivity of the $L\alpha$ channel in the vacuum chamber, with a windowless hydrogen source and the MacPherson 224 monochromator. To avoid source instability, it was found easier to calibrate separately the telescope and the spectrometer. A beam mapper with a calibrated detector measured the incident flux at the entrance of the telescope and a second calibrated detector placed at the aft of the slit in the spectrometer measured the flux entering the spectrometer; the ratio of these two values gives the telescope efficiency. The detectors were calibrated against the NBS photodiode. The results are given in Table X, separately for the telescope and the spectrometer. Time did not allow us to make a calibration at $L\beta$ before delivery of the instrument.

G. ARTZNER ET AL.

TABLE X

The instrument sensitivity measured with different techniques at different times. Units: count/photon

	Ca II H	Ca II K	Mg II h	Mg II k	L α	L β
Calibration of individual elements 1971, 1972, 1973, 1974	6.8×10^{-3}	8×10^{-3}	2.9×10^{-3}	2.9×10^{-3}	2.6×10^{-4}	1×10^{-3}
Calibrations with IAP Black body, May 1974	1.2×10^{-3}	3.1×10^{-3}	1.6×10^{-3}	2.4×10^{-3}	—	—
Vacuum UV calibrations at LPSP, May 1974						
Telescope	0.5	0.5	0.57	0.57	0.27	Not measured
Spectrometer	2.9×10^{-3}	8.6×10^{-3}	1.6×10^{-3}	1.9×10^{-3}	5.5×10^{-5}	Not measured
Global	1.45×10^{-3}	4.3×10^{-3}	9.1×10^{-4}	1.1×10^{-3}	1.5×10^{-5}	Not measured
UV calibrations at Hughes Aircraft, April 1975	1.5×10^{-3}	3.6×10^{-3}	1.2×10^{-3}	1.6×10^{-3}	8×10^{-5}	5×10^{-4}

6.3.4. Calibrations at Hughes Aircraft Company

These calibrations were done 6 weeks prior to launch using a Hughes Aircraft vacuum chamber equipped with cryogenic pumping. This calibration was done at the same time on both the LPSP and the LASP instruments. The same method as described in (c) above was used, with the exception that we had no monochromator at our disposal. This problem was overcome by filtering the light from the source before it was measured by the detector on the beam mapper, so that we knew what the intensity of the light entering the instrument was at a given wavelength. The sources and the methods of filtering differed for each channel.

(a) Ca II and Mg II

We used hollow cathode sources and narrow band interference filters. The measurements were easy for Ca II. However for Mg II, the presence of several lines of Mg II and Mg I made it necessary to separate the contribution of the two resonance lines from the others. Hence, the calibration is less accurate for Mg II.

(b) At L α we used a hydrogen source and a small spectrometer, generously lent to us by LASP, which had a resolution of $\approx 1 \text{ \AA}$. Hence, the flux from only the L α line was measured and we obtained accurate measurements.

(c) At L β , we measured the flux with a spiraltron covered with an indium filter. The same problem as for Mg II occurs here because the hydrogen lamp contains many lines in addition to L β itself. The results are given in the last line of Table X.

6.3.5. Discussion of the Results

Calibration of individual elements leads to an overall efficiency systematically higher than measured by the other methods. We think that this is due, at least partly, to the

THE LPSP EXPERIMENT ON OSO-8. I

fact that the sensitivity of each detector was an average over the area of the photocathode while only one small portion of it is actually used in the instrument. This can explain, in particular, the difference observed between the Mg II h and k channels. With the exclusion of this first method for Ca II, they all agree within 30%.

At $L\alpha$, the low efficiency obtained at Chalais-Meudon, as compared to the results obtained with the first method was found to be due to a defect in the pulse discriminator which was changed subsequently. The values of line 6 of Table X are those obtained after this modification.

At $L\beta$, the results agree reasonably well with the expectations given by the first method.

6.3.6. Scattered Light and Dark Count

We undertook the measurement of scattered light in both the telescope and the spectrometer at Chalais-Meudon. We were particularly concerned with light coming from low orders of diffraction not perfectly blocked out by the filters. For all channels, except $L\beta$, the stray light from any order of diffraction was not measurable. For $L\beta$, lines from the 15th, 13th, 12th and 11th order were identified easily but no contribution from the lower orders could be detected.

Apart from the light coming from the wing of the diffraction pattern, no scattered light due to spurious reflections in the telescope tube could be detected. The dark counts for each detector were very low as indicated in Table VIII allowing us to use very weak signals for extraction of scientific information. These low values for the dark count have been confirmed in orbit.

7. Conclusion and Preliminary Results

OSO-8 was placed into a nearly circular orbit of 544 km perigee and 560 km apogee with a 33° inclination by a Delta rocket on the morning of June 21, 1975 (7:47 A. M. Eastern Daylight Time). The high voltages on the Ca II and Mg II channels were turned on at orbit 30 on June 23, and at orbit 45 on June 24 for the $L\alpha$ and $L\beta$ channels. Figure 14 shows the spectra for the Mg II and $L\alpha$ channels, obtained during the early orbits using the full capabilities of the spectral scanner. Figure 15 shows detailed simultaneous profiles of $L\alpha$ and $L\beta$ for the quiet Sun and Figure 16 is a series of simultaneous $64'' \times 64''$ internal rasters made in the core of the 6 lines. From these preliminary results, we could assess that spectral and spatial resolutions were nominal in orbit for all wavelengths.

The LPSP instrument on OSO-8 represents one of the largest and most complex UV experiments of the French space program. The financial support for the hardware came from CNES under grants 70 CNES 220, 71 CNES 202, 72 CNES 202, 73 CNES 202, 74 CNES 202, 75 CNES 202. Special funding was also provided by C.N.R.S. for the salaries of 7 LPSP scientists and programmers in charge of operating the instrument at Boulder during the period of operations.

G. ARTZNER ET AL.

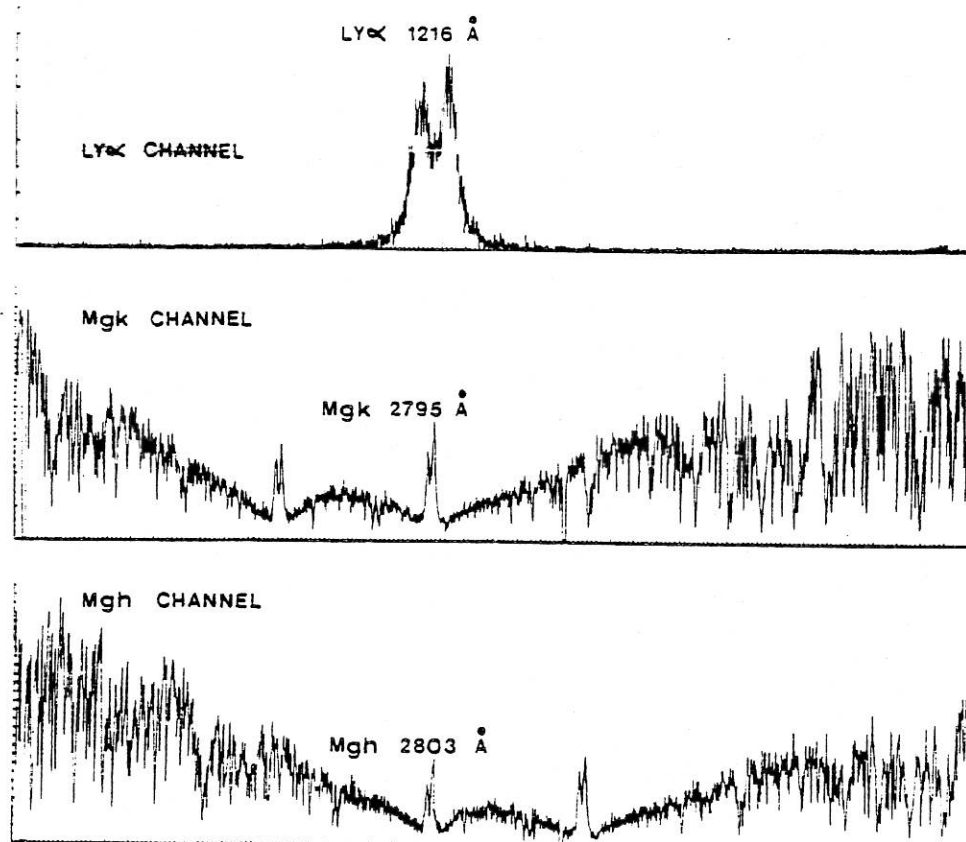


Fig. 14. The solar spectrum in the Mg II and $\text{Ly}\alpha$ channels. The wide exit slit was used at $\text{Ly}\alpha$ giving a resolution of 0.2 Å.

Acknowledgements

It is our pleasure to express our warm acknowledgements to several people and institutions. It would not have been possible to design and build this experiment without the support of CNES and more particularly of Dr A. Lebeau, Director of Programs and Plans, who made every effort to make this program a success. We would also like to thank Dr C. Poher who provided support, particularly during the qualification tests at the Centre Spatial de Toulouse. We have been very impressed by the level of effort spent by MM. Cazenave, Feaugas and Barria who are in charge of data handling at CNES. Invaluable assistance was offered to us by the engineers of the Goddard Space Flight Center. It would be a lengthy process to name them all, however, it would be unfair to omit mentioning the names of J. Thole, R. Pickard, J. Donley, R. White, J. F. Osantovsky, J. Mangus and W. Worrall. Impressive also was the work accomplished by the engineers of Hughes Aircraft Company who built one of the most complex and impressive space solar observatories. The very

THE LPSP EXPERIMENT ON OSO-8. I

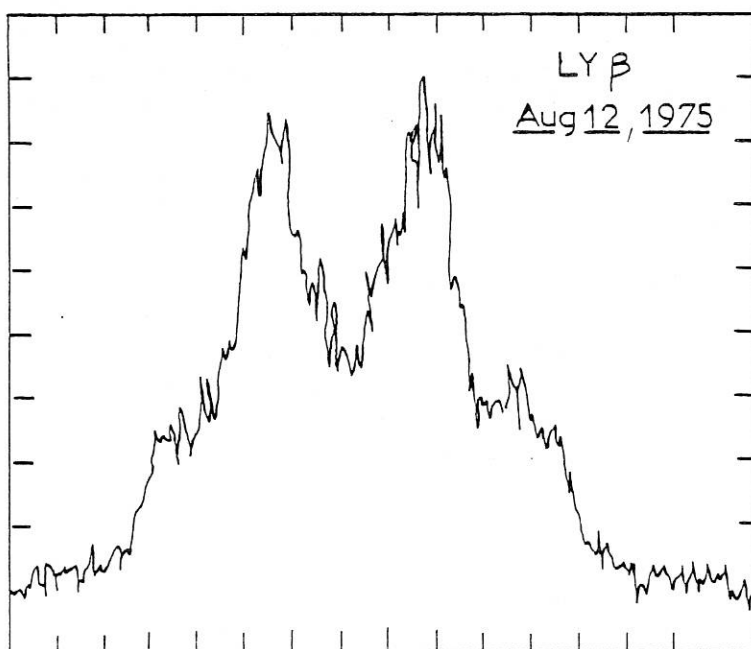
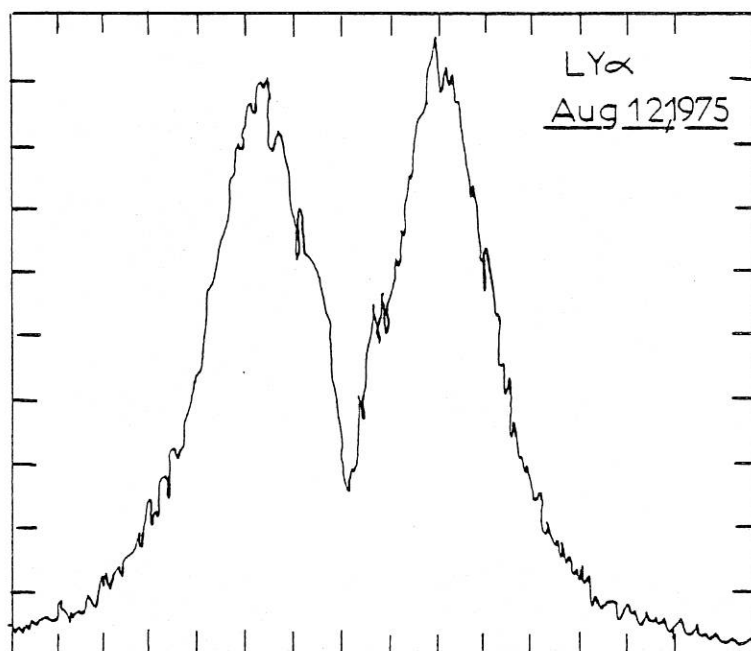


Fig. 15. Average quiet Sun detailed profiles of the $L\alpha$ and $L\beta$ lines using the $6'' \times 6'$ slit.

G. ARTZNER ET AL.

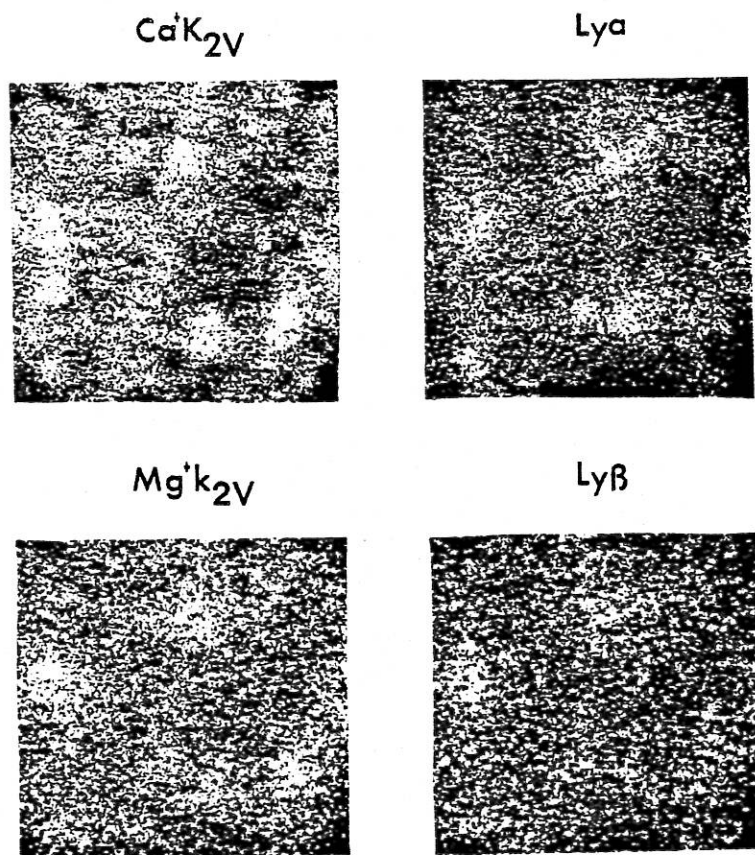


Fig. 16. 64×64 square arcseconds images generated by internal raster (one arcsecond increments). $\text{Ca } \Pi_{K2V}$, $\text{Mg } \Pi_{K2V}$, $L\alpha$ and $L\beta$ (July 6, 1975, 19:00 G.M.T.) are taken simultaneously.

existence of this program owes itself to numerous scientists who have always been ready to fight to keep OSO-8 alive. We think in particular of the international solar physics community, of our Guest Investigators and of the members of our Selection Committee. This committee was placed under the chairmanship of Prof. J. C. Pecker who accomplished a delicate and more than often diplomatic task. The operations of the experiment from Boulder would not have been possible without the kind hospitality of the LASP personnel, in particular its Director, C. Barth and Dr E. Bruner, Principal Investigator on the University of Colorado experiment. Our warm acknowledgements are also addressed to Drs A. Skumanich and O. R. White of H.A.O. for their continuous assistance and their sympathetic welcome. One of us is now with the Lockheed Palo Alto Research Laboratory. We would like to thank Dr L. Acton for kindly permitting him to continue working on this program.

The accomplishment of this program created heavy loads on nearly everybody at LPSP and all LPSP personnel must be acknowledged for their assistance, comprehension and often times their sacrifices for this program.

THE LPSP EXPERIMENT ON OSO-8, I

We are particularly indebted to the ONERA and to its Director, Mr Contensou, and to Mr Hilaire for their hospitality at Chalais-Meudon.

Dr Peyturaux and Mr Vitry of the Institut d'Astrophysique provided a very valuable assistance in the calibration for the instrument, as well as for the rocket instruments.

Finally, it is our pleasure to thank here Prof. J. L. Steinberg, who provided us assistance in the design and fabrication of the electronics.

References

1. Labeque, A., Vite, M., and Bourguignon, G.: *Space Sci. Instr.* 1, 419 (1975).
2. Wouters, F. and Vite, M.: in preparation (1976).
3. Reeves, E. M. and Parkinson, W. H.: Harvard College Observatory, Technical Report No. 12, 1969.
4. Bradford, A. P., Hass, G., Osantowski, J. F., and Toft, A. R.: *Appl. Opt.* 8, 1183 (1969).

Article II

THE LPSP INSTRUMENT ON OSO-8

II.: In-flight performance and preliminary results

R.M. BONNET, P. LEMAIRE, J.C. VIAL, G. ARTZNER, P. GOUTTEBROZE
A. JOUCHOUX, J.W. LEIBACHER, A. SKUMANICH and A. VIDAL-MADJAR

THE LPSP INSTRUMENT ON *OSO 8*. II. IN-FLIGHT PERFORMANCE AND PRELIMINARY RESULTS

R. M. BONNET, P. LEMAIRE, J. C. VIAL, G. ARTZNER, P. GOUTTEBROZE,
 A. JOUCHOUX, J. W. LEIBACHER,* A. SKUMANICH,† AND A. VIDAL-MADJAR

Laboratoire de Physique Stellaire et Planétaire, C.N.R.S., France

Received 1977 August 29; accepted 1977 November 8

ABSTRACT

The in-flight performance for the first 18 months of operation of the French, pointed instrument on board *OSO 8* are described. The angular and spectral resolution, the scattered light level, and various other instrumental parameters are evaluated from the observed data and shown to correspond mostly to nominal design values. The properties of the instrument are discussed, together with their evolution with time. The distribution of the first 8363 orbits between various observing programs is given. Preliminary results are also described. They include studies of the chromospheric network, sunspots and active regions, prominences, oscillations in the chromosphere, chromosphere-corona transition lines, and aeronomy.

Subject headings: instruments — Sun: chromosphere — Sun: prominences — Sun: spectra — Sun: sunspots — ultraviolet: spectra

I. INTRODUCTION

One of the major goals of solar physics is to understand the nature, origin, and evolution of the various features present in the solar atmosphere. Some, like the granulation, represent dynamical responses to the convection zone. Others, like spots or the more dispersed magnetic flux tubes (e.g., network fragments), represent symptoms of a magnetic process. Any advance in our understanding of such interior processes must come from high angular and spectral resolution observations of the line profiles of such features.

The NASA orbiting solar satellite *OSO 8*, launched on 1975 June 21, carried in its pointed section two instruments designed for the highest angular and spectral resolution achieved by spacecraft to date. One of these instruments was the responsibility of the Laboratory for Atmospheric and Space Physics (LASP) of the University of Colorado, the other was that of the Laboratoire de Physique Stellaire et Planétaire (LPSP) of the Centre National de la Recherche Scientifique (France).

In this paper, we describe the performance achieved in orbit and outline the main results obtained with the LPSP instrument after 18 months of successful operation. Most of these results are in a preliminary state. A complete description of the instrumentation has been given in Artzner *et al.* (1977), hereafter referred to as Paper I.

II. SUMMARY OF THE INSTRUMENT CAPABILITIES

Because of the limitations imposed by the size of the spacecraft (although considerably larger than the previous *OSOs*), the LPSP telescope was a Cassegrainian with a diameter of 16 cm. Consequently we limited our observations to the most intense chromospheric lines. Because the chromosphere is of limited depth, the spectrometer was designed so as to simultaneously observe six lines:

Ca II H (396.9 nm) and K (393.4 nm);

Mg II *h* (280.3 nm) and *k* (279.6 nm);

H I $L\alpha$ (121.6 nm) and $L\beta$ (102.5 nm).

A very rapid and versatile spectral scanner made it possible to also study the lines of O VI (103.2 nm) and Si III (120.6 nm) nearly simultaneously with those listed above and enabled us to study propagation effects and to obtain height resolution from the upper-photosphere to the lower corona. Table 1 summarizes the main characteristics of the spectrometer, which operates with two different spectral resolutions.

Two methods were available to make spectroheliograms. One was by means of spacecraft rasters: two image sizes were available, $44' \times 40'$ and $2'75 \times 2'3$ (nominal). The reader is referred to Paper I (Table 2) for more details on these rasters. In addition, the LPSP telescope had an articulated secondary mirror which was moved by a two-axis stepping mechanism. Accordingly the solar image could be moved step by step. Each step was $1''$ on the solar surface while the maximum area covered was $64'' \times 64''$.

A slit wheel mechanism, at the focus of the telescope, was used to select various slit sizes ranging

* Lockheed Palo Alto Research Laboratory, Palo Alto, CA.
 † High Altitude Observatory, National Center for Atmospheric Research; and University of Colorado, Boulder. The NCAR is sponsored by the NSF.

LPSP INSTRUMENT ON *OSO 8*

TABLE 1

DESIGN CHARACTERISTICS OF THE *OSO 8* LPSP SIX-CHANNEL HIGH-RESOLUTION SPECTROMETER

CENTRAL LINE	(nm)	SPECTRAL RESOLUTION (nominal)			MAXIMUM SPECTRAL RANGE (nm)	SPECTRAL INCREMENT PER GRATING STEP (nominal) (nm)
		Low Mode (nm)	High Mode			
			(nm)	km s ⁻¹		
Ca II H.....	396.9	0.1	0.0020	1.51	395.164-398.244	0.00149
Ca II K.....	393.4	0.02	0.0020	1.52	391.444-394.942	0.00169
Mg II h.....	280.3	0.1	0.0025	2.67	277.739-282.264	0.00219
Mg II k.....	279.6	0.02	0.0025	2.68	277.005-281.551	0.00220
H I L α	121.6	0.02	0.0020	4.93	120.569-122.291	0.00083
H I L β	102.5	0.1	0.0060	17.65	101.686-103.229	0.00074

NOTE.—Wavelength units are nanometers (nm).

from $1'' \times 1''$ to $1'' \times 40''$ as well as one corresponding to $6'' \times 2''$.

III. IN-FLIGHT PERFORMANCE

Prior to launch, the instrument was submitted to numerous tests and calibrations, the results of which are given in Paper I. Here we present the actual performance measured in flight.

a) Angular Resolution

The ground tests of the telescope led us to expect an instrumental profile with a full width at half-maximum (FWHM) of $2''$. Two methods have been used to estimate the angular resolution in orbit:

i) Images of Limb Shape

Repeated scans of the solar limb, as observed with a $1'' \times 1''$ aperture using the internal raster mode in the

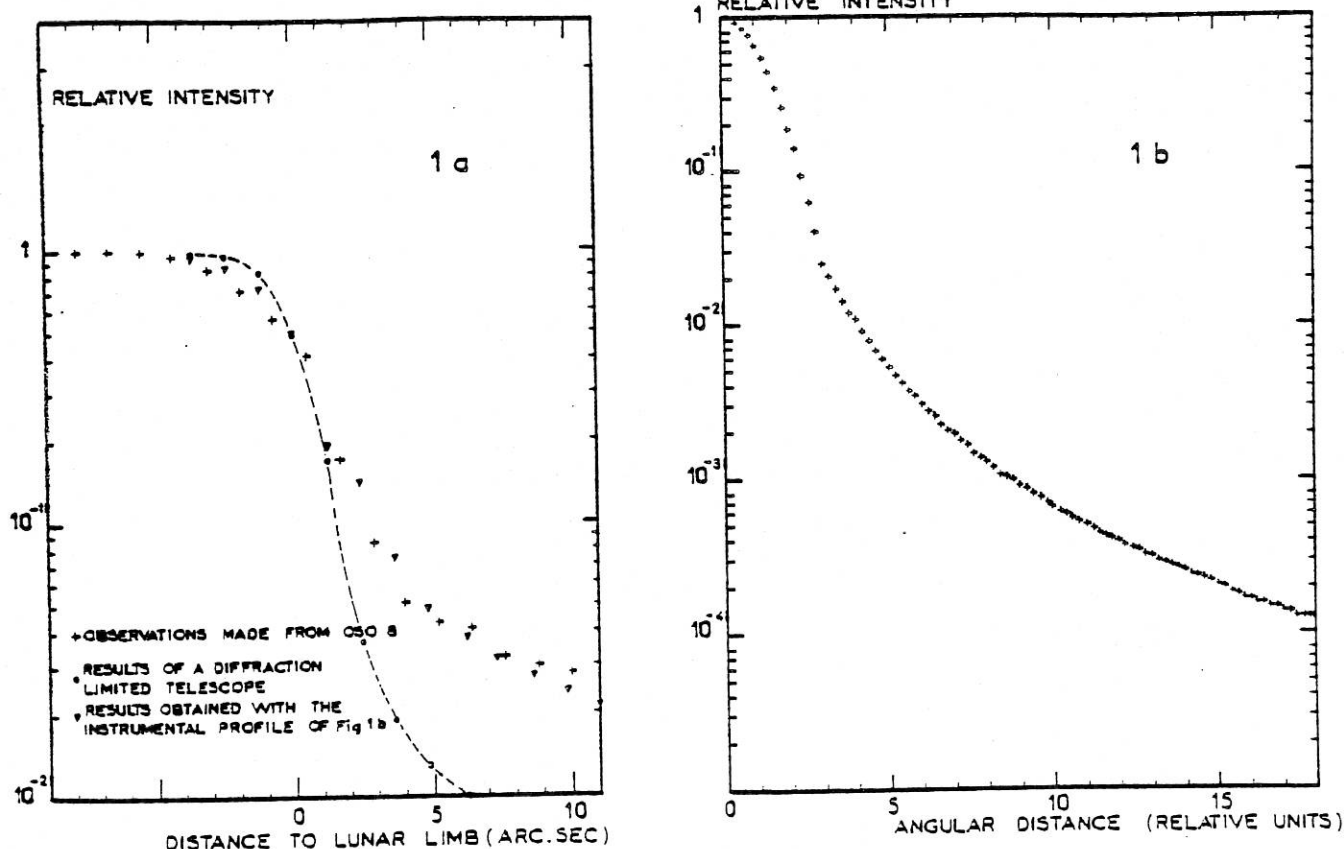


FIG. 1.—(a) Internal raster scans across the lunar limb in Ca K. The dots show the results one would obtain assuming the telescope to be diffraction limited. The triangles show the results one obtains assuming the instrumental profile to be that represented on (b), the telescope instrumental profile.

far wings of the Ca II line, show a limb darkening with a 50% decrease over an angular distance of 2".

However, this method does not separate the resolution of the telescope from the jitter of the pointing system. Rapid, one-dimensional scan of the solar limb as well as other methods allowed us to estimate the amplitude of the rms jitter as 0.5.

ii) Partial Solar Eclipses

On 1976 April 29 and October 23, two partial eclipses of the Sun were visible from *OSO 8*. Figure 1a represents spatial scans laterally across the lunar limb measured in relative intensity units. The actual observations are compared with the results of a computation assuming the 16 cm Cassegrainian telescope to be diffraction limited, and to have an instrumental profile as given in Figure 1b. The fit using the profile of Figure 1b represents a good approximation. We therefore conclude that the instrumental profile has a FWHM of 2.5 ± 0.5 .

b) Spectral Resolution

i) $L\alpha$ and $L\beta$ Channels

For these we take advantage of the narrow absorption line due to geocoronal hydrogen. By applying a method developed for the study of interstellar absorption lines (Vidal-Madjar *et al.* 1977), we obtain a spectral resolution in flight of 0.002 ± 0.0005 nm at $L\alpha$, and 0.006 ± 0.001 nm at $L\beta$.

ii) Calcium and Magnesium Channels

We compare the solar spectra obtained by our instrument with ground based (Ca II channels) and balloon- or rocket-borne observations (Mg II channels).

In Figure 2 we show the full range Ca II K and Mg II k spectra from *OSO 8*. The variation with wavelength of the sensitivity of the instrument has been corrected for, and the spectra are deconvoluted from the instrumental profile. The comparison with the spectrum of the Kitt Peak Preliminary Solar Atlas (Brault and Testerman 1972), which has a spectral resolution of 0.0024 nm, shows that our resolution in orbit is better than this value. In the case of the Mg II channels, comparison with the spectra of Lemaire and Skumanich (1973) and Kohl and Parkinson (1976) yields a resolution of 0.0025 ± 0.00025 nm. This value is equal to the nominal design value (cf. Table 1).

c) Dispersion and Grating Mechanism (Spectral Scanner) Stability

The dispersion law of the spectrometer was determined in orbit by measuring the position, in units of a grating step, of 11 solar absorption lines of known wavelengths in the Ca II and Mg II channels. For the $L\beta$ channel we used the O I lines at 130.48 and 130.6 nm and N I at 119.9 nm (which appear in the 11th and 12th orders of diffraction).

Because of the lack of lines in the $L\alpha$ channel, we deduce the dispersion law from that at $L\beta$. The absorption line of geocoronal hydrogen provides an absolute

reference. This proved to be valuable due to the appearance of positioning uncertainties (± 1 grating step) in the movable $L\alpha$, $L\beta$ exit slit mechanism. The dispersion law was measured repeatedly to check for long-term variations. Over 1 year we found that the correspondence between absolute wavelength and grating step number varied by no more than ± 3 grating steps (cf. last column of Table 1).

To check the mechanism stability over one orbit, we measured the position of the photospheric line 391.52 nm in the wings of Ca II K. Any departure from the orbital Doppler effect could be attributed to photospheric Doppler shifts and/or changes in the spectrometer. The result is shown on Figure 3. One can easily recognize the 300 s photospheric Doppler oscillations after removal of the orbital Doppler shift, measured for the first time from space. The amplitude of the residual noise on this curve amounts to ± 30 m s⁻¹. The stability of the mechanism over a full orbit day is better than one grating step and exceeds our design expectations. We are able to easily and accurately measure Doppler shifts of photospheric and chromospheric lines (see § Vc below).

d) Scattered Light Background and Dark Current

The level of scattered light in the telescope plus spectrometer was determined from partial eclipses of the Sun. From Figure 1 we see that at 11" from the lunar limb this level amounts to 2% of the intensity of the disk in the calcium channels. For Mg II it is 4%. For $L\alpha$ and $L\beta$ these figures become 10% and 20%, respectively, which indicates that the scattered light level may vary with wavelength, roughly as $1/\lambda^2$.

No simple and unambiguous method was available to measure separately and give an absolute value for the amount of scattered light in the spectrometer due to wavelengths well away and near the wavelength of interest.

In the case of the Ca II and Mg II channels, we could compare the performance of our spectrometer with those of other ground-based or rocket-borne instruments. The result of this comparison appears in Table 2, where we give the ratio of intensities at Ca II H_1 and K_1 , Mg II h_1 and k_1 , relative to those of the Ca II and Mg II line wings. We notice that our performance is excellent for the Ca II channels, for which these ratios are smaller than those deduced from the Utrecht (Minnaert, Mulders, and Houtgast 1940) and the Air Force (Beckers, Bridges, and Gilliam 1976) atlases. We also compare our values with those of Linsky (1970) and of White and Suemoto (1968) who used particularly good optical systems. The Utrecht Atlas was used to evaluate the ratio of the H_3 and K_3 intensities relative to that of the continuum at 400.0 nm. The results are:

$$\frac{I_{H_3}}{I_{400.0}} = 0.053, \quad \frac{I_{K_3}}{I_{400.0}} = 0.065, \quad \text{for } OSO 8,$$

while White and Suemoto (1968) find 0.071 ± 0.0015 and 0.061 ± 0.001 , respectively, and Linsky (1970)

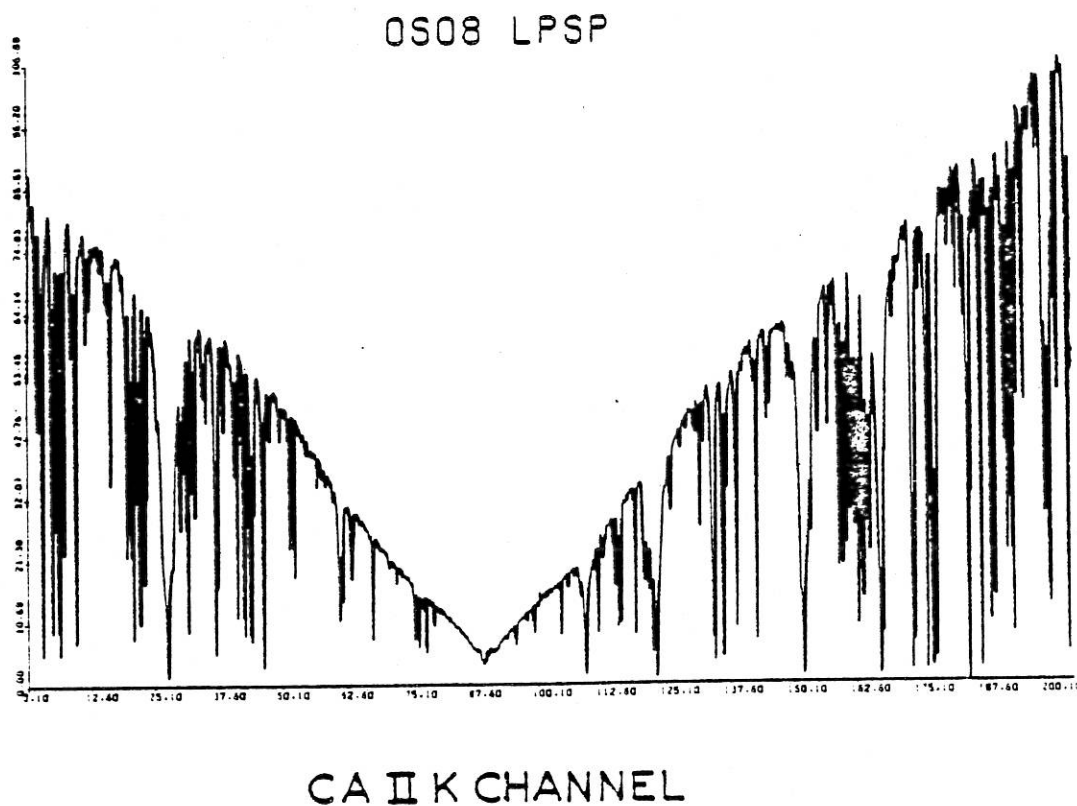
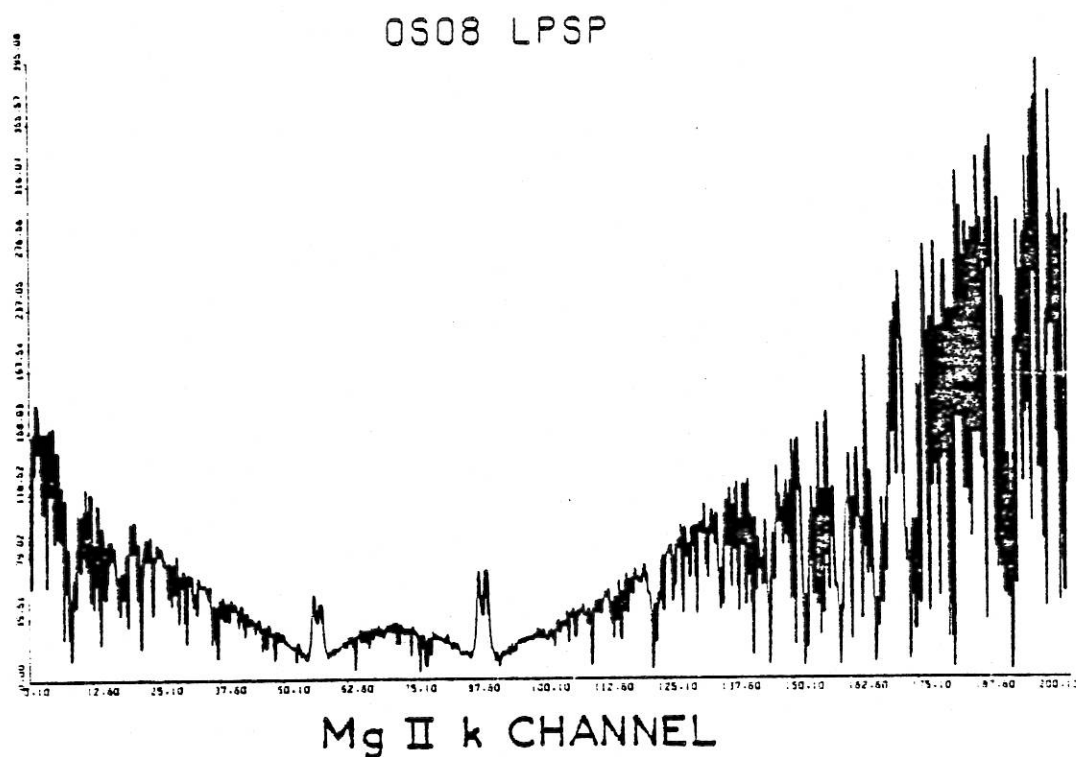


FIG. 2.—Full range spectral scans in the Ca II K and Mg II k channels using a $1'' \times 3''$ entrance slit. The ordinates are counts per gate. Instrumental sensitivity variations over the wavelength range have been corrected for. Notice the reversed asymmetries in the Mg II *h* and *k* lines. It takes approximately 50 s to go from Mg II *k* to *h*, and the asymmetries reflect time variations in the line profiles over 50 s.

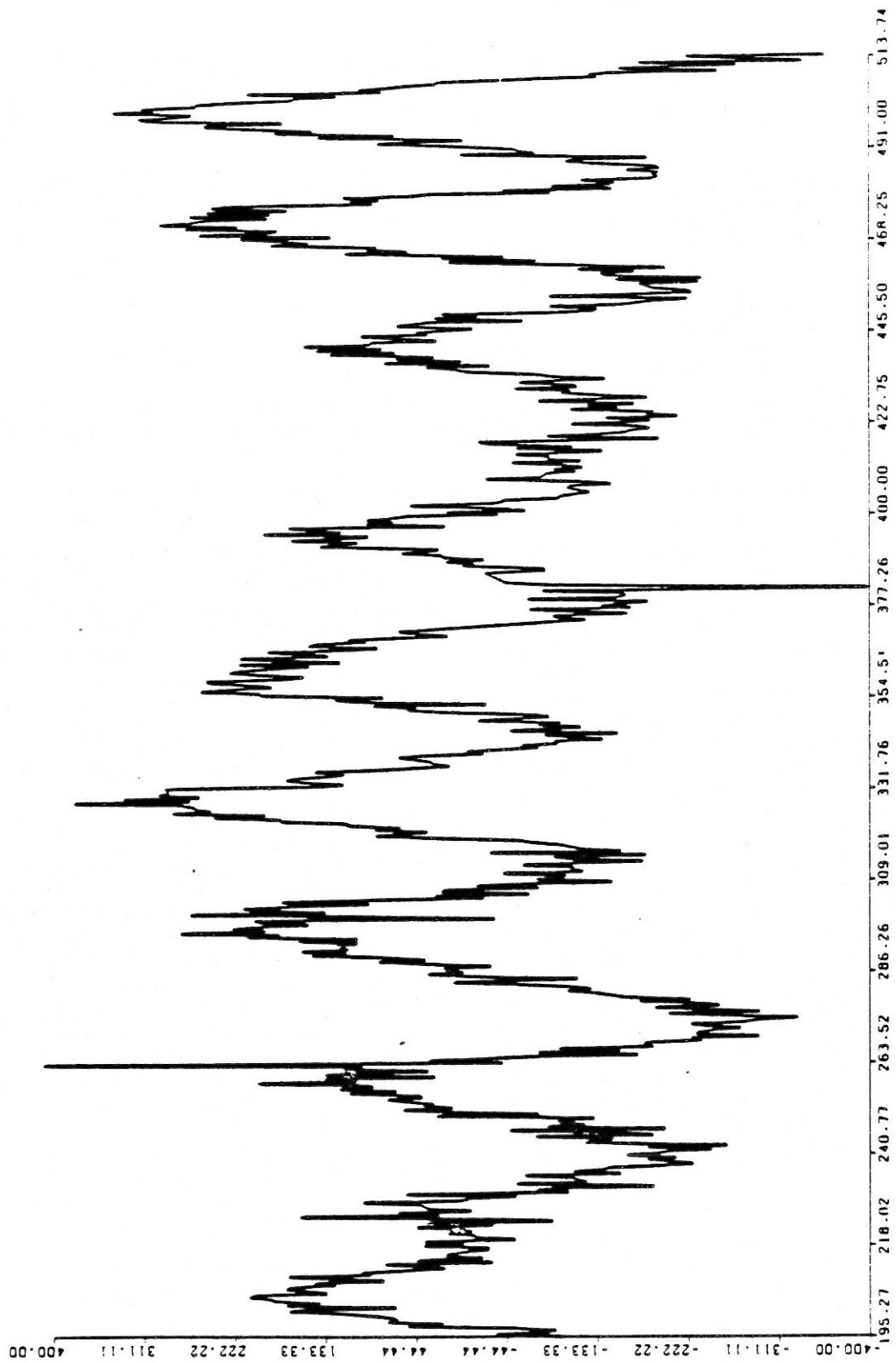


FIG. 3.—Relative velocity of the 391.52 nm photospheric line observed in the Ca II K channel. The 300 s oscillation is easily evidenced. The spacecraft Doppler shift has been removed. Spikes are identified as telemetry noise. The vertical scale is in m s^{-1} ; the horizontal scale is in units of 10 s.

LPSP INSTRUMENT ON OSO 8

TABLE 2

RATIO OF INTENSITIES AT THE λ POSITIONS K_1 , H_1 , k_1 , AND h_1 TO INTENSITIES MEASURED IN THE WINGS OF Ca II AND Mg II LINES IN THE OSO 8 CHANNELS

Channel	Ratio	OSO 8	Utrecht Atlas (Minnaert <i>et al.</i> 1940)	Air Force Atlas (Beckers <i>et al.</i> 1976)	Kohl and Parkinson (1976)*
Ca II H.....	$I(395.18)/I(H_1)$	0.084	0.085
	$I(398.13)/I(H_1)$	0.077	0.090
Ca II K.....	$I(391.47)/I(K_1)$	0.078	0.088	0.087	...
	$I(394.85)/I(K_1)$	0.083	0.096	0.095	...
Mg II h.....	$I(k_1r)/I(277.73)$	0.079	0.048
	$I(k_1v)/I(282.01)$	0.063	0.045
	$I(h_1v)/I(277.73)$	0.046	0.028†
	$I(h_1v)/I(282.01)$	0.037	0.025†
Mg II k.....	$I(k_1r)/I(277.73)$	0.048	0.048
	$I(h_1v)/I(277.73)$	0.03	0.028†

NOTE.—The results are compared with the same ratios evaluated from Solar Atlases or available published data. r and v referred to the red and the blue part of the lines.

* We are indebted to Dr. J. Kohl for providing original records of his spectra.

† These values are probably uncertain due to the difficulty of measuring the solar intensity at k_1 .

0.0409 \pm 0.0022 and 0.0434 \pm 0.0011 for the same ratios. Our results are intermediate between these two, confirming the very good performance of the Ca II channels.

For Mg II we have used the spectrum of Kohl and Parkinson for comparison. Excellent agreement is obtained in the k channel, our spectra indicating nearly exactly the same amount of scattered light as in the comparison spectrum. The agreement is, however, poor in the case of the h channel. Both the h and k lines can be observed in this channel together with the reference wavelength at 277.73 nm, allowing direct comparison between the two channels. As a result, we notice that the h channel has a much higher level of scattered light. This might be the result of degraded spectral resolution, due to a defective adjustment of the common coma and astigmatism corrector used in the Mg II channels whose delicate adjustment was optimized for the k channel.

For the $L\alpha$ and $L\beta$ channels we have made computations using the instrumental profiles, determined by ray tracing techniques, and the expected properties of the baffling inside the instrument; and we find that the level of scattered light is approximately 3% of the maximum flux in both channels.

Dark-current measurements were performed systematically each orbit during the first year and every 2 or 3 days in the second year. The dark current was found to be stable, with nearly no change during 18 months. The values are respectively 1.3, 1.1, and 0.1 counts s^{-1} for Mg II, $L\alpha$, and $L\beta$, respectively.

The calcium channel dark current was typically 200 counts s^{-1} . This comparatively bad performance is due to a leak in the enclosure system (skin).

e) Photometric Standardization

Photometric sensitivities have been measured regularly in orbit relatively to their values at launch. Such measurements are made every day or two with

the 1" \times 10" entrance slit at disk center quiet Sun, in the high spectral resolution mode for Ca II and Mg II and low resolution mode for $L\alpha$ and $L\beta$. The number of counts at certain standard wavelengths (see below) measures the relative efficiency, whose variation as a function of time is shown in Figure 4.

The interpretation of these curves may be of interest to those who plan to utilize similar instruments in space. The telescope mirrors, the collimator, the grating, and all surfaces in the $L\alpha$, $L\beta$, and Mg II channels were coated at the Goddard Space Flight Center, with Al+LiF (Bradford *et al.* 1969). Elaborate precautions were taken in the storing and handling of optics throughout the mounting and calibration of the instrument. In fact, a special 300 square meter facility was built with air cleanliness and with temperature carefully controlled and humidity always kept below 30% (Salvetat 1975). A loss of sensitivity such as the one reported here is very unlikely due to a contamination in the instrument before the launch and should rather be regarded as caused by the outgassing of the spacecraft and the instrument once placed in the space vacuum. In that case, the greater the number of reflections, the larger the degradation. The presence of steps which appear at nearly the same time on all the curves of Figure 4 is probably the signature of sudden outgassing periods. The significant differences noticeable between the individual curves, however, are indicative of causes of degradation proper to each channel, affecting either the mirrors, the filters, or the detectors.

The two Lyman channels show nearly the same behavior, with the larger loss at $L\alpha$ attributed to the larger number of reflections in this channel (seven at $L\alpha$ versus five at $L\beta$). At day 540, i.e., 18 months after launch, the sensitivity at $L\alpha$ and $L\beta$ was 10^{-3} and 5.10^{-3} , respectively, of the value at launch. Assuming that each reflection is affected equally by the contamination (which is certainly a crude approximation), these numbers indicate that each reflection has reached 35% at $L\alpha$ and 37% at $L\beta$ of its value at

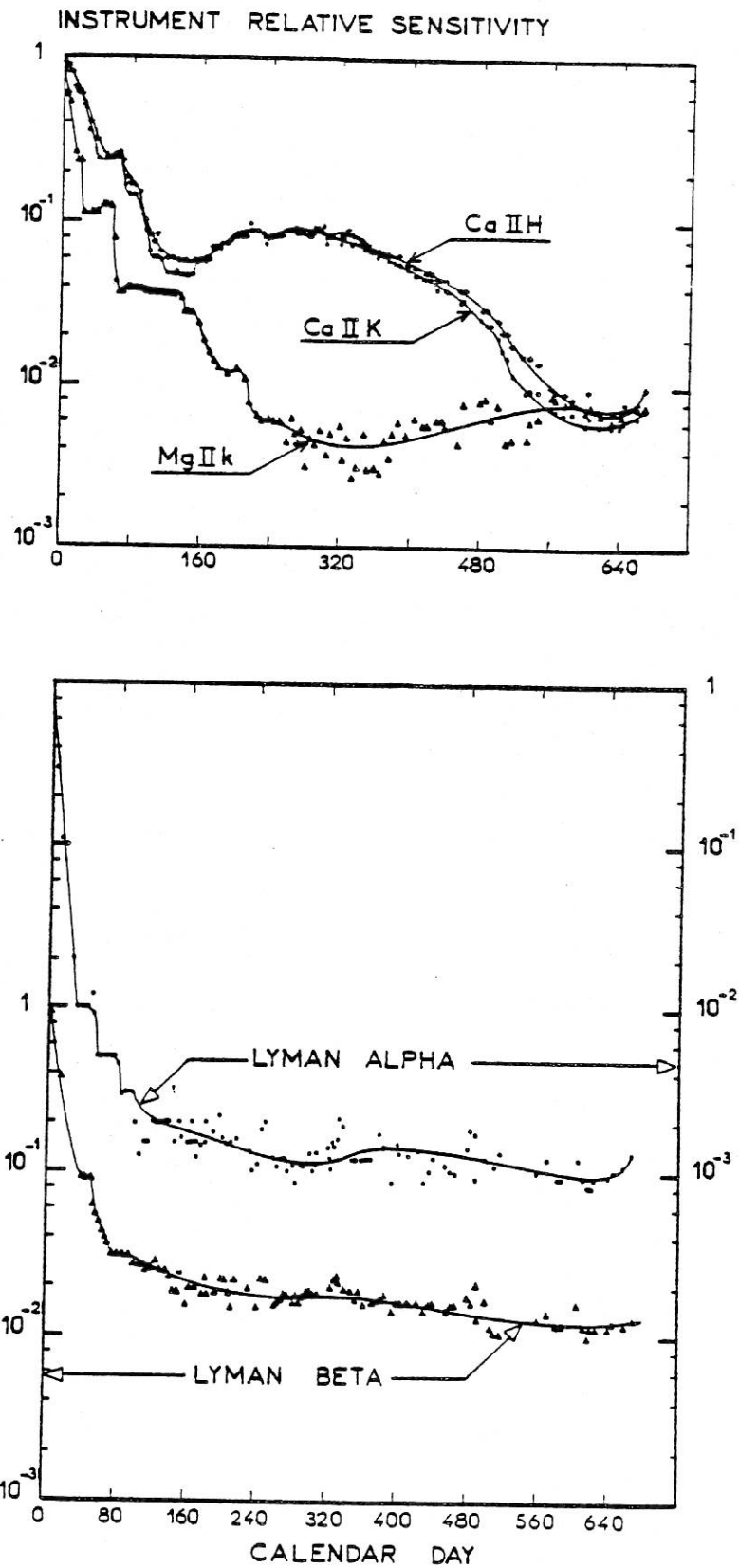


FIG. 4.—Variations of the instrument sensitivity relative to its value at launch. Time is in days after launch.

LPSP INSTRUMENT ON OSO-8

day zero. Such results are not particularly dramatic when compared with the photometric behavior of other solar space instruments (Huber *et al.* 1973).

However, the combined effect of outgassing and the baking of the secondary mirror surface by a flux of more than 18 "solar constants" is likely to be responsible in a large proportion for the sensitivity loss. A simulation made a few weeks prior to launch at NASA on Al+LiF coated samples illuminated by 17 "solar constants" and placed in a normally outgassing environment showed a decay in efficiency from 63% to 58% and from 67% to 35% at $L\alpha$ and $L\beta$, respectively, only 52 hours after pumpdown.

Obvious solutions, such as closing a shutter in front of the telescope during the first orbits when outgassing is high, were unfortunately not possible and would have delayed the launch several months.

Assuming, arbitrarily, that the secondary mirror is responsible for a loss of a factor 10 at both $L\alpha$ and $L\beta$, each surface would have reached an efficiency of 46% of its value at launch, which is more or less normal.

Totally unexpected and more striking is the behavior of the Mg and Ca channels. Although of yet unknown origin, outgassing might also be responsible for the degradation observed in these channels, at least until day 160 when the sensitivity reaches 1/40 and 1/20, respectively, of the value at launch. This corresponds to an average loss per reflection of 48% and 55%. After day 160 the sensitivity in the two Ca channels rises again. At the same time a faster decay is observed in the Mg channels. This peculiar behavior is attributed to interference phenomena, probably complementary, in Ca and Mg within thin films of contaminant(s) deposited on any one of the optical surfaces. Deteriorations of the interference filters which are used in all these channels may also contribute. In the case of the Mg channel it is also very likely that the detector itself is responsible for the loss of sensitivity. This is apparently not the case for the two Ca channels since their sensitivity follows nearly the same variation with time, which more likely reflects a variation in the optics used in common.

The overall loss of sensitivity compromised certain aspects of the observing program. However, the versatility of the instrument made it possible to obtain scientific data of high quality and value throughout the mission.

f) Absolute Calibration

The calcium channels were calibrated by comparison with the data of Linsky (1970) and Livingston and White (1978) which represent average quiet Sun conditions. The absolute intensity at our standard wavelengths H_1 and K_2 were taken as 0.0751 and 0.0687, respectively, in units of the continuum intensity at 400 nm.

For the magnesium channels we attempted to improve Bonnet's 1967 results (Bonnet 1968) and designed a high spectral resolution instrument calibrated against a blackbody constructed by R. Peyturaux at the Institut d'Astrophysique de Paris. This instrument was launched twice on the LASP rockets number 21029 on 1975 July 28, and 21030 on 1976 February 18, but because of malfunctions in the electronics it did not give reliable results. We prefer therefore to rely on other recent measurements—e.g., those of Kohl and Parkinson (1976). The absolute intensity at the standard wavelengths h_1 and k_2 were taken as 8 and 6×10^{-12} ergs $\text{cm}^{-2} \text{s}^{-1} \text{sr}^{-1} \text{cm}^{-1}$, respectively.

For the Lyman channels we also used the above rocket program to carry packages consisting of $\frac{1}{2}$ m Ebert-Fastie spectrometers, measuring the integrated solar disk to calibrate the LASP and LPSP instruments separately. Only the second flight yielded good calibration data. The results are given in Table 3 and are compared there with other measurements. The LPSP values are somewhat high; however, they are in the direction suggested by geophysicists (Levasseur *et al.* 1976). To use these integrated intensities in $L\alpha$ and $L\beta$, we use quiet Sun average profiles computed for the whole disk (Fig. 5). We have taken into account the center-to-limb variation in an approximate way that will ultimately be improved upon by means of entire Sun raster-generated profiles (i.e., profiles constructed from spectroheliograms), when these become available from the data tapes. The absolute flux at the standard wavelength (core of the line) used to monitor the $L\alpha$ relative sensitivity was taken to be 3×10^{10} photons $\text{cm}^{-2} \text{s}^{-1} \text{nm}^{-1}$.

IV. REAL TIME OPERATION AND PROBLEMS

The various modes of operation of the instrument have been described in Paper I. Here we discuss the "real-time" operation mode which allowed one, for

TABLE 3
INTEGRATED SOLAR FLUX MEASUREMENTS OBTAINED WITH CALIBRATION ROCKETS AT $L\alpha$ AND $L\beta$

CALIBRATED FLUX	CALIBRATION ROCKETS			OSO 5† 1975 Aug. 8	AE/C‡ 1975 Apr. 11
	1975 July 28 LASP*	1976 Feb. 18 LPSP	1976 Feb. 18 LASP*		
$F(10.7 \text{ cm}) (10^{-22} \text{ W m}^{-2} \text{ Hz}^{-1})$	75.5	70.1	70.1	70	
$F(L\alpha) (\text{ergs cm}^{-2} \text{ s}^{-1})$	4.02	$5.46 \pm 20\%$	$4.05 \pm 20\%$	4.25	none
$F(L\beta) (\text{ergs cm}^{-2} \text{ s}^{-1})$	none	$0.078 \pm 20\%$	none	none	0.050

* Rottman 1977.

† Vidal-Madjar 1977.

‡ Hinteregger 1976.

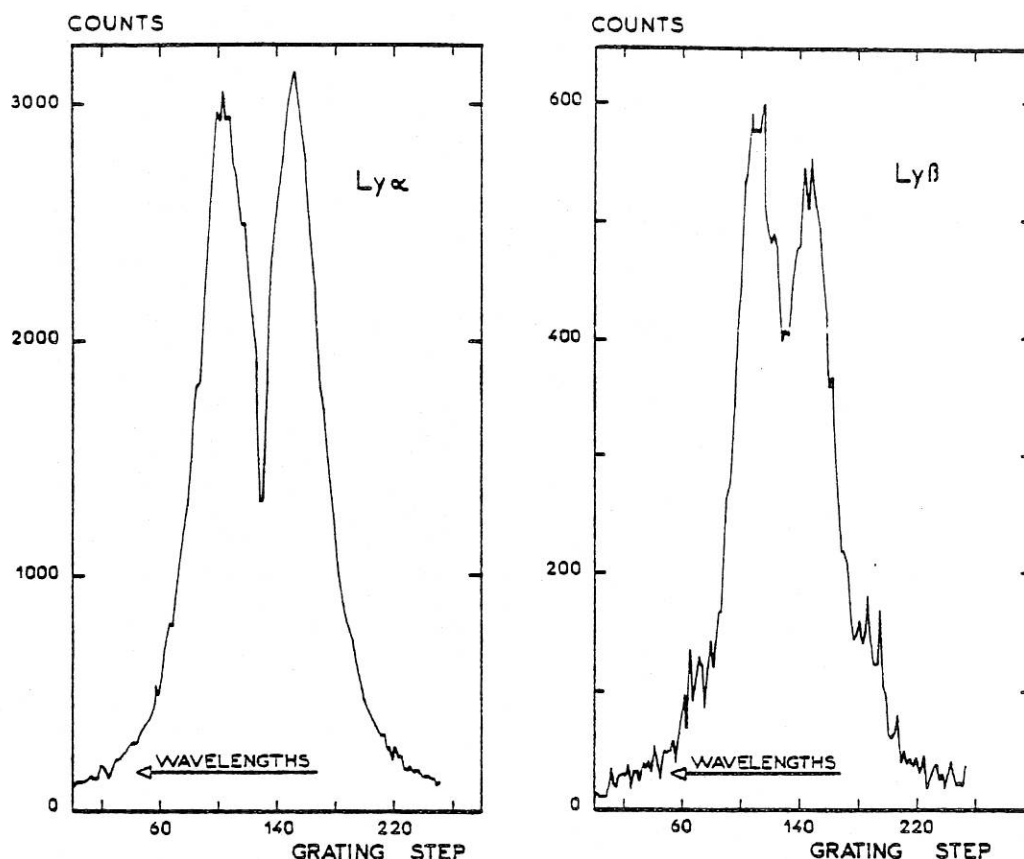


FIG. 5.—Full Sun average $L\alpha$ and $L\beta$ profiles. Wavelengths increase to the left. The conversion into λ units can be made using the values of the last column of Table 1.

the first time, to point from an orbiting observatory with an absolute accuracy of nearly $1''$. The LPSP and LASP instruments were both operated from LASP (Boulder, Colorado) with "resident" LPSP scientists and guest investigators involved in the daily operations. Target selection alternated daily between LPSP and LASP until 1976 April and then weekly. For a more complete description of the operations command generation and quick-look facilities, see Jouchoux and Hansen (1978).

a) Pointing System Problems

The pointing system of the "sail" section of *OSO 8* uses either one of two Sun sensors (SEAS), designed by Hughes Aircraft Company, mounted on each instrument. These devices coalign the SEAS pointing axis with the optical axis of the associated telescope. This corrects for drifts of the optical axis with respect to the mechanical structure of the instruments.

Because of an electronic problem, the SEAS on the LPSP instrument failed after 56 days in orbit and all subsequent operations made use of the other SEAS. Consequently thermal and other drifts between the LPSP axis and the LASP axis had to be known. To determine these, we measure relative positions ($\pm X$, $\pm Y$) of the solar limb (in the X - Y frame of the satellite) during one orbit using images from the

internal raster mode. We corrected for these drifts by programming the secondary mirror when it was necessary to stay within $1''$ of the target.

Variations in the SEAS scale factor and zero point (Sun-center line of sight) proved to be more troublesome. A weekly determination of the absolute four positions of the solar limb in the X - Y frame of the satellite was necessary. Using such data, from spacecraft and internal rasters, an extrapolated scale and zero point could be found for the particular day of observation. This proved to be successful, and we were able to position targets at the very center of our field of view, often without the need for corrections. Finally, the repeatability of the pointing system at the limb was found to be within $1''$ or $2''$, but with occasional jumps of $5''$.

b) Target Acquisition

Nearly 80% of the orbits under LPSP control were dedicated to studies of selected targets, often as small as a few seconds of arc. This mode of observation from an unmanned observatory involves a fairly complex procedure which requires considerable care and dispatch from the observer. We illustrate this in Figure 6 and describe the acquisition of the core of a sunspot.

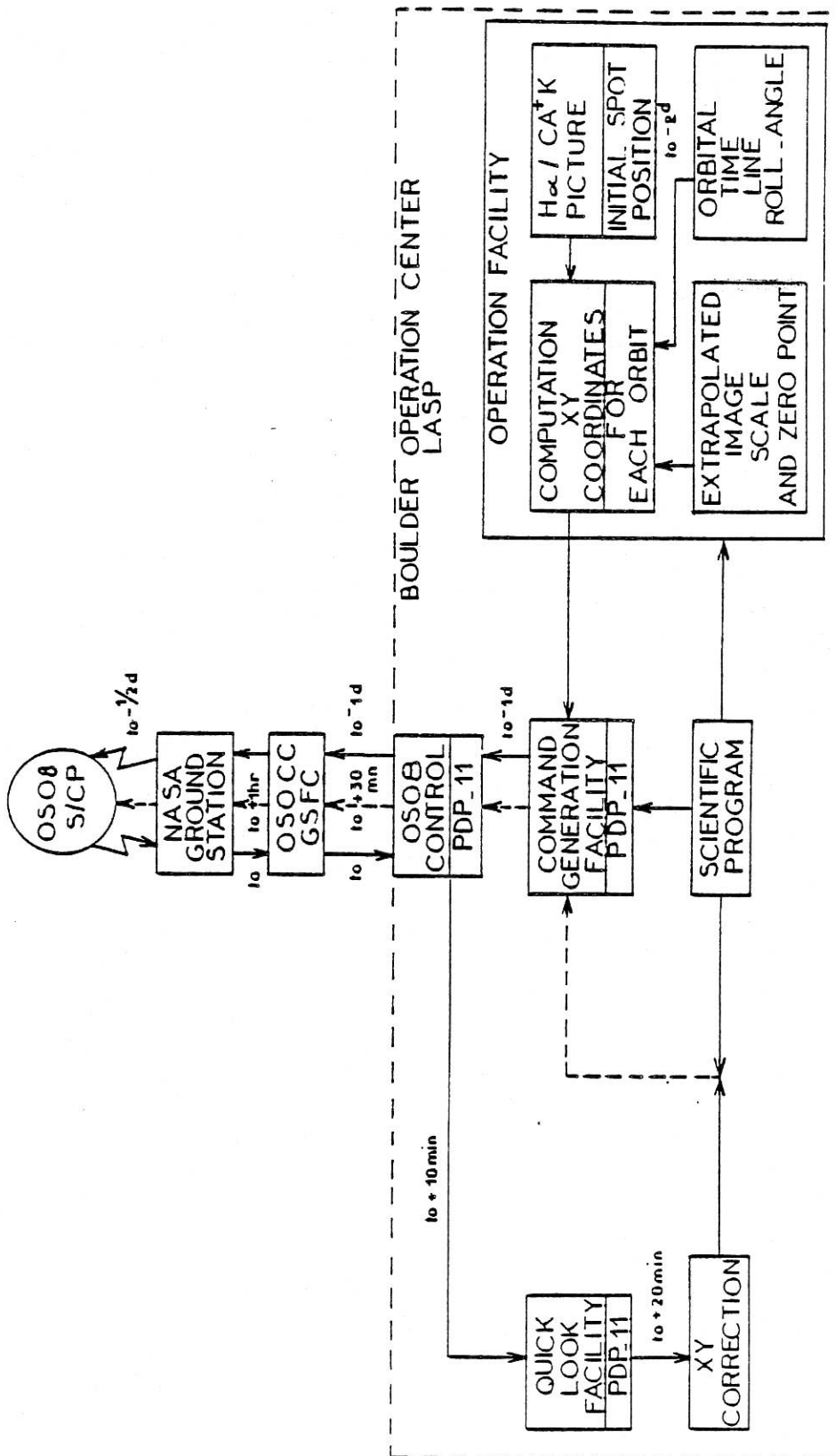


FIG. 6.—Block diagram showing the circuitry of telemetry and telecommand data between Boulder and NASA and illustrating "real-time" acquisition of a solar target (t_0 is the execution time).

BONNET ET AL.

As soon as a spot is visible on either a $H\alpha$ picture (taken daily by NOAA/NBS in Boulder) or the $Ca II K$ picture transmitted by telephone from Sacramento Peak Observatory, we determine its Stonyhurst coordinates for the time of the photograph. These coordinates are then transformed and oriented into the satellite spin frame of reference for the projected time of observation. Finally the scale distortion of the pointing system is corrected for. The instrument commands and associated pointing commands are generated and sent to NASA on the day before the date of observation. During the day of observation an internal image of the spot, $64'' \times 64''$, is executed in the far wings of $Ca II$ or $Mg II$ during a real-time pass of the satellite over a ground station. These real-time data are received by telephone via GSFC on the PDP 11 computer at Boulder, where they are subsequently decoded and displayed as an image. Any corrections to the position of the spot are determined from the image and are sent by telephone to NASA who uplink the corrections to the spacecraft. The time delay between the real-time pass and execution of pointing corrections can be as short as the time interval between two successive ground station passes, namely, $1\frac{1}{2}$ hours. This apparently straightforward operation is made more difficult because of the need to extrapolate the scale distortion parameters and to correct for the drifts of the line of sight already mentioned.

c) $L\alpha$ Modulation

The $L\alpha$ signal was discovered to be occasionally modulated with an amplitude which may reach 10% of the signal at precisely the rotation period of the spacecraft wheel except during the first 2 minutes after sunrise when sometimes a period distinctly shorter than the wheel period was found.

All attempts made to detect a similar phenomenon in the other channels have failed, suggesting that it is not caused by a pointing problem. Indeed we have sometimes observed oscillations in the pointing axis with periods equal to that of the wheel rotation and an amplitude of 0.5, but these affect all channels at the same time.

The phenomenon has to be taken into account when analyzing time series and profiles of the $L\alpha$ line. As described in Paper I, the duration of every individual measurement is the product of 0.16 s gate time by a power of 2, and the most commonly used values are 10.24 s (64 grating steps) and 20.48 s (128 grating steps). The period of rotation of the wheel of the spacecraft varies from 10.7 to 9.5 s and for spectral scans with a time base equal to or larger than 10.24 s, the modulation induces a "beat" of period ranging from infinity to 131 s.

Figure 7 plots the raw data for the first moment of the wavelength of the line versus time. A strong 800 s period is evident. If the individual data points are corrected for the modulation with a period equal to that of the wheel and the first moment is recomputed, then the circles in Figure 7 show that the 800 s oscillation is suppressed.

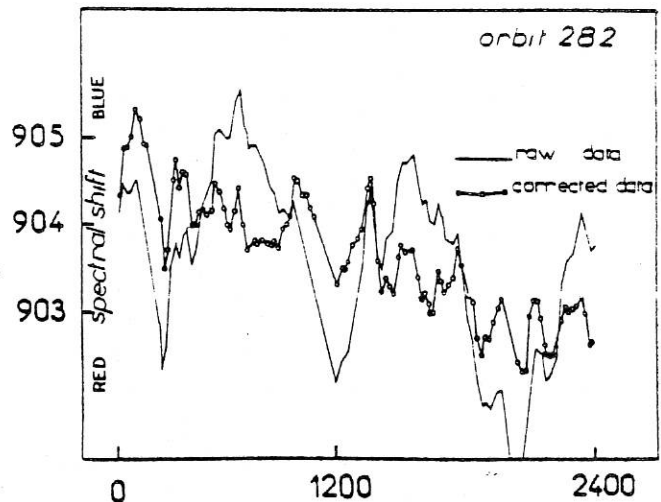


FIG. 7.—Variation with time of the position of the first moment of $L\alpha$. The solid line variation shows a strong oscillation of ~ 800 s period. Circles represent the same data after correcting the $L\alpha$ profiles for the instrumental modulation: the 800 s oscillations have vanished. Abscissa is time (in seconds); ordinate is grating step number.

This proves without ambiguity that the phenomenon is purely instrumental and that the possibility of its solar origin, should be definitely disregarded.

V. PRELIMINARY RESULTS

Spacecraft (playback) data are sent by NASA to Boulder by telephone line and recorded there on magnetic tapes. Mass production tapes of this data are prepared by NASA and mailed to the Centre National d'Etudes Spatiales (CNES) (Toulouse, France), which is in charge of the processing and distribution of the final data tapes to the LPSP investigators and guest investigators. The results presented below have been obtained mostly from playback data at Boulder.

a) Observational Program

Table 4 presents a summary of the various types of observations that were programmed during the first 8363 orbits. No distinction is made in the table with regard to pointing control. Orbits with problems in either the instrument, the spacecraft, or the command system represent only 2% of the total.

The column headings in the table describe the modes of operation of the instrument while the rows indicate the scientific question or the solar feature under study.

Orbits labeled "Line Profiles" usually correspond to spectral scans ranging from 64 to 512 grating steps centered at either the six chromospheric lines or the $O VI$ line at 103.2 nm. The "Others" columns indicate studies in either the wings of the $Ca II$ and $Mg II$ lines or the $O V$ and $Si III$ lines at 121.8 nm, 120.6 nm, respectively. Other lines such as $O I$, $N I$, etc., were observed in the $L\beta$ channel by making use of the different grating orders. During these orbits the satellite was in the pointed mode.

TABLE 4
SCIENTIFIC PROGRAM OF THE FIRST 8363 ORBITS

PARAMETER	LINE PROFILES				SPECTROHELIOGRAMS				VELOCITY FIELDS AND OSCILLATIONS	TRANSIENTS	LARGE λ SCANS	GUEST OBSERVER ORBITS
	6 Lines	O VI 103.2	Others	6 Lines	O VI 103.2	Others	6 Lines	O VI 103.2				
Quiet Sun:												
Chromospheric network.....	554	194	...	465	126	95	80	126	310	257	254	463
Limb studies.....	483	180	25	208	209	7		209	132	138	30	249
Active regions.....	583	175	31	276	184	1		184	20	56	2	117
Sunspots.....	455	107	8	120	40	11		40	4	5
Coronal holes.....	42	87	14	25	20	1		20	25
Prominences.....	63	23	3	33	35	...		35
Filaments.....	55	23	...	26				
Full Sun images:												
R 128s }.....		High resolution (20")		73	87	16		87
R 128f }.....		Low resolution (40")		13	2	3		2
R 64.....				135	1	...		1
Photometric and pointing calibration.....	360	123	...		123
Instrumental tests and miscellaneous.....	421	...		421

NOTE.—Numbers represent full day orbits.

Under "Spectroheliograms" we classify orbits for which most of the time is spent rastering, using either the internal or the satellite raster mode. Morphology and long-term variability studies of solar features were of interest here.

During orbits labeled "Velocity Fields and Oscillations" we spent most of the time in the pointed mode studying rather small areas of the disk, not more than $64'' \times 1''$. Here, special spectral scans were made. For example, short-period waves ($T < 40$ s) were searched for by scanning rapidly through the line profiles using wavelength position separated by 16 grating steps.

Under "Transients" are grouped orbits observed with the fast, low-resolution satellite rasters. The short time constant of such modes allows one to observe rapidly propagating shocks and any other rapid phenomena.

"Large λ Scans" represent the full scanning capability of the grating and were performed either to study lines in the low orders of the $L\beta$ channel or to standardize the Mg II and Ca II line cores with respect to their far wings.

For most orbits, sunset and sunrise experiments were performed in order to measure atmospheric extinction at various wavelengths of interest (see § Vg below).

"Chromospheric Network Studies" include not only morphology and time evolution but also line profiles for center-to-limb and cell-network comparisons. "Limb Studies" include orbits dedicated to the shape of the limb, spicules, and the vertical extension of the solar atmosphere in various lines.

"Photometric Calibration" has already been described in § III; for these orbits the satellite is pointed at disk center in a quiet region.

The last five rows of Table 4 include scientific as well as instrument or satellite calibration orbits. Also included are orbits devoted to eclipse observations, to studies of the geocoronal hydrogen line, and to the search for lines such as Fe XIII 121.64 nm and He II 102.5 nm.

b) Quiet Sun and Chromospheric Studies

Figure 8 (Plate 21) represents an example of our study of the network and the quiet Sun. Such internal raster images along with associated profiles will permit an intercomparison of cell and network properties.

Figure 9 compares profiles obtained at the center of a cell and in a network fragment. One can notice the strong variation in intensity, particularly in Mg II k and $L\alpha$, between the two regions. This is due partly to a decreasing line background contribution as well as differential temperature sensitivity. The asymmetry of $L\alpha$ is always much less pronounced than in the case of Mg II h and k , presumably because of smaller velocity gradients at the $L\alpha$ height of formation.

Figure 10 shows average quiet Sun profiles of $L\alpha$ and $L\beta$ taken with a $6'' \times 2''$ slit at disk center and near the limb ($\mu = 0.14$). Notice the two lines of O I at 130.48 and 130.59 nm in the wings of $L\beta$ (observed in the 11th order). By the insertion into the light beam of a MgF₂ filter one can block out all photons below

115 nm and observe only the two O I lines. Differencing permits one to reconstruct the $L\beta$ profile. The result of this procedure is shown on Figure 11. The remaining slight anomaly at grating step 180, might be due to the H β line of He II (102.53 nm). Center-to-limb measurements at the corresponding wavelength show appreciable limb brightening. Investigations are under way to confirm this observation.

The variation of the distance between peaks of the $L\alpha$ and $L\beta$ lines from center to limb is apparent together with the variation of the ratio of the peak to core intensities (see Table 5). The values in Table 5 at $\mu = 0.14$ are close to those calculated by Vernazza (1972).

One noticeable feature is the reversed intensity asymmetry between the $L\alpha$ and $L\beta$ shortward and longward peaks at the disk center. In $L\alpha$ the shortward peak is generally higher than the longward peak while the reverse holds in $L\beta$. At the limb, both $L\alpha$ and $L\beta$ profiles become symmetrical. It is possible that this effect may not be intrinsic but is either an instrumental effect or the effect of unresolved lines at $L\beta$. The matter is under study.

To study the morphology of network fragments and their evolution in time, monochromatic images have been obtained simultaneously in the six lines alternately with broad-band images in O VI (103.2 nm) for a number of observing sequences (Fig. 12). Preliminary analysis of a 20 hr sequence shows that significant evolutionary changes can occur over a 12 hr period. The larger size K_2 fragments are easily identified in the $L\alpha + L\beta$ (= H Lyman) and O VI images where they do not appear as extended as indicated by the ATM data (Reeves 1976). This is supported by an analysis of the $L\alpha$ brightness distribution. Applying the method of Skumanich, Smythe, and Frazier (1975) to both the present *OSO 8* sequence and ATM data, one finds a fractional $L\alpha$ network area of 37% and 41%, respectively. The ratio of mean network to mean cell brightness proved to be 1.9 and 2.1, respectively. For comparison the *OSO 8* Ca II distribution yielded a fractional area of 27% and brightness ratio of 1.3.

c) Quiet Chromospheric Oscillation and Transients

We have already mentioned in § IIIc (cf. Fig. 3) our successful detection of the 300 s oscillation of photospheric lines in the wings of Ca II H and K.

TABLE 5

CENTER-TO-LIMB COMPARISONS OF THE DISTANCE BETWEEN THE BLUE AND RED PEAKS AND OF THE RATIO BETWEEN THE AVERAGE PEAK INTENSITY AND THE CORE INTENSITY OF THE $L\alpha$ AND $L\beta$ LINES

LINE	SEPARATION OF PEAKS (nm)		$I_{\text{peak}}/I_{\text{core}}$	
	$\mu = 1.0$	$\mu = 0.14$	$\mu = 1.0$	$\mu = 0.14$
$L\alpha$	0.043	0.05	$1.3 \pm 50\%$	2.2
$L\beta$	0.027	0.031	$1.4 \pm 50\%$	1.5

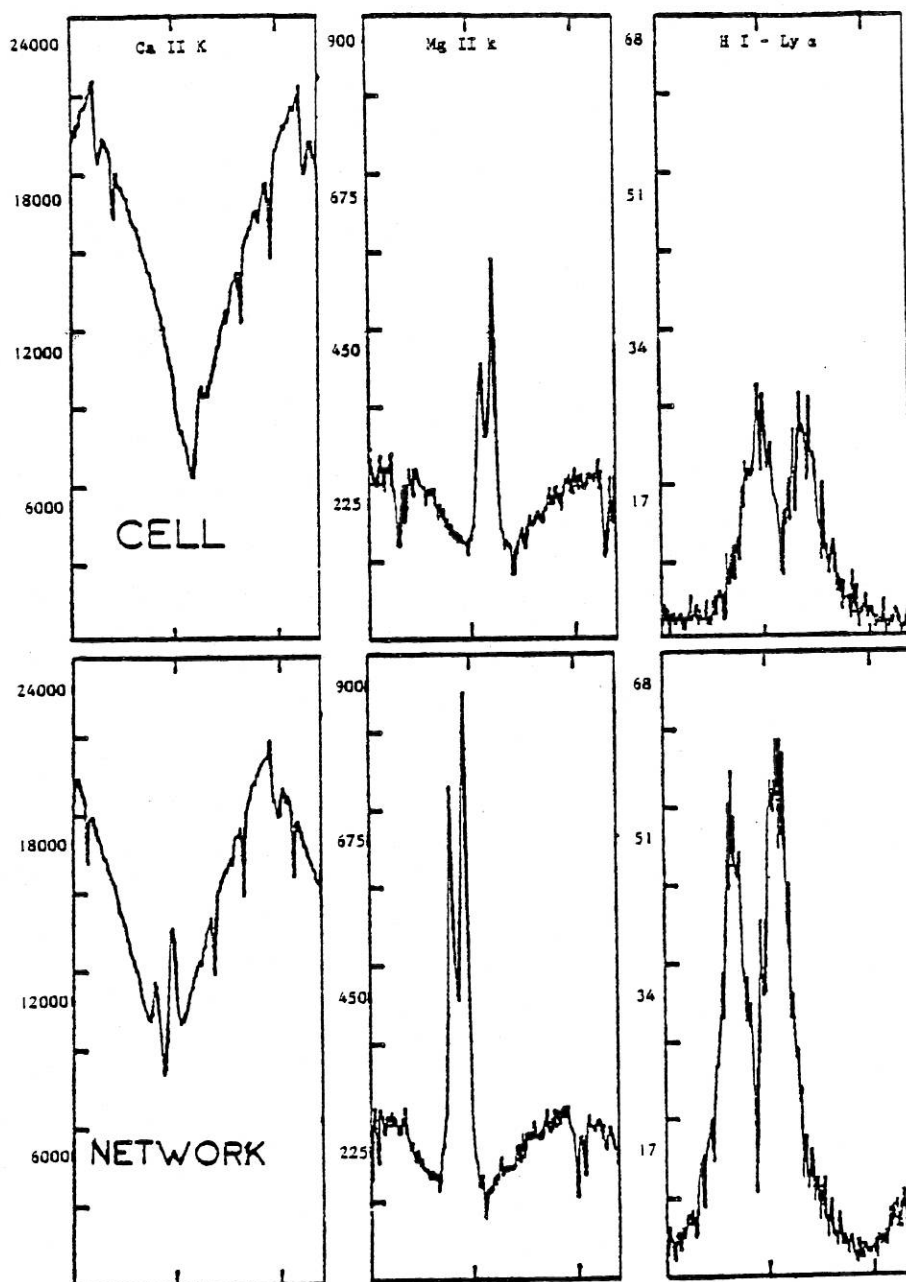


FIG. 9.—Comparison between simultaneous observations of Ca II K, Mg II k, and Ly α profiles in the network and at the center of a supergranulation cell. The slit size is $1'' \times 10''$. Units are counts per counting gate.

The Mg II k and Ca II K lines (Fig. 13) show oscillations of ~ 200 s period. We parametrize the profile of Mg II k as a difference of two Gaussians:

$$I(\lambda) = E_1 \exp\left(\frac{\lambda - E_2}{E_3}\right)^2 \left[1 - A_1 \exp\left(\frac{-A_2}{A_3}\right)^2 \right],$$

where E_1 and A_1 represent the intensities of the emission and absorption components of the profile, respectively, and E_2 and A_2 the average wavelength position (or "first moment of the wavelength") of the emission and absorption components. We should point out

that no physical meaning is to be attached to this parametrization. The time behavior of these various parameters is shown on Figure 14.

The oscillation of the parameter E_2 or average emission position covers a range of ± 0.00186 nm or ± 2 km s $^{-1}$. For A_2 or average absorption position, this value is doubled. This clear difference might be interpreted as the amplification, with increasing height in the atmosphere, of a wave, if one assumes, as usual, that the core of Mg II k is formed at a higher altitude than the wings. The average "bluer" position of E_2 (emission) compared to A_2 (absorption) reflects the

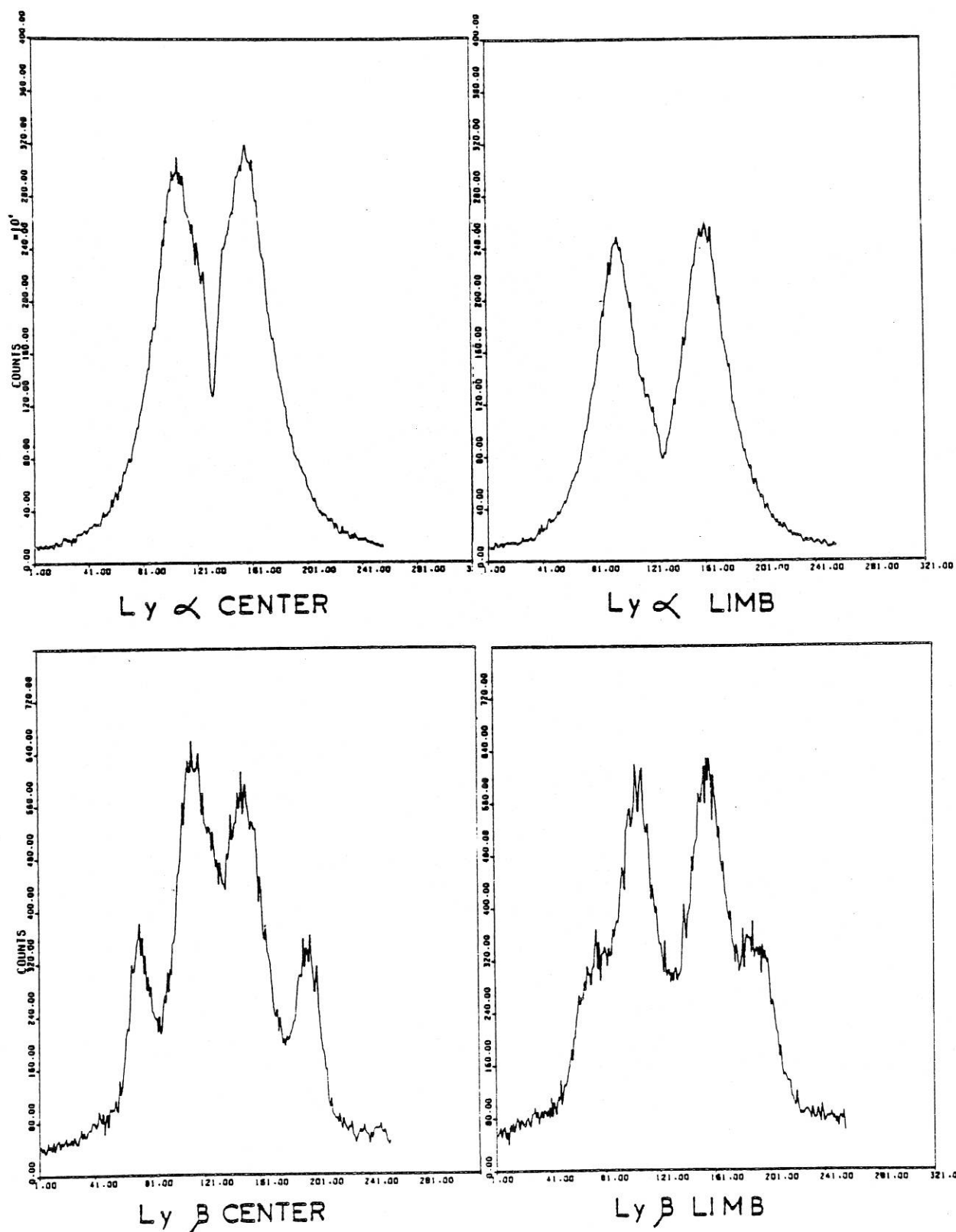
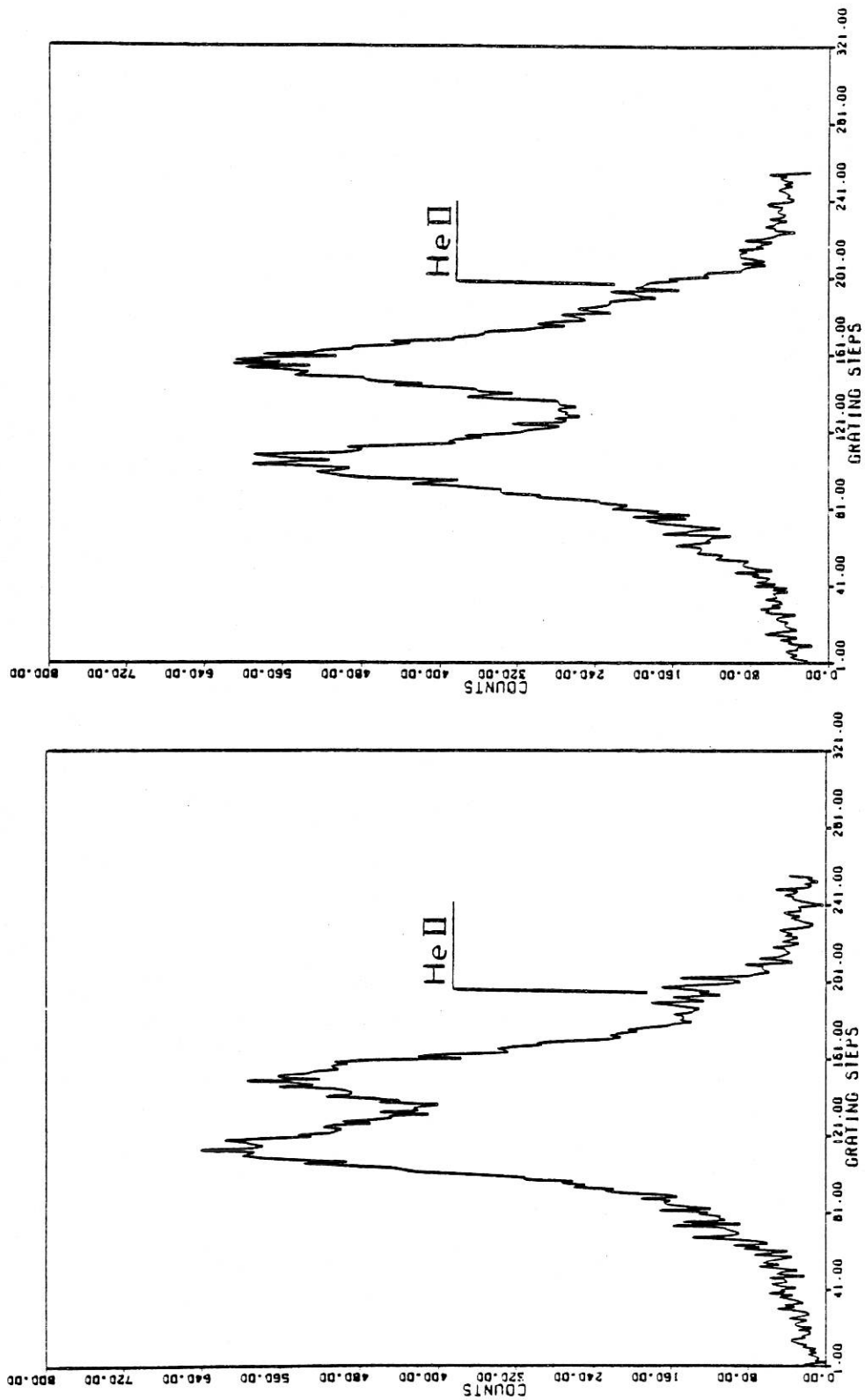


FIG. 10.—Ly α and Ly β profiles at the center and at the limb of the Sun obtained with a $6'' \times 2'$ resolution. The two lines in the wings of Ly β are O I 130.48 nm and 130.59 nm appearing in the 11th order of diffraction. Wavelengths increase to the left. The abscissae are grating step numbers. For conversion in λ units, see Table 1.



LIMB

CENTER

FIG. 11.— $L\beta$ profiles after the subtraction of the $O\ I$ lines made by inserting a $Mg\ F_2$ filter in the beam. Wavelengths increase to the left. For conversion into λ units, see Table 1.

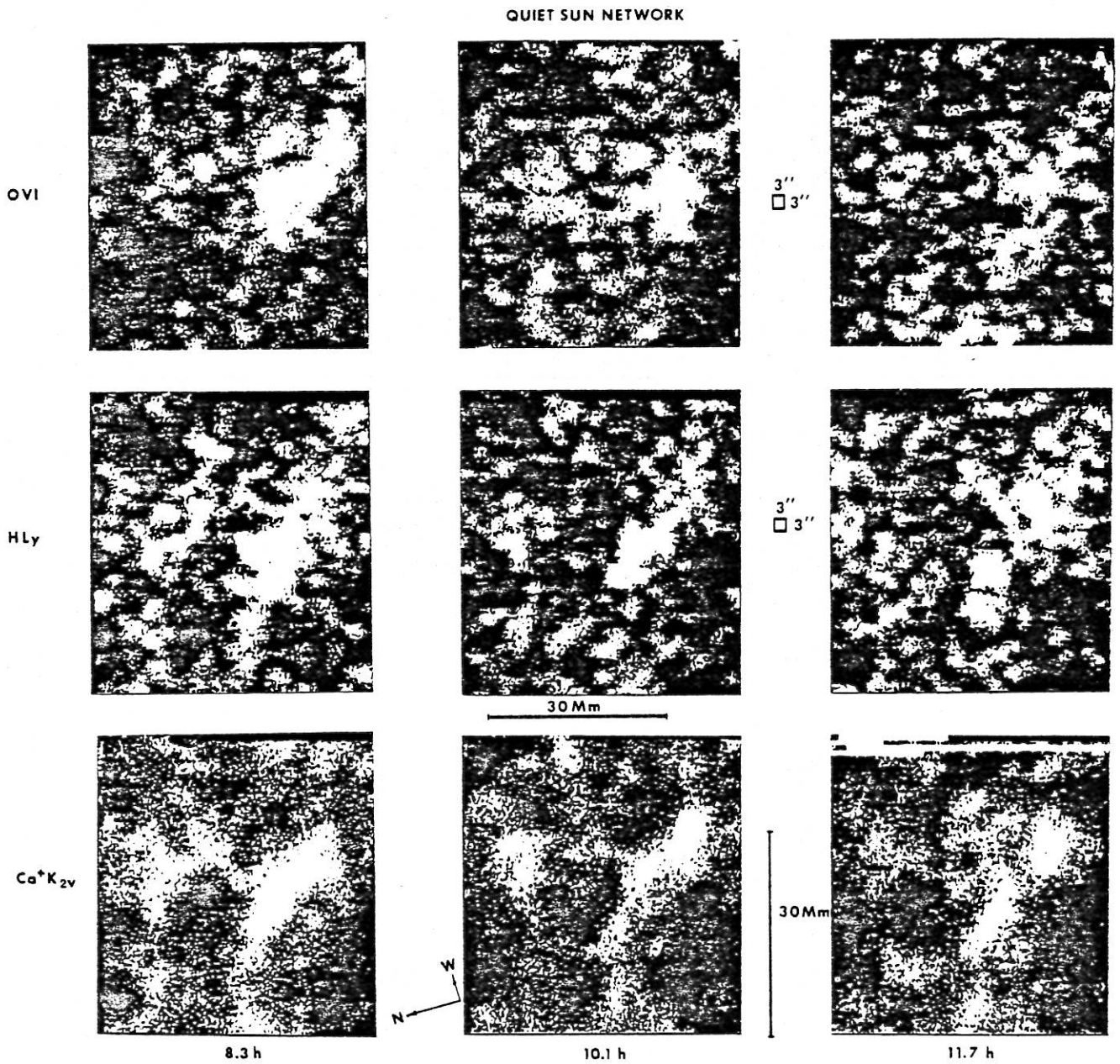


FIG. 12.—Evolution with time of network fragments, observed with $64'' \times 64''$ internal rasters in O VI, $\text{L}\alpha$, and Ca II lines

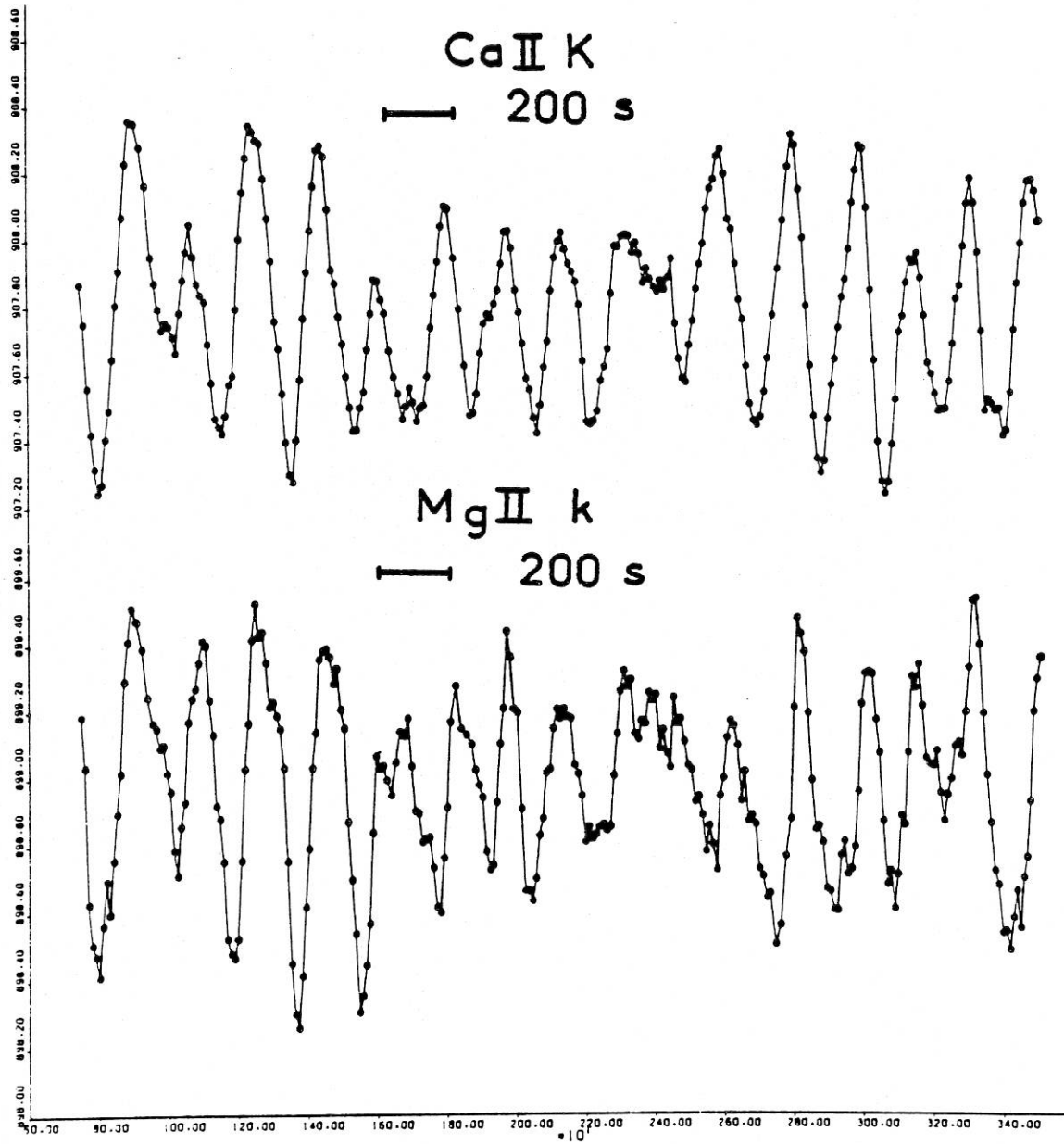


FIG. 13.—Oscillations of the center of symmetry of the Ca II (*upper curve*) and Mg II (*lower curve*) emission components. Horizontal units are multiples of 10 s.

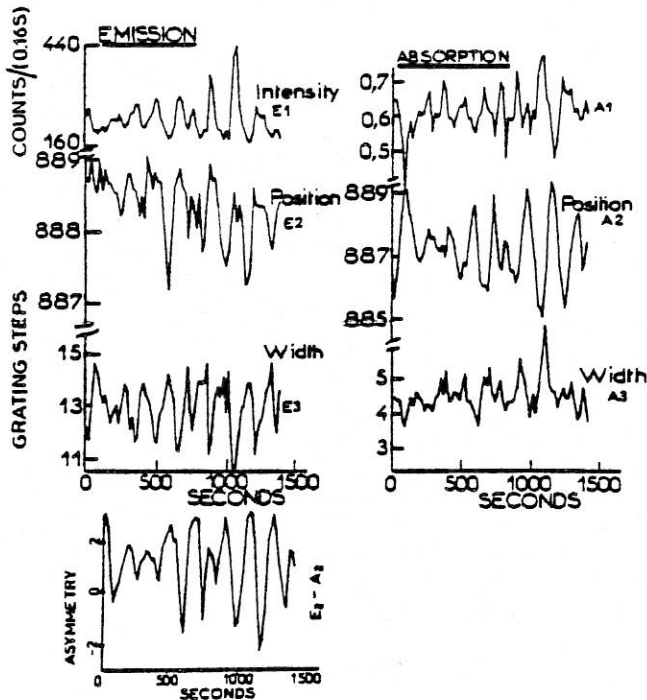


FIG. 14.—Time variations of the various parameters of the analytical function used to represent $\text{Mg II } k$. Observations are made at disk center.

fact that the average $\text{Mg II } k$ profile in the Sun is asymmetric, with k_{2v} stronger than k_{2r} . This is illustrated also on Figure 15, where we see that the line shape varies from a strongly asymmetrical profile ($k_{2v} > k_{2r}$) to a nearly perfect symmetrical profile ($k_{2v} = k_{2r}$).

In Figure 16 we see the variation over 40 s of the Mg II and $\text{Ca II } K$ profiles observed simultaneously.

The Mg II lines exhibit the same periods as the Ca II lines. We have a broad set of observations which contain wave trains lasting in general no longer than a few cycles with periods ranging from 250 s down to 130 s. A search for shorter periods was undertaken, in particular by guest observers, but no clear evidence has yet emerged from these investigations at this early stage of data analysis.

The good results obtained in Mg II encouraged us to search for a possible oscillation of $L\alpha$. The large contribution function of the line, which tends to smooth out the effects of any wave on the profile, together with the low photon count in this channel made this observation a particularly difficult one. We first tried to detect intensity fluctuations by integrating the number of photons over ± 0.025 nm from line center. We did not find any obvious evidence of variations, other than random, a result in accord with the previous attempts made from studies of *Skylab* results (Vernazza et al. 1975).

To overcome the low photon statistics problem, we tried to correlate the shape of $L\alpha$ with that of $\text{Mg II } k$ profiles. We definitely see evidence for a correlation, the bluer k profiles corresponding to redshifted $L\alpha$ profiles. The amplitude of the shift is of the order of 2 grating steps (3 km s^{-1}). More work is under way, but we may state at this stage that the oscillations seen in $\text{Mg II } k$ have an influence higher in the chromosphere, at the altitudes where $L\alpha$ is formed (Artzner et al. 1978).

Several orbits were devoted to the study of oscillations in the O I , Si III , and O VI lines, but have not yet been analyzed. Transient and short time phenomena have been observed. Numerous tachograms dedicated

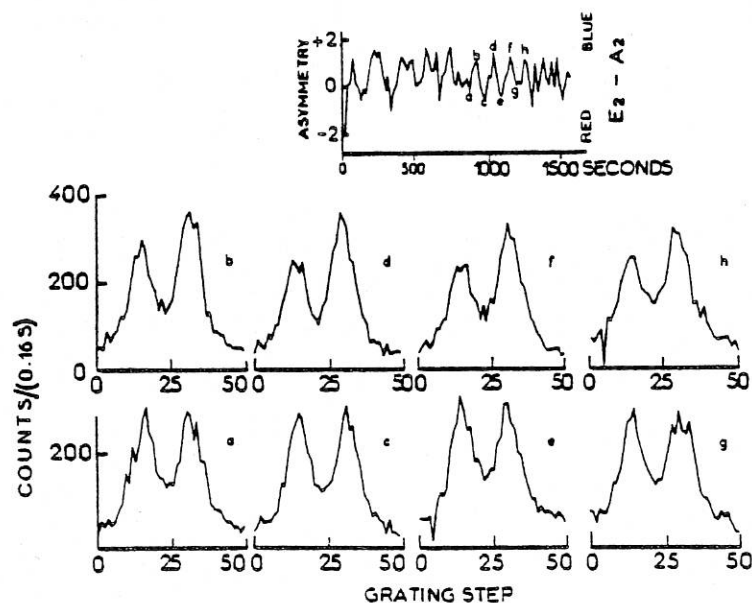


FIG. 15.— $\text{Mg II } k$ profiles observed at the maxima and minima of the oscillations of the line center of gravity, showing obvious occurrence of asymmetrical blue peaked profiles at maxima and symmetrical or slightly asymmetrical red peaked profiles at minima. Wavelengths increase to the left.

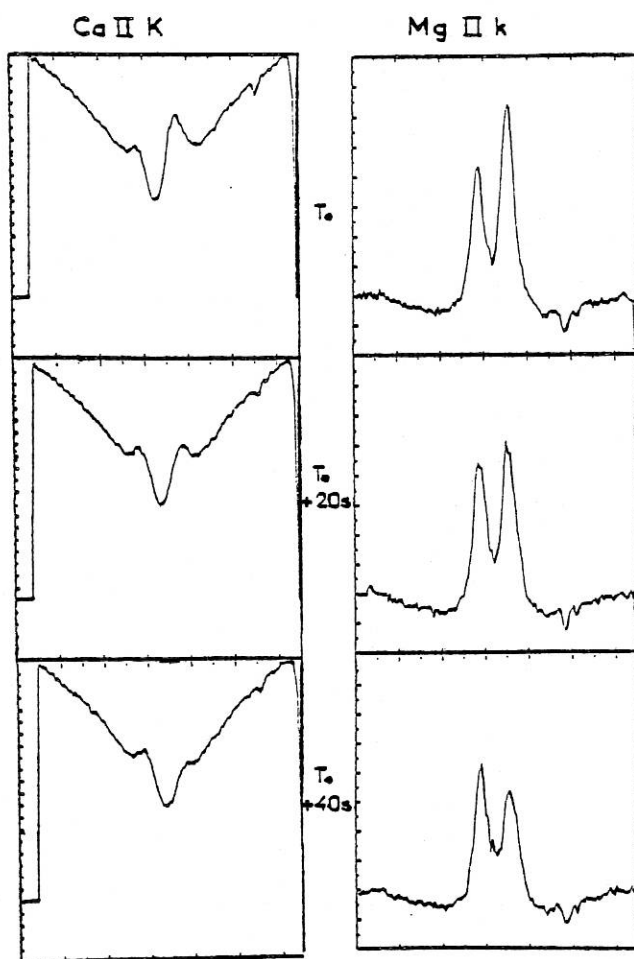


FIG. 16.—Observation of a temporal event, simultaneously in Ca II K and Mg II k as it propagates through the line profile. Wavelengths increase to the left. Vertical scale is in relative units.

to the investigation of transients and other flows in the chromosphere have been programmed and are under study.

d) Study of Sunspots and Active Regions

Sequences of high-resolution images and spectra taken 1" apart show the evolution of spot morphology and profiles in space and time. Umbral flashes have been observed as well as oscillations. Nearly simultaneous observations of lines from the photosphere to the transition region should allow us to study the vertical structure of spots.

A preliminary analysis of spacecraft rasters made with the 1" × 10" entrance slit, and LPSP internal rasters made with the 1" × 1", 1" × 3" entrance slit, show that regions of strongly enhanced O VI 103.2 nm emission very often tend to be distributed other than directly above sunspot umbrae. This is the case both for some unipolar single spots as well as multipolar spot groups. However, we do find circumstances when single spots show the transition region "plume"

directly over the spot as reported by Foukal *et al.* (1974).

Figure 17 shows this phenomenon, where isophotes are represented in photospheric light, L α , and O VI.

We have also found examples of steplike changes in the distribution of the enhanced O VI emission (Fig. 18). If we assume that the enhanced O VI emission is associated with a specific magnetic field connectivity, then our results imply "step" changes in field connectivity. The general O VI emission in the active region was found to be approximately 10 times brighter, with strongly enhanced features approximately 100 times brighter, than the average quiet Sun. Simultaneous observations in L α , L β , Mg II, and Ca II also show the general active-region enhanced emission as well as strongly enhanced features. The L α and L β features are identical, but show systematic horizontal displacement with respect to the Ca II and Mg II emission features. Little or no correlation is found with the O VI structures. With regard to the profiles of the resonance lines, the self-reversal is weak or absent above regions as shown on Figure 19. Presumably the line-forming region has reduced opacity.

e) Studies of Prominences

Temporal evolution of, and velocity field in, prominences were studied with consecutive monochromatic spacecraft rasters. Figure 20 shows, at the top, Ca II images at wavelengths ranging from -0.012 nm to +0.03 nm from line center. The main loop is clearly visible only at line center; this is confirmed by spectra constructed from the different monochromatic images of the prominence which show a single emission peak with a FWHM of 0.020 nm which is typical of quiescent prominences (Engvold and Livingston 1971). This is consistent with a mean turbulent velocity of 9 km s⁻¹ and a temperature $T_e = 8500$ K. At the bottom of Figure 20 are two simultaneous L α and L β images.

Several observations were made to study the thermal structure and evolution of active and eruptive prominences. Figure 21 shows an internal raster performed with a slit of 1" × 1" above active region McMath No. 14127.

The first three simultaneous images in L α , L β , and Ca II K $_2$ v show a loop system with a rather faint contrast in K $_2$ v as compared to the plage at the limb, but a higher contrast in L α (and L β). The next three images are separated by 11 minutes (raster repetition rate) and are made in O VI 103.2 nm. They trace out the high-temperature evolution of the region (O VI being formed at approximately 350,000 K). The first O VI image shows a faint high loop, the second some residual brightness around the foot of the loop, and the third an important enhancement at this same point. Then within 20 min the loop disappeared, as can be seen on the next three images in L α , L β , and Ca II K.

Many images and spectra have been obtained that will allow the study of temperature, density, and velocity variations during loop evolution (Vial *et al.* 1978).

OCTOBER 6th 1975 ORBIT 1608

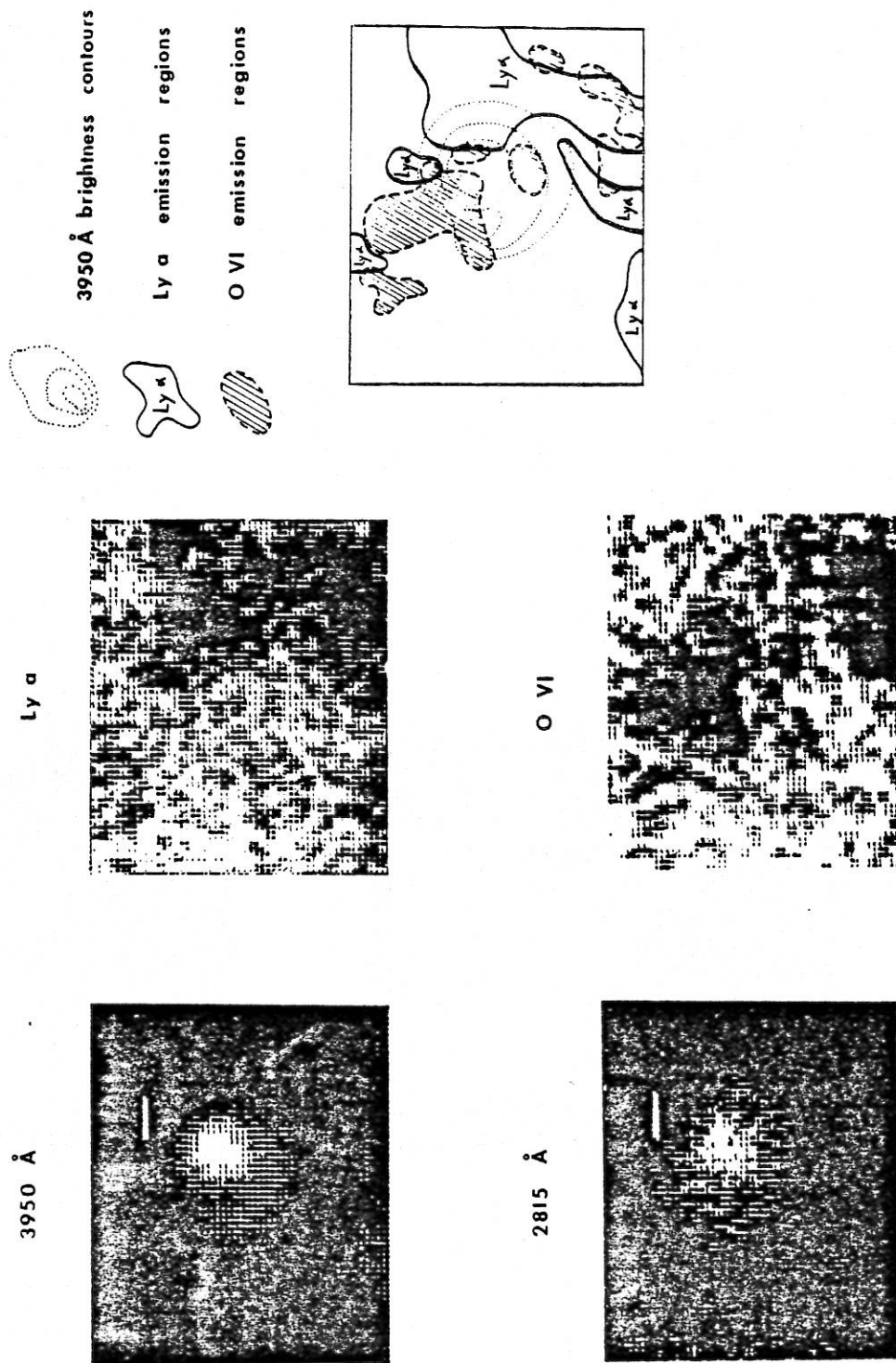


FIG. 17.—The variation with wavelength in the shape of a spot; the superposition of O VI, Ly α and "White light" isophots evidence a deformation with height in the solar atmosphere.

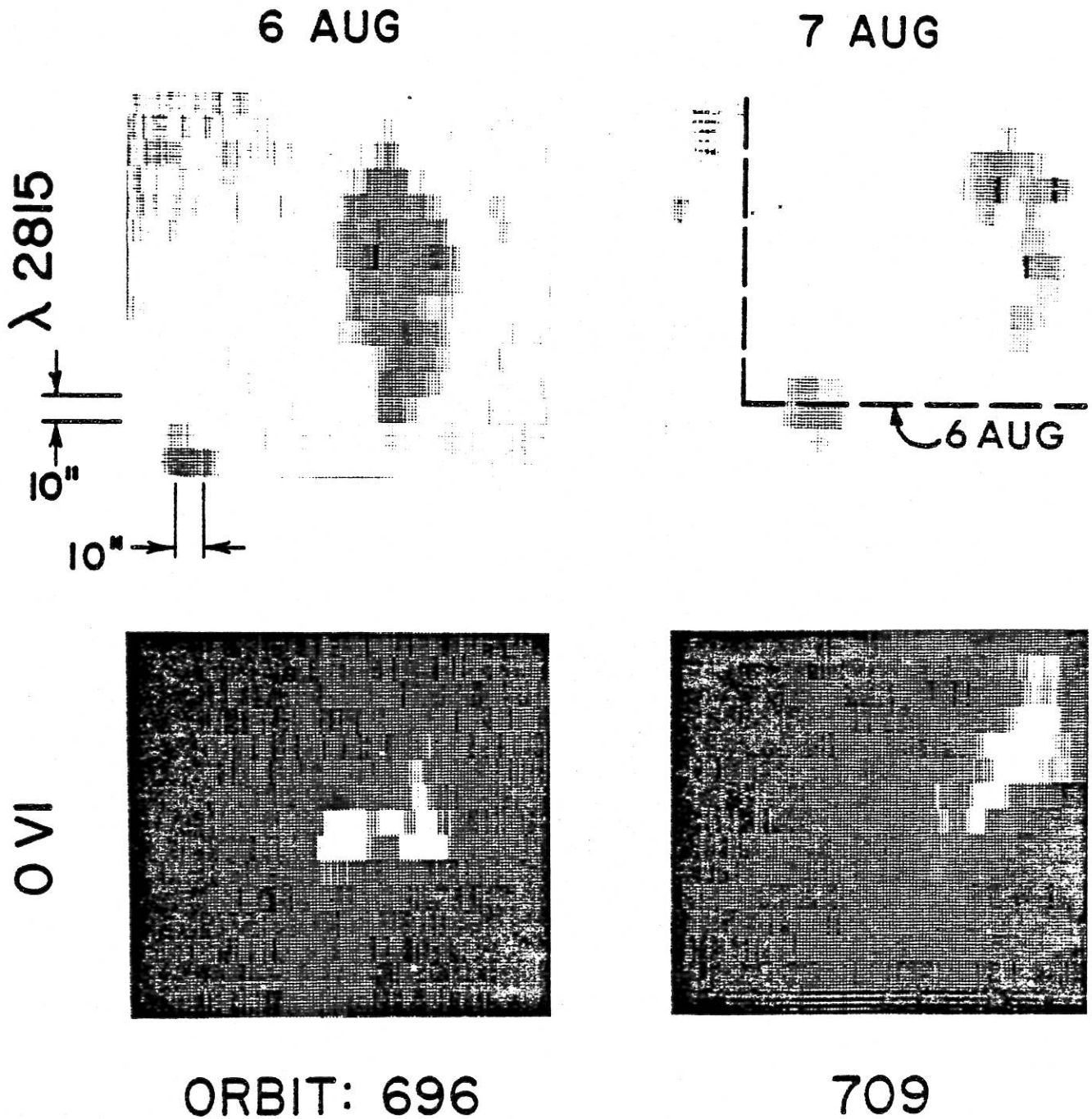


FIG. 18.—Illustration of step changes in field connectivity of spot evolution. The two upper pictures are satellite rasters made in the wings of Mg II k . The two lower pictures are taken simultaneously in O VI. The evolution of the sunspot group is continuous when observed in white light and discontinuous in O VI.

LPSP INSTRUMENT ON OSO 8

Figure 22 represents observations of an active region at the limb on 1975 July 7. The slit was parallel to the limb and probably intersected it slightly, as indicated by the presence of scattered light in the wings of the Ca II profiles. On the left portion of Figure 22, full and dotted lines correspond to profiles taken at positions separated by only $1''$. The emission maxima in Ca II and Mg II are displaced shortward with an amplitude corresponding to about 20 and 15 km s^{-1} , respectively. These maxima may in fact correspond to K_2v and k_2v , while K_2r and k_2r are barely visible and show up only as asymmetries in the line profile. $L\alpha$ is not displaced and shows the geocoronal reversal with no apparent self-reversal. The distance between its emission peaks is only 0.022 nm, leading to an optical depth of only 500 at line center. On the right panel of Figure 22, solid and dotted lines show temporal variations for a 22 min interval. Orbital Doppler effects have not been corrected for on the figure; but if they are corrected for, a shift to the longward is still found for Ca II and Mg II with an amplitude of 5 km s^{-1} . Moreover, Ca II and Mg II lines have essentially the same intensity while $L\alpha$ has increased by a factor of 2.

f) Chromosphere-Corona Transition Lines

The two lines Si III 120.65 nm ($3s^1S-3p^1P^o$) and O VI 103.19 nm ($2s^2P-2p^2P^o$) are formed in the chromosphere-corona transition region at 40,000 K and 350,000 K, respectively (Jordan 1969). They are observed with the LPSP instrument with a spectral resolution of 0.002 and 0.006 nm, respectively.

The shape of transition-region line profiles may indicate whether there is any propagation of either acoustic or magnetohydrodynamic waves (McWhirter 1977). The presence of such waves may be symptomatic of coronal heating mechanisms.

Figure 23 shows an average (single orbit) Si III profile at the center of the disk (quiet Sun) observed with a resolution of $1'' \times 40''$. The FWHM is 0.015 nm and, if we assume that the line is optically thin, the rms (line-of-sight) nonthermal velocity is 22 km s^{-1} . This value is 4 km s^{-1} higher than the values obtained by Nicolas *et al.* (1976) for the Si III lines at 128.9 and 189.2 nm.

Quiet and active Sun profiles of the O VI line at the center of the disk are given on Figures 24a and 24b. This line is optically thin, and the FWHM is 0.021 nm nearly identical for both quiet and active Sun; the rms line-of-sight nonthermal velocity is 30 km s^{-1} . A departure from a purely Gaussian profile can be noticed in both profiles. The line appears asymmetric and may indicate the effect of a velocity structure in the region of formation of the line.

Figure 24c shows a quiet limb O VI profile, averaged over several positions above the limb ($+2'' + 6''$). The FWHM is now 0.026 nm, equivalent to a rms line-of-sight nonthermal velocity of 38 km s^{-1} . This is larger by 11 km s^{-1} than the value previously quoted by Moe and Nicolas (1977).

The chromosphere and transition region height distribution is shown on Figure 25 as derived from

TABLE 6
CHARACTERISTICS OF SPECIES IN THE EARTH'S ATMOSPHERE
OBSERVED WITH THE LPSP INSTRUMENT

OSO 8 Channel	Component	Wavelength (nm)	Range of Altitudes in the Earth Atmosphere (km)
Mg II.....	O3	277.7-282.3	60-80
Mg II.....	OH	281.6	> 75
L α	O2	120.6-122.3	90-110
L α	H	121.6	> 500
L β	O2	101.7-103.2	150-200
L β	H	102.5	> 500

internal raster scans simultaneously in the wing of Mg II h , Mg II h_3 , O V 121.8 nm, and Ni II 119.95 nm.

As is apparent from the figure, the h_3 chromosphere appears to have an additional contribution, which may likely be due to spicules that appear to peak at about the same height as the O VI component. Separate measurements of O VI (and for the far wing of Mg II h) show a similar behavior as O V. These results would argue for an inhomogeneous transition between chromosphere and corona (cf. Doschek, Feldman, and Tousey 1975).

g) Aeronomy Investigations

At orbital sunsets and sunrises, the solar UV light is absorbed by successively denser layers of the Earth's atmosphere. Vertical distribution of number densities of several components may be studied by this technique as indicated in Table 6. The light in the Ca channels is not attenuated and provides a pointing reference.

The measurement of the width and depth of the hydrogen geocoronal absorption was undertaken during several orbit days. This is a new and very promising observational technique to measure simultaneously the exospheric temperature at each point of the orbit and the atomic hydrogen density at the exobase, which may solve the question of what mechanism(s) control(s) the hydrogen distribution at the exobase. The preliminary results of aeronomy investigation have been published in Vidal-Madjar *et al.* (1976).

VI. CONCLUSION

We have described here the actual performance of one of the most complex solar physics instruments launched into space and the main results obtained with the first high-resolution multichannel UV and visible spectrometer placed in orbit by OSO 8. For the first time, an absolute pointing accuracy of nearly $1''$ could be achieved in orbit with real time operations. It undoubtedly represents the largest and most complex experiment of the French space program in solar physics. Although the bulk of the data has not yet

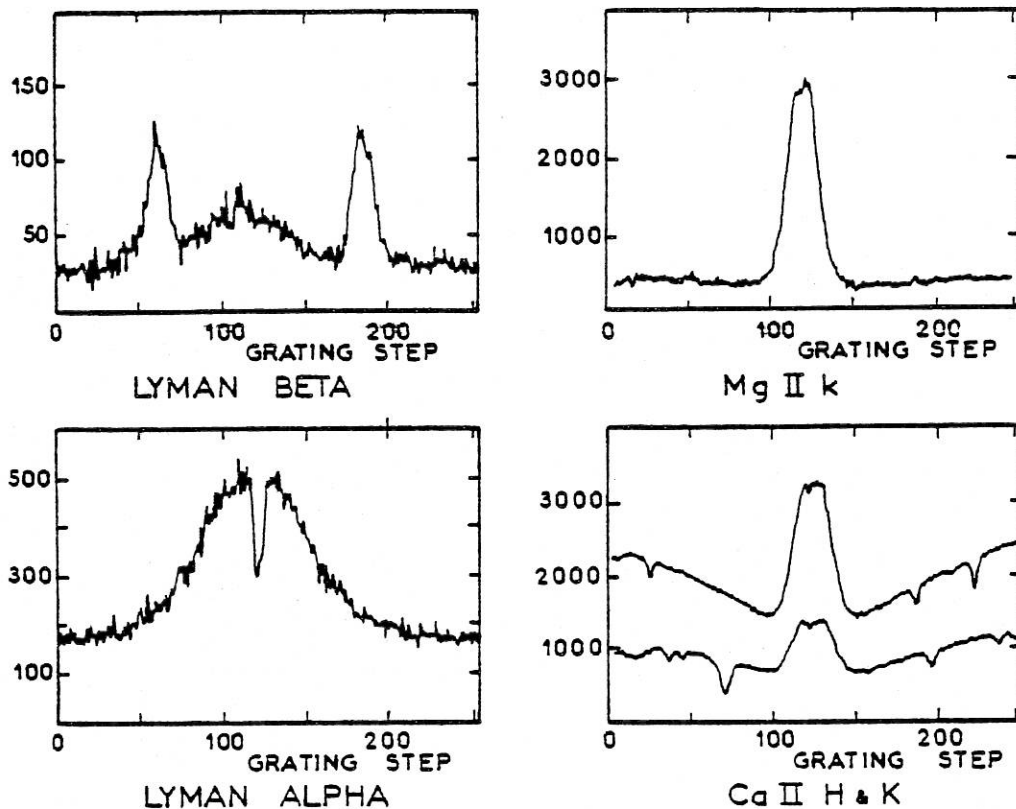


FIG. 19.—Profiles of Ca II K, Mg II k, L_{α} , and L_{β} observed simultaneously over an active region. All lines are free from the central self-reversal usually observed over quiet Sun areas. The two peaks in the L_{β} profile are the two O I lines. For conversion into λ units, see Table 1. Wavelengths increase to the left.

been examined in detail, preliminary analyses show that the performance of the instrument was nominal and at times beyond nominal expectations. The results presented here are only isolated samples of what has been obtained in the first 18 months. The instrument continues to perform nominally and has begun its third year of operation. This will allow us to obtain more data on active regions and particularly on flares which were very rare during the first 18 months. Indeed, only one flare, that of 1977 April 19, has been observed so far (Jouchoux *et al.* 1977).

The operation of the instrument has been very exhausting, and we have benefited from the assistance of many people. Our experience with regard to the remote management of an entirely automated complex instrument is, we feel, of great value for similar experiments in the future.

The accomplishment of this experiment would not have been possible without the support of CNES and particularly of Dr. A. Lebeau, former Director of Programs and Plans, and Professor M. Levy, former President. We would like to thank collectively the NASA and CNES engineers who have contributed to this experiment.

The operations of the instrument from Boulder would not have been possible without the kind

hospitality of LASP, in particular of its Director, Professor C. Barth. We also thank the LASP *OSO 8* staff for their contributions. We are indebted to NASA and LASP for access to space on the American calibration rockets. The excellent spirit of cooperation and the dedicated service of the *OSO 8* Control Center at the Goddard Space Flight Center was certainly a key to the success of real time acquisition and of the daily programming of observations in general. The observations of sunspots, active regions, and flaring regions could not have been done without the generous assistance of NOAA, Big Bear Solar Observatory, Meudon Observatory, Sacramento Peak Observatory, and Lockheed Research Laboratory. We wish to express our warmest acknowledgements to these numerous and often anonymous people who played such an important although thankless role in the daily work required by the continuous observation of the Sun during several years. Highly appreciated were the contribution of Drs. P. Bruston and M. Malinovsky of LPSP in the preparation and checkout of observing programs. Invaluable and continuous support in the daily operations was provided by M. Bruston (Mrs.) and N. Dionneau of LPSP. We also thank J. Borsenberger (Institut d'Astrophysique de Paris) and B. Phissamay (LPSP) for their important contribution.

Last but not the least, all of the Guest Investigators who have assisted our team in the operation and

*OSO 8 LPSP*SEQUENCE: 6
 $\Delta\lambda = +0.030$ nm.SEQUENCE: 12
 $\Delta\lambda = +0.017$ nm.SEQUENCE: 15
 $\Delta\lambda = +0.010$ nm.SEQUENCE: 18
 $\Delta\lambda = +0.002$ nm.SEQUENCE: 19
 $\Delta\lambda = 0.000$ nm.SEQUENCE: 20
 $\Delta\lambda = -0.003$ nm.SEQUENCE: 22
 $\Delta\lambda = -0.009$ nm.SEQUENCE: 24
 $\Delta\lambda = -0.012$ nm.Ly α
Integrated from
0.005 to 0.018 nm.Ly β
whole line

FIG. 20.—Series of satellite raster negative images, taken at different positions in the Ca K line ranging from -0.012 nm to $+0.03$ nm from line center. At the bottom are two simultaneous images of the loop prominence in $L\alpha$ and $L\beta$. Image size is $2\frac{1}{3} \times 2\frac{1}{7}$, repetition rate 82 s, resolution $10'' \times 10''$.

planning should be acknowledged here. They are: D. Dravins, S. Dumont, E. Frazier, K. Fredga, U. Grossman-Doerth, M. Hersé, S. Jordan, H. P. Jones, F. Kneer, P. McWhirter, W. Mattig, D. J. Mullan, J. C. Noens, J. Pasachoff, J. C. Pecker, G. Sharmer, G. Simon, J. O. Stenflo, M. von Uexuel, and A. Wyller.

The contribution, calibration, and operation of this instrument were funded under CNES contracts 70-220, 71-202, 73-202, 74-202, 75-202, 76-202, and

77-202. Special funding was provided by CNRS for the salaries of the seven LPSP scientists and programmers in charge of the operations at Boulder. The Guest Investigator Program was funded in the USA under NASA grant NSG 7130.

Additional acknowledgement must go to G. Sharmer for his extensive and supportive contributions which far exceeded his role as Guest Investigator.

OSO 8 LPSP

ACTIVE REGION 688 , WEST LIMB

MARCH 25 , 1976

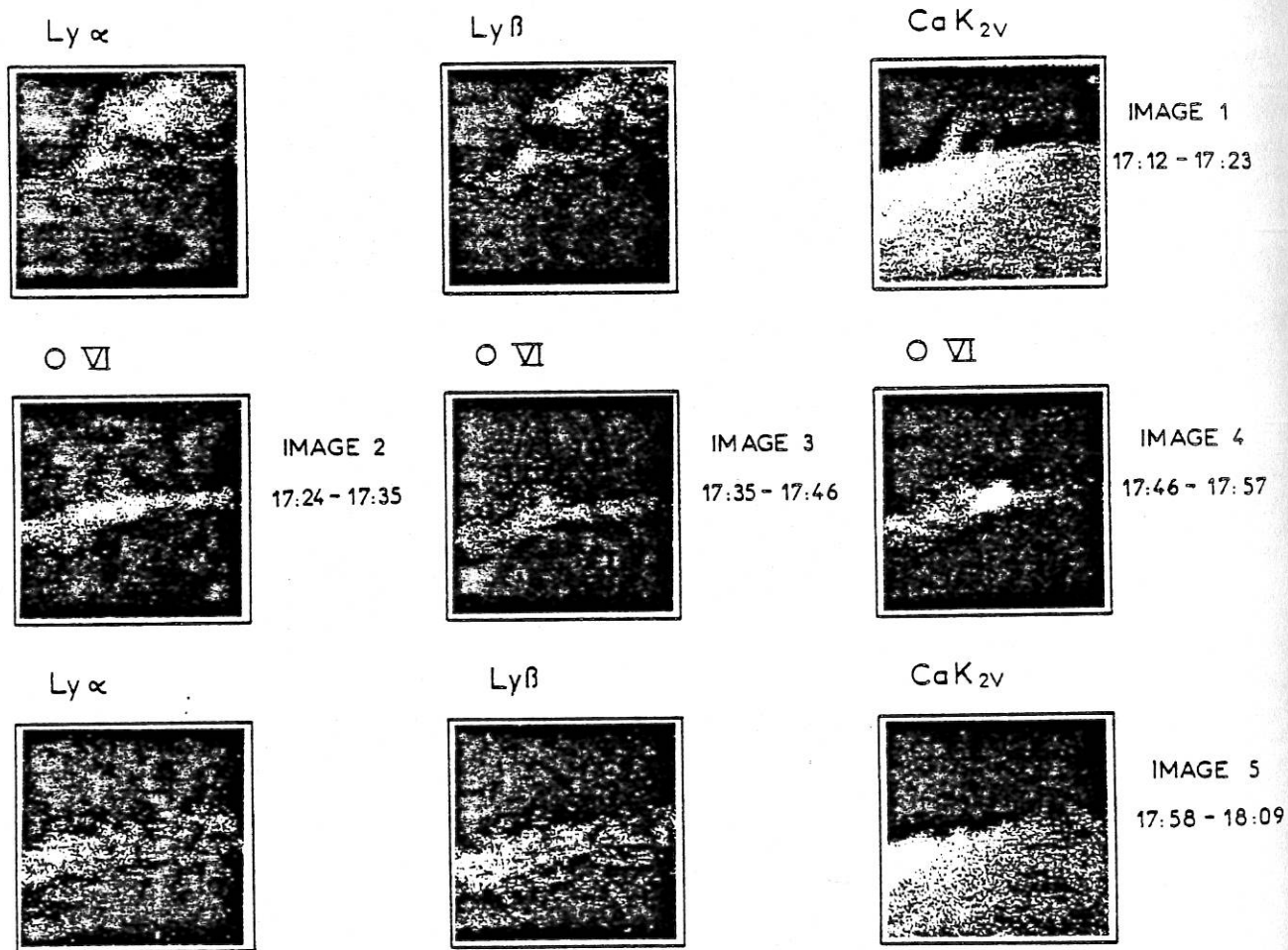


FIG. 21.—Development and evolution of an eruptive prominence associated with Active Region 14127 (McMath number) when it crossed the west limb.

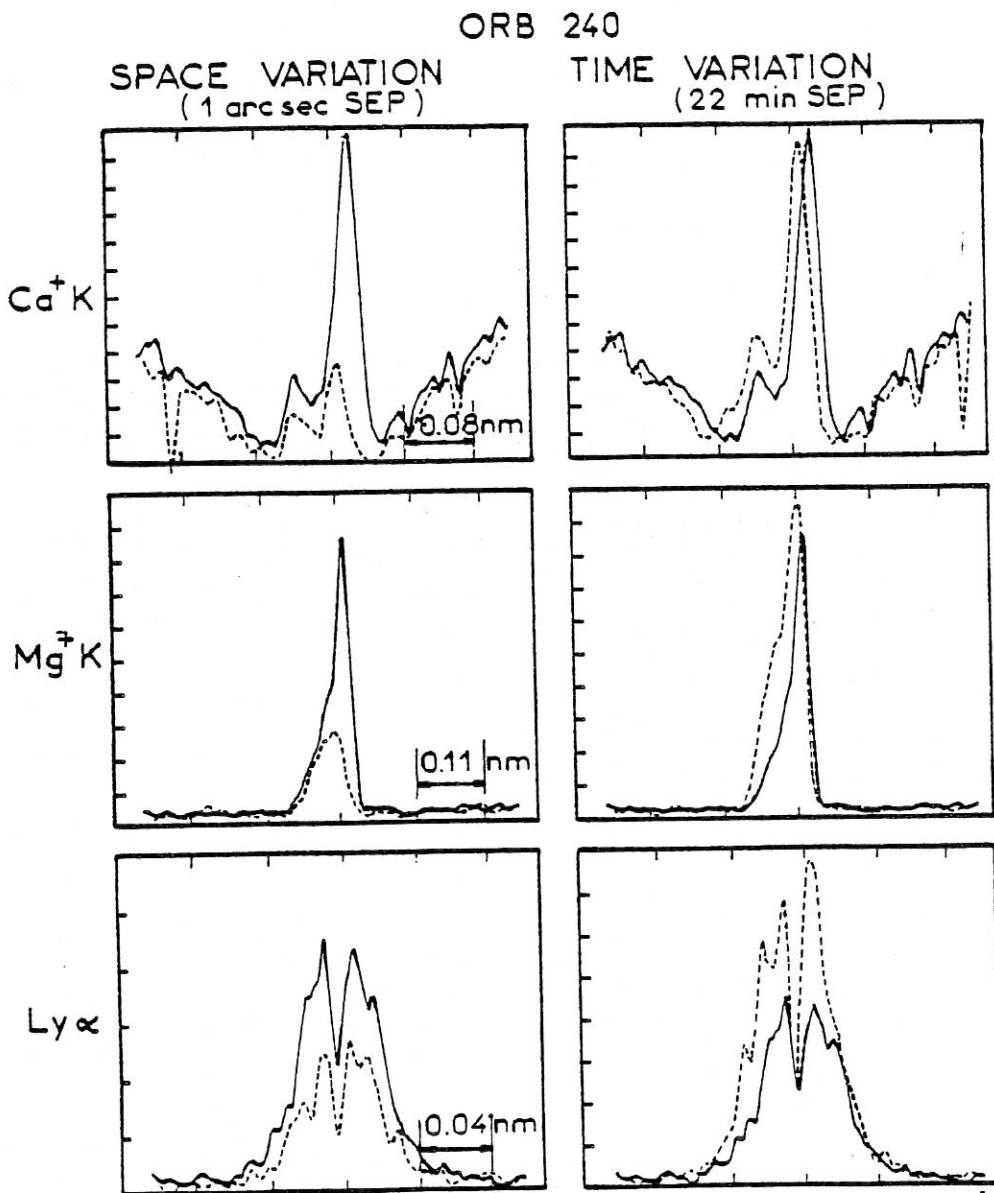


FIG. 22.—Profiles taken over an active region visible at the limb on 1975 July 7. The set of profiles on the left (*solid* and *dashed lines*) correspond to two points 1" apart. On the right, *solid* and *dashed* profiles correspond to profiles taken 22 min apart, in time.

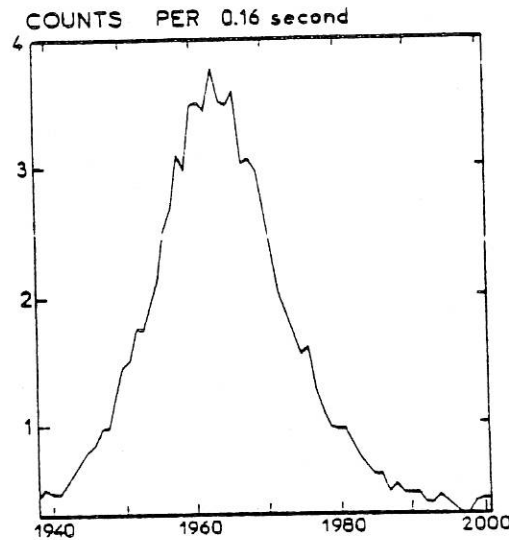


FIG. 23.—Profile of the Si III 120.6 nm line observed at Sun center with a resolution of $1'' \times 40''$. Wavelengths increase to the left. For conversion into λ units, see Table 1. Counts represent an average over one orbit.

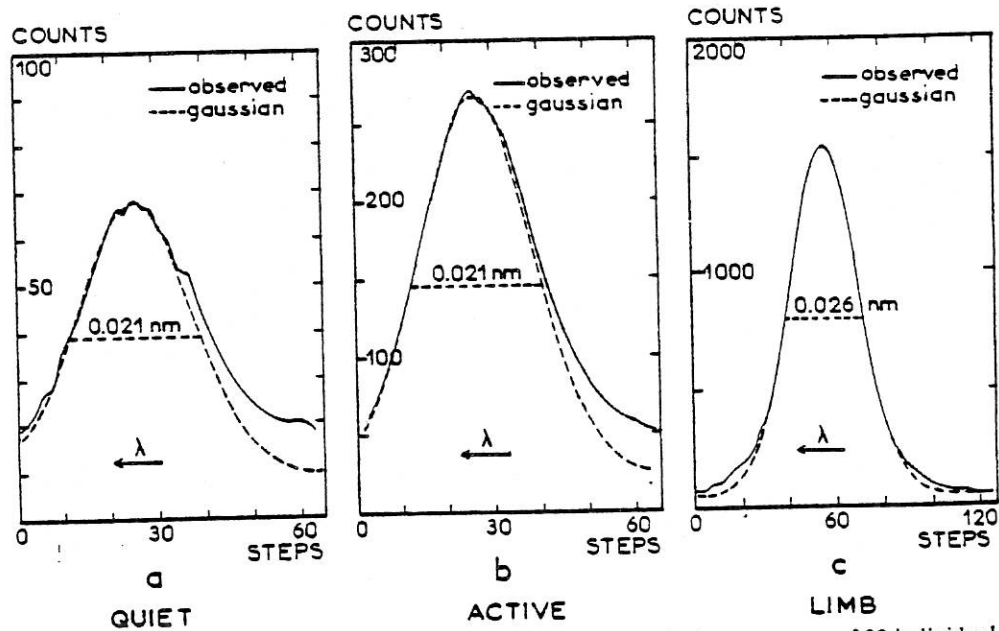


FIG. 24.—(a) Quiet and (b) active Sun profiles of O VI at Sun center. Each profile is an average of 20 individual profiles. The full lines represent the observations; the dashed line, a best Gaussian fit. The resolution is $1'' \times 40''$. Wavelengths increase to the left. For conversion into λ units, see Table 1. Profile (c) refers to the limb; it is also an average, but the individual profiles were observed at another orbit, and the units cannot be compared with those of profiles (a) and (b).

LPSP INSTRUMENT ON OSO 8

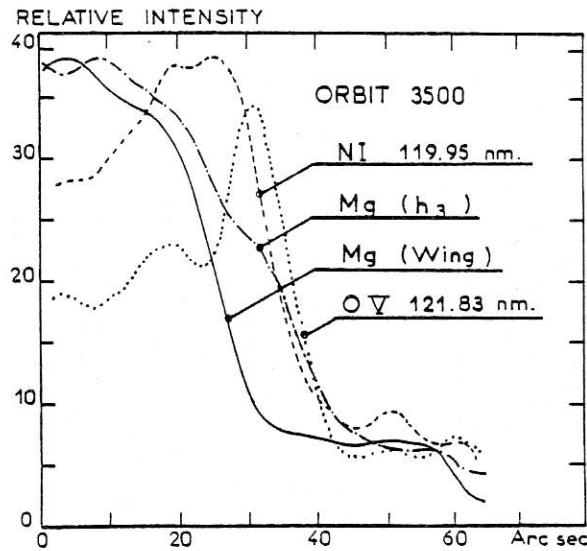


FIG. 25.—Limb "darkening" profiles, in Mg II h_3 , the far wing of Mg II k , NI 119.95 nm, and O V 121.83 nm. Distance is measured in arcsec (arbitrary origin).

REFERENCES

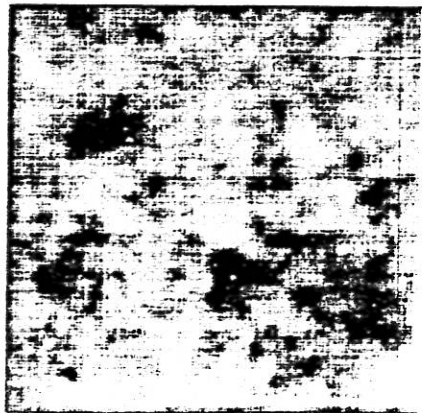
- Artzner, G. E., Bonnet, R. M., Lemaire, P., Vial, J. C., Jouchoux, A., Leibacher, J., Vidal-Madjar, A., and Vite, M. 1977, *Space Sci. Instrum.*, 3, 131 (Paper I).
- Artzner, G. E., et al. 1978, in preparation.
- Beckers, J. M., Bridges, C. A., and Gilliam, Lou B. 1976, Air Force Geophysics Laboratory Report AFGL-TR-76-0126 (II).
- Bonnet, R. M. 1968, *Ann. d'Ap.*, 31, 597.
- Bradford, A. P., Hass, G., Osantowski, J. F., and Toft, A. R. 1969, *Appl. Optics*, 8, 1183.
- Brault, J. M., and Testerman, L. 1972, unpublished.
- Doscheck, G. A., Feldman, U., and Tousey, R. 1975, *Ap. J. (Letters)*, 202, L151.
- Engvold, O., and Livingston, W. 1971, *Solar Phys.*, 20, 375.
- Foukal, P. V., Huber, M. C. E., Noyes, R. W., Reeves, E. M., Schmahl, E. J., Timothy, J. G., Vernazza, J. E., and Withbroe, G. L. 1974, *Ap. J. (Letters)*, 193, L143.
- Hinterreger, H. E. 1976, *J. Atmos. Terr. Phys.*, 38, 791.
- Huber, M. C. E., Dupree, A. K., Goldberg, L., Noyes, R. W., Parkinson, W. H., Reeves, E. M., and Withbroe, G. L. 1973, *Ap. J.*, 183, 291.
- Jordan, C. 1969, *M.N.R.A.S.*, 142, 501.
- Jouchoux, A., Skumanich, A., Bonnet, R. M., Lemaire, P., Artzner, G. E., Leibacher, J., Vial, J. C., and Vidal-Madjar, A. 1977, paper presented at the 150th Meeting of the American Astronomical Society, Atlanta.
- Jouchoux, A., and Hansen, E. 1978, in preparation.
- Kohl, J. L., and Parkinson, W. H. 1976, *Ap. J.*, 205, 599.
- Lemaire, P., and Skumanich, A. 1973, *Astr. Ap.*, 22, 61.
- Levasseur, A. C., Meier, R. R., and Tinsley, B. A. 1976, *J. Geophys. Res.*, 81, 5587.
- Linsky, J. L. 1970, *Solar Phys.*, 11, 355.
- Livingston, W. C., and White, O. R. 1978 (to be published).
- McWhirter, R. W. P. 1977, in *Proceedings of IAU Coll. 36, The Energy Balance and Hydrodynamics of the Solar Chromosphere and Corona*, ed. R. M. Bonnet and P. Delache (Nice), p. 220.
- Minnaert, M., Mulders, G. F. W., and Houtgast, J. 1940, *Photometric Atlas of the Solar Spectrum from $\lambda 3612$ to $\lambda 8771$* (Amsterdam: North-Holland).
- Moe, O. K., and Nicolas, K. R. 1977, *Ap. J.*, 211, 579.
- Nicolas, K. R., Brueckner, G. E., Tousey, R., Tripp, D. A., White, O. R., and Athay, R. G. 1976, submitted to *Solar Phys.*
- Reeves, E. M. 1976, *Solar Phys.*, 46, 53.
- Rottman, G. E. 1977, private communication.
- Salvetat, P. 1975, in *Technology of Scientific Space Experiments*, ed. CNES (Paris, May 1975), p. 445.
- Skumanich, A., Smythe, C., and Frazier, E. N. 1975, *Ap. J.*, 200, 747.
- Vernazza, J. E. 1972, thesis, Harvard University.
- Vernazza, J. E., Foukal, P. V., Huber, M. C. E., Noyes, R. W., Reeves, E. M., Schmahl, E. J., Timothy, J. G., and Withbroe, G. L. 1975, *Ap. J. (Letters)*, 199, L123.
- Vial, J. C., et al. 1978, in preparation.
- Vidal-Madjar, A. 1977, private communication.
- Vidal-Madjar, A., Laurent, C., Bonnet, R. M., and York, D. G. 1977, *Ap. J.*, 211, 91.
- Vidal-Madjar, A., Roble, R. G., Mankin, W. G., Artzner, G. E., Bonnet, R. M., Lemaire, P., and Vial, J. C. 1976, in *Atmospheric Physics from Spacelab*, ed. J. J. Berger et al. (Dordrecht: Reidel), p. 117.
- White, O. R., and Suemoto, Z. 1968, *Solar Phys.*, 3, 523.

G. ARTZNER, R. M. BONNET, P. GOUTTEBROZE, A. JOUCHOUX, P. LEMAIRE, J. C. VIAL, and A. VIDAL-MADJAR: Laboratoire de Physique Stellaire et Planétaire-C.N.R.S., P.O. Box 10, 91370 Verrieres-le-Buisson, France

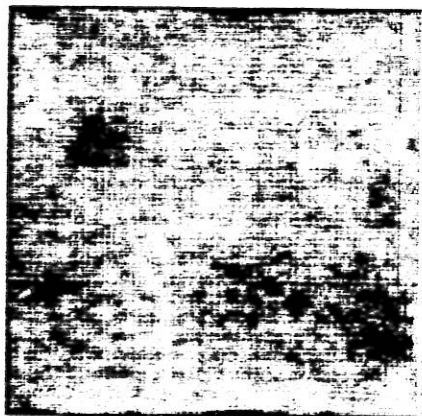
J. LEIBACHER: Lockheed Palo Alto Research Laboratory, 3251 Hanover St., Palo Alto, CA 94040

A. SKUMANICH: High Altitude Observatory, NCAR, Boulder, CO 80307

CA H & K



MG K & H



LY A & B

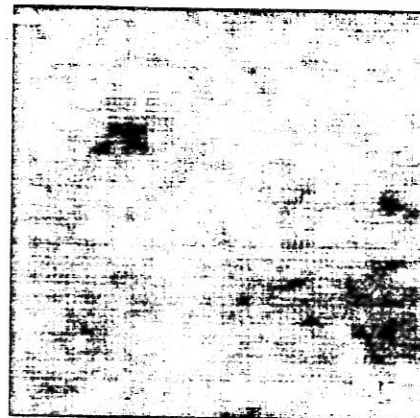
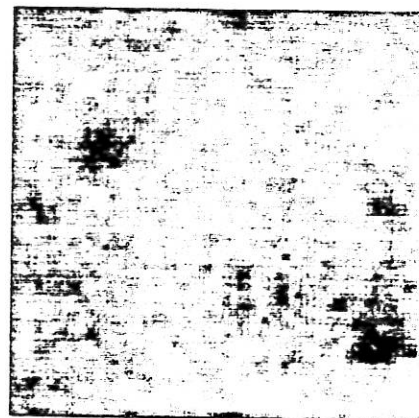
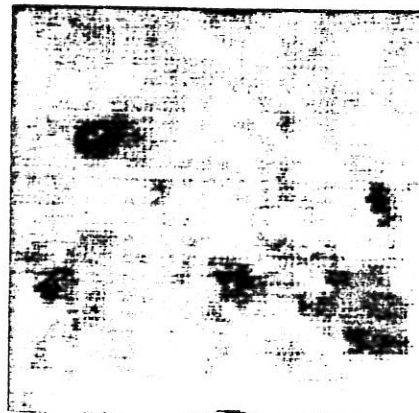
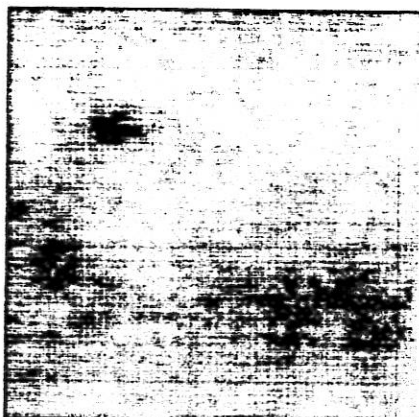


FIG. 8.—Internal raster images of the quiet Sun chromospheric network in Ca II K and H, Mg II h and k, $L\alpha$, and $L\beta$. The field is $64'' \times 64''$, the slit size $1'' \times 1''$.

BONNET *et al.* (see page 1044)

II - OBSERVATIONS DES PROTUBERANCES SOLAIRES.

1 - Etat des observations et des modèles.

Dans les comptes-rendus du colloque UAI 44 (août 1978 à Oslo), désigné ici par P.S.P. ("Physics of Solar Prominences"), le papier de revue de Hirayama (page 4, PSP) fait le point sur les observations spectroscopiques. Il est alors à peu près établi que le noyau froid d'une protubérance est à 4500-8500°K, les températures plus élevées étant obtenues à partir des mesures du continu de Lyman. Les régions faibles (ou externes) sont en général plus chaudes. La vitesse de turbulence est de l'ordre de 3 à 8 km s⁻¹ et croît vers l'extérieur (10 à 20 km s⁻¹). Les densités électroniques varient de 10¹⁰ à 10^{11.4} cm⁻³ et le degré d'ionisation (mesuré par $\frac{n_p}{n_1}$) varie de 1 à 10. Un désaccord existe enfin sur l'abondance de l'hélium. \bar{n}_1 . Les observations radio, u.v. et X (Schmahl, PSP p. 102) révèlent des cavités coronales au-dessus des protubérances et conduisent à une pression dans l'interface protubérance-couronne inférieure à la pression de la transition chromosphère-couronne.

Au point de vue théorique, les modèles proposés par Heasley and Mihalas (1976) Heasley and Milkey (1976, 1978) sont compatibles avec les observations à condition d'inclure un facteur de pénétration du continu de Lyman, ce qui augmente l'ionisation et la température au centre. Des désaccords existent entre intensités prédites (Ishizawa, 1971) et mesurées des raies du calcium ionisé (Landman and Illing, 1977).

Assez peu d'observations nouvelles sont intervenues depuis⁽¹⁾. Landman et al. (1978), Stellmacher (1979) observent des raies H et K non optiquement minces (K/H ~ 1.4), même dans les régions de faible émission. A partir d'observations du triplet infra-rouge de Ca II, Landman (1980) confirme l'existence de 2 régions de température, la plus froide étant à 7000°K (avec $n_e = 10^{11}$ cm⁻³) ; la région plus chaude est introduite pour expliquer les ailes des raies. Kubota (1980) trouve que dans 12% des cas, les profils H et K sont renversés et conclut à l'existence de couches froides absorbantes à la surface de la protubérance. Engvold et al. (1980) jettent le doute sur les mesures de largeur (et de décalage) de raies faites à moyenne résolution. Enfin, Engvold (1980) montre que les changements temporels des structures fines impliquent que le plasma peut être en état non stationnaire.

Dans la région de transition avec la couronne, Kanno et al. (1980), Orrall and Schmahl (1980) estiment que le degré d'ionisation ne dépasse pas 2. Lantos et Raoult (1980) montrent que la dépression radio observée sur le disque a son origine dans la transition protubérance-couronne et donnent la préférence au modèle e₂ de Heasley and Milkey (1976).

Enfin, en contradiction avec les résultats de Dunn (1960) et Engvold (1976), Martres et al. (1980) mettent en évidence des mouvements ascendants sur les filaments. A ces 2 types d'observations, Mercier and Heyvaerts (1977), Ribes et Unno (1980) proposent des explications.

(1) Nous n'envisageons pas ici les importants travaux sur le champ magnétique (Leroy, 1981).

2 - Les possibilités offertes par l'instrument français sur OSO-8.

La plupart des observations mentionnées ont été faites dans quelques domaines spectraux bien déterminés sur la même protubérance. Quand la comparaison est faite entre plusieurs raies (ou continus) elle n'est possible qu'à des moments différents (et dans des régions différentes) d'un même objet ou encore sur des objets différents. C'est le cas, par exemple, des observations du groupe d'Hawaï qui couvrent une gamme très large de raies malheureusement obtenues en des régions et des temps différents. Quand les observations sont vraiment simultanées (c'est le cas du polychromateur u.v. sur Skylab), elles concernent uniquement la région de transition et aucun profil de raie n'est mesuré.

L'instrument LPSP à bord du satellite NASA OSO-8 mesure simultanément les profils de 6 raies, émises par des atomes ou des ions de masses très diverses. Ces raies sont sensibles à des températures différentes et ont des opacités comprises entre 1 et 10^5 . Ceci est illustré par le tableau I où nous avons calculé les opacités au centre des raies observées, en prenant une couche homogène ($n_e = 2.10^{10} \text{ cm}^{-3}$, degré d'ionisation $\frac{n_e}{n_1} = 3$) isotherme ($T_e = 8.10^3 \text{ K}$, vitesse de turbulence de 8 km s^{-1}) d'épaisseur 5.10^3 km .

Tableau I

Raie	$\lambda(\text{\AA})$	Opacité au centre τ_0
L β (H I)	1025	$0.4 \cdot 10^5$
L α (H I)	1216	$1.9 \cdot 10^5$
Mg II k	2796	150
Mg II h	2803	75
Ca II K	3934	7.3
Ca II H	3969	3.8

Les raies métalliques permettent de faire un diagnostic des vitesses non thermiques et des mouvements organisés le long de la ligne de visée. La mesure des deux raies d'un même doublet (Mg II, Ca II) permet une estimation des opacités. La raie L α (et L β) qui joue un rôle important dans le bilan radiatif, donne accès à la région d'interface avec la couronne. Cette zone de transition est d'ailleurs étudiée avec l'une des raies du doublet de résonance de l'ion O VI ($\lambda = 1032 \text{ \AA}$), formée à une température égale (ou supérieure) à 3.10^5 K .

La mesure des profils sur une protubérance est rendue plus intéressante encore par la mesure quasi-simultanée des profils des raies chromosphériques qui "illuminent" la protubérance.

Une excellente résolution (spatiale et spectrale), la possibilité de sonder de petites régions, permettent donc -à priori- une étude fine et cohérente des protubérances. Il a fallu toutefois compter avec des contraintes instrumentales qui nous ont amené à réviser nos objectifs, et qui ont compliqué les programmes d'observations... et le traitement des données.

3 - Problèmes instrumentaux.

Ils sont décrits dans les deux articles précédents. Certains prennent toutefois une importance particulière dans les observations faites hors du disque solaire.

a) Lumière diffusée.

Le profil de lumière diffusée dans le télescope est donné dans l'article II (Figure 1). A environ 10" du bord, le niveau de lumière diffusée est de l'ordre de 2% en Ca II, 4% en Mg II, 10% en L α et 20% en L β .

b) Bruit de fond.

Il y a superposition du bruit de fond propre des détecteurs, et d'un bruit de fond optique (pour les voies Ca II) ou d'un parasitage interne (voies Mg II) ou externe (particules).

La Figure II.1. indique (en coups par porte de comptage) le niveau de bruit de fond optique (pour la raie H), dans le champ total de balayage de l'instrument (44' x 40'). Les Figures II.2 a et b donnent pour Ca H et Ca K la variation temporelle de ce bruit de fond, alors que l'instrument vise le centre du soleil, pour deux orbites différentes. Mentionnons encore la variation (aléatoire) de 1 coup par porte sur les voies Mg II.

c) Transmission instrumentale.

Les problèmes mentionnés deviennent critiques quand le signal mesuré est faible. C'est le cas quand la sensibilité de l'appareil chute d'un facteur 10^2 en deux mois. Il devient alors impératif de suivre très soigneusement les variations temporelles de la transmission et d'avoir de bonnes mesures de référence proches des observations. Les méthodes employées pour aboutir aux profils absolus sont décrites au fil des quatre articles qui suivent ; la standardisation photométrique est traitée plus en détail dans l'article n° VI (en particulier la méthode employée pour les raies Mg II). Les Figures II.3. donnent la variation de la transmission (relative) des 6 voies en fonction du temps. Nous avons superposé une approximation (par splines) qui permet de connaître la transmission orbite par orbite.

Le choix des références photométriques, la conversion en intensités absolues et sa précision sont discutés dans l'article VI (§ I.c.3). Notons qu'entre l'article III et les suivants, une révision photométrique de l'ordre de 25% est intervenue pour la raie L α (voir Lemaire et al., 1978 et 1981).

Les Figures II.3. donnent le facteur de conversion à appliquer aux comptages obtenus dans les six raies (après soustraction du bruit de fond). Il correspond aux références solaires suivantes :

H_{1V} , K_{1V} , h_{1V} , k_{1V} (bande passante 20 mÅ)

L α (intensité centrale, 0,2 Å) et L β (intensité intégrée, 1 Å).

pour une région calme au centre du disque. La configuration instrumentale type est

- (porte de comptage (130 ms, sauf 65 ms pour Mg II
- (fente d'entrée 1" x 10"

20	26	16	26	21	24	75	47	27	24	23	14	21	22	17	15	21	26	30	25	31	35	30	31	54	54	55	50	56	62	60	44
21	20	14	14	20	16	10	14	16	20	20	15	16	24	17	19	25	25	27	19	24	31	34	30	33	43	49	51	58	45	59	53
23	19	19	25	22	27	25	25	33	16	28	15	32	15	33	33	19	29	20	25	33	19	45	36	38	41	52	57	55	64	76	62
17	25	17	21	20	15	18	25	38	11	14	14	22	22	21	14	27	24	37	32	24	40	31	50	36	50	54	49	55	51	76	46
19	21	21	13	24	12	13	17	24	31	20	26	13	18	20	19	26	28	25	34	32	39	39	28	37	40	45	54	46	58	68	68
17	21	14	15	16	22	10	16	24	17	26	13	19	16	30	20	18	21	28	37	24	28	40	43	38	52	49	52	44	65	72	67
24	20	22	13	18	30	22	16	9	22	16	13	29	11	16	14	20	19	31	36	40	34	31	40	36	50	61	60	58	65	61	66
26	18	49	14	22	15	22	11	25	10	21	17	13	20	21	23	22	25	29	31	18	35	35	40	28	48	33	47	50	46	63	69
18	14	29	23	16	14	44	17	25	21	24	21	19	28	21	21	22	31	24	24	24	41	72	41	43	57	45	70	68	78	68	65
21	20	21	11	21	21	20	8	20	15	20	21	14	28	19	15	26	36	26	29	32	35	34	46	47	42	50	59	70	67	97	68
20	19	18	16	18	16	26	12	17	18	21	20	24	19	28	33	24	36	27	30	33	31	42	32	45	46	48	51	77	93	78	78
34	15	25	23	15	15	19	17	30	21	17	13	23	21	22	16	28	25	13	25	27	30	38	42	53	63	62	54	64	59	68	66
17	22	19	18	19	17	22	15	21	19	18	13	26	31	19	20	18	38	25	34	22	38	36	36	44	50	64	61	58	53	66	67
18	16	31	25	17	26	13	18	15	35	21	18	14	20	31	18	22	26	33	26	42	44	51	41	53	56	53	65	56	72	76	84
17	14	29	29	13	29	25	22	21	18	18	13	22	24	29	15	11	24	33	25	27	31	43	38	68	59	51	69	57	85	70	68
20	31	20	14	12	18	25	18	19	24	18	19	22	21	20	24	15	26	22	37	34	36	38	44	58	60	64	72	72	59	79	72
26	20	22	20	13	20	17	22	14	30	29	25	25	20	13	23	24	33	35	25	26	30	42	42	39	59	54	58	52	65	65	78
22	30	13	21	14	21	22	19	24	25	21	14	15	18	20	23	26	32	19	33	38	34	43	29	59	59	43	61	61	69	79	78
29	20	26	25	29	19	20	22	27	16	16	14	25	27	23	33	48	25	21	41	35	33	47	52	59	60	68	66	73	63	70	75
25	15	21	19	21	27	18	19	8	22	16	22	28	16	20	17	43	24	20	30	35	44	37	41	50	53	62	65	73	73	53	86
16	20	15	16	20	26	21	19	13	16	22	21	23	22	8	26	24	21	37	21	35	41	45	33	46	55	68	65	76	59	59	75
20	18	17	16	22	20	13	14	33	22	14	16	19	26	20	26	22	25	26	33	26	29	42	57	57	60	72	59	63	92	85	96
35	18	23	21	29	29	33	24	23	10	16	23	21	16	23	17	29	35	38	27	31	36	58	44	50	54	66	73	77	88	85	83
24	26	15	20	20	19	27	16	19	21	30	25	24	30	21	23	25	35	31	29	36	43	39	54	57	66	59	58	72	76	70	82
23	17	24	18	22	24	12	27	18	26	18	23	17	19	24	23	28	32	19	39	41	40	40	43	54	55	73	57	91	68	80	81
24	24	29	11	16	18	18	25	31	21	22	20	19	16	26	26	20	26	25	29	39	34	42	47	48	53	64	62	85	76	70	79
27	22	29	17	23	16	13	24	24	13	20	13	13	26	24	23	22	24	29	26	35	38	46	57	62	51	57	72	79	77	98	100
17	24	18	17	23	22	18	15	15	22	28	24	23	22	23	21	18	31	23	23	33	61	51	52	55	72	65	62	82	69	86	93
28	19	15	24	28	21	25	24	13	27	23	24	25	17	21	27	20	24	37	47	35	35	32	55	51	59	63	76	80	86	84	70
22	17	19	25	18	24	25	20	20	13	17	25	15	15	24	21	24	23	30	33	33	46	44	51	49	64	66	73	65	84	91	84
18	19	23	19	24	23	24	21	23	13	21	19	30	12	21	30	28	29	34	33	56	41	44	45	51	57	78	75	65	73	73	82
21	20	17	17	26	25	37	21	25	20	19	22	18	23	22	28	26	31	29	27	26	29	41	45	62	69	69	80	70	57	89	93
33	30	14	14	24	27	19	26	21	14	19	19	20	14	23	17	25	27	29	37	37	40	60	59	55	54	72	71	65	76	109	92
22	20	22	19	18	22	25	24	19	37	29	22	24	19	27	21	21	21	35	36	37	39	42	61	58	67	74	65	79	76	91	74
17	22	27	18	19	22	18	25	24	14	19	12	24	23	16	28	38	34	21	44	33	37	45	57	67	75	69	84	84	85	83	115
28	21	24	24	20	22	25	16	14	24	19	33	24	25	26	29	24	22	25	36	41	43	43	62	64	61	72	80	61	93	82	81
19	29	20	18	22	26	24	26	17	22	27	23	7	21	34	24	33	30	39	27	47	54	64	67	80	88	75	72	102	93	94	
21	31	24	28	26	27	36	22	25	13	28	15	22	21	24	25	30	30	26	36	38	41	54	59	71	82	67	65	72	85	85	76
15	13	28	21	24	15	19	19	32	31	20	22	25	20	27	20	35	24	37	32	40	43	54	53	70	67	63	84	76	87	66	102
22	16	16	27	24	20	23	17	26	26	19	23	31	20	24	36	29	25	53	35	51	36	49	40	83	76	89	86	86	103	92	110
24	22	28	26	23	14	16	25	32	27	21	19	25	42	18	30	26	27	46	30	42	65	55	63	59	81	70	74	35	89	95	94
21	24	24	28	26	13	28	14	25	34	25	17	18	30	27	24	35	27	60	39	53	36	42	57	65	76	78	59	83	89	93	95
29	20	17	25	18	26	29	27	22	19	28	24	25	15	28	32	28	28	27	31	33	54	41	63	56	66	72	97	87	79	85	94
25	24	28	29	19	23	20	19	23	28	18	25	28	29	33	29	26	35	27	41	42	45	60	45	64	65	70	91	75	82	101	103
23	17	24	19	19	20	31	18	24	16	29	27	29	24	29	27	35	29	48	47	35	48	52	41	75	72	84	83	73	93	112	107
27	22	16	25	17	19	29	25	28	26	33	24	18	26	20	25	24	24	34	47	43	45	63	66	53	80	67	102	82	101	110	
25	24	20	19	25	31	25	26	24	19	24	34	29	30	22	29	30	26	30	23	42	55	50	49	73	77	63	82	86	84	117	110
29	24	25	33	23	21	25	28	28	22	26	13	16	21	23	35	22	31	33	38	42	49	53	54	76	81	73	80	86	93	103	91
20	23	21	22	30	21	18	18	25	26	23	27	28	29	24	27	32	46	37	46	43	49	70	66	60	82	75	89	94	97	92	115
31	22	25	26	31	26	24	23	14	31	19	22	18	42	30	20	28	35	30	46	37	56	56	69	66	74	92	107	102	90	114	83
23	24	22	26	25	27	27	24	25	23	29	15	33	37	36	28	31	27	31	46	43	38	61	52	56	78	93	98	105	97	105	108
23	39	25	35	25	35	19	26	29	24	18	22	24	24	27	32	27	26	39	37	52	31	65	67	81	63	95	77	117	91	99	113
22	24	29	28	26	30	31	29	39	20	20	29	18	27	19	18	23	27	42	31	48	40	57	60	67	79	75	97	91	106	112	124
20	17	20	21	37	35	17	21	22	26	24	21	28	19	28	19	35	27	34	49	48	53	53	47</								

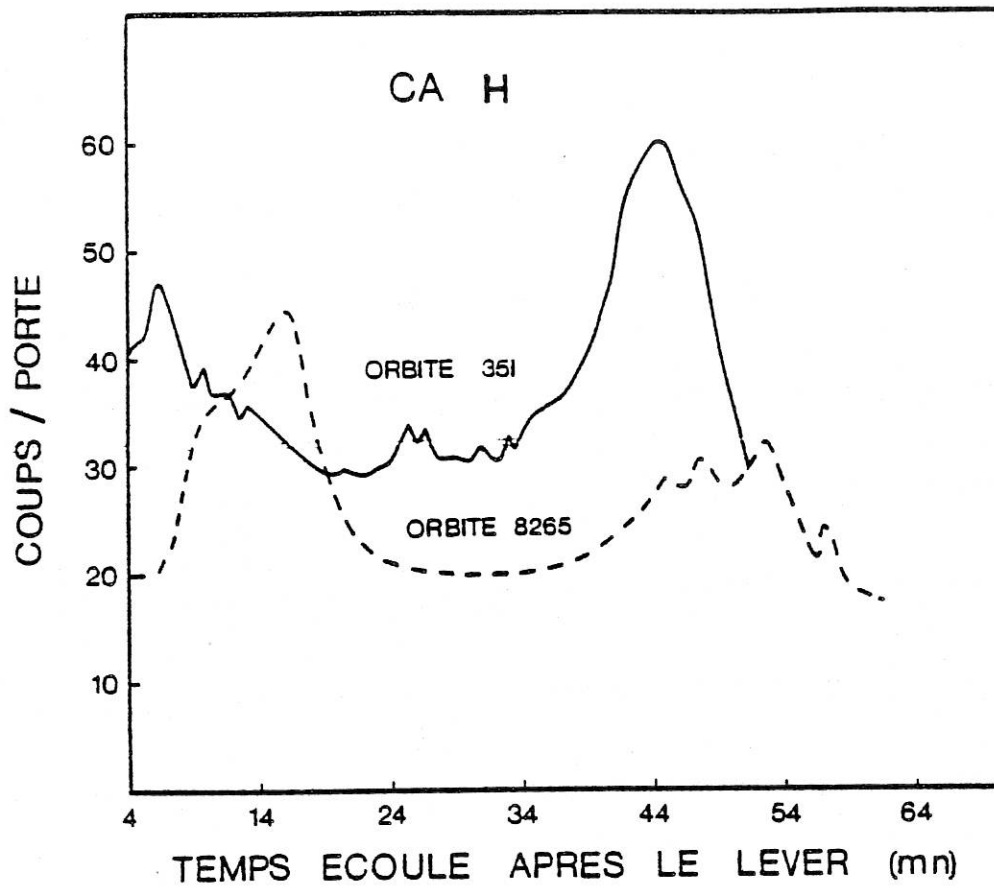


FIG. II.2.a: Variation temporelle (sur une orbite) du bruit de fond optique sur la voie Ca H. (coups/porte de comptage). La mesure est faite au centre du disque solaire pour 2 orbites différentes.

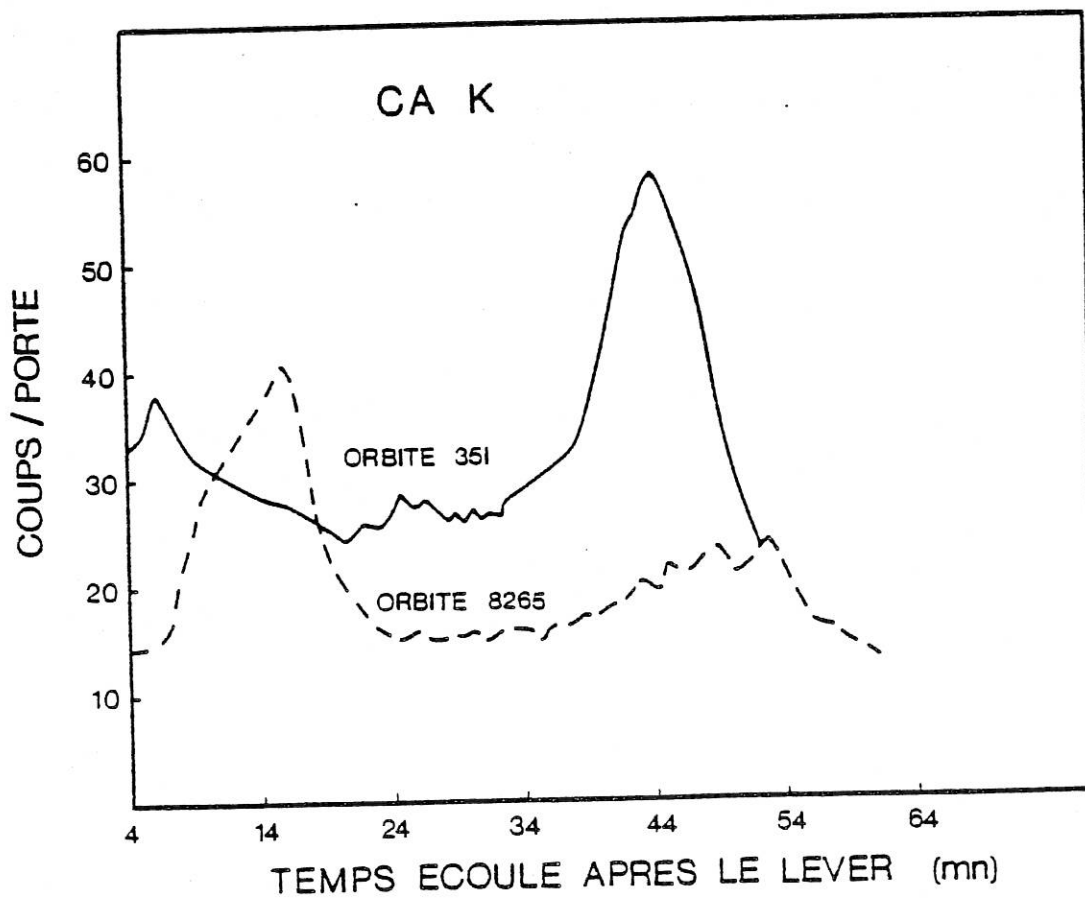


FIG. II.2.b. : mêmes paramètres pour Ca K

CA H1V

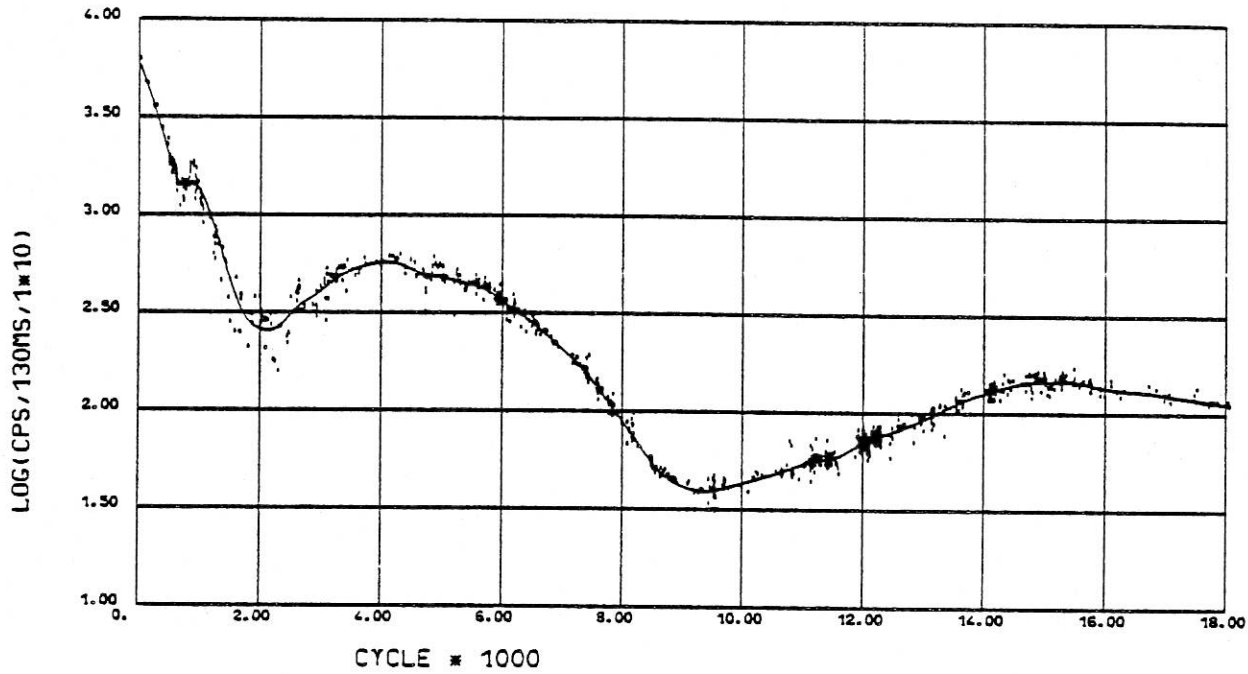


FIG.II.3.a et 3.b

CA K1V

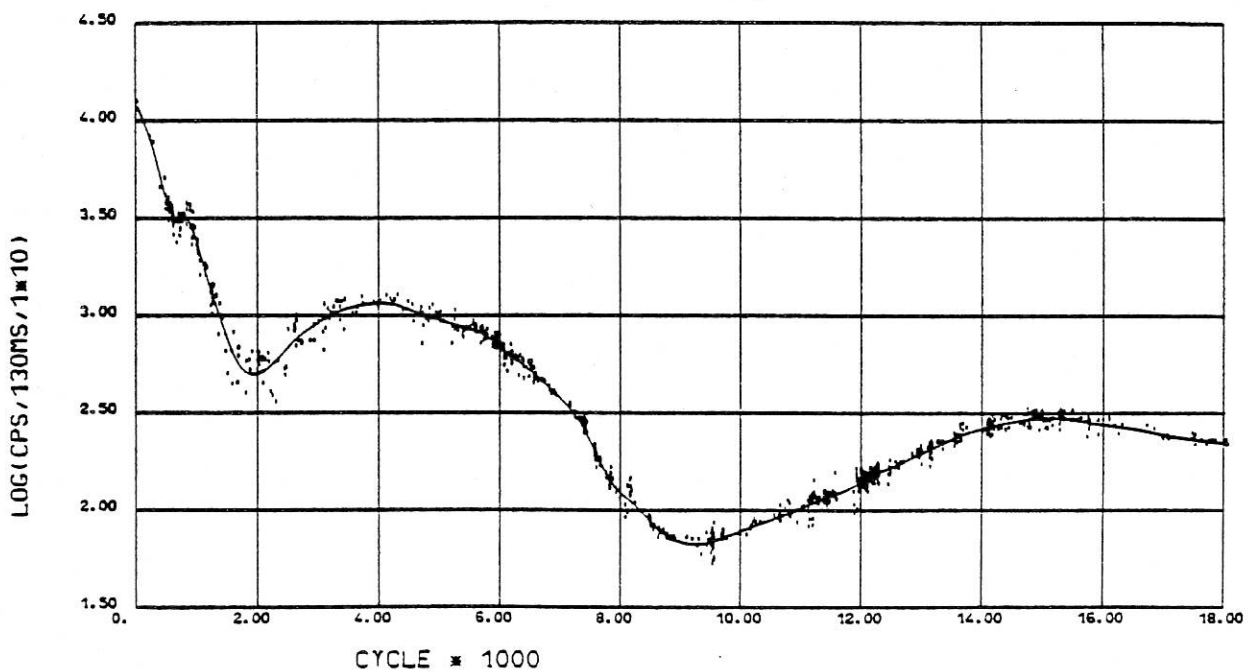
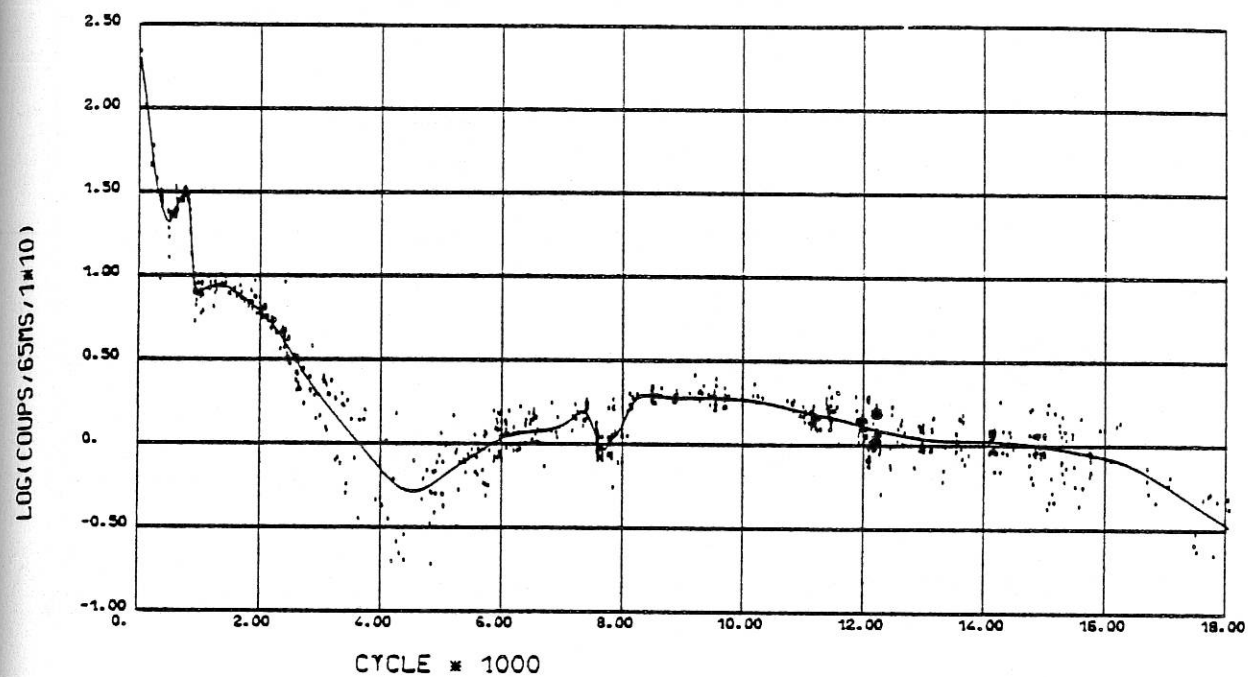


FIG. II.3. : Variation du signal mesuré dans les 6 raies en fonction du numéro d'orbite (temps écoulé depuis le lancement du satellite). La courbe d'approximation permet de calculer la transmission de l'instrument pour n'importe quelle orbite.

MG H1 (MOYENNE DE V ET R)



MG K1 (MOYENNE DE V ET R)

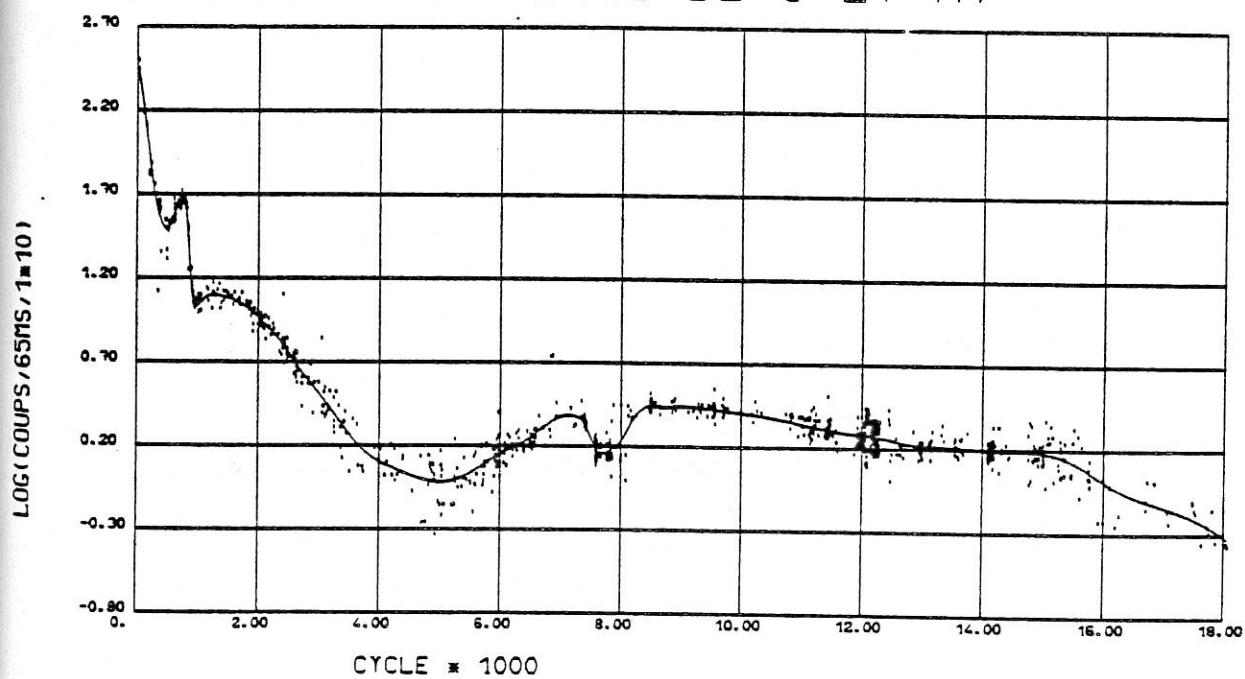


FIG. II.3.c et 3.d

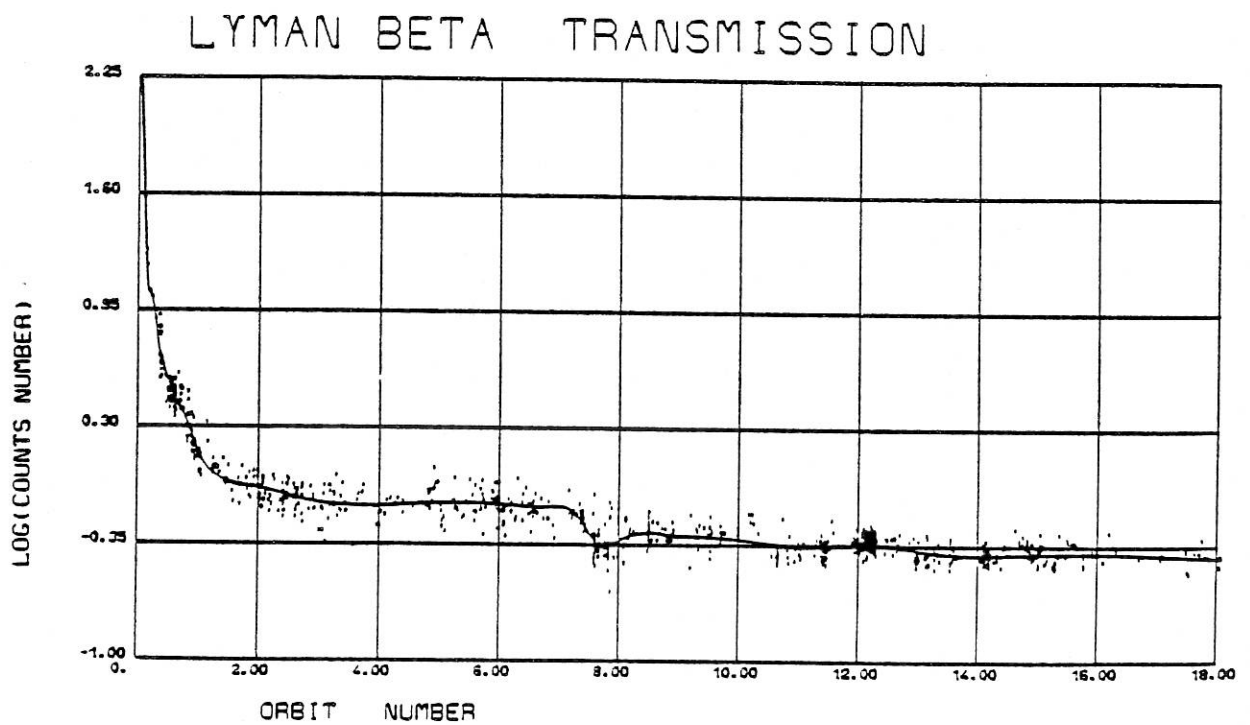
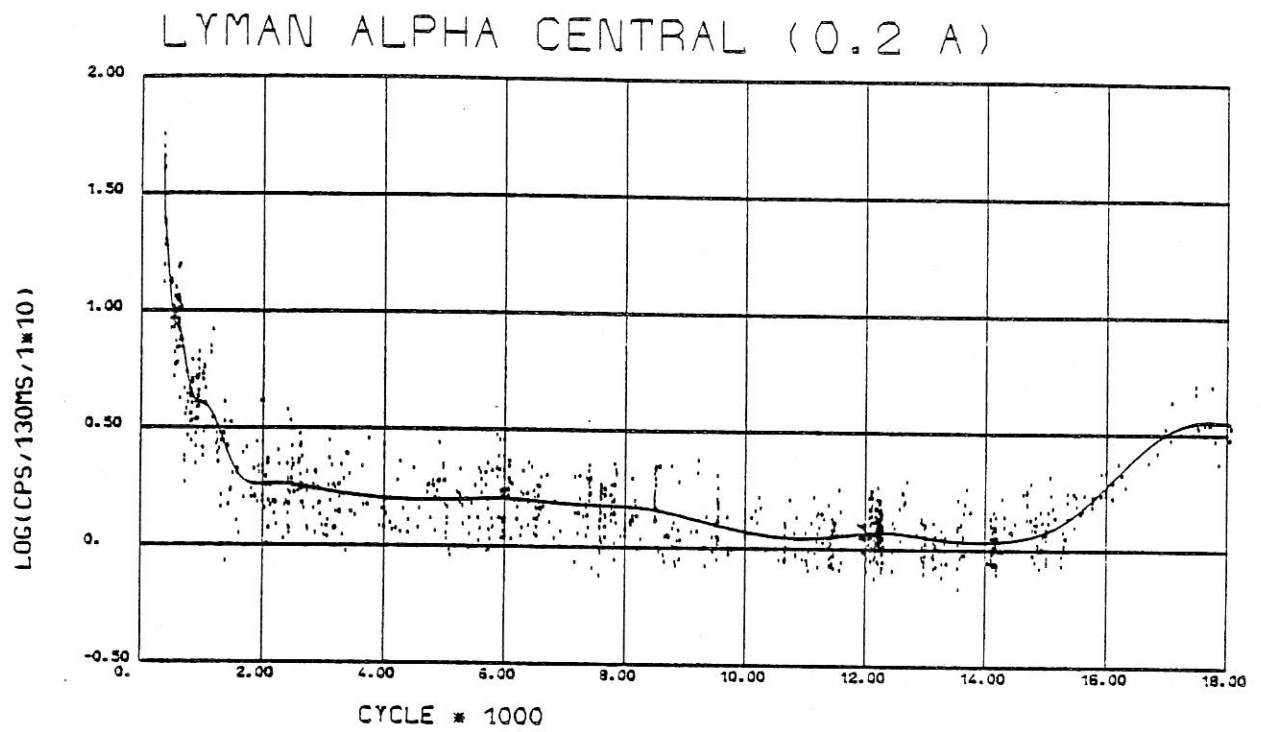


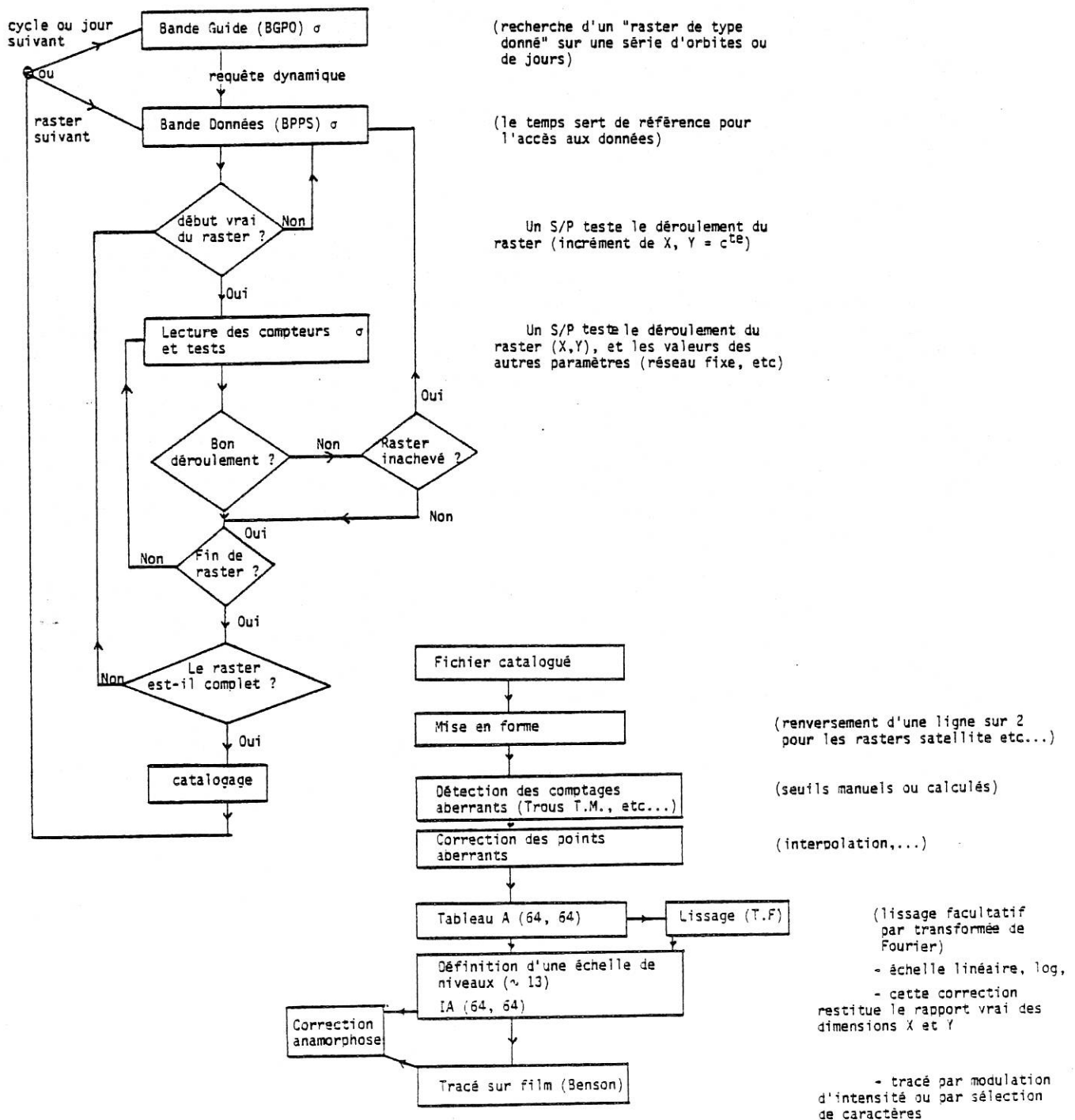
FIG. II.3.e. et 3.f

4 - Modes d'observation et traitement des données.

Les modes d'observation sont décrits notamment dans les articles III et VI. Nous n'insisterons pas sur les nombreux problèmes de traitement de masse des données. Signalons que 1100 bandes de données (1600 bpi) ont été créées par le centre de calcul du CNES à Toulouse pour les quelques 18000 orbites d'observations.

A titre d'illustration, nous donnons l'organigramme de la méthode d'obtention d'images, celle-là même utilisée pour les 6 images du réseau chromosphérique (Figure 8 du papier II).

Création d'un FICHIER IMAGES.



ARTICLES III et IV.

Ces articles donnent les résultats de 2 orbites qui sont au début d'une journée entière (7-8 juillet 1975) consacrée à une protubérance active qui passait au bord ouest. Nous avons bien pointé l'objet visé mais nos mesures ont été gênées par l'Anomalie Sud Atlantique et la défaillance du balayage "raster" du satellite.

Article III.

Nous publions les premiers profils des raies $L\alpha$, et h et k (Mg II) sur protubérance (active). Nous mettons en évidence des champs de vitesse croissants à la périphérie (pouvant atteindre 20 km s^{-1}). Nous calculons directement l'opacité de la raie $L\alpha$ ($\tau_0 \sim 10^5$). Nous trouvons des rapports "anormaux" des raies (k,h) ($k/h \sim 2$) et (K,H) ($K/H \sim 1.1$), c'est-à-dire en contradiction avec les abondances.

Article IV.

Il s'agit des premiers profils O VI absolus sur protubérance, au bord et au centre du soleil calme. Nous avons, à la périphérie de l'objet, à la fois un maximum de décalage de raie (vitesse de l'ordre de 8 km s^{-1}) et un minimum de largeur de la raie (cf. Figure 5). Nous discutons l'augmentation de largeur de la raie dans la couronne au-dessus de la protubérance. La mesure de l'intensité absolue et de la largeur de la raie, nous permet de conclure que la raie observée ne se forme pas à $3 \cdot 10^5 \text{ K}$. La contrainte supplémentaire fournie par des mesures de densité électronique (intégrée sur la ligne de visée) nous donne la mesure d'émission. La température ainsi obtenue ($\sim 10^6 \text{ K}$) réduit les vitesses non thermiques à des valeurs nettement subsoniques. Ces résultats sont confirmés par des mesures faites sur les autres orbites de la journée (non publiées).

Nous concluons que la protubérance elle-même est le siège d'agitations non thermiques réduites (influence de B), que les vitesses (sur la ligne de visée) se prolongent de la région froide à la transition avec la couronne et que la région au-dessus de la protubérance, est à une température de l'ordre de 10^6 K , avec des vitesses inférieures à 50 km s^{-1} .

D'autres objets "actifs" ont été également étudiés (voir la liste complète des publications OSO-8) en particulier un "post-flare loop prominence system" (Vial et Bruston, 1978, et Figure 21 du papier II).

Article III

Profiles of H I ($L\alpha$), Mg II (h and k), Ca II (H and K)
lines of an active filament at the limb, with the
LPSP instrument aboard the OSO-8 satellite

J.C. VIAL, P. GOUTTEBROZE, G. ARTZNER and P. LEMAIRE

PROFILES OF H I ($L\alpha$), Mg II (h and k), Ca II (H and K) LINES OF AN ACTIVE FILAMENT AT THE LIMB, WITH THE LPSP INSTRUMENT ABOARD THE OSO-8 SATELLITE

J. C. VIAL, P. GOUTTEBROZE, G. ARTZNER, and P. LEMAIRE

*Centre National de la Recherche Scientifique, Laboratoire de Physique Stellaire et Planétaire,
Verrières-le-Buisson, France*

(Received 11 June; in revised form 5 October, 1978)

Abstract. We scanned the H I $L\alpha$, Mg II h and k, Ca II K and H lines simultaneously with the LPSP instrument on OSO-8, to investigate the low and moderate temperature regions of an 'active region filament'. The $L\alpha$ line is not reversed except for the innermost position in the prominence. Intensity (k/h), (K/H) ratios are respectively 2 and 1.1, indicating that the Mg II lines are optically thin, and that Ca II K is saturated, although not clearly reversed. The results obtained during the second sequence of observations (K saturated before $L\alpha$ for example) indicate that within the size of the slit ($1'' \times 10''$) we are not observing the same emitting features in the different lines.

We also observe an important line-of-sight velocity at the outer edge of the feature, increasing outwards from a few km s^{-1} to 20 km s^{-1} within $2''$. Less than half an hour later, this velocity is reduced to 15 km s^{-1} while the intensities increase. Full width at half maximum intensities for this component indicate turbulence variations from 22 to 30 km s^{-1} . The observed high velocities at the top of the prominence can be compared with radial velocities that Mein (1977) observed in H α at the edges of an active filament and interpreted as velocity loops slightly inclined on the axis of the filament.

1. Introduction

With space-borne experiments, the UV spectral range is now available for prominence observations. Previous OSO and Skylab results refer to the prominence-corona interface as observed in the EUV lines formed at temperatures ranging from a few times 10^4 K to 10^6 K . Noyes *et al.* (1972) noticed that prominences appear as faint objects for temperatures above $3 \times 10^5 \text{ K}$; Schmahl *et al.* (1974) showed that prominence material is optically thick in the $L\alpha$ line and Lyman continuum of H I. Rocket slitless spectra obtained during the 1970 eclipse (Gabriel *et al.*, 1971; Orrall and Speer, 1974) led to the same conclusions. The comparison between prominence and disk brightnesses for the whole set of lines recorded on Skylab makes an 'emission measure' analysis possible (Orrall and Schmahl, 1976) for the prominence-corona interface.

As far as the cool part of a prominence is concerned, photometric measurements have been made, from the ground, in visible hydrogen, helium and calcium lines: recent results are found in Landman and Illing (1977), Landman *et al.* (1978), Engvold (1976). Brightnesses or line ratios may be compared to the results of theoretical models; for example, those of Ishizawa (1971), Heasley and Milkey (1976), Poland *et al.* (1971), which assume departures from LTE.

On the other hand, line profiles can provide data on the opacity, temperature, and turbulent motions in prominences. Analysis of visible hydrogen and helium lines has

J. C. VIAL ET AL.

established a low temperature ($T \approx 6000$ K) and a turbulence of about 6 km s^{-1} for quiescent prominences and higher values for active prominences (see Tandberg-Hanssen's *Solar Prominences*, p. 16). Ca II profiles have been measured by Engvold and Livingston (1971), Morozhenko (1974), and more recently by Mouradian and Leroy (1977) together with $H\alpha$, Landman *et al.* (1977) with $H\beta$ and D_3 and Engvold (1978) with $H\alpha$ and D_3 . Inferred temperature and turbulence values are in the ranges 8000 – $10\,000$ K and 5 to 8 km s^{-1} ; moreover, Landman *et al.* (1977) called attention to a two component structure of the profiles that would have been missed had only brightness measurements been available.

A few measurements have been made in the h and k lines of Mg II. Bonnet *et al.* (1967) first detected Mg II emission on a medium resolution (0.4 \AA) spectrum cutting across a prominence on January 13, 1967, Fredga (1969) obtained an image, and Feldman and Doschek (1977b) measured both profiles above an active region with a 0.12 \AA resolution and derived nonthermal velocities ranging from 15 to 25 km s^{-1} for distances $4''$ to $8''$ above the limb. Hydrogen Balmer series profiles give velocities between 0 to 15 km s^{-1} at $2''$ above the limb (Feldman and Doschek, 1977c), but these authors found low velocities in the transition zone between quiescent prominences and the corona.

The $L\alpha$ line of H I which is formed at higher temperatures has been extensively studied by Hirayama (1964), Yakovkin and Zeldina (1968), Burns (1970), and Poland *et al.* (1971). Kawaguchi (1964) suggested that, although detailed balance may hold in the interior of the prominence, the $L\alpha$ radiation may be transferred to Lyman continuous quanta as a result of absorption of the Balmer continuous radiation and subsequent recombination to the ground level at the surface. This is a way to take into account the need for a strong penetration of the UV radiation field in the prominence, established by the non LTE computations of Heasley and Mihalas (1976), and Heasley and Milkey (1976). Until now no emergent $L\alpha$ profile has been computed or measured.

We present below simultaneous profiles of H I ($L\alpha$), Mg II (k and h), and Ca II (H and K) lines, obtained with the LPSP instrument on OSO-8, on an 'active region filament' (following Tandberg-Hanssen's definition) as it crossed the west limb. Profiles of these 5 lines have also been obtained for quiescent prominences and will be published later.

The $L\alpha$ and Mg II profiles on a prominence with a 20 m\AA resolution are the first to be reported in the literature.

2. Observations

The feature studied in this paper is a long filament, one foot of which was located above the spot of active region MacMath No. 13738. We observed it on 7 July 1975 at 10 UT when it was at the west limb, while the spot was already beyond it. Internal images were generated during the passage of the spacecraft through the South Atlantic Anomaly and could not be used for localization purposes. This was done

LINE PROFILE MEASUREMENT ABOARD SATELLITE

instead using the scarce material available, namely the Boulder $H\alpha$ spectroheliogram of the day and a $H\alpha$ coronagraphic picture taken at 18:54 UT at Meas Solar Observatory. $H\alpha$ spectroheliograms, daily maps of the Sun and $H\alpha$ synoptic charts enabled us to locate precisely 4 prominences which are visible on the coronagraphic plate. On the other hand, the spacecraft pointing quality was checked and corrected for non-linearity effects. From this data we computed the actual position of the slit above the limb and were able to locate it on the $H\alpha$ coronagraphic plate. Figure 1 shows an enlargement of the $H\alpha$ image: the pointed structure is about $12''$ high above the occulting disk; the size and the orientation of the slit are also shown.

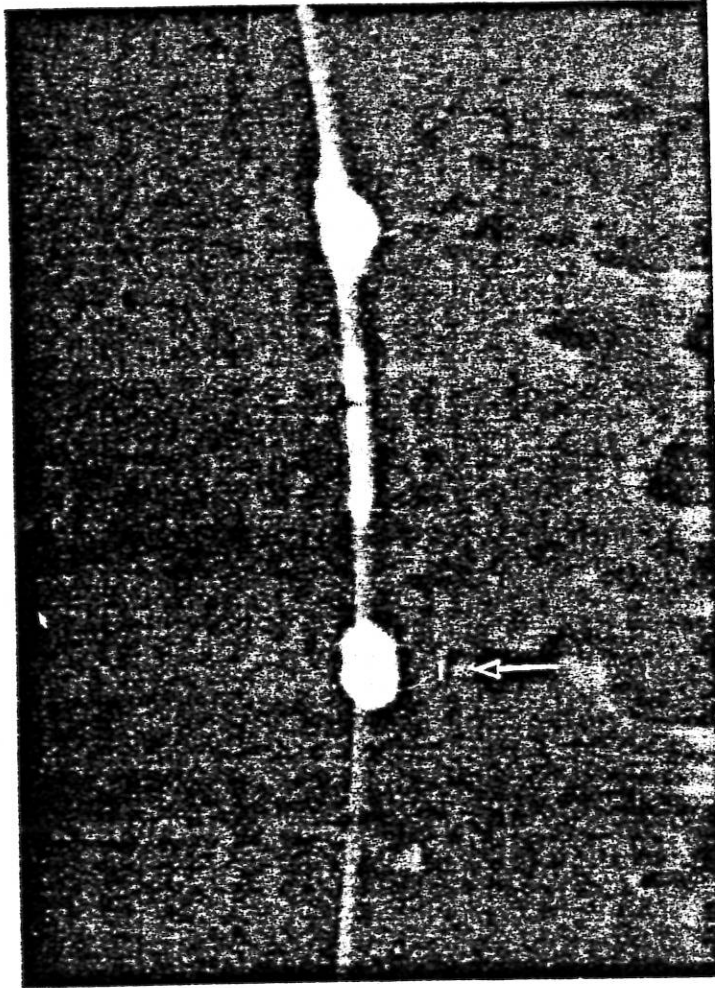


Fig. 1. Part of the $H\alpha$ coronagraphic image obtained at 18:54 UT, 7 July 1975 (Courtesy Meas Solar Observatory, Hawaii). The structure and the slit are indicated with an arrow.

2.1. OBSERVING PROCEDURE

Information on the instrument and the observing techniques is given by Artzner *et al.* (1977) and Bonnet *et al.* (1978).

Using the instrument's own rastering capability, we observed the prominence in eight radial steps of one arc sec, using a $1'' \times 10''$ slit. We then returned to the first position, and repeated the sequence. At each position we made a spectral scan with 256 consecutive grating positions from -1.1 to $+1.0$ Å in $L\alpha$, -2.3 to 2.1 Å in $Ca II$, and -2.8 to 2.6 Å in $Mg II$ lines. The equivalent gate time was 0.52 s for each of the 256 steps and the spectral resolution was 20 mÅ.

2.2. RAW DATA

Hereafter, we refer to the 8 positions as 27, 28, ..., 34, in order of increasing distance from the limb. These numbers are the actual azimuthal values of the position of the secondary mirror in an internal $64'' \times 64''$ raster. The scanning direction was nearly perpendicular to the solar limb. The number of counts per 0.13 s is lower than predicted, based on the size of the slit and the transmission of the instrument. We compared the observed $Ca K$ and H wings with the wings computed from the measured instrumental scattered light at the same distance from the solar limb. The rapid increase of the scattered light in proportion with the aging of the instrument, made the comparison difficult. We concluded that the slit could not be properly opened by a maximum area factor of 2. Most of our results will therefore be given as count numbers but absolute intensities are also computed, roughly.

2.3. THE REDUCTION PROCEDURE

Each detector's dark current (measured every 3 mn) was subtracted from the signal. The scattered light was removed with the following method: profiles obtained at the outermost part of the spatial scan (position 34) were found to result from the instrumental diffusion of disk light; for each line, they were averaged and the resulting profile was subtracted with the appropriate factor, from the other profiles (Lemaire, 1978).

For the $L\alpha$ line, since the position and width of the geocoronal reversal are well known (and are used as a wavelength reference, see Section 3.1.b), we removed the geocoronal feature from the $L\alpha$ line by a parabolic least-square fit.

The profiles were then deconvolved from the spectrometer profile (including grating ghosts) and smoothed with a Fourier technique, following Brault and White (1971).

3. Analysis of Data

Each profile required about 164 s observing time, and the full sequence of observations covering positions 27 to 34 was completed in almost 21 min. We have two sequences, for positions 27, 28, 29, 30 (first sequence, Figure 2), and positions 27, 28,

LINE PROFILE MEASUREMENT ABOARD SATELLITE

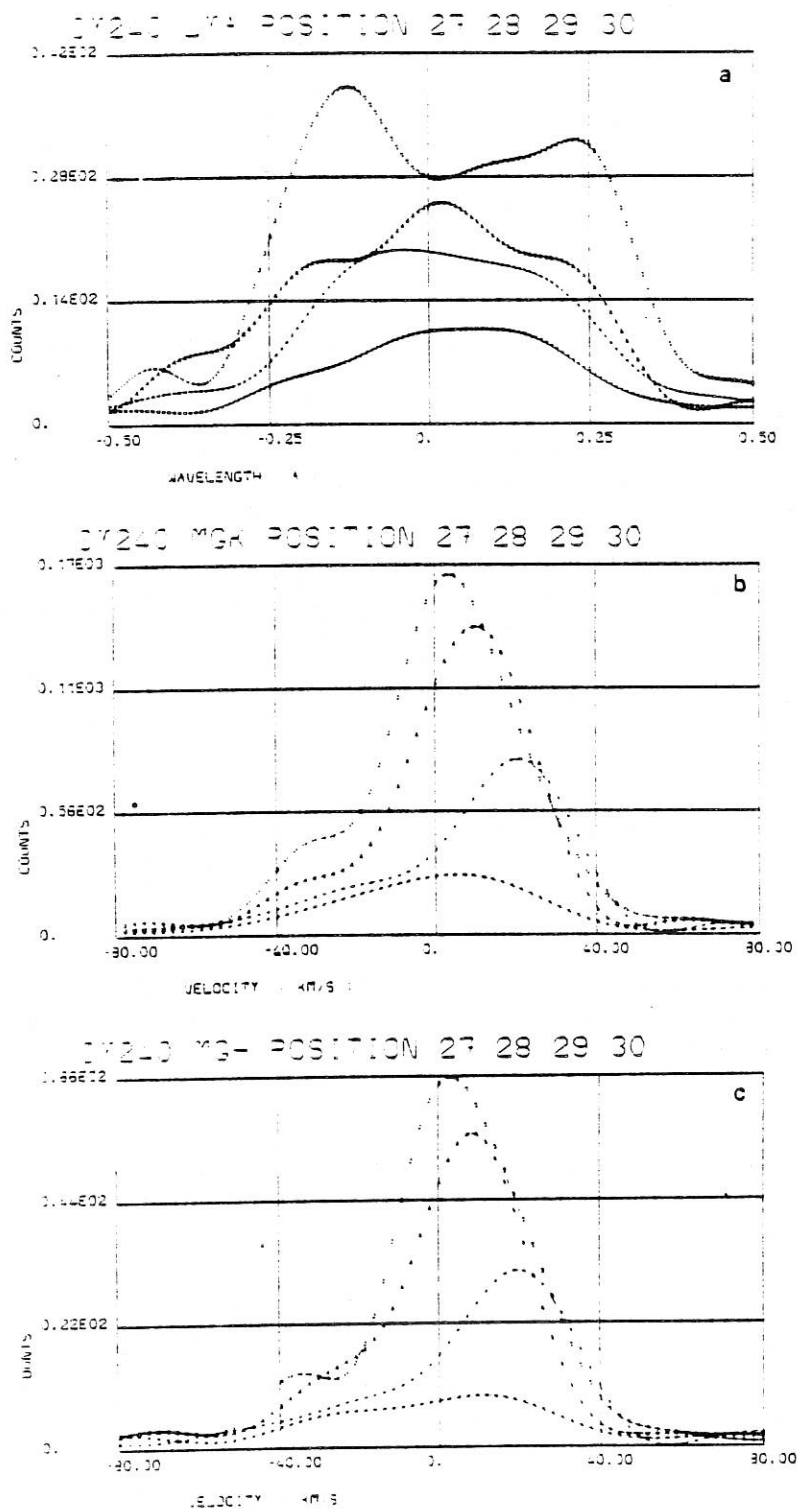


Fig. 2a-c.

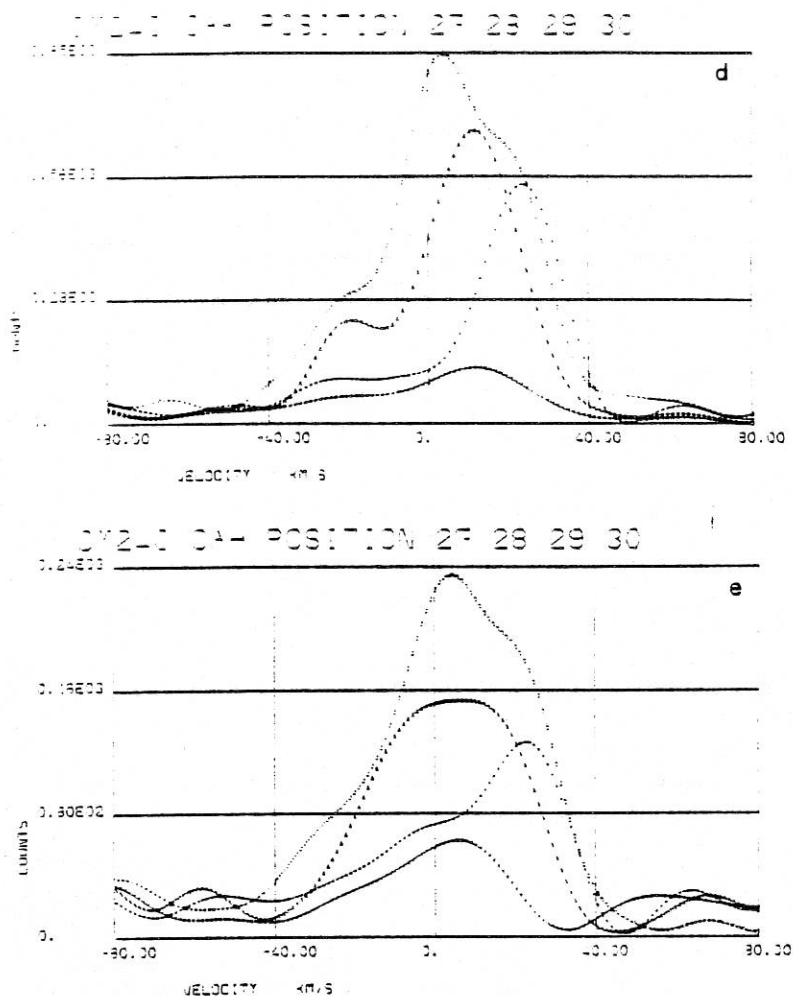


Fig. 2d-e.

Fig. 2a-e. Deconvolved $L\alpha$, k, h, K, H profiles superimposed for positions 27, 28, 29, 30 (first sequence). (Abscissae: velocity (km s^{-1}) except for $L\alpha$ where the distance to the center of the line is in \AA ; ordinates: total number of counts for the counting gate, 0.52 s). (a): $L\alpha$; (b): k; (c): h; (d): K; (e): H. For all lines: \circ (circles) - position 27; Δ (triangles) - position 28; + (plus) - position 29; \times (crosses) - position 30. $L\alpha$ geocoronal reversal has been removed.

29 (second sequence, Figure 3), scanned 21 min later. In Figure 2, we include spectra obtained at position 30 to show that the prominence emission decreases rapidly as we move the slit outwards.

3.1. SPATIAL ANALYSIS

Figures 2 and 3 show the $L\alpha$, h, k, K, and H profiles, superimposed for different consecutive positions. The wavelength scale is in \AA for $L\alpha$, and in velocity units for the other lines. The determination of the 'zero' velocity is discussed at the end of this paragraph and positive velocities correspond to movements detected

LINE PROFILE MEASUREMENT ABOARD SATELLITE

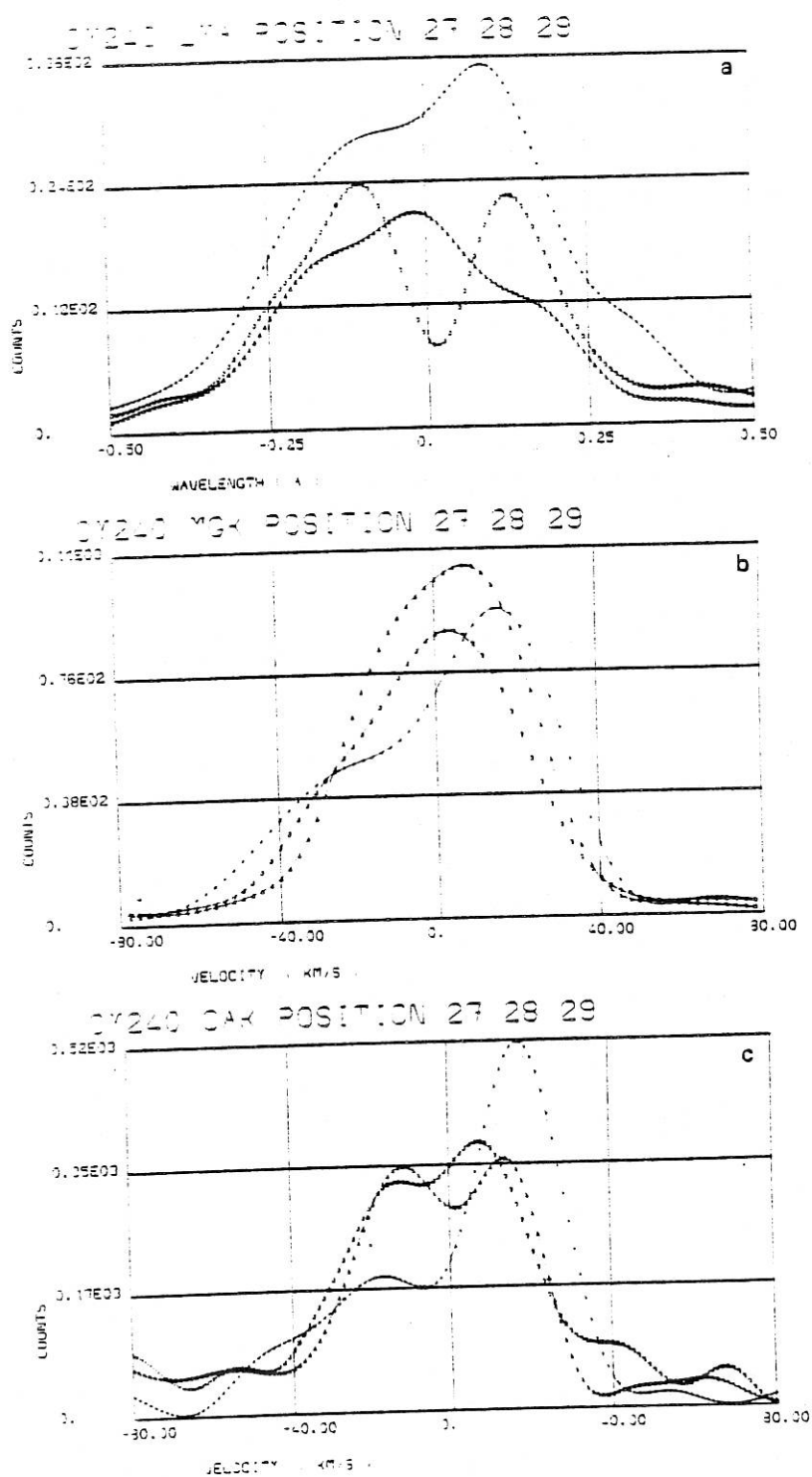


Fig. 3a-c. L α , Mg II k and Ca II K profiles superimposed for positions 27, 28, 29 (second sequence). Same units and symbols as for Figure 2. (a) refers to L α , (b) to k, (c) to K lines.

towards the observer. We concentrate our attention on the cores of the lines, and limit the profiles to $\pm 0.5 \text{ \AA}$ for $L\alpha$ and $\pm 80 \text{ km s}^{-1}$ for the metallic lines.

3.1.a. First Sequence (Figure 2)

$L\alpha$ profile: Figure 2a shows the change from a slightly reversed profile (position 27) to non-reversed profiles with a statistical accuracy of 3%. Full widths at half maximum (FWHM) range from 0.58 to 0.41 \AA (Table Ia).

TABLE Ia

Full widths at half maximum (FWHM) for sequence 1 (units are \AA for $L\alpha$, km s^{-1} for other lines; asterisk (*) refers to profiles where both blue and red components are mixed)

Line	Position			
	27	28	29	30
$L\alpha$	0.58	0.52	0.48	0.41
k (Mg II)	36	36	35	(52)*
h (Mg II)	37	37	37	(65)*
K (Ca II)	38	29	24	(>38)*
H (Ca II)	45	47	(43)*	(>38)*

TABLE Ib

FWHM for sequence 2 (\AA for $L\alpha$; km s^{-1} for other lines)

Line	Position		
	27	28	29
$L\alpha$	0.46	0.45	0.43
k	52	55	50
h	51	51	39
K	—	—	27
H	—	—	(47)*

Mg k profile: In Figure 2b, we recognize two components: the main component has a positive velocity which increases outwards from position 27 to 29.

Mg h profile: Inspection of Figure 2c shows the same behaviour as for Mg k. The positions of the main components given in Table IIa do not differ for Mg k and h by more than 2 km s^{-1} , corresponding to 1 grating step. The FWHM of this component, given in Table Ia, also do not differ by more than 2 km s^{-1} for k and h. The negative (red-shifted) component is centered around -33 km s^{-1} but fades out in the outer parts of the prominence (position 29).

LINE PROFILE MEASUREMENT ABOARD SATELLITE

TABLE IIa

Velocity of the main component for metallic lines as a function of the spatial position (unit: km s^{-1}) for sequence 1

Position Velocity	27	28	29	30
k	4	10.5	21.5	5
h	3	8.5	19.5	8
K	4	11	23.5	11
H	4	6	23	6

TABLE IIb

Velocity of the main component (unit: km s^{-1}) for sequence 2

Position Line	27	28	29
k	3	7.5	15
h	9	7.5	16
K	7.5	14	18
H	3	9	16

Ca II H and K profiles: (Figures 2d, e). They display a complex velocity structure, but contain a main component which shifts increasingly to the blue (positive velocities) as we go from position 27 to 29 and a secondary component centered at about -21.5 km s^{-1} . Despite these similarities, H and K show differences. These differences, already present in the h and k profiles, are more important here and include differences in the ratio of intensities and the widths of the blue and the red components (see discussion in Section 3.1.b).

This is illustrated, for instance, by the broad width at line center of the H profile at position 28, compared to a two-component K profile. This made the determination of the FWHM and the position of the blue component sometimes impossible (Tables Ia and IIa).

3.1.b. Second Sequence

Figures 3a, b, c, show spectra obtained 21 min after the first sequence for $\text{L}\alpha$, Mg k and Ca K. Mg h and Ca H are similar to Mg k and Ca K, respectively. Tables Ib and IIb summarize the blue peak FWHM and positions for all 5 lines.

$\text{L}\alpha$: From Figure 3a, position 27 is the only one which gives a reversal; position 29 is very bright but unreversed.

Mg k (and h): From Figure 3b and Table Ib, the FWHM are constant except for Mg h at position 29 where the FWHM is smaller. The blue component, as measured

in k and h, is consistent for positions 28 and 29 ($+7.5$ and 15.5 km s^{-1}) but not for position 27 (see below).

Ca K (and H): The Ca K line, in Figure 3c, shows an important red component between -12 and -18 km s^{-1} . As a result, the FWHM of the blue component could not be evaluated for positions 27 and 28. The peak position of this last component varies from $+7.5$ to 18 km s^{-1} .

A careful inspection of Tables Ia, b, IIa, b, raises questions concerning the differences between k and h, K and H. As far as velocities are concerned, the sources of error are due to the determination of the 'zero velocity' position, the dispersion and the statistics. In the Mg II and Ca II channels, no reliable photospheric line is present in the spectra and we relied upon spectra performed a few orbits later at Sun center. The precision of this determination is ± 1 step, and it has been shown by Lemaire (1978) that the thermal drift within one orbit is the same for all lines and is less than one grating step.

The dispersion law is very well established and gives a relative position determined better than 0.1 step at small distances from the central position. For most profiles, the statistics are high enough to allow for a ± 0.5 step precision in the computation. This means that the overall precision for the position of the blue component is better than ± 2 grating steps, corresponding to $\pm 4.8 \text{ km s}^{-1}$ for the lines of Mg II, and $\pm 2.4 \text{ km s}^{-1}$ for the lines of Ca II. Our precision is twice as good for the FWHM since in this case no absolute velocities are needed, i.e. $\pm 2 \text{ km s}^{-1}$ for $\text{L}\alpha$, ± 2.4 for Mg II and $\pm 1.2 \text{ km s}^{-1}$ for Ca II. However, due to poor statistics and larger difficulties in correcting for stray light, the Ca II H line shows a somewhat different profile from the Ca II K one.

The discrepancies between the Mg and Ca lines may be explained as due to the presence of numerous emitting structures which vary differently with time and position in the two sets of lines.

Contrary to Landman *et al.* (1977), we did not attempt to split the profiles into two (or more) gaussian functions and evaluate the contribution of each one to the observed intensity. Nevertheless, we can clearly identify two components, an important 'blue' component with velocity varying between 4 to 20 km s^{-1} (sequence 1) and 6 to 16 km s^{-1} (sequence 2) for positions differing only by $2''$ above the limb, and a weaker 'red' component.

3.2. TEMPORAL VARIATIONS

The profiles obtained during the first and second sequence are superimposed in Figures 4a, b, c (position 27), Figures 5a, b, c (28), and Figures 6a, b, c, (29). Most lines show a lower intensity in sequence 2 for positions 27 and 28 and the main component remains at $+4 \text{ km s}^{-1}$ (27) and 8 km s^{-1} (28). At position 28_2 (second sequence) Ca K exhibits a somewhat different behaviour with equally bright blue and red components at velocities of $\pm 14 \text{ km s}^{-1}$. However, at position 29, the $\text{L}\alpha$ and Mg k profiles are notably brighter during the second sequence whereas the Ca II K lines are equally bright. The blue shift is about 4 km s^{-1} smaller during sequence 2.

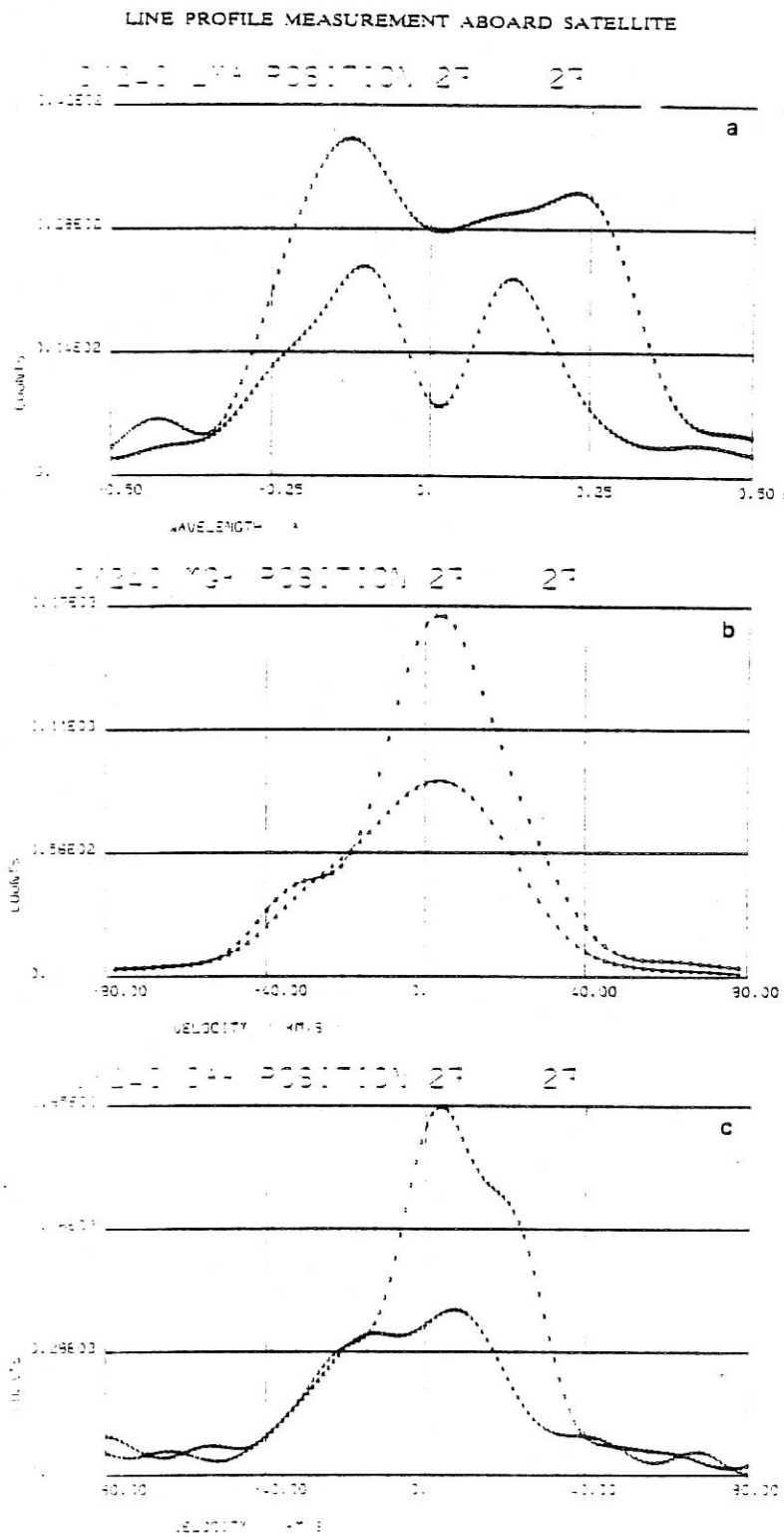
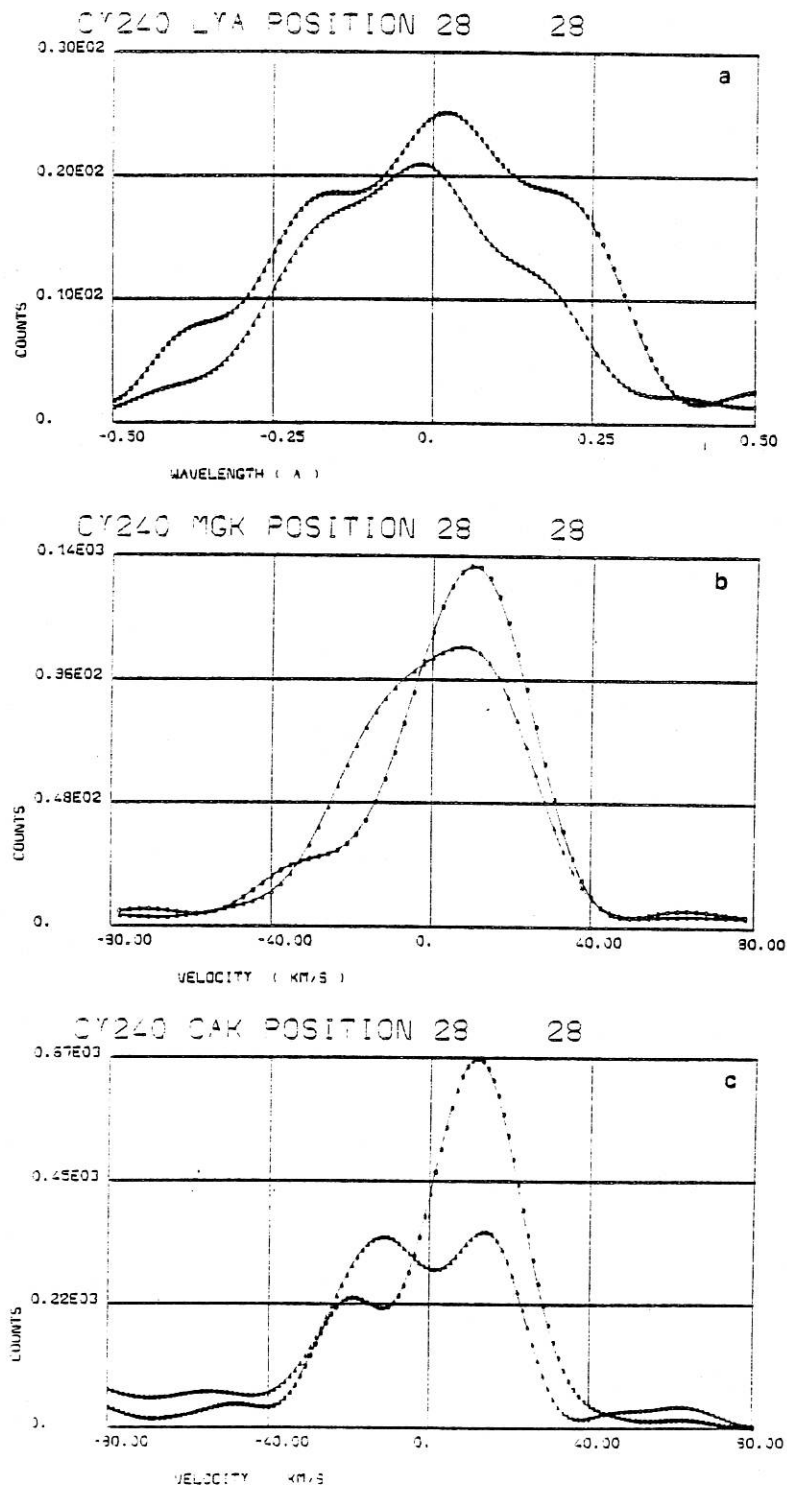
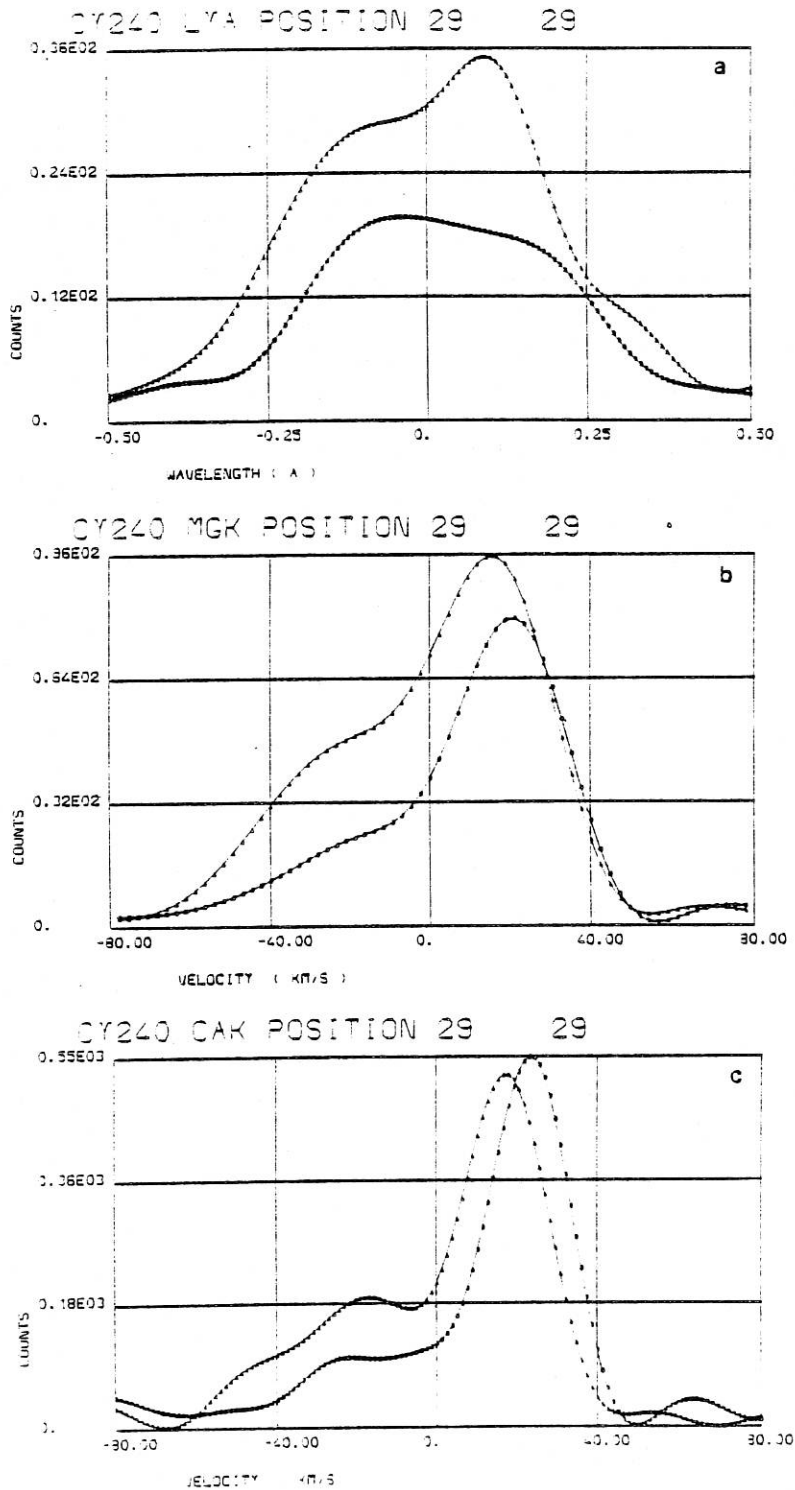


Fig. 4a-c. Superimposed $L\alpha$, Mg k, Ca K profiles for positions 27₁ and 27₂ (first and second sequence). Not different from Mg k and Ca K, h and H lines have been omitted in Figures 4, 5, and 6. (a) refers to $L\alpha$, (b) to k, (c) to K. ○ (circles) - sequence 1; △ (triangles) - sequence 2.

J. C. VIAL ET AL.

Fig. 5a-c. Same as Figure 4 for positions 28₁, 28₂.

LINE PROFILE MEASUREMENT ABOARD SATELLITE

Fig. 6a-c. Same as Figure 4 for positions 29₁, 29₂.

3.3. INTEGRATED INTENSITIES AND POSITIONS IN THE PROMINENCE

We added all the counts within the ranges $(-0.5, +0.5 \text{ \AA})$ for $L\alpha$ and $(-80, +80 \text{ km s}^{-1})$ for all other lines and present in Figure 7 the variation of this total number of counts versus the radial position for sequences 1 and 2. The first sequence shows the edge of the observed structure. The second one indicates that this edge has moved outwards during 21 min in the Mg II and Ca II lines and the relative intensities of the five lines are somewhat different (28 is the peak position for k and H, the lowest for K, and intermediate for h). In particular, the $L\alpha$ line shows a strong enhancement at position 29 where the error bar corresponds to the statistical accuracy. The examination of the Ca II H and K wings showed that no pointing variation between sequence 1 and sequence 2 could account for these differences.

3.4. LINE INTENSITY CORRELATIONS

We now compare integrated intensities as has been done previously for the hydrogen

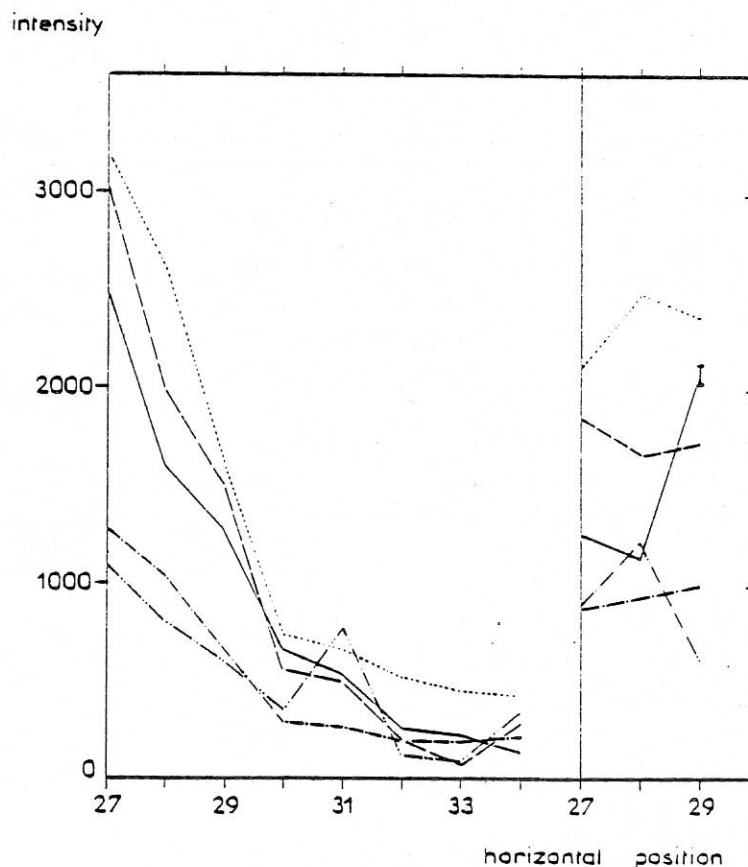


Fig. 7. Integrated intensities (total number of counts within the range $(-0.5, +0.5 \text{ \AA})$ for $L\alpha$ and $(-80, +80) \text{ km s}^{-1}$ for other lines plotted against the horizontal position —: $L\alpha$, -----: Mg k, ---: Ca K, -.-.-.-: Mg h, -.-.-.-: Ca H. Left-hand side refers to sequence 1; right-hand side to sequence 2. The total number of counts should be multiplied by 10 for Ca K and Ca H.

LINE PROFILE MEASUREMENT ABOARD SATELLITE

lines (Stellmacher, 1969) and the Ca^+ and He lines (Illing *et al.*, 1975; Landman and Illing, 1976, 1977; Landman *et al.*, 1978). We compute integrated intensities as the sum of recorded counts, corrected for the different exit slit widths, grating step sizes and instrument sensitivities. We compared profiles obtained on a quiet region a few orbits later with calibrated spectra (Kitt Peak Atlas; White and Suemoto, 1968; Kohl and Parkinson, 1976) to determine the relative sensitivities for k, h, K and H. Transmission ratios are 1.2 ± 0.4 for k/h and 2.0 ± 0.3 for K/H.

Figure 8a shows the results for Ca K and H. A large scatter exists around a least squares linear correlation which we attribute to poorer statistics in the Ca H channel. When respective sensitivities are taken into account, the intensity ratio averaged on position 27, 28, 29 turns to be 1.05 ± 0.3 . This is a particularly low value, as compared to Engvold (1978) and would imply a high saturation of the K line.

The Mg k and h data in Figure 8b contain only a few points which depart from a straight line. These points are for the second sequence of observations and are shown as 27₂, 28₂, 29₂. When statistical accuracy is taken into account (see error bars), they are very close to the line. From the slope of this line, we derive an intensity ratio of 2 ± 0.6 , the value given by the oscillator strengths.

On Figure 8c, which correlates k to $\text{L}\alpha$, one straight line can not fit the observations and we have drawn two possible lines corresponding to low and high intensity regions. This lack of correlation is not surprising since these lines are probably formed at different temperatures. The observed correlation for low k and $\text{L}\alpha$ intensities can be explained if resonance scattering of chromospheric k and $\text{L}\alpha$ lines is the source of emission: intensities are then proportional to line-of-sight populations.

The correlation is better between Ca K and $\text{L}\alpha$ (Figure 8d). The last two correlation plots indicate some Mg^+ k and Ca^+ K saturation when the intensities are large for the second sequence of observations (points 27₂, 28₂, 29₂). The (Mg k, Ca K) correlation (Figure 8e) indicates that these points lie on a straight line but with a negative slope (line 2). We wish to stress that all the lines are recorded simultaneously through the same entrance slit. Moreover, we checked carefully that the pointing system worked properly. Thus the negative correlation (Figure 8e) must be solar. Jefferies and Orrall (1958) suggested that H and He lines are formed in different regions. Is this also true for Ca^+ , Mg^+ , and H? The lack of simple linear correlations among the lines may also be simply the result of the different ways $\text{L}\alpha$, k, h, and K, H lines are formed. $\text{L}\alpha$ is formed by photoionization and subsequent cascade (a radiation effect) and hence is sensitive to the Lyman continuum incident radiation, while the Mg^+ k intensity decreases when Mg^+ is ionized (perhaps a thermal effect).

3.5. ABSOLUTE INTENSITIES

Despite the slit problem mentioned above, we estimated the emergent intensities (Table III) using the *maximum* slit area factor of 2. When we take into account the uncertainty of the positioning of the slit (measured from the scattered light), the

J. C. VIAL ET AL.

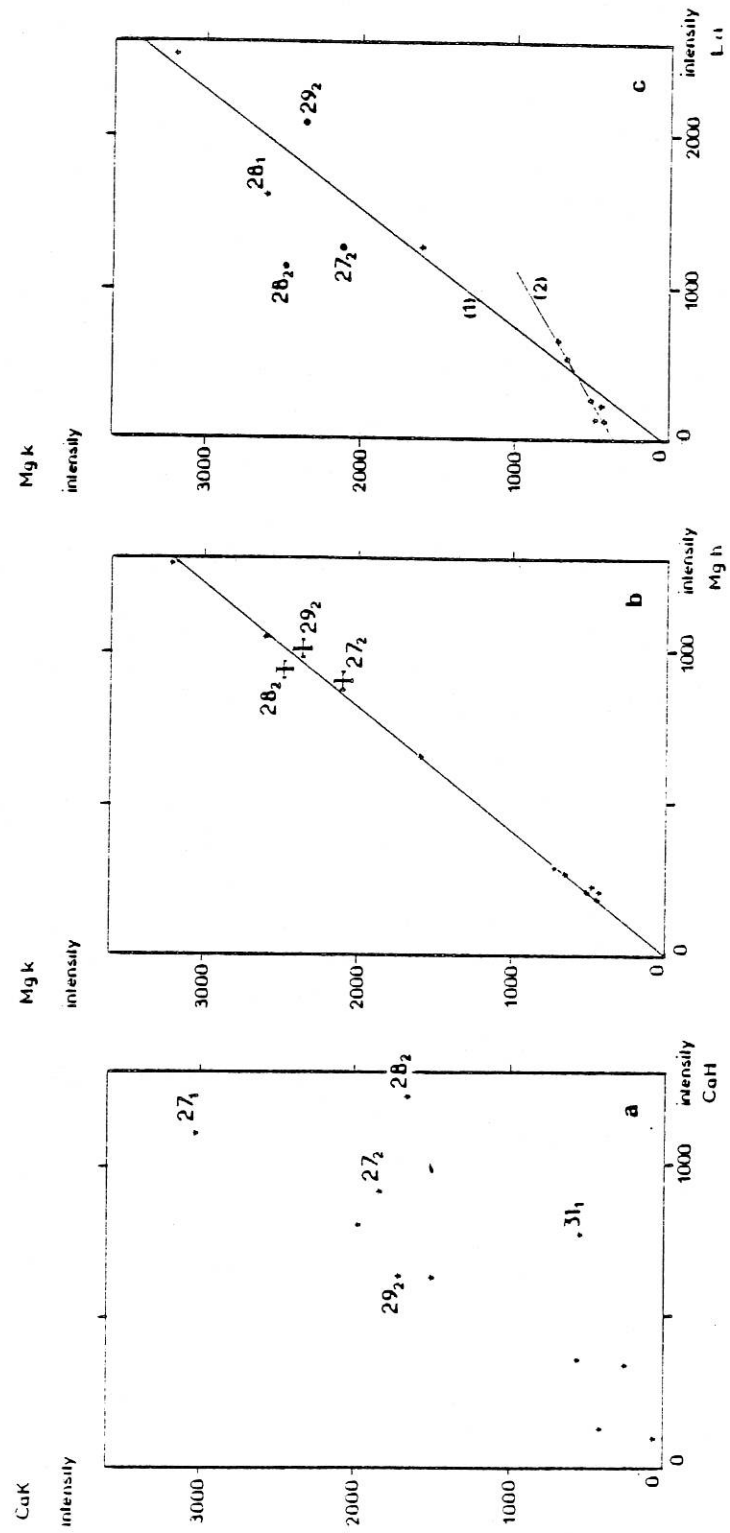


Fig. 8a-c.

LINE PROFILE MEASUREMENT ABOARD SATELLITE

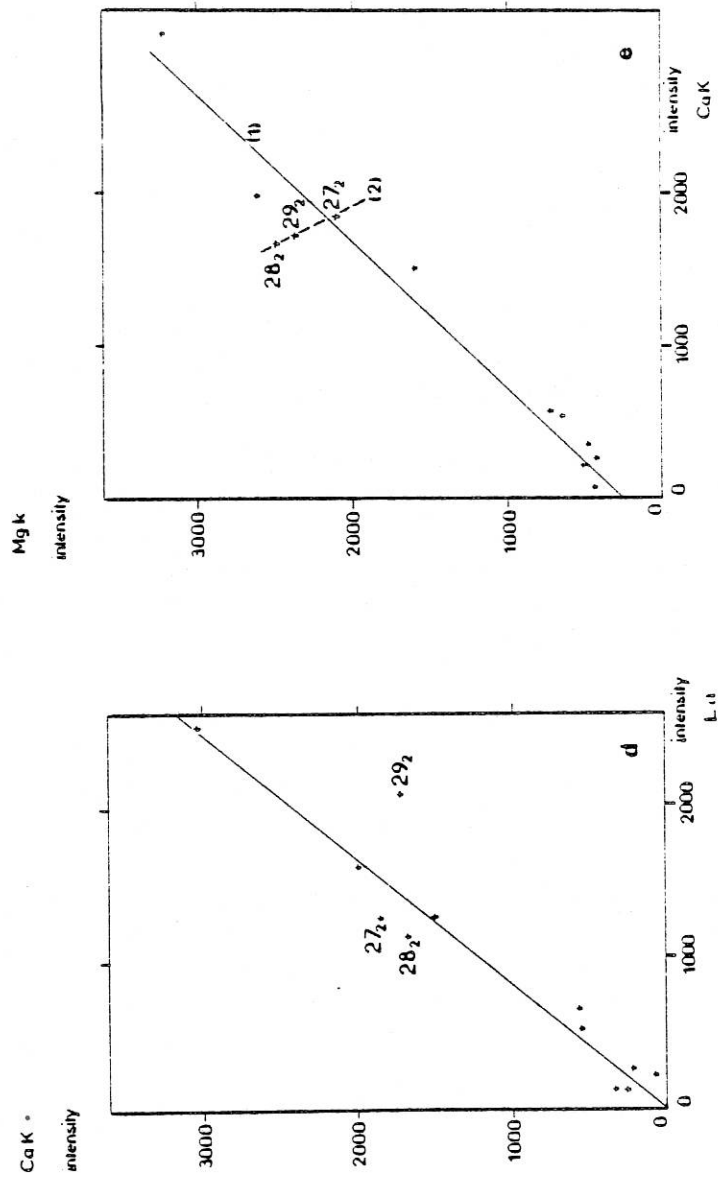


Fig. 8d-e.

Fig. 8a-e. Correlations between integrated intensities of lines. (a): (Ca K, Ca II); (b): (Mg k, Mg h); (c): (Mg k, $L\alpha$); (d) (Ca K, $L\alpha$); (e): (Mg k, Ca K). Ca K, Ca II number of counts should be multiplied by 10.

TABLE III
Line intensities for both sequences of observations (units: $\text{ergs s}^{-1} \text{cm}^{-2} \text{sr}^{-1}$)

Line Position	$\text{L}\alpha_{(10^4)}$	$\text{Mg k}_{(10^4)}$	$\text{Mg h}_{(10^4)}$	$\text{Ca K}_{(10^3)}$	$\text{Ca H}_{(10^3)}$
27 ₁	2.2	3.1	1.6	7.4	5.7
28 ₁	1.4	2.6	1.3	4.9	4.15
29 ₁	1.1	1.6	0.8	3.7	3.25
27 ₂	1.1	2.1	1.1	4.5	4.7
28 ₂	1.0	2.4	1.1	4.1	6.4
29 ₂	1.8	2.3	1.2	4.2	3.3

precision of the relative sensitivity determination, and the precision of the absolute intensities (see Lemaire, 1978), we estimate the following accuracies in the absolute intensity measurements: $-56, +6\%$ for K, $-55, +5\%$ for H, $-74, +16\%$ for h and k, $-85, +35\%$ for $\text{L}\alpha$.

Ca II H and K intensities exceed the values of Landman and Illing (1977), but are consistent with the measurements reported by Heasley *et al.* (1977), Engvold and Livingston (1971) and Engvold (1978) on quiescent prominences.

Mg II intensities show that the brightest point is one half as intense as k_{10} on the disk ($\frac{1}{3}$ for h_{10}). All values are comparable with those reported by Feldman and Doschek (1977-a) for an active region $12''$ above the limb (1.8 and $1.1 \times 10^4 \text{ ergs cm}^{-2} \text{ s}^{-1} \text{ sr}^{-1}$ for k and h).

$\text{L}\alpha$ is as bright in the prominence at position 27 as on the disk. Vernazza and Reeves (1978) found fainter off-limb active regions, but our values are in the low range of intensities computed by Heasley and Mihalas (1976) for different quiescent prominences models. Their computations (see their Table 2) show that the $\text{H}\alpha$ intensity is not very different from the $\text{L}\alpha$ intensity. $\text{H}\alpha$, then, should be as high as $5 \times 10^{-2} B_0$, and be easily visible on spectroheliograms. It is necessary to point out, however, that active filaments are variable objects with complex structures compared to quiescent prominences. Since our measured $\text{L}\alpha$ intensity is quite uncertain we directly compared our values with measurements performed at Sun center a few orbits before and after. With an accuracy of $(-53, +3\%)$, we find that the ratio of measured $\text{L}\alpha$ intensity in the prominence to the intensity in a quiet region at Sun center ranges from 1.35 to 0.6 (positions 27₁ and 28₂, respectively).

4. Interpretation of the Data

Most of our observed profiles of metallic lines indicate two systematic flows, relatively faint material with a receding velocity of the order of 20 km s^{-1} and bright material with an approaching velocity as high as 20 km s^{-1} . We have established that this line of sight velocity increases outwards. We compare here these features with

other observations on different filaments. On the July 15, $H\alpha$ synoptic chart, the filament is 37° inclined on the Equator. We can first consider the observed line-of-sight velocities as the projections of velocities parallel to the filament (and 1.25 times higher). Smith (1968) noticed an absorption or emission flow along the axis of the filament directed towards a sunspot seen on the disk. In our data the flow appears to come from the spot, which is located behind the limb. Our filament can be compared with the arch filament system described by Bruzek (1967) in that our filament has a mass flow along the filament as high as 20 km s^{-1} and some expansion with a velocity of $\sim 1 \text{ km s}^{-1}$ (as measured, here, by the difference between sequences 1 and 2). Moreover, we noticed an increasing flow towards the edge over a distance scale of only $2''$. This result and the existence of two components (at least) may indicate that within an area of $3'' \times 10''$ we are looking at two shallow arches with flows originating from a common footpoint located at the very limb.

$H\alpha$ observations of an activated filament by Mein (1977) showed an increasing radial velocity towards the edges of the filament with opposite signs on both sides. Velocity loops inclined at small angles on the axis of the filament were suggested by Mein. Such a picture may be valid here, if we consider that, at the limb, we are observing the top of such loops, where velocities are horizontal.

Engvold *et al.* (1978) recently report that one third of quiescent prominences show moving edge features, with average line shifts of $30\text{--}40 \text{ km s}^{-1}$ and dimensions perpendicular to the edge, of $1\text{--}2 \text{ arc sec}$; their emission line profiles also consist of several components. The authors suggest that these moving edge features are the result of magnetic reconnection between the prominence and the surrounding cavity fields.

None of the above pictures can be ruled out in the case of our observations.

Most of our observed profiles are not reversed. $L\alpha$ is reversed only for position 27, for which the peak separation $\Delta\lambda_p$ is 0.35 \AA and 0.25 \AA for sequences 1 and 2 respectively. If we assume that the source function decreases monotonically along the line of sight from the position where the peaks are formed to the position where the reversed part is formed, we can derive the line center optical depth τ_0 by

$$\tau(\Delta\lambda_p/2) = \tau_0 \exp \left[- \left(\frac{\Delta\lambda_p}{2\Delta\lambda_D} \right)^2 \right] = 1,$$

where we assume a Doppler absorption profile, incoherence within 3 Doppler widths ($\pm 0.18 \text{ \AA}$), and the Barbier-Eddington approximation.

The Doppler width, taken as constant, is computed with the local mean temperature and velocity ($T \sim 10\,000 \text{ K}$, $v \sim 8 \text{ km s}^{-1}$), leading to τ_0 of the order of 10^5 and 10^3 for position 27₁ and 27₂.

In spite of high uncertainties in the determination of lines ratios, K/H and k/h ratios of 1.05 and 2 (respectively) indicate that Ca II lines are saturated while Mg II lines are not. This fact contradicts the higher abundance of Mg , compared to Ca . Previous observations show that K/H ratio may be as low as 1 for bright prominences

(Engvold, 1978) and k/h ratio as high as 1.95, 20" above an active region at the limb (Feldman and Doschek, 1977a). But these observations refer to different structures. We suggest that the temperature in the region of the prominence we observed is low enough (≈ 6000 K) to prevent full Mg ionization and still allows for Ca ionization.

The FWHM for metallic lines, measured on the main blue component, are about 37 km s^{-1} and 50 km s^{-1} for sequences 1 and 2. Neglecting the small thermal contribution, we find turbulent velocities of 22 and 30 km s^{-1} , respectively. These values are compatible with active filament velocities (described by Liszka, 1970), but we cannot separate microturbulence from macroturbulent 'clouds'.

We notice also that the FWHM do not change appreciably with height above the limb. Hirayama (1971) noticed a rise of the kinetic temperature from the central to the outer part of a quiescent prominence (6000 to 12 000 K) and of the turbulent velocity (7.9 to 20 km s^{-1}). Such a result is not found for the main (blue-shifted) component of the active region prominence we observed.

5. Conclusion

With the first simultaneous profiles of H I $\text{L}\alpha$, Mg II k and h , Ca II K and H lines obtained for an active region prominence above the limb, we find the following features:

- (1) A complex velocity structure with an approaching line-of-sight velocity that increases towards the periphery of the prominence and reaches 20 km s^{-1} . This structure is persistent for 21 min despite intensity changes. These changes are not the same for $\text{L}\alpha$ as for other lines, perhaps due to the different mechanisms of line formation.
- (2) The turbulence of the approaching component remains in the range 22 to 30 km s^{-1} for 21 min.
- (3) We do not notice an increase of the excitation at the outer edge of the prominence.
- (4) Our $\text{L}\alpha$, Mg II k and h , Ca II H and K brightnesses are comparable with previously measured or computed ones. While most of our $\text{L}\alpha$ profiles are not reversed and the intensity ratio $k/h=2$, the Ca II lines seem to be saturated ($K/H=1.1$).

Acknowledgements

The authors wish to thank R. M. Bonnet for many helpful comments and criticism, F. O. Orrall for giving the $\text{H}\alpha$ image, J. L. Leroy, M. J. Martres, and A. Mangeney for fruitful discussions, and the anonymous referee who carefully corrected the first version of the manuscript.

The OSO-8 French program has been financed through CNES contract 73/74/75/76/77 CNES 202.

All computations have been performed on CNES computer facilities in Toulouse.

LINE PROFILE MEASUREMENT ABOARD SATELLITE

References

- Artzner, G., Bonnet, R. M., Lemaire, P., Vial, J. C., Jouchoux, A., Leibacher, J., Vidal-Madjar, A., and Vite, M.: 1977, *Space Sci. Instrum.* **3**, 131.
- Bonnet, R. M., Blamont, J. E., and Gildwarg, P.: 1967, *Astrophys. J. Letters* **148**, L115.
- Bonnet, R. M., Lemaire, P., Vial, J. C., Artzner, G., Gouttebroze, P., Jouchoux, A., Leibacher, J., Skumanich, A., and Vidal-Madjar, A.: 1978, *Astrophys. J.* **221**, 1032.
- Brault, J. and White, O. R.: 1971, *Astron. Astrophys.* **13**, 169.
- Bruzek, A.: 1967, *Solar Phys.* **2**, 451.
- Burns, J. E.: 1970, Ph.D. Thesis, University of Hawaii.
- Engvold, O.: 1976, *Solar Phys.* **49**, 283.
- Engvold, O.: 1978, *Solar Phys.* **56**, 87.
- Engvold, O. and Livingston, W.: 1971, *Solar Phys.* **20**, 375.
- Engvold, O., Malville, J. M., and Livingston, W.: 1978, Preprint.
- Feldman, U. and Doschek, G. A.: 1977a, *Astrophys. J. Letters* **212**, L147.
- Feldman, U. and Doschek, G. A.: 1977b, *Astrophys. J. Letters* **216**, L119.
- Feldman, U. and Doschek, G. A.: 1977c, *Astrophys. J.* **212**, 913.
- Fredga, K.: 1969, *Solar Phys.* **9**, 358.
- Gabriel, A. H., Garton, W. R. S., Goldberg, L., Jones, T. J. L., Jordan, C., Morgan, F. J., Nicholls, R. W., Parkinson, W. J., Paxton, H. J. B., Reeves, E. M., Shenton, C. B., Speer, R. J., and Wilson, R.: 1971, *Astrophys. J. Letters* **169**, 595.
- Heasley, J. N. and Mihalas, D.: 1976, *Astrophys. J.* **205**, 273.
- Heasley, J. N. and Milkey, R. W.: 1976, *Astrophys. J.* **210**, 827.
- Heasley, J. N. and Milkey, R. W.: 1978, *Astrophys. J.* **221**, 677.
- Heasley, J. N., Milkey, R. W., and Engvold, O.: 1977, *Solar Phys.* **51**, 315.
- Hirayama, T.: 1964, *Publ. Astron. Soc. Japan* **16**, 104.
- Hirayama, T.: 1971, *Solar Phys.* **17**, 50.
- Illing, R. M. E., Landman, D. A., and Mickey, D. L.: 1975, *Solar Phys.* **45**, 339.
- Ishizawa, T.: 1971, *Publ. Astron. Soc. Japan* **23**, 75.
- Jefferies, J. T. and Orrall, F. Q.: 1958, *Astrophys. J.* **127**, 714.
- Kawaguchi, I.: 1964, *Publ. Astron. Soc. Japan* **16**, 86.
- Kohl, J. L. and Parkinson, W. H.: 1976, *Astrophys. J.* **205**, 599.
- Landman, D. A. and Illing, R. M. E.: 1976, *Astron. Astrophys.* **49**, 277.
- Landman, D. A. and Illing, R. M. E.: 1977, *Astron. Astrophys.* **55**, 103.
- Landman, D. A., Edberg, S. J., and Laney, C. D.: 1977, *Astrophys. J.* **218**, 888.
- Landman, D. A., Illing, R. M. E., and Mongillo, M.: 1978, *Astrophys. J.* **220**, 666.
- Lemaire, P.: 1978, Orbital Technical Handbook, Rapport interne LPSP T60.
- Liszka, L.: 1970, *Solar Phys.* **14**, 354.
- Mein, P.: 1977, *Solar Phys.* **54**, 45.
- Morozhenko, N.: 1974, *Solar Phys.* **35**, 395.
- Mouradian, Z. and Leroy, J. L.: 1977, *Solar Phys.* **51**, 103.
- Noyes, R. W., Dupree, A. K., Huber, M. C. E., Parkinson, W. H., Reeves, E. M., and Withbroe, G. L.: 1972, *Astrophys. J.* **178**, 515.
- Orrall, F. Q. and Schmahl, E. J.: 1976, *Solar Phys.* **50**, 365.
- Orrall, F. Q. and Speer, R. J.: 1974, in R. G. Athay (ed.), 'Chromospheric Fine Structure', *IAU Symp.* **56**, 193.
- Poland, A. I., Skumanich, A., Athay, R. G., and Tandberg-Hanssen, E.: 1971, *Solar Phys.* **18**, 391.
- Schmahl, E. J., Foukal, P. V., Huber, M. C. E., Noyes, R. W., Reeves, E. M., Timothy, J. G., Vernazza, J. E., and Withbroe, G. L.: 1974, *Solar Phys.* **11**, 42.
- Smith, S. F.: 1968, in K. O. Kiepenheuer (ed.), 'Structure and Development of Solar Active Regions', *IAU Symp.* **35**, 267.
- Stellmacher, G.: 1969, *Astron. Astrophys.* **1**, 62.
- Vernazza, J. E. and Reeves, E. M.: 1978, *Astrophys. J.*, to be published.
- White, O. R. and Suemoto, Z.: 1968, *Solar Phys.* **3**, 523.
- Yakovkin, N. A. and Zeldina, M. Y.: 1968, *Soviet Astron.* **12**, 40.

Article IV

O VI ($\lambda = 1032 \text{ \AA}$) Profiles in and above an active
region prominence, compared to quiet Sun center
and limb profiles

J.C. VIAL, P. LEMAIRE, G. ARTZNER, and P. GOUTTEBROZE

O VI ($\lambda = 1032 \text{ \AA}$) PROFILES IN AND ABOVE AN ACTIVE REGION PROMINENCE, COMPARED TO QUIET SUN CENTER AND LIMB PROFILES

J. C. VIAL, P. LEMAIRE, G. ARTZNER, and P. GOUTTEBROZE

Laboratoire de Physique Stellaire et Planétaire, C.N.R.S., P.O. Box 10, 91370 Verrières le Buisson, France

(Received 3 November, 1979; in revised form 3 April, 1980)

Abstract. O VI ($\lambda = 1032 \text{ \AA}$) profiles have been measured in and above a filament at the limb, previously analyzed in H I, Mg II, Ca II resonance lines (Vial *et al.*, 1979). They are compared to profiles measured at the quiet Sun center and at the quiet Sun limb.

Absolute intensities are found to be about 1.55 times larger than above the quiet limb at the same height (3"); at the top of the prominence (15" above the limb) one finds a maximum blue shift and a minimum line width. The inferred non-thermal velocity (29 km s^{-1}) is about the same as in cooler lines while the approaching line-of-sight velocity (8 km s^{-1}) is lower than in Ca II lines.

The O VI profile recorded 30" above the limb outside the filament is wider (FWHM = 0.33 \AA). It can be interpreted as a coronal emission of O VI ions with a temperature of about 10^6 K , and a non-thermal velocity (NTV) of 49 km s^{-1} . This NTV is twice the NTV of quiet Sun center O VI profiles. Lower NTV require higher temperatures and densities (as suggested by K-coronameter measurements). Computed emission measures for this high temperature regime agree with determinations from disk intensities of EUV lines.

1. Introduction

Profiles of H I ($L\alpha$), Mg II (h and k), Ca II (H and K) lines above an active region filament have been observed at the limb with the LPSP instrument on OSO-8 (Vial *et al.*, 1979, referred hereafter as Paper I). Significant line-of-sight velocities (up to 20 km s^{-1}) and turbulent velocities ranging from 22 to 30 km s^{-1} were found at the prominence top. Intensity ratios for k/h (Mg II) and K/H (Ca II) were found to be 2.0 and 1.1, respectively.

About one and a half hour later, O VI ($\lambda = 1032 \text{ \AA}$) profiles were measured above the same filament. This line is formed at a temperature of about 300 000 K, in the chromosphere-corona and prominence-corona transition regions. The prominence-corona interface has been extensively studied with the help of space-borne experiments (see Schmahl's review, 1978). The analysis of this large amount of data (mainly intensity measurements) led to the picture of a prominence-corona interface which is not very different from the chromosphere-corona region, except that the electron pressure was found to be lower around prominences. Only three sets of line profiles have been discussed up to now. That of Feldman and Doschek (1977) implied a turbulence free region above the disk, corresponding presumably to a quiescent prominence. That of Kjeldseth Moe *et al.* (1979) who studied lines spanning the 10 000–300 000 K region, implied, on the contrary, that the turbulence in prominences increases with temperature from less than 10 km s^{-1} to about 30 km s^{-1} .

That of Mariska *et al.* (1979a) did not contradict the former observations but for temperatures higher than 4×10^4 K, important spatial variations of NTV were found and these authors noticed decreasing NTV with increasing radial height above the limb. Due to the instrumental sensitivity cut-off, no high resolution spectra were obtained before the launch of OSO-8 below 1100 Å. Our O VI profiles reported here, in and above an active region prominence, are the first to be reported in the literature.

The instrumental configuration and observing sequence are given in Section 2. Data processing and calibration are described in Section 3, along with the location of the limb. The observations are presented in Section 4: The structure of the limb, and the characteristics of the O VI profiles above the prominence are analyzed in Section 4.1; O VI profiles above the quiet Sun limb are given in Section 4.2 for comparison. In Section 5, the discussion deals with the profiles at the top of the prominence and about 15" above the prominence: temperature, non-thermal velocities, and emission measures are computed. The results are summarized in Section 6.

2. Instrumental Configuration and Observing Sequence

The LPSP instrument package on board OSO-8 is a multichannel high resolution spectrometer coupled with a 16 cm aperture Cassegrainian telescope. The 6 channel spectrometer (H I $L\alpha$ and $L\beta$, Mg II h and k, Ca II H and K) scans through the core and wings of the six lines simultaneously with a spectral resolution of 0.02 Å (0.06 Å for $L\beta$ and O VI). An internal raster capability allows one to observe a 64×64 arc sec field with steps of 1 arc sec (Artzner *et al.*, 1977; Bonnet *et al.*, 1978).

The present observations refer to a neutral line filament in the active region McMath No. 13738 (see Paper I) as it crossed over the West limb in July 7, 1975, at 12:00 UT. The morphology of the observed region is given in Figure 1, which is a composite of a Ca K₃ Meudon spectroheliogram taken at 07:49 UT and a H α coronagraphic image from the Meas Solar Observatory at 18:54 UT.

The grating of the spectrometer was rotated in order to scan the O VI line at 1032 Å in the $L\beta$ channel, while the far red wings of Mg II h and k, and $L\alpha$ lines were simultaneously recorded. The $1'' \times 10''$ slit was parallel to the limb and was stepped across the prominence radially every arc sec along a 32 arc sec line (Figure 1). At each position, we made a spectral scan of 0.447 Å range around the O VI line with 16 steps separated by 30 mÅ. At the end of the 32" line, the line of sight returned to the first position and the same observing sequence was repeated. Six such spatial scans were made within half an hour.

3. Data Processing, Calibration and Location of the Limb

3.1. DATA PROCESSING

We average the observed profiles over 4 consecutive spatial positions in order to improve the statistics and we obtain 6 temporal sequences of 8 profiles over a $10'' \times 4''$

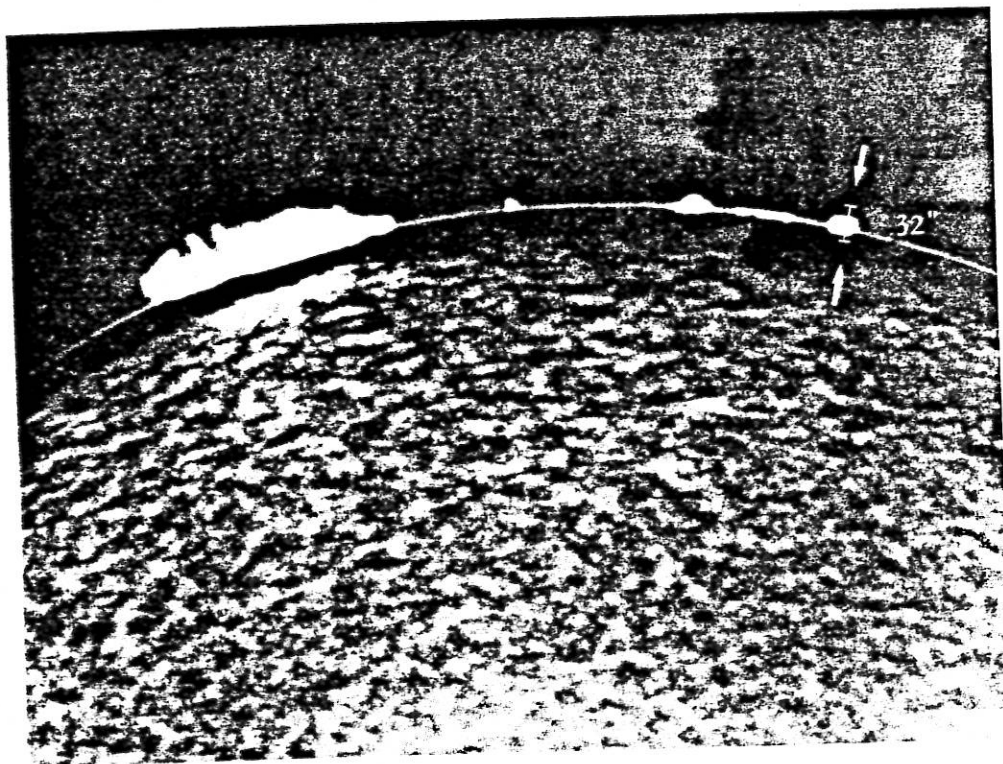
O VI ($\lambda = 1032 \text{ \AA}$) PROFILES IN AND ABOVE AN ACTIVE REGION PROMINENCE

Fig. 1. Superposition of a K_3 Meudon spectroheliogram with an $H\alpha$ coronagraphic picture from Meas Solar Observatory. The distance between the two limbs is not the actual one and was chosen for convenience. The size and location of the radial 32 arc sec long scan are indicated by the segment between the two arrows.

area. Since time variations are not evident during the 32 min of the observations, we also average over the 6 temporal sequences in order to get a mean profile corresponding to each of the 8 spatial positions (see Figure 4).

As the slit is moved outside the limb, the number of counts measured in all channels decreases, until a very low and constant value is reached at the outermost positions (refer Figure 2). We average them and label the resulting profile as '7 + 8'.

This profile recorded at a distance of $15''$ above the prominence has a FWHM of 0.33 \AA which is broader than the disk profile by 150 m\AA which indicates an origin different from the disk scattered light: at a distance of $30''$ off the limb the detected signal contains two contributions: the light scattered by the instrument and the light emitted by the outer layers of the Sun. The measured scattered light is about 20% of quiet Sun center emission (Lemaire, 1978), less than the measured intensity. The corona is known to have an O VI emission extending out to a few arc min above the limb (Reeves and Parkinson, 1970). We therefore conclude that the observed broad profile is probably due to the coronal emission and not to instrumental scattering. In the following, this so-called coronal contribution is not subtracted from the profiles observed at positions 1 to 6. However, the detector's dark current which was

J. C. VIAL ET AL

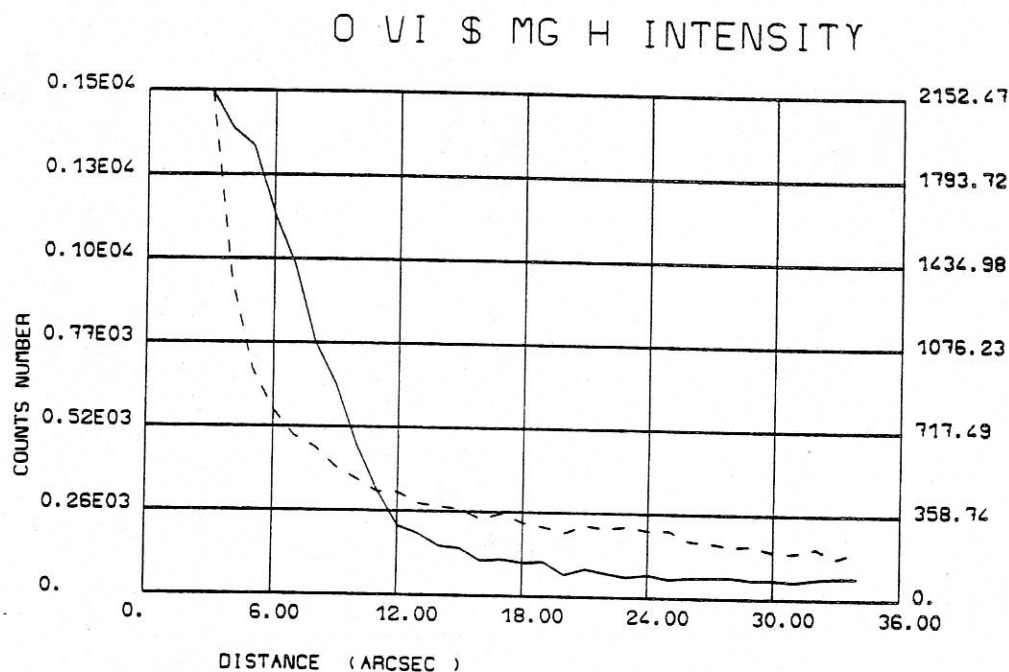


Fig. 2. The variation of integrated intensities of O VI line and Mg II wing with radial position. *Abcissae*: Distance (in arc sec); position 0 is located at the photospheric limb. *Ordinates*: Total number of counts (integrated over the line): In the O VI line (—) and in the Mg II k far wing (---).

measured every 3 min during the orbit is systematically removed from the measured counting rates. Contrary to what was observed in the previous orbit (Paper I), the level of scattered light in the Mg wing was comparable to laboratory measurements, and we concluded that the slit was properly open.

In the $L\beta$ channel, the spectrometer profile is nearly Gaussian (Lemaire, 1978) with a full width at half maximum (FWHM) of 0.064 \AA , and the observed profile widths are corrected for it.

3.2. CALIBRATION

An absolute calibration of the OSO-8 instrument was made during a rocket flight, on February 18, 1976 (Lemaire *et al.*, 1978). The O VI flux at Earth, integrated over the profile measured during this flight is $0.051 \pm 0.015 \text{ erg s}^{-1} \text{ cm}^{-2}$ (Lemaire, 1979). From the resolved O VI solar image obtained on OSO-8 on the same day we derive an integrated intensity of $300 \text{ erg s}^{-1} \text{ cm}^{-2} \text{ sr}^{-1}$ (± 115) at quiet Sun center. This is about the value of $314 \pm 110 \text{ erg s}^{-1} \text{ cm}^{-2} \text{ sr}^{-1}$ given by Vernazza and Reeves (1978) for a quiet Sun (center) average.

The discrepancy between these two results is well within the uncertainties in the absolute calibrations ($\pm 38\%$) and the intrinsic solar variability between 1973 to 1976 (Reeves *et al.*, 1977). In the following, our data are given in the absolute units derived from the LPSP calibration.

O VI ($\lambda = 1032 \text{ \AA}$) PROFILES IN AND ABOVE AN ACTIVE REGION PROMINENCE

In order to convert into absolute units a number of counts measured in the $L\beta$ channel, at a given time, the variation of sensitivity with the time $L\beta$ channel, from the date of the absolute calibration, to the different dates of our observations (above the prominence, at quiet Sun center and at quiet Sun limb) has to be taken into account. To do so, quiet Sun center average profiles were frequently measured in the O VI and $L\beta$ lines; the integrated intensities in these lines were computed as a function of time, and the variation of sensitivity versus time was derived with the assumption that the solar variability over 8 months is well within the uncertainties of the determination.

3.3. LOCATION OF THE LIMB

The accuracy of the OSO-8 S/C pointing system at the limb is $\approx \pm 5$ arc sec. To improve on the determination of the solar limb position, the variation of intensity in the Mg II wing (photospheric radiation) recorded simultaneously to the O VI intensity is used. The variation of intensity along the radial scan was compared to the decrease of scattered light measured in the telescope (Lemaire, 1978). The match between these two sets of data allowed us to locate the spatial scan: we found that the first position of the scan was 3 to 4 arc sec outside the photospheric limb. The accuracy of this determination is ± 1 arc sec. The numbers of counts integrated over the spectral scan for the O VI line and the Mg II wing are plotted on Figure 2 as a function of distance from the photospheric limb. The top of the prominence, as observed in chromospheric lines (Paper I), is located at about $15''$ above the limb (position labelled '27' in Paper I).

4. Data Analysis

4.1. PROMINENCE

4.1.1. Limb Structure

The rapid decrease of the O VI emission (a factor of 6 within $8''$, Figure 2) indicates that we scan through the outer part of the bright O VI limb (Reeves and Parkinson, 1970). This bright ring is located 3 to $4''$ above the photospheric limb, instead of $5''$ for the O V line (Bonnet *et al.*, 1978). In order to compare the scan across the prominence with similar scans across the quiet Sun limb, we convert the count numbers into absolute intensities. The results for the prominence and the quiet solar limb are shown on Figure 3. As a reference, observations from the HCO/Skylab experiment (Mariska and Withbroe, 1975) are also plotted, using the conversion factor give by Reeves *et al.* (1977). The correction for scattered light or underlying continuum was not made because the scan across the quiet Sun limb was performed with a different instrumental configuration (a 1 \AA wide exit slit).

Though no correction was made in Figure 3, we notice, however:

- A rather good agreement between our O VI quiet Sun limb variation and the Skylab data;

J. C. VIAL ET AL

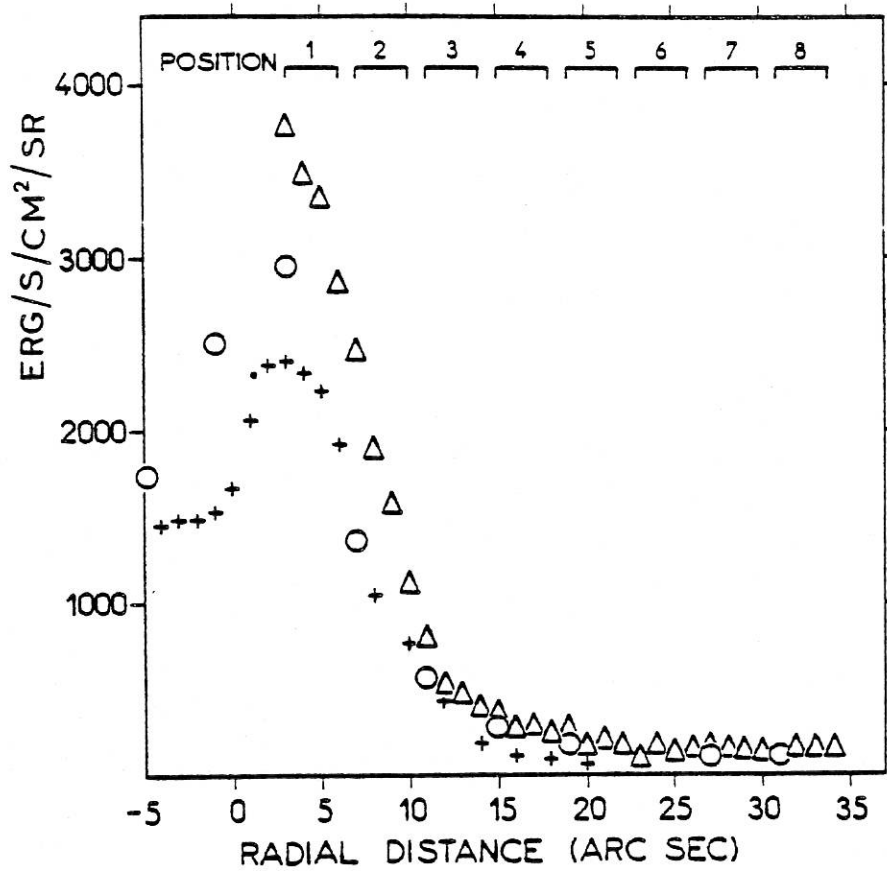


Fig. 3. The variations of O VI (filament and quiet Sun limb) intensities with radial position. OSO-8 data refer to the present observations (Δ) and to quiet Sun limb observations (+). Harvard data refer to the quiet Sun limb (\circ). *Abcissae*: Distance (in arc sec) from the photospheric limb. *Ordinates*: Absolute intensity in $\text{erg s}^{-1} \text{cm}^{-2} \text{sr}^{-1}$. OSO-8 data have been obtained from a rough conversion from counting rates to intensities.

– the difference between the scan across the prominence and the scan across the quiet Sun limb. The ratio of intensities measured at position 1 of the 32 arc sec scan across the prominence and at the corresponding position above the quiet Sun limb, is

$$I(\text{prominence})/I(\text{quiet Sun limb}) \approx 1.55$$

(at this step, no spatial smoothing over $4''$ has yet been done, nor any underlying continuum subtracted from the profiles). This ratio will be computed again with the Gaussian fits to profiles averaged over $4''$ and discussed in Section 5.1.

4.1.2. O VI Profiles

They are shown in Figure 4 for positions 1, 3 and 7+8 together with a reference profile (Figure 4d) obtained the same day above a quiet Sun center area of ($32'' \times 10''$); a Gaussian fit through the profiles obtained by least-mean squares methods is superposed. The Gaussian fit allowed us to remove the underlying

O VI ($\lambda = 1032 \text{ \AA}$) PROFILES IN AND ABOVE AN ACTIVE REGION PROMINENCE

O VI POSITION 1

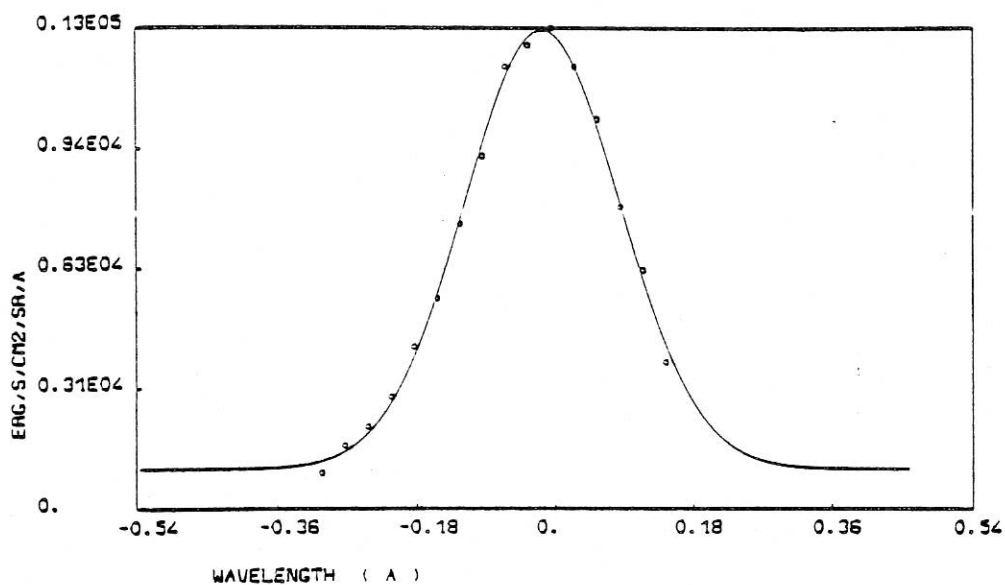


Fig. 4a.

O VI POSITION 3

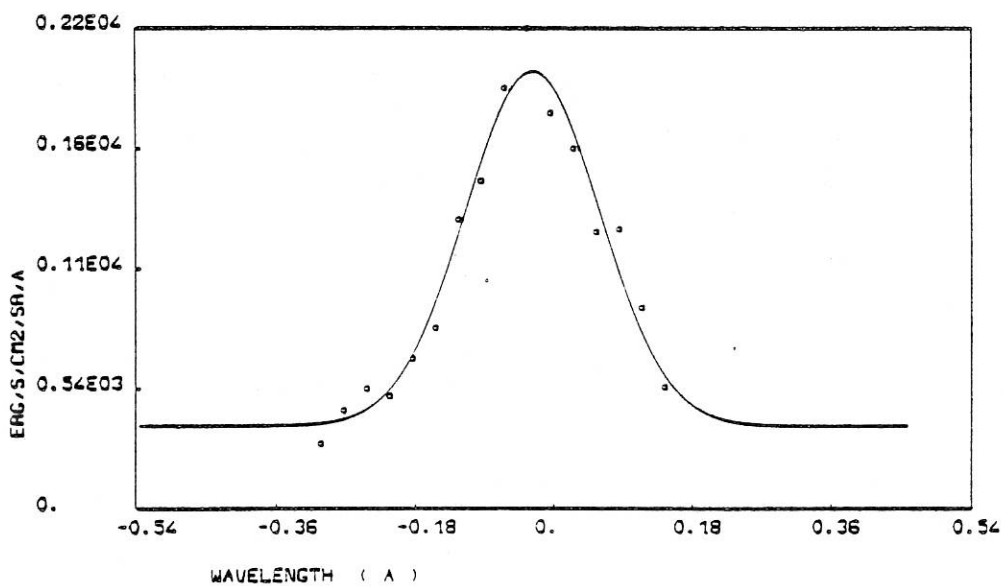


Fig. 4b.

Fig. 4a-d. O VI ($\lambda = 1032 \text{ \AA}$) profiles obtained at positions 1, 3 and (7+8) in and above the filament (Figures 4a to 4c) with a reference profile (Figure 4d) obtained at Sun center. *Ordinates*: Specific intensities in $\text{erg s}^{-1} \text{cm}^{-2} \text{sr}^{-1} \text{\AA}^{-1}$.

J. C. VIAL ET AL

O VI POSITION 7 + 8

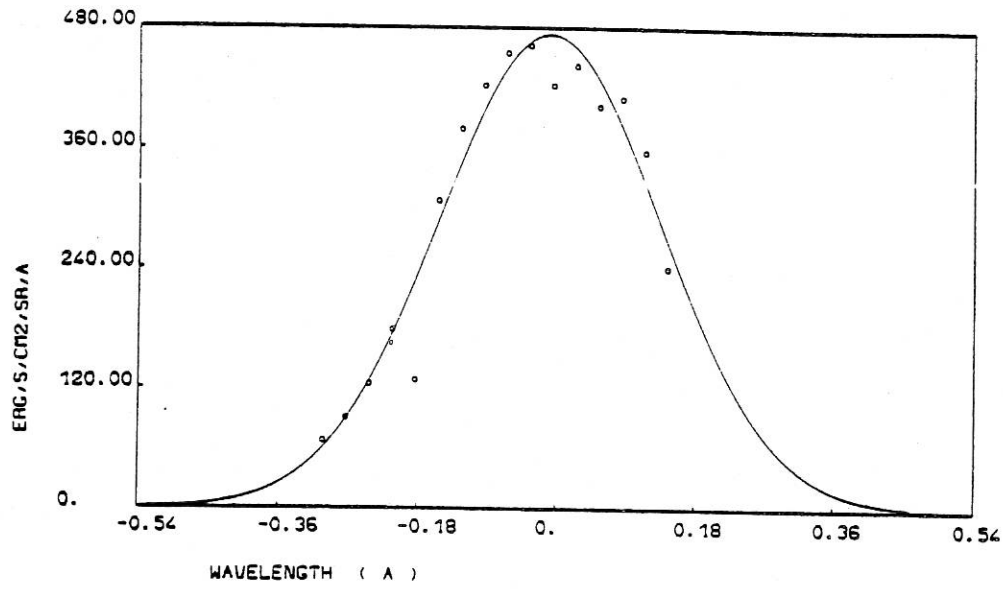


Fig. 4c.

MU=1 O VI

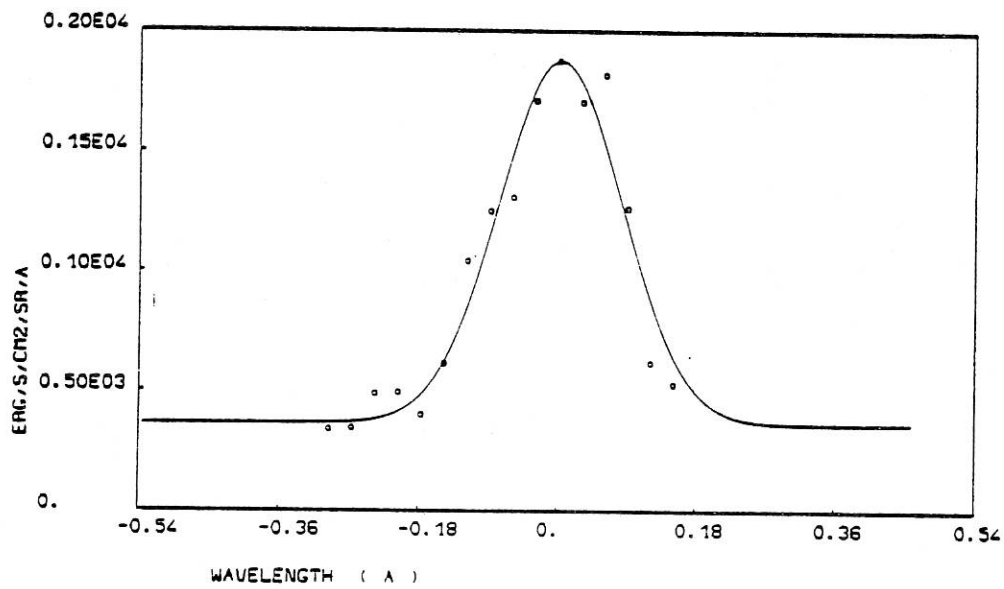


Fig. 4d.

O VI ($\lambda = 1032 \text{ \AA}$) PROFILES IN AND ABOVE AN ACTIVE REGION PROMINENCE

continuum. But, since we had no reliable reference data across the limb, we could not subtract quiet Sun profiles: in this respect, our prominence profiles also contain some chromosphere-corona (and corona) contribution.

(i) *Line shifts.* The central wavelength of the observed O VI line at the quiet Sun center is determined from the Gaussian fit (Figure 4d) and used as a reference. The central position of the O VI line (in km s^{-1}) is given for each location (1 to 7+8) on Figure 5. The blue shift increases with distance away from the limb from 5 to 8 km s^{-1} (position 1 to 3 and 4) and then decreases to about 3 km s^{-1} (position 7+8). Error bars (95% confidence level for the determination of the line position) range from $\pm 0.8 \text{ km s}^{-1}$ (position 1) to $\pm 4 \text{ km s}^{-1}$ (position 7+8). A systematic error in the determination of the position of the reference profile would result in the same shift (about 2 km s^{-1}) for all points of Figure 5.

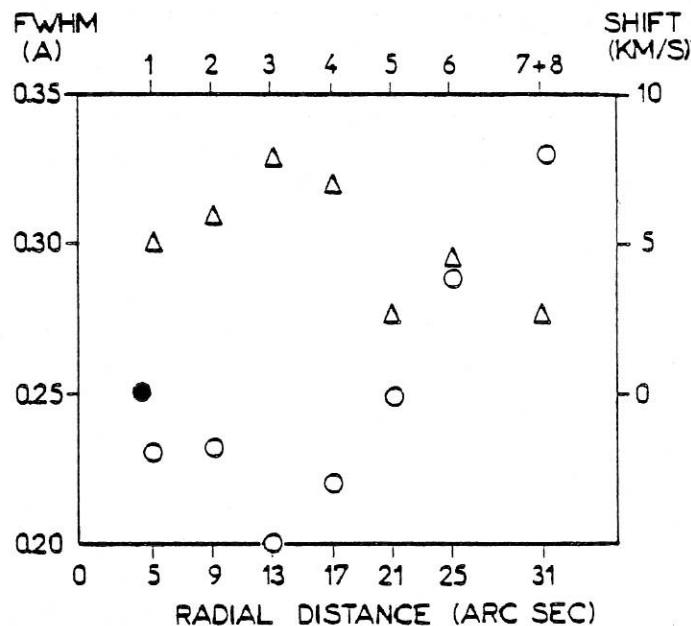


Fig. 5. The variation of the O VI line shift and FWHM (full width at half maximum) with radial distance from the limb. *Abcissae*: Distance (in arc sec) from the photospheric limb. *Ordinates*: Shift (km s^{-1}): Δ and FWHM (\AA): O; FWHM of the quiet Sun limb profile: \bullet .

The observed blue shift (8 km s^{-1}) at position 3 is significantly smaller than the shift measured in cooler metallic lines (Ca II H and K, Mg II h and k) where approaching line-of-sight velocities were found to increase toward the top of the prominence and reached values of $15\text{--}20 \text{ km s}^{-1}$ within $2''$ (Paper I). This fact is discussed in Section 5.2.

(ii) *Full widths at half maximum (FWHM).* The FWHM for positions 1 to (7+8) are also plotted on Figure 5. The error bars (corresponding to a 95% level of

J. C. VIAL ET AL

confidence) range from 0.01 \AA (position 1) to 0.1 \AA (position 7+8). The minimum in the FWHM ($0.20 \pm 0.03 \text{ \AA}$) corresponds to position 3 (and 4), where the maximum blue shift is reached. With a temperature of formation of $3 \times 10^5 \text{ K}$ (Jordan, 1969), the non-thermal velocity (NTV) is 29 km s^{-1} (see Section 5.2). With the same temperature, the NTV increases to 55 km s^{-1} at position 7+8, where the FWHM is equal to $0.33 (\pm 0.1) \text{ \AA}$ (see Section 5.3).

4.2. O VI PROFILES AT THE QUIET SUN LIMB

Typical quiet Sun O VI profiles taken at 4 positions above the limb in May 1976 are used as references in the following discussion. Two consecutive positions are radially separated by 1 arc sec; the slit size corresponds to $1'' \times 40''$. The profile shown in Figure 6 corresponds to position 1 of the $32''$ scan (3 or 4" above the photospheric limb). The characteristics of these profiles are discussed, below, in connection with the prominence observations.

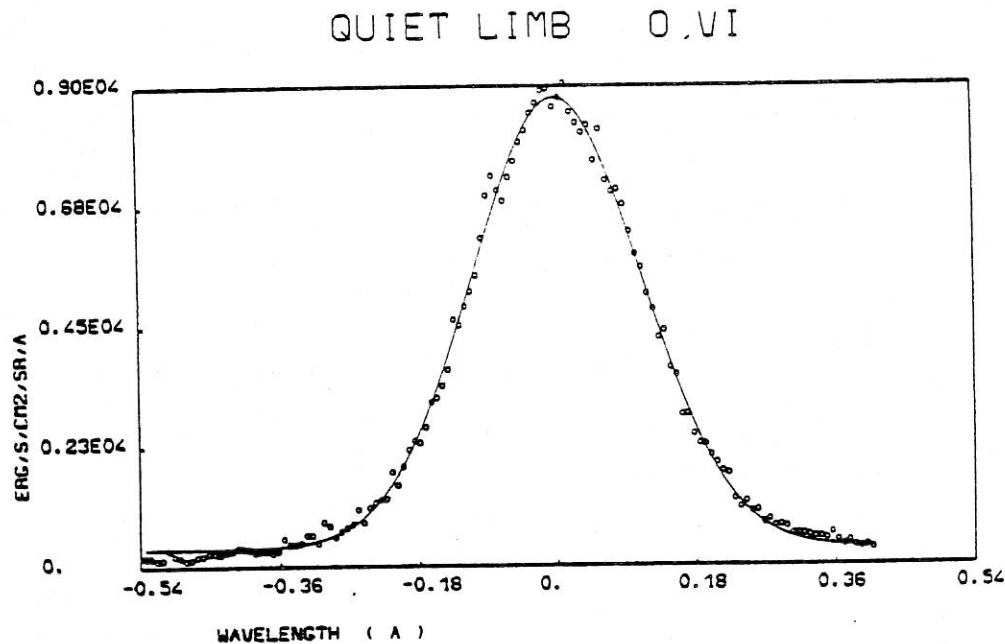


Fig. 6. A typical O VI profile obtained in the quiet Sun O VI brightening at the limb. *Abcissae*: Wavelength (\AA). The center of the quiet Sun center profile has been taken as a reference. *Ordinates*: Specific intensities in $\text{erg s}^{-1} \text{ cm}^{-2} \text{ sr}^{-1} \text{ \AA}^{-1}$.

5. Discussion

5.1. ABSOLUTE INTENSITIES

Absolute integrated intensities are now obtained by integration over the Gaussian representation of the profiles and are compared to quiet Sun center profiles. We obtain:

$$I(\text{quiet Sun limb})/I(\text{quiet Sun center}) = 7.2 \pm 0.7 \quad (1)$$

and

$$I(\text{prominence position 1})/I(\text{quiet Sun center}) = 9.7 \pm 1. \quad (2)$$

The first ratio is close to the value derived from Mariska and Withbroe (1975) when extrapolating their data to quiet Sun center.

From these two ratios, we derive

$$(\text{prominence position 1})/I(\text{quiet Sun limb}) = 1.35 \pm 0.15. \quad (3)$$

The ratio computed, before any spatial smoothing, at $3''$ above the limb is 1.55 (4), the same as the one computed from the raw data (Section 4.1.1). We notice that the intensity variation with radial distance is not very different from what is observed at the quiet Sun limb (Figure 3) and that the peak of emission is located about 3 arc sec above the photospheric limb for both the O VI filament and the quiet limb.

These results are in accord with the picture of a filament made of a cool core surrounded by an optically thin, hot sheath, not very different from the transition region chromosphere-corona (see Schmahl's review, 1978): Because of a complex geometry we do not observe 2 interface regions as Orrall and Schmahl (1976) did above quiescent prominences (observed perpendicularly) and our ratio (4) is consequently lower than 2.

More information can be obtained from the more detailed study of profiles below.

5.2. SHIFTS AND WIDTHS AT THE TOP OF THE FILAMENT

From the set of OSO-8/LPSP data so far analyzed, our O VI observations above the quiet Sun limb (Figure 6) do not demonstrate any evidence for line shifts, contrary to what is observed by Shine *et al.* (1976) for the C IV (1584 \AA) line. We conclude that the maximum blue shift observed at position 3 (Figure 5) is specific to the filament under study. This effect may be explained in different ways as Shine *et al.* suggest.

Thus, one may have either:

- Downward velocities projected on the line-of-sight;
- horizontal isotropic flows, of which approaching ones dominate because of the optical opacity;
- scattering of photons emitted by falling elements.

The filament is not very extended vertically (less than $20''$) and therefore the projection of a radial velocity on the line-of-sight is one order of magnitude lower than the radial velocity: the observed line-of-sight velocity being about 8 km s^{-1} , the downward velocity would have to be 80 km s^{-1} , higher than the sound speed. Very high velocities have been observed already (Brueckner, 1976) but above active or very small regions. Since the region studied is rather far from the plage and the spot is beyond the limb, and our slit angular area is $4'' \times 10''$, we rule out the first interpretation. The radial opacity at the center of the line inferred from absolute intensities (see Section 5.4) is less than 0.1 and the second interpretation no longer applies. Similarly, the third interpretation is discarded because the low radial opacity should allow for the scattering of photons throughout the filament and give the same

J. C. VIAL ET AL

wavelength shifts at positions 1, 2, and 3 (except if a radial velocity gradient exists between 1 and 3).

From observations of metallic lines, line-of-sight velocities increasing from a few km s^{-1} within $2''$ at the upper edge of the filament were found one hour and a half earlier (Paper I). Following Mein (1977), we interpreted them as actual flows along loops inclined to the axis of the filament. The observed O VI velocity (8 km s^{-1}) at $15''$ above the photospheric limb is lower than the Ca II or Mg II velocities. It is probably due to the spatial smoothing by the slit aperture both radial ($4'' \times 10''$) and tangential (along the line-of-sight). Consequently, we interpret the O VI velocity at the top of the filament as an organized flow in loops located above the cool core.

The top of the filament also possesses the smallest FWHM (0.20 \AA) measured in the sequence: if a formation temperature of $3 \times 10^5 \text{ K}$ is assumed for O VI, the corresponding non-thermal velocity (NTV) is 29 km s^{-1} . This is consistent with values measured in cooler lines (22 to 30 km s^{-1} , Paper I) as well as values (extrapolated to $T = 3 \times 10^5 \text{ K}$) given by Kjelseth Moe *et al.* (1979) for quiescent prominences.

This NTV is not very different from the value given by Mariska *et al.* (1979b) of 33 km s^{-1} at $12''$ above the quiet Sun limb. Because of the uncertainty in the FWHM determination (15%), a clear distinction between the top of the filament and a quiet region located at the same height cannot be made. With the adopted temperature ($3 \times 10^5 \text{ K}$), it seems that the top of the filament has the same NTV in cool and hot regions. This is discussed again in Section 5.4.

5.3. CORONAL PROFILE

The profile obtained at position (7 + 8) where we observe a small blue shift (3 km s^{-1}) and a large FWHM (0.33 \AA), is the first one measured of a O VI line at this radial distance ($30''$), reported in the literature. The total intensity is about 0.6 the quiet Sun center intensity, i.e. $180 \text{ erg s}^{-1} \text{ cm}^{-2} \text{ sr}^{-1}$ (± 70). The FWHM (0.33 \AA) is much larger than all other FWHM measured in O VI (1032 \AA) at Sun center or limb (see Table I) and the observed emission is very likely of coronal origin (cf. Section 3.1).

Thermal and non-thermal contributions to the O VI profile at this distance from the limb can be estimated through the relation

$$\text{FWHM} = 2(\log_e 2)^{1/2} \left(\frac{2kT}{m} + \xi^2 \right)^{1/2} \frac{\lambda}{c}, \quad (5)$$

where symbols have their usual meaning, $T = T_e = T_i$ and ξ is the non-thermal velocity (NTV). They can be separated if we take into account the measured absolute intensity. Following Mariska and Withbroe (1978), the emergent intensity I at a distance ρ (in units of the solar radius) from Sun center, is given by

$$I(\rho) = 1.73 \times 10^{-16} A f G(T) \int_{-\infty}^{+\infty} n_e^2 ds, \quad (6)$$

where A is the oxygen abundance relative to H , f the oscillator strength, n_e the

O VI ($\lambda = 1032 \text{ \AA}$) PROFILES IN AND ABOVE AN ACTIVE REGION PROMINENCE

TABLE I
Comparison of FWHM and NTV measured at different solar locations

Position	FWHM (\AA)	NTV (km s^{-1}) (with $T = 3 \times 10^5 \text{ K}$)
Quiet Sun center	0.18	26 (± 7.5)
Quiet Sun limb	0.25	40 (± 1)
Filament position		
1	0.23	36 (± 2)
2	0.23	36 (± 6)
3	0.195	29 (± 6)
4	0.22	33 (± 9)
5	0.25	40 (± 11)
6	0.29	48 (± 16)
7+8	0.33	55 (± 19) (49 km s^{-1} for $T = 10 \times 10^5 \text{ K}$)

electron density at a positions along the line-of-sight, and $G(T)$ is a function that depends on the ionization, the Gaunt factor and the excitation potential of the line. We assume in (6) that the coronal plasma along the line-of-sight is isothermal, a reasonable assumption since position 7+8 corresponds to $\rho = 1.03$. We take $A = 10^{-3.37}$, $f = 0.131$, following Mariska and Withbroe (1978). Mariska and Withbroe (1975) used two calculations for $G(T)$, from Allen and Dupree (1969) (called ADW), and from Jordan (1969). They differ by more than a factor 2 at temperatures around 10^6 K .

In order to determine $G(T)$, we have to evaluate the emission measure (e.m. = $\int n_e^2 ds$). We observe about $15''$ above the filament a region possibly deficient in electrons as coronal cavities are usually above quiescent prominences (Tandberg-Hanssen, 1974). If we adopt a quiet equatorial corona model, a maximum electron density is possibly chosen which leads to the minimum value of $G(T)$, and through (6) to the maximum value for the temperature and hence the minimum NTV (through 5). In fact, we have two temperature solutions for a given G but we reject the small one below $3 \times 10^5 \text{ K}$, as not representative of coronal conditions. The other computed coronal temperature ranges from 10^6 K (Jordan) to $1.7 \times 10^6 \text{ K}$ (ADW). For the given quiet Sun density model (Saito, 1970), we adopt the electronic temperature of about 10^6 K at $\rho = 1.03$. The emission measure (e.m.) is $7.4 \times 10^{27} \text{ cm}^{-3} \text{ cm}^{-2}$. The effects of using ADW values and changing the emission measure will be discussed in Sections 5.4 and 5.5 respectively.

From the analysis of Mg x and O vi data, Mariska and Withbroe (1975) also derived a temperature of 10^6 K inside the cavity above a prominence and Schmahl (1978) obtains also the same temperature (with a 10% admixture of $2 \times 10^6 \text{ K}$). A subsequent analysis by Mariska and Withbroe (1978), suggests a radial temperature gradient from 1.03 to $1.4R_0$, but any positive temperature gradient in our computation would still lower our temperature at $r = 1.03R_0$ and increase the NTV.

J. C. VIAL ET AL.

Adopting the temperature 10^6 K compatible with our density model, we derive a NTV of 49 km s^{-1} . The uncertainty of $\pm 19 \text{ km s}^{-1}$ comes from the estimation in the FWHM. From rocket data, Feldman and Behring (1974) found 30 km s^{-1} in the corona. Tsubaki (1975) observed a non-thermal turbulent motion of 6 to 16 km s^{-1} around a quiescent prominence. The results of Mariska *et al.* (1979b) give a NTV close to 40 km s^{-1} at $20''$ above the quiet Sun limb. We definitely observe here a higher value; this specific problem is discussed in Section 5.4. We also notice that we do not have any systematic west to east flow of the coronal material contrary to what is observed by Tsubaki (1975) in the green line.

3.4. NON-THERMAL VELOCITIES

The importance of the determination of the NTV is emphasized by recent studies connected to coronal heating, especially by acoustic waves. From Si IV profiles obtained with OSO-8, Roussel-Dupré *et al.* (1979) found a small anisotropy in the NTV, possibly in contradiction with the existence of acoustic waves propagating upward. Contrary to Doschek *et al.* (1976), Mariska *et al.* (1978, 1979b) find an increasing radial velocity up to 33 km s^{-1} at $12''$ (for lines spanning the 4×10^4 – 2×10^5 K temperature range).

Our results are summarized in Table I, where we give the FWHM for a quiet Sun center profile, a quiet Sun limb (for 2 positions separated by less than $3''$) and for the 7 positions in and above the observed filament. We also compute the NTV with $T = 3 \times 10^5$ K for all observations and with $T = 10^6$ K for our coronal position '7 + 8':

- At Sun center, the observed NTV (26 km s^{-1}) is about the same as the value observed by Boland *et al.* (1975) on the disk for $T = 10^5$ K;
- at the quiet Sun limb, the FWHM is large (0.25 \AA), but it may be due to an increased opacity of the line as we show now. The line center opacity is given by

$$\tau_0 = \int n_1 \frac{h\nu_0}{4\pi} B_{12} \phi_0 ds, \quad (7)$$

where n_1 is the population of O^{+5} ions, in the ground state, ϕ_0 the absorption profile $[(1/\sqrt{\pi})(\Delta\nu_D)^{-1}]$, and the integration is carried out along the line-of-sight. We write n_1 as

$$\frac{n_1}{n(\text{O}^{+5})} \times \frac{n(\text{O}^{+5})}{n(\text{O})} \times \frac{n(\text{O})}{n(\text{H})} \times \frac{n(\text{H})}{n_e} \times n_e$$

and assume

$$\begin{aligned} \frac{n_1}{n(\text{O}^{+5})} &= 1, & \frac{n(\text{O}^{+5})}{n(\text{O})} &= 0.25 & (\text{see Heroux } et al., 1972), \\ \frac{n(\text{O})}{n(\text{H})} &= 10^{-3.37}, & \frac{n(\text{H})}{n_e} &= 0.8. \end{aligned}$$

For the radial thickness of the emitting layer, Dupree (1972) gives 250 km ; we take

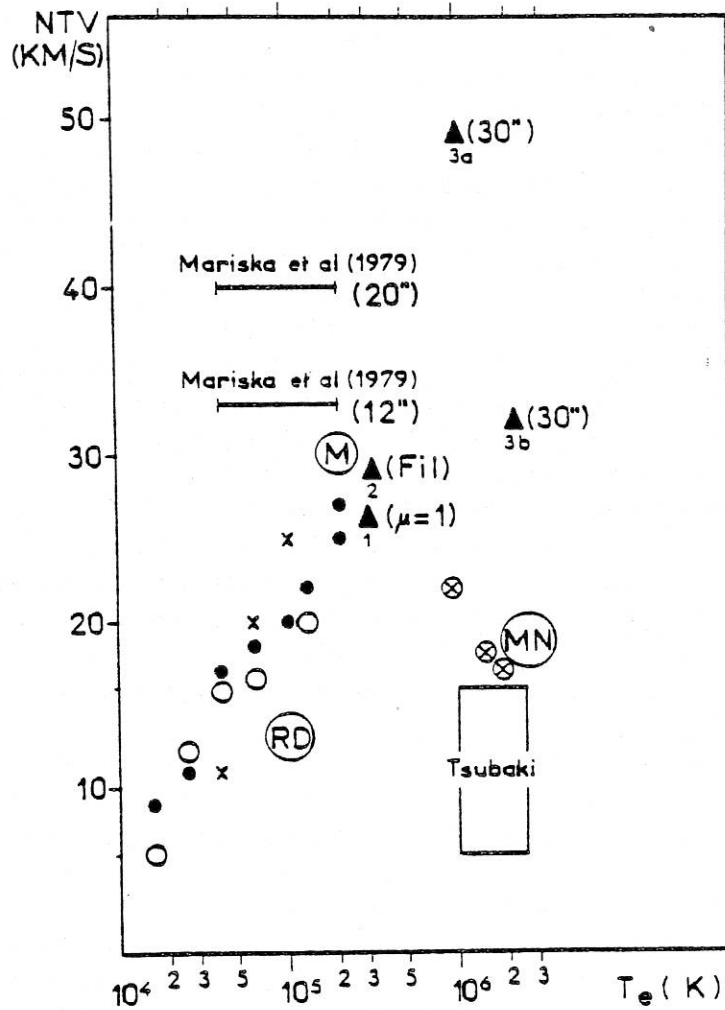
O VI ($\lambda = 1032 \text{ \AA}$) PROFILES IN AND ABOVE AN ACTIVE REGION PROMINENCE

Fig. 7. The variation of NTV (non thermal velocity) in km s^{-1} with the electronic temperature (K). OSO-8 O VI measurements (\blacktriangle) are compared with data from different authors:

- $\blacktriangle 1$. O VI NTV (OSO-8) at Sun center;
- $\blacktriangle 2$. O VI NTV (OSO-8) above the filament;
- $\blacktriangle 3a$ } O VI NTV (OSO-8) 30'' above the limb { low density model }
- $\blacktriangle 3b$ } { high density model } see Section 5.
- x Boland *et al.* (1975).
- Mariska *et al.* (1978).
- Doschek *et al.* (1976).
- RD Roussel-Dupré *et al.* (1979).
- M Kjeildseth Moe *et al.* (1979).
- MN Kjeildseth Moe et Nicolas (1977).
- ⊗ Cheng *et al.* (1979).

as a minimum value, 100 km. With a constant electronic density of 10^9 cm^{-3} and an electronic temperature of $3 \times 10^5 \text{ K}$, the computed line center opacity is close to 1. So, the true NTV is possibly lower than the value given in Table I (40 km s^{-1});

- in the prominence (at position 1), the NTV is also large (36 km s^{-1}) and it may be due to the same opacity effect mentioned for the quiet Sun limb. As compared to the quiet Sun limb, the NTV is slightly smaller however; since the line is about 1.35 times more intense and probably more saturated, it means that the NTV is lower in the filament. This is particularly evident at the top of the filament (position 3) where the NTV is as low as 29 km s^{-1} . Since filaments are supported (and insulated) by a strong magnetic field (as compared to the quiet corona), this result seems to indicate some inverse correlation between the NTV and the magnetic field. This effect may be compared to what is obtained by Cheng *et al.* (1976) above the sunspots although there the magnetic field is much stronger;

- at $30''$ above the photospheric limb (position 7+8) $T = 10^6 \text{ K}$, the computed NTV (49 km s^{-1}) is much higher than any previous determination.

We now plot in Figure 7 NTV measurements versus the electronic temperature (i.e. the temperature of formation of the lines used in the observations). We compare our 3 determinations (at Sun center, at the top of the filament, in the corona, $30''$ above the limb) with other extreme ultra-violet (most from Skylab) and green line measurements.

At Sun center (point 1 in Figure 7), O VI NTV agrees with measurements of Mariska *et al.* (1978) and Doschek *et al.* (1975) made at the limb in lines formed at temperatures of about $2 \times 10^5 \text{ K}$. No agreement is reached with our quiet Sun limb NTV (40 km s^{-1} , if we neglect the opacity effect mentioned earlier) and with measurements from Mariska *et al.* (1979b) at $12''$ and $20''$ above the limb. This is discussed later.

At the top of the filament (point 2 in Figure 7), the NTV agrees with quiescent prominences NTV determined by Kjeldseth Moe *et al.* (1979) and extrapolated to $T = 3 \times 10^5 \text{ K}$. It is in the upper part of the range of values found by Mariska *et al.* (1979a) in a quiescent prominence.

In the corona (point 3a in Figure 7), our O VI NTV lies well above most other values. Lines formed at temperatures higher than 10^6 K exhibit NTV lower than 23 km s^{-1} : Cheng *et al.* (1979) find about 18 km s^{-1} at $T = 1.7 \times 10^6 \text{ K}$; a similar result was obtained by Kjeldseth Moe and Nicolas (1977); Tsubaki's NTV is below 16 km s^{-1} .

We now discuss the large spread of NTV for temperatures higher than 10^5 K , in Figure 7.

As can be seen for lines spanning the 4×10^4 – $2 \times 10^5 \text{ K}$ region, the computed NTV apparently increases with distance from the limb: at Sun center, most authors find about 20 km s^{-1} ; Mariska *et al.* (1979b) find 33 km s^{-1} at $12''$ and 40 km s^{-1} at $20''$. The O VI line shows a similar variation: 29 km s^{-1} at position 3, 49 km s^{-1} at position (7+8). At distances of 20 – $30''$ above the limb, the line-of-sight goes through high temperature regions: residual ions at high temperatures can contribute significantly

O VI ($\lambda = 1032 \text{ \AA}$) PROFILES IN AND ABOVE AN ACTIVE REGION PROMINENCE

to the emission and give a broader profile of emission. We obtained such a result with the O VI line, since we derived a temperature of about 10^6 K and NTV of 49 km s^{-1} .

Is it possible to obtain a higher temperature and a lower NTV?

First, our FWHM uncertainty at position 7+8 is very high ($\pm 0.1 \text{ \AA}$). But the steady FWHM increase from position 3 to position 7+8 is indicative of a systematic effect; moreover, our fit of profiles with Gaussian functions maximizes the background intensity and minimizes the width of the line.

Second, the observed broad profile may result from the addition of two narrow blue and red shifted profiles: they would be emitted by two systems of loops with flows running in opposite directions. We have no way of checking this hypothesis.

Third, ADW's function $G(T)$ allows for a higher temperature ($1.8 \times 10^6 \text{ K}$) and a consequently lower NTV (38 km s^{-1}).

Fourth, the electronic density may be higher in the vicinity of the prominence than above the quiet Sun limb. K -coronameter measurements (HAO) made on the same day in the active region (Hansen, 1979) indicate that one arc minute above the limb, pB (polarization times brightness) is about twice the one measured above the quiet equator. Let us assume that:

- (1) This ratio is the same at $30''$ above the limb;
- (2) the emission is limited to a finite volume where the electronic density is constant; and
- (3) this volume is the same for the quiet and the active corona.

Then the electronic density is twice at our position '7+8' (since pB is proportional to n_e , see Billings (1966)). The emission now becomes $3 \times 10^{28} \text{ cm}^{-3} \text{ cm}^{-2}$, the electronic temperature $2.2 \times 10^6 \text{ K}$ ($2.5 \times 10^6 \text{ K}$ with ADW's function). The NTV is correspondingly lower (32 km s^{-1}). The corresponding point is shown as 3b in Figure 7. If we assume, instead of 3, that the emitting volume is twice in the active region, then the electronic density is the same and the emission measure is $1.5 \times 10^{28} \text{ cm}^{-3} \text{ cm}^{-2}$: the electronic temperature becomes $1.3 \times 10^6 \text{ K}$ (or $2.2 \times 10^6 \text{ K}$ with ADW). In any case, the introduction of K -coronameter measurements leads to a *minimum* temperature of formation of 10^6 K , a *maximum* NTV of 49 km s^{-1} .

In view of the many uncertainties encountered in the observations and the computations, a solution with low NTV and high temperature (and density) should not be discarded. The fact that Cheng *et al.*'s data do not show any variation with radial distance, i.e. no sensitivity to high temperatures, still remains to be explained except if they actually observed isothermal loops extending high in the corona.

5.5. EMISSION MEASURE (e.m.)

At $30''$ above the limb, we have shown that a minimum temperature of 10^6 K imposes a minimum emission measure (e.m.) of $7.4 \times 10^{27} \text{ cm}^{-3} \text{ cm}^{-2}$, compatible with a quiet equator density model. Raising the electronic densities by a factor 2 leads to an e.m. of $5.5 \times 10^{28} \text{ cm}^{-3} \text{ cm}^{-2}$ and a temperature of $2.2 \times 10^6 \text{ K}$. It is interesting to compare this range of values with the e.m. obtained at position 1 in the prominence. Here, for

a temperature of 3×10^5 K, we obtain $8 \times 10^{26} \text{ cm}^{-3} \text{ cm}^{-2}$. The e.m. increase by an order of magnitude (or more) corresponds to a temperature increase from 3×10^5 K to 10^6 K (or more). We notice that U.V. measurements made at Sun center in different lines spanning this temperature range provide with the same behaviour of the radial e.m. (Gabriel, 1976, Figure 1). Our procedure is different in the fact that we use a spatial scan above the limb to investigate different temperature regions and it is possible only because the $G(T)$ function for the O VI line has an extended high temperature tail. Such an agreement with EUV disk measurements adds more confidence in the validity of our procedure.

The determination of the e.m. at position 1 in the prominence ($7.4 \times 10^{27} \text{ cm}^{-3} \text{ cm}^{-2}$) allows us to compute the thickness of the transition region between the prominence and the corona: keeping with the picture of two sheaths along the line-of-sight (Orrall and Schmahl, 1976), adopting $n_e = 10^{10} \text{ cm}^{-3}$, we find a layer 40 km thick, identical to what Schmahl *et al.* (1974) obtained for quiescent prominences.

6. Conclusion

For the first time, O VI (1032 Å) line profiles are observed above a neutral line filament at the limb. The observations add to the observations performed in H I, Mg II, and Ca II resonance lines and reported in Paper I.

Absolute intensities are about 1.55 times larger than above Sun limb. The peak intensity of the O VI bright ring is 10 times greater than the Sun center intensity. The first result is in relative disagreement with the filament model of a cool core surrounded by a hot sheath which is physically similar to the chromosphere-corona interface.

The top of the filament is characterized by a maximum (blue) shift and a minimum width of the O VI line. With a temperature of formation of 3×10^5 K, the inferred NTV (29 km s^{-1}) is about the same as the one observed in cooler lines: its low value can be interpreted as due to the effect of the magnetic field inside the filament. The approaching line-of-sight velocity measured (8 km s^{-1}) in the O VI line is lower than what is found in cooler lines. It is interpreted as a horizontal flow along inclined loops.

A broad O VI profile (FWHM = 0.33 Å) is found at the outermost positions of our scan (30" above the limb), corresponding to coronal emission. From the absolute intensity (about 0.6 the Sun center value) and the measured Doppler width of the line, we separate thermal and non-thermal contributions. Assuming a quiet Sun density model, we obtain $T_e \approx 10^6$ K and NTV $\approx 49 \text{ km s}^{-1}$. The NTV is about twice the velocity measured at Sun center (26 km s^{-1}) and is higher than Skylab determinations. However, K -coronameter measurements indicate that our density model may be too low by a factor of 2: T_e and NTV become 2.2×10^6 K and 32 km s^{-1} respectively. The existence of a high temperature of formation for the O VI line ($T_e > 10^6$ K) imposes a minimum value of the emission measure ($7.4 \times$

O VI ($\lambda = 1032 \text{ \AA}$) PROFILES IN AND ABOVE AN ACTIVE REGION PROMINENCE

$10^{27} \text{ K cm}^{-3} \text{ cm}^{-2}$) in the corona. The computed increase of the emission measure with height (i.e. with temperature) is in agreement with determinations from EUV line intensities at Sun center.

Acknowledgements

The authors thank Drs R. M. Bonnet and A. Skumanich for their critical reading of the manuscript, P. Mein for a helpful discussion and S. Hansen for providing us with her coronal data. The LPSP experiment on board NASA OSO-8 spacecraft was funded by CNES (Centre National d'Etudes Spatiales). We thank LASP and LPSP staff members who were involved in the observing programs at LASP (University of Colorado). Computations have been performed on CNES computer through contracts 77-78 CNES 202.

References

- Allen, J. W. and Dupree, A. K.: 1969, *Astrophys. J.* **155**, 27.
 Artzner, G., Bonnet, R. M., Lemaire, P., Vial, J. C., Jouchoux, A., Leibacher, J., Vidal-Madjar, A., and Vite, M.: 1977, *Space Science Instrumentation* **3**, 131.
 Billings, D. E.: 1966, *A Guide to the Solar Corona*, Academic Press, New York.
 Boland, B. C., Dyer, E. P., Firth, J. G., Gabriel, A. H., Jones, B. B., Jordan, C., MacWhirter, R. W. P., Monk, P., and Turner, R. F.: 1975, *Monthly Notices Roy. Astron. Soc.* **171**, 697.
 Bonnet, R. M., Lemaire, P., Vial, J. C., Artzner, G., Gouttebroze, P., Jouchoux, A., Leibacher, J., Skumanich, A., and Vidal-Madjar, A.: 1978, *Astrophys. J.* **221**, 1032.
 Brueckner, G. E.: 1976, in R. M. Bonnet and P. Delache (eds.), 'The Energy Balance and Hydrodynamics of the Solar Chromosphere and Corona', *IAU Colloq.* **36**, 104.
 Cheng, C.-C., Doschek, G. A., and Feldman, U.: 1976, *Astrophys. J.* **210**, 836.
 Cheng, C.-C., Doschek, G. A., and Feldman, U.: 1979, *Astrophys. J.* **227**, 1037.
 Doschek, G. A., Feldman, U., Van Hoosier, M. E., and Bartoe, J.-D. F.: 1976, *Astrophys. J. Suppl.* **31**, 417.
 Dupree, A. K.: 1972, *Astrophys. J.* **178**, 527.
 Feldman, U. and Behring, W. E.: 1974, *Astrophys. J. Letters* **189**, L45.
 Feldman, U. and Doschek, G. A.: 1977, *Astrophys. J. Letters* **216**, 119.
 Gabriel, A. G.: 1976, in R. M. Bonnet and P. Delache (eds.), 'The Energy Balance and Hydrodynamics of the Solar Chromosphere and Corona', *IAU Colloq.* **36**, 315.
 Hansen, S. F.: 1979, Private Communication.
 Heroux, L., Cohen, M., and Malinovsky, M.: 1972, *Solar Phys.* **23**, 369.
 Jordan, C.: 1968, *Monthly Notices Roy. Astron. Soc.* **142**, 501.
 Lemaire, P.: 1978, *Orbital Technical Handbook*, LPSP Report T 60.
 Lemaire, P.: 1979, private communication.
 Lemaire, P., Charra, J., Jouchoux, A., Vidal-Madjar, A., Artzner, G. E., Vial, J. C., Bonnet, R. M., and Skumanich, A.: 1978, *Astrophys. J. Letters* **223**, L55.
 Mariska, J. T. and Withbroe, G. L.: 1975, *Solar Phys.* **44**, 55.
 Mariska, J. T., Feldman, U., and Doschek, G. A.: 1978, *Astrophys. J.* **226**, 698.
 Mariska, J. T., Doschek, G. A., and Feldman, U.: 1979a, *Astrophys. J.* **232**, 929.
 Mariska, J. T., Feldman, U., and Doschek, G. A.: 1979b, *Astron. Astrophys.* **73**, 361.
 Mariska, J. T. and Withbroe, G. L.: 1978, *Solar Phys.* **60**, 67.
 Mein, P.: 1977, *Solar Phys.* **54**, 45.
 Kjølseth Moe O. K. and Nicolas, K. R.: 1977, *Astrophys. J.* **211**, 579.
 Kjølseth Moe, O. K., Cook, J. W., and Mango, S. A.: 1979, *Solar Phys.* **61**, 319.
 Orrall, F. Q. and Schmahl, E. J.: 1976, *Solar Phys.* **50**, 365.

J. C. VIAL ET AL

- Reeves, E. M. and Parkinson, W. H.: 1970, *Astrophys. J. Suppl. Ser.* **181**, Vol. 21, ('An Atlas of Extreme-Ultraviolet Spectroheliograms from OSO-IV').
- Reeves, E. M., Timothy, J. G., Huber, M. C. E., and Withbroe, G. L.: 1977, *Appl. Opt.* **16**, 849.
- Roussel-Dupré, R., Francis, M. H., and Billings, D. E.: 1979, *Monthly Notices Roy. Astron. Soc.* **187**, 9.
- Saito, K.: 1970, *Ann. Tokyo Astron. Obs., Ser. 2*, **12**, 53.
- Schmahl, E. J.: 1978, in E. Jensen, P. Martby, and F. Q. Orrall (eds.), 'Physics of Solar Prominences', *IAU Colloq.* **44**.
- Schmahl, E. J., Foukal, P. V., Huber, M. C. E., Noyes, R. W., Reeves, E. M., Timothy, J. G., Vernazza, J. E., and Withbroe, G. L.: 1974, *Solar Phys.* **39**, 337.
- Shine, R. A., Roussel-Dupré, D., Bruner, E. C., Jr., Chipman, E. G., Lites, B. W., Rottman, G. J., Athay, R. G., and White, O. R.: 1976, *Astrophys. J. Letters* **210**, 107.
- Tandberg-Hanssen, E.: 1974, *Solar Prominences*, D. Reidel Publ. Co., Dordrecht, Holland.
- Tsubaki, T.: 1975, *Solar Phys.* **43**, 147.
- Vernazza, J. E. and Reeves, E. M.: 1978, *Astrophys. J. Suppl. Ser.* **37**, 485.
- Vial, J. C., Gouttebroze, P., Artzner, G., and Lemaire, P.: 1979, *Solar Phys.* **61**, 39 (Paper I).

ARTICLES V et VI.

"Mais rien ne prouve que la diffusion des vapeurs s'arrête là, et tout nous porte à croire qu'elles s'étendent beaucoup plus loin, mais à un état qui ne leur permet pas de nous envoyer de radiations lumineuses assez considérables pour que nous puissions les observer dans les circonstances ordinaires". (Secchi, Le Soleil, I.405).

Nous avons observé deux protubérances quiescentes dans des conditions très différentes : nous avons pu mettre ainsi en évidence des propriétés communes aux deux objets. Il est toutefois prématuré de les considérer comme typiques d'une protubérance "canonique" qui reste à définir.

Article V.

Le mode d'observation consiste en une série d'images monochromatiques (longueur d'onde variable) à partir desquelles on reconstitue les profils. Le balayage spectral a malheureusement été incomplet, surtout dans la raie $L\alpha$. Nous avons tenté une étude morphologique mais nous avons été gênés par la résolution spectrale modérée (10×5 arcsec) : c'est ainsi que contrairement à Engvold et al. (1978), on n'observe pas de vitesses importantes au bord des structures. Il existe d'ailleurs des raies très larges à fort décalage spectral (cf. Figure 5). Les rapports des raies de Mg II et Ca II sont ici encore "anormaux" ($K/H \sim 1.2$ et $k/h \sim 1.7$). Enfin, le rapport $L\alpha/\text{Ca K}$ varie peu (Figure 7), ce qui indique une faible variation du degré d'ionisation. Il est plus fort au bord des structures (à cause de l'intensité quasi constante de $L\alpha$). Une régression linéaire donne (cf. Figure II.4).

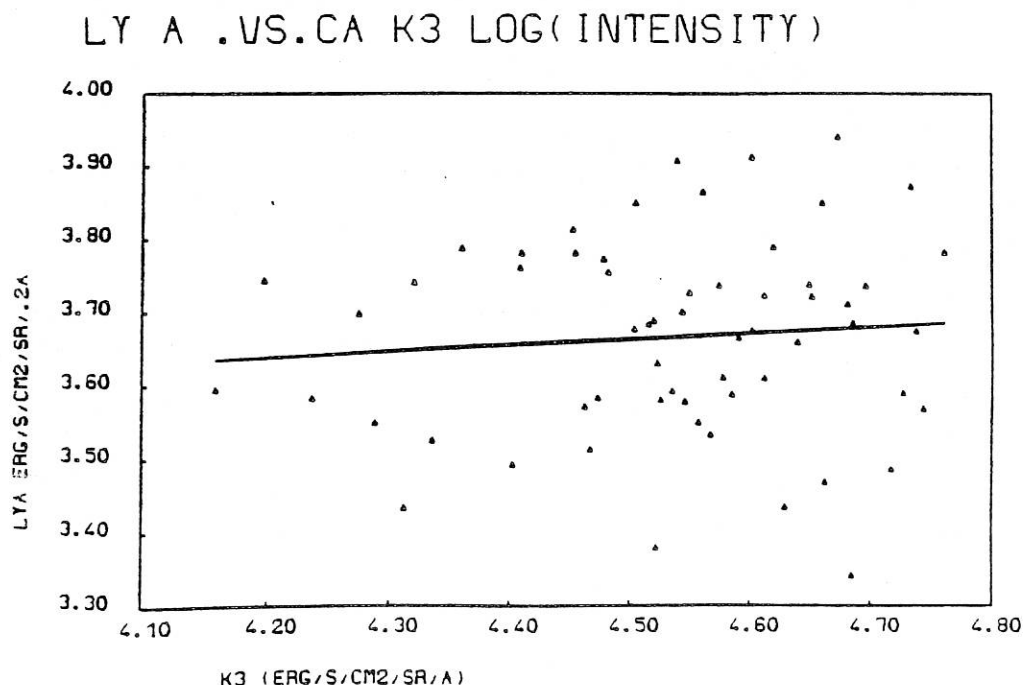


FIG. II.4. : Corrélation entre les intensités $L\alpha$ et Ca II K_3 mesurées sur une protubérance quiescente (article V).

$$I_{L\alpha} = 1937 (I_{K_3})^{0.084}$$

où les intensités sont exprimées en $\text{erg s}^{-1} \text{cm}^{-2} \text{sr}^{-1} (\text{\AA}^{-1})$ pour K_3 , $(0.2 \text{\AA})^{-1}$ pour $L\alpha$. Malgré un balayage spectral insuffisant en $L\alpha$, nous essayons d'évaluer $L\alpha/L\beta$ et trouvons une valeur moitié du rapport chromosphérique. L'objet a subi une disparition brusque quelques jours plus tard.

Article VI.

Nous disposons là d'un jeu d'observations cohérentes, malheureusement situées loin après le lancement du satellite et donc souffrant d'un manque cruel de photons sur les détecteurs, aggravé par le faible éclat de l'objet.

Les différents modes utilisés ont permis :

a) Une étude de la structure de la protubérance (différente en $L\alpha$ et Ca K). Une image obtenue en O VI montre que l'intensité dans la protubérance est bien plus faible que celle de l'"anneau brillant" observé dans la même région.

b) Une mesure des vitesses (le long de la ligne de visée). Nous observons des vitesses de signes opposés de part et d'autre de la boucle supérieure, ce qui implique une structure hélicoïdale.

c) L'observation de profils "typiques" dans les 6 raies, les premiers profils $L\alpha$, Mg II (k et h) obtenus dans des protubérances quiescentes.

Les résultats sont résumés dans la Table I de l'article. Notons que les raies métalliques ne sont pas renversées, des rapports de raies encore "anormaux" ($K/H = 1.45$, $k/h = 1.3$) et une largeur (non thermique) de la raie Mg II double de celle de Ca II. Les raies $L\alpha$ et $L\beta$ sont renversées : la distance des pics de l'ordre de $0.3 - 0.35 \text{\AA}$ implique des opacités de l'ordre de 10^5 . On a $L\alpha/L\beta \sim 60$.

d) La mesure de profils à travers la structure (à l'aide du balayage spatial interne). Nous mettons en évidence des variations de la raie $L\alpha$, probablement dues à des "effets de bord". Le rapport K/H tend vers 1 vers le limbe sans que les intensités K et H croissent (mais il est possible que notre méthode de soustraction de lumière diffusée élimine l'émission dans les ailes). Le rapport $L\alpha/\text{Ca K}$ varie très peu (ce qui montre que le continu de Lyman pénètre partout). A partir de ce rapport, nous calculons schématiquement le degré d'ionisation : nous trouvons :

$$\frac{n_p(\text{proton})}{n_1(\text{neutre})} \sim 2 \text{ à } 3.$$

Les rapports K/H et k/h sont toujours contraires aux rapports d'abondances : nous les interprétons comme résultant du rayonnement chromosphérique incident dont la diffusion domine le transfert pour toutes les raies.

Les profils obtenus en c) et d) sont comparés aux calculs dans l'article VII

Article V

L α , L β (of H I), K and H (of Mg II), K and H (of Ca II)
observations in a quiescent prominence with the OSO-8
LPSP instrument

J.C. VIAL, M.J. MARTRES, and J. SALM-PLATZER

$L\alpha$, $L\beta$ (OF H I), K AND H (OF Mg II), K AND H (OF Ca II) OBSERVATIONS IN A QUIESCENT PROMINENCE WITH THE OSO-8 LPSP INSTRUMENT

J. C. VIAL, M. J. MARTRES,* and J. SALM-PLATZER

Laboratoire de Physique Stellaire et Planétaire, P.O. Box 10, 91370 Verrières-le-Buisson, France

(Received 1 April; in revised form 9 September, 1980)

Abstract. A sequence of images taken at different positions in the resonance lines of Ca II, Mg II, and H I was obtained over a quiescent prominence with the LPSP instrument on OSO-8. Ca II K (and H) profiles are reconstructed at different locations in the prominence with a (10×5) arc sec² resolution. Significant variations of FWHM and line shifts are found: FWHM range from 0.14 Å to 0.5 Å; blue shifts reach about 14 km s⁻¹. The ratio of K to H absolute intensities shows a large spread around the average value of 1.2. The same ratio for the Mg II lines in the whole prominence is higher (1.7), a fact already noticed at the edge of an active prominence (Vial *et al.*, 1979). The ionization degree, as measured by the $L\alpha$ /Ca K ratio, shows noticeable variations within the prominence. The $L\alpha$ intensity is about 0.3 times the intensity measured in the quiet Sun, and the $L\alpha/L\beta$ ratio is less than one half the disk value. These results indicate important variations of the thermal conditions inside the prominence.

1. Introduction

Much attention has been paid, in the past, to the fine structure of quiescent prominences and especially to the physical conditions in the central and outer parts (see Table 3 in Hirayama, 1978). Engvold and Malville (1977), Engvold *et al.* (1978) observed important line-of-sight velocities (up to 80 km s⁻¹) at the edges of quiescent prominences.

After Mein (1977), Vial *et al.* (1979) noticed systematic flows from metallic lines (Mg II, Ca II), at the top of an active region prominence. Hirayama (1971) and Engvold *et al.* (1978) reported an increase of the excitation towards the external regions, while it was not confirmed by observations of Mouradian and Leroy (1977). We took advantage of the fact that the LPSP instrument on OSO-8 observes simultaneously lines of different temperatures and opacities, to perform spatial and spectral scans in a quiescent prominence. If the moderate spatial resolution does not allow to draw a firm conclusion on the physical conditions at the edges, some information can be obtained on opacities, non-thermal velocities and ionization.

2. The Instrument and the Observing Sequence

The LPSP instrument on board NASA Spacecraft OSO-8 is described in Artzner *et al.* (1977) and Bonnet *et al.* (1978). The resonance lines of Ca II, Mg II, H I (and $L\beta$ of H I) are recorded simultaneously with a spectral resolution of 20 mÅ for metallic lines, 0.2 Å and 1 Å for $L\alpha$ and $L\beta$, respectively.

* DASOP, Observatoire de Paris, 92190 Meudon, France.

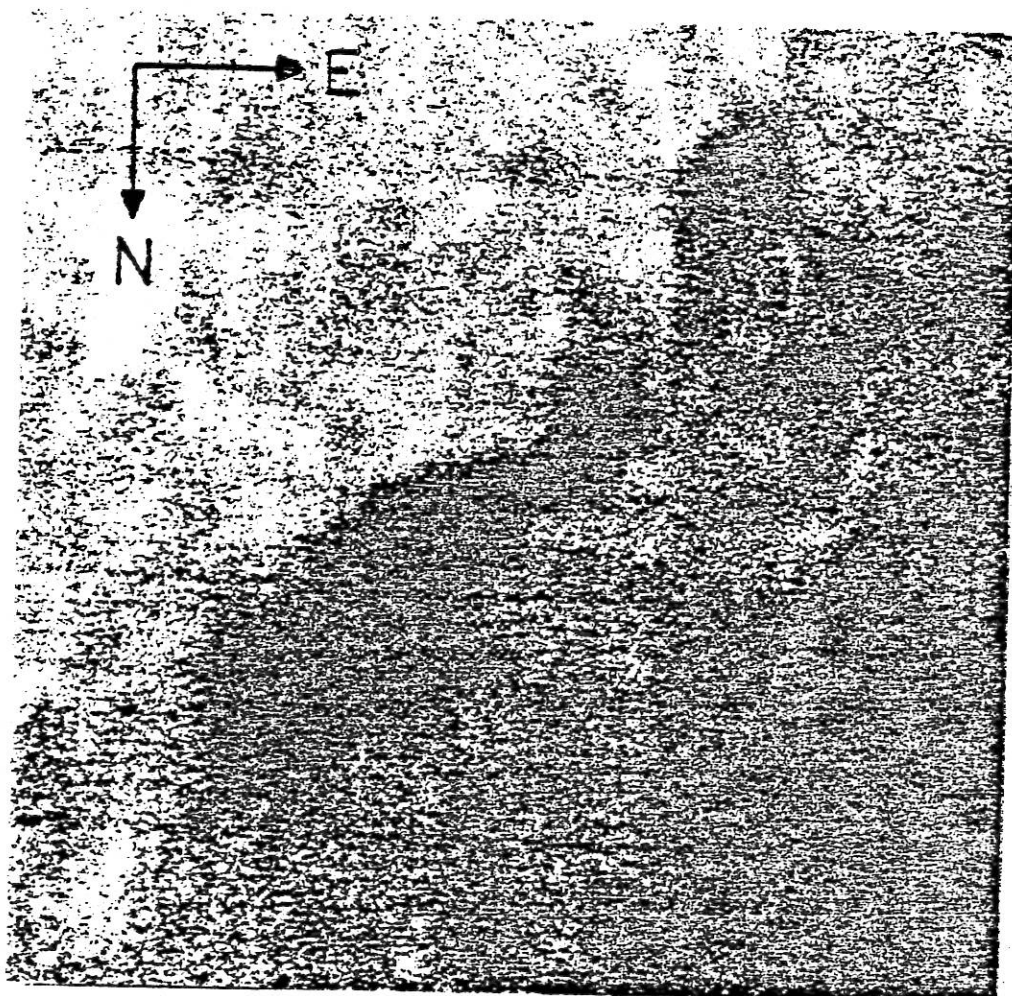


Fig. 1. $H\alpha$ spectroheliogram (about (2.7×2.7) arc min²) obtained at Meudon Observatory on October 23, 1975 at 9 UT. It shows the prominence projected on the disk, about 6 days after the OSO-8 observations.

In the spacecraft 'raster' mode (16 lines, 32 columns), an entire image of (2.7×2.5) arc min² is generated every 82 s. The spatial resolution is (5×10) arc sec². At the end of a raster, the wavelength is automatically changed and the raster repeated. The Ca II, Mg II, and $L\alpha$ lines were analyzed from -0.12 to 0.40 Å, -0.11 to 0.4 Å, and -0.04 to 0.15 Å, respectively. The sequence lasted 24 min.

The observed filament was at the East limb ($PA = 43^\circ$) on the 17th of October 1975 at 23:00 UT. It is shown in $H\alpha$, 5 days later, in Figure 1. It was an elongated structure which underwent at least 3 rotations and a disparition brusque between the 23rd and the 24th of October. It is shown in Figure 2, as seen by the instrument in the Ca II (K_3) and $L\alpha$ lines. At that time, the head of the filament was about 8° behind the plane of sky, which means that we cannot observe structures lower than 10 arc sec.

3. Data Reduction

We paid a special attention to the following parameters:

(1) **Wavelength calibration.** Disk areas located close to the limb in the monochromatic images were used to build reference profiles and derive the dispersion properties of the spectrometer. For the Ca II and Mg II lines, solar rotation was taken into account. For the $L\alpha$ line, the geocoronal absorption feature was used as a wavelength landmark.

(2) **Scattered light.** It was measured in the lower and upper part of the image where no particular out-of-limb emission was found at any wavelength. It was subtracted from the monochromatic prominence intensities in the 6 channels.

Since our spectral scans are incomplete in the blue part of Ca II and Mg II lines, it was found difficult to evaluate how our representation of these profiles as Gaussian functions (see Section 4) is correct. It affects the determination of full widths at half

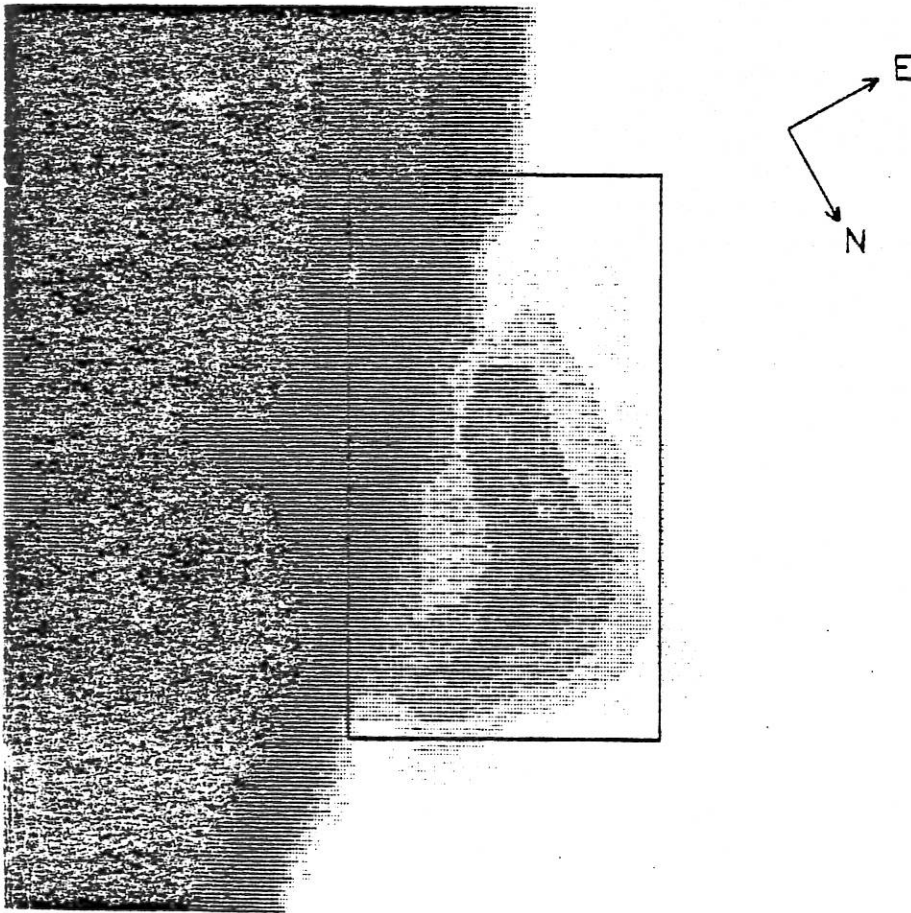


Fig. 2a.

Fig. 2a-b. Spacecraft prominence spectroheliogram in Ca II K_3 (a) and $L\alpha$ (b). Size image is (2.7×2.5) arc min². Dark areas correspond to bright regions.

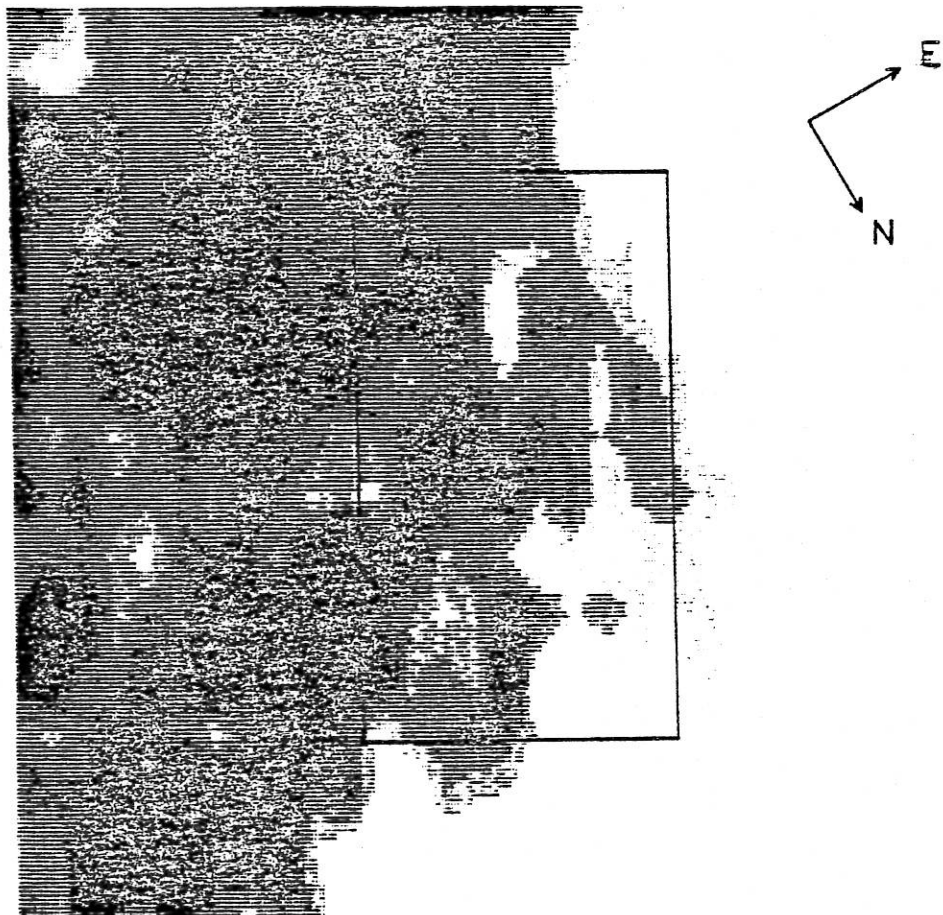


Fig. 2b.

maximum (FWHM) and line shifts (and especially for blue shifts higher than 9 km s^{-1}). This is the reason why no error bar was computed.

4. Data Analysis

We could fit to Gaussian functions the Ca II profiles, computed at each of the 32×16 locations extended over $(5 \times 10) \text{ arc sec}^2$. Wavelength shifts (in km s^{-1}), full widths at half maximum (FWHM, in \AA) computed from the fits to the K profiles, are given as functions of position in Figures 3a and 3b. We have restricted, here and in Figures 3c and 3d, our attention to the smaller area, defined in Figure 2, that fully contains the prominence.

Wavelength shifts are dominantly to the blue in the upper part of the image and reach 14 km s^{-1} in a region of low $L\alpha$ and K_3 intensity. We find some red shifts (up to 7 km s^{-1}) in the lower part, mainly at the edges. The body of the prominence does not show any shift within the accuracy of our measurements (about 2 km s^{-1}). FWHM

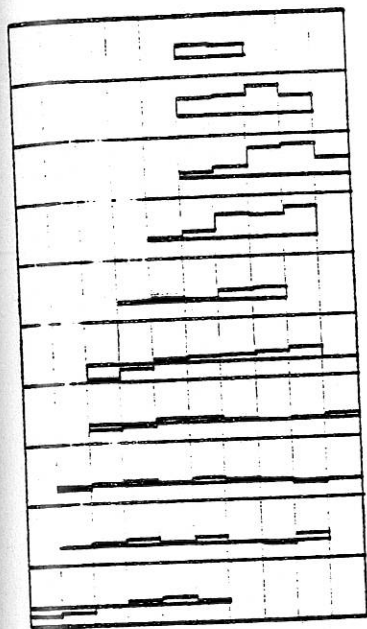
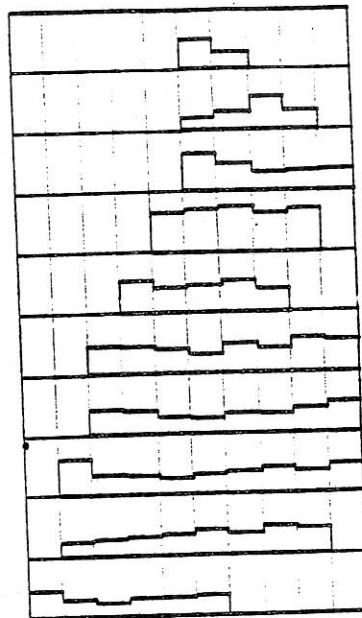
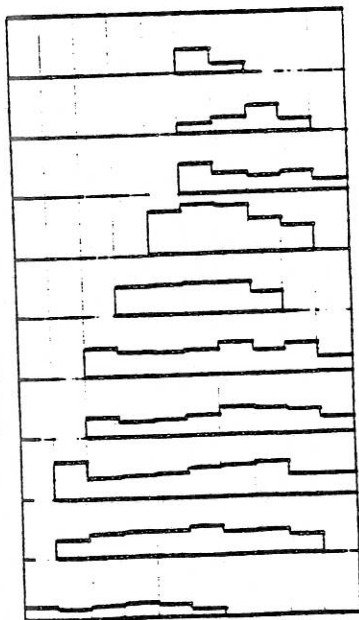
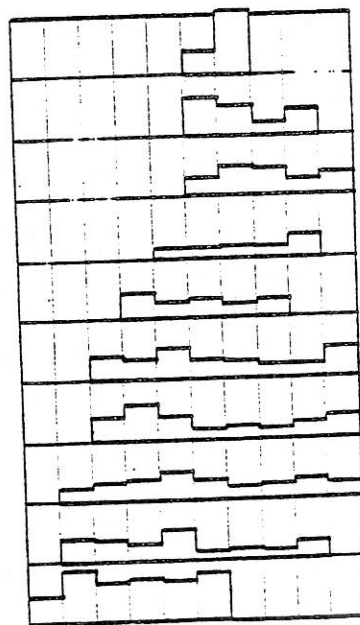
Shift (CaK) ± 10 KM/SFWHM (CaK) $\pm 0.25 \text{ \AA}$ Intensity (CaK) $\pm 10^{-6} \text{ ERG/S/CM}^2/\text{SR}$  $L\alpha / \text{CaK} \pm 1$

Fig. 3a-d. Maps of the variations of profiles parameters across the prominence. The area being studied (see Figure 2) is divided into 10×10 regions. For each region, the height of the plotted line measures the importance of the parameter. Plotted parameters are: (a) Ca II K shift (km s^{-1}); (b) Ca II K FWHM (\AA); (c) Ca II K integrated intensity ($\text{erg s}^{-1} \text{ cm}^{-2} \text{ sr}^{-1}$); and (d) $L\alpha$ (over 0.2 \AA)/Ca K intensity ratio.

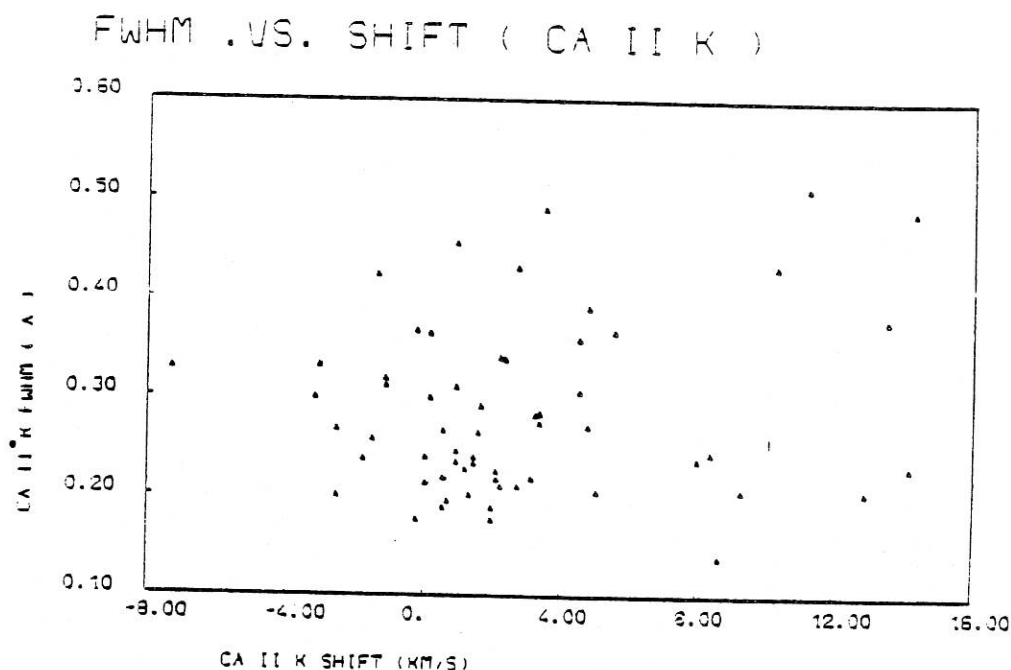


Fig. 4. Correlation between FWHM (\AA) and shift (km s^{-1}) for the Ca II K line.

ranges between 0.14 and 0.50 \AA . The higher values are obtained in the upper part where large line of sight velocities are found (however, both regions do not coincide exactly). They seem to be larger at the edges but this is not always true (lines 5 and 6 for instance). We do not have a unique relationship between FWHM and line shifts, as evidenced in Figure 4 where both quantities are plotted.

The absolute Ca II K intensities are computed from the Gaussian fits to profiles and given in Figure 3c as a function of position in the prominence. The spatial distribution roughly mimics the FWHM distribution. Intensities range from 3500 to 22 800 $\text{erg s}^{-1} \text{cm}^{-2} \text{sr}^{-1}$, all below one tenth of the disk intensities.

The Ca II H line gives about the same information, as far as FWHM and shifts are concerned. However, the ratio signal/noise is lower for this line than for Ca II K. We consequently concentrate on integrated intensities only, after a careful selection of 43 profiles (out of 60) with a statistical accuracy better than 6%. Such a selection eliminates predominantly low intensity profiles located in the outer regions. We plot in Figure 5 the K versus H intensities. The linear regression gives an average $\langle K/H \rangle$ ratio of 1.2, close to the value (1.4) found by Landman *et al.* (1978) for strong emission in 11 prominences (see their Table 1 and Figure 3a).

We also computed average profiles in the prominence: FWHM, shifts and absolute intensities are summarized in Table I. The averaging clearly leads to smaller shifts and larger FWHM. The $\langle K \rangle / \langle H \rangle$ ratio is now 1.1; it is lower than the $\langle K/H \rangle$ ratio (1.2), because the ratio of averaged intensities gives more weight to the bright areas for which the K/H ratio is closer to 1. Because of the very low statistics, we could only

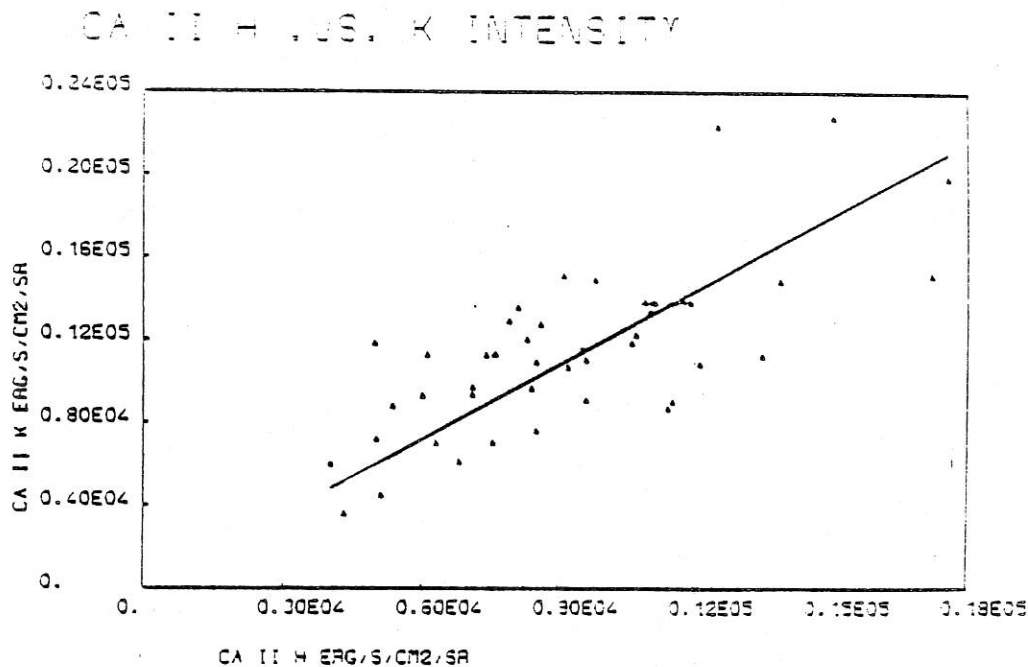


Fig. 5. Correlation between Ca II K and H intensities.

TABLE I
Average profiles parameters for the whole prominence

	Ca H	Ca K	Mg h	Mg k	L α	L β
FWHM (\AA)	0.37	0.32	0.42	0.44	-	-
Shift (km s^{-1})	2	2	0	0	-	-
Intensity ($\text{erg s}^{-1} \text{cm}^{-2} \text{sr}^{-1}$)	10200	10900	13970	24230	4870 ^a	500

^a Intensity over a 0.2 \AA bandpass (from -0.05 to 0.15 \AA).

compute average Mg II h and k profiles. Their characteristics are given in Table I: the resulting $\langle k \rangle / \langle h \rangle$ ratio is 1.7.

As far as the L α line is concerned, the spectral scan did not go further than 0.15 \AA in the red part of the line (0.25 \AA , if we take into account the width of the exit slit). Since the counts number is maximum at 0.15 \AA , a peak to peak distance (0.3 \AA) and a ratio of peak to center intensities (1.2) are derived. The intensity is computed between the center and the red peak of the line: within the 60 different areas in the prominence, it varies from 2190 to 8660 $\text{erg s}^{-1} \text{cm}^{-2} \text{sr}^{-1} (0.2 \text{\AA})^{-1}$.

We then compute the ratio of L α (from -0.05 to 0.15 \AA) to Ca K intensities: it varies by a factor 6 (except for a unique value of 8). As shown in Figure 3d, high values correspond to the upper part of the prominence (in the image) where we noticed important K line shifts.

After correcting for the geocoronal absorption, the average $L\alpha$ value for the whole prominence is $4870 \text{ erg s}^{-1} \text{ cm}^{-2} \text{ sr}^{-1} (0.2 \text{ \AA})^{-1}$. At line center, we have $3860 \text{ erg s}^{-1} \text{ cm}^{-2} \text{ sr}^{-1} (0.2 \text{ \AA})^{-1}$. The average $L\beta$ intensity is $500 \text{ erg cm}^{-2} \text{ s}^{-1} \text{ sr}^{-1}$. If we assume that the $L\alpha$ profile in the prominence has the same shape as the chromospheric profile, we can derive from the central value an absolute integrated intensity. We find about $19\,300 \text{ erg s}^{-1} \text{ cm}^{-2} \text{ sr}^{-1}$. Since the prominence profile is narrower than the chromospheric one, this is a maximum value. It leads to a maximum $L\alpha/L\beta$ ratio of 39, to be compared with 86 in the quiet Sun (Vernazza and Reeves, 1978).

5. Discussion

We do not observe in Ca II lines the larger line-of-sight velocities mentioned by Engvold *et al.* (1978) at the edges of prominences, that they interpreted as matter ejecta. This is probably due to our moderate spatial resolution and possibly also to the unfavourable geometry: if their interpretation as matter ejections is retained, they would occur perpendicularly to the filament, but, it is obvious from Figure 1, that our line-of-sight is parallel to the filament. We notice, however, some large (up to 14 km s^{-1}) velocities directed toward the observer. They are located in a region where the intensity is moderate but the FWHM are rather large.

This region does not belong to the body of the prominence but, as shown by the absorption feature at the limb, probably corresponds to a bridge to a leading filament at lower latitude. In the other regions, our observations (with a $5 \times 10 \text{ arc sec}^2$ resolution) do not firmly confirm the increase of excitation in the external region, mentioned by Hirayama (1971).

From the low values of $\langle K/H \rangle$ (and $\langle K \rangle/\langle H \rangle$), we conclude that the opacity in the Ca II lines is high. The Ca II FWHM (Table I) also indicate an appreciable opacity (or non thermal velocity, up to 16 km s^{-1}), or both. The Mg II FWHM are still larger and correspond to a non thermal velocity of 28 km s^{-1} , or a very high opacity. The $\langle k \rangle/\langle h \rangle$ ratio is 1.7, however. We found the same results at the edge of an active prominence (Vial *et al.*, 1979) where $k/h > K/H$ and $\text{FWHM}(h, k) > \text{FWHM}(H \text{ and } K)$ (in km s^{-1}). Both results cannot be understood in terms of opacity and non thermal velocity only, since, for a given turbulence, the Mg II lines should be more saturated than the Ca II lines, which is contrary to line ratios measurements. Other parameters (radial velocities, temperature distribution, ...) should be invoked to explain the behaviour of the Ca II and Mg II resonance lines.

The $L\alpha$ intensity is rather low, as compared to active prominence intensity (Vial *et al.*, 1979). The peak distance (0.3 \AA) is typical of quiescent prominences. Since we only scanned a small part of the line, the $L\alpha/\text{Ca K}$ ratio should be regarded as a relative one. However, its variations is an interesting parameter. The Ca K intensity is roughly proportional to the neutral hydrogen population (see Tandberg-Hanssen, 1974; or Hirayama, 1978). The $L\alpha$ intensity is proportional to n_2/n_1 . It has been shown, both theoretically and observationally (see Hirayama, 1978), that n_2^2/n_2 does

not change with varying conditions in prominences. As a consequence, the $L\alpha/\text{Ca K}$ ratio is representative of $(n_e/n_1)^2$. Since our $[L\alpha(-0.05, +0.15 \text{ \AA})]/\text{Ca K}$ ratio varies by a factor 6, we derive that the ionization degree changes by a factor 2.5 within the prominence. As shown in Figure 6, where we plot $L\alpha/\text{Ca K}$ as a function of Ca K, we observe a saturation of the $L\alpha/\text{Ca K}$ ratio at high Ca K intensity.

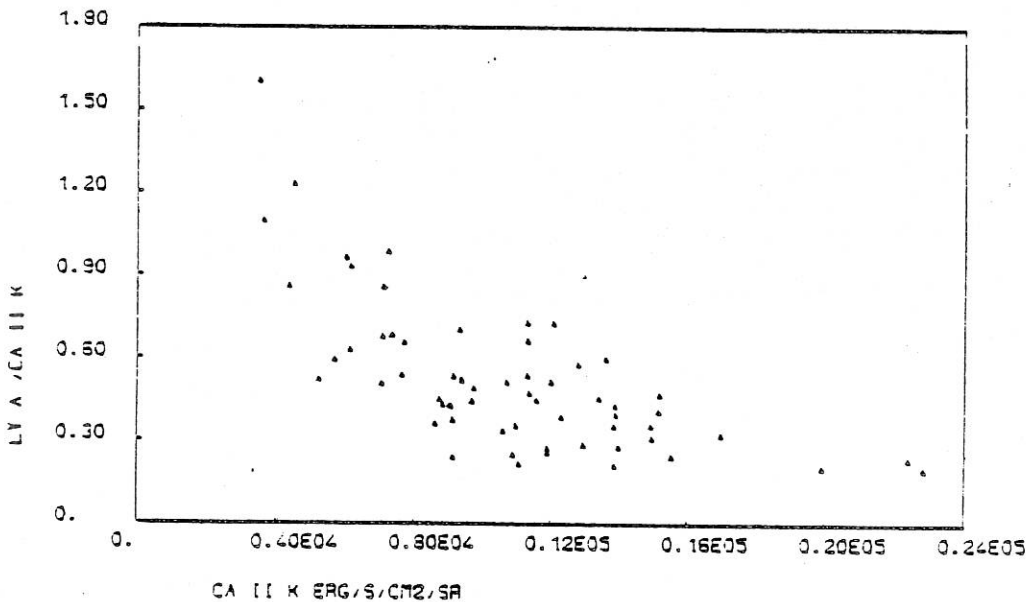


Fig. 6. Correlation between $L\alpha/\text{Ca K}$ ratio and Ca K intensity.

At line center, we have $L\alpha(\text{prominence})/L\alpha(\text{quiet Sun}) \sim 0.3$ and $K_3(P)/K_3(\odot) \sim 0.16$. These values would reflect the variation of the dilution factor from a line with quite no darkening ($L\alpha$) to a limb-darkened line (K). The 'anomalous' $L\alpha/L\beta$ ratio (less than one half the chromospheric value) is similar to the ratio observed in active regions (Vernazza and Reeves, 1978), or flares (Machado *et al.*, 1979). In spite of a low spatial resolution, these results evidence typical features of a quiescent prominence observed in Ca II (H and K), Mg II (h and k), H I ($L\alpha$ and $L\beta$) lines.

Acknowledgements

The authors thank Dr P. Mein for a helpful discussion. They thank LASP and LPSP staff members who were involved in the observing programs at LASP (University of Colorado). They express their gratitude to NOAA and Meudon Observatory (DASOP) for assistance in ground-based observations. Computations have been performed on CNES computer through contracts 77-78-79 CNES 202. The authors thank Mr Perthuis and the CNES computer team who provided with the data tapes.

References

- Artzner, G., Bonnet, R. M., Lemaire, P., Vial, J. C., Jouchoux, A., Leibacher, J., Vidal-Madjar, A., and Vite, M.: 1977, *Space Sci. Instrum.* 3, 131.
- Bonnet, R., Lemaire, P., Vial, J. C., Artzner, G., Gouttebroze, P., Jouchoux, A., Leibacher, J., Skumanich, A., and Vidal-Madjar, A.: 1978, *Astrophys. J.* 221, 1032.
- Engvold, O. and Malville, J. M.: 1977, *Solar Phys.* 52, 369.
- Engvold, O., Malville, J. M., and Livingston, W.: 1978, *Solar Phys.* 60, 57.
- Hirayama, T.: 1971, *Solar Phys.* 17, 50.
- Hirayama, T.: 1978, in Jensen, Maltby, and Orrall (eds.), 'Physics of Solar Prominences', *IAU Colloq.* 44, Landman, D. A., Illing, R. M. E., and Mongillo, M.: 1978, *Astrophys. J.* 220, 666.
- Machado, M. E., Avrett, E. H., Vernazza, J. E., and Noyes, R. W.: 1979, preprint.
- Mein, P.: 1977, *Solar Phys.* 54, 45.
- Mouradian, Z. and Leroy, J. L.: 1977, *Solar Phys.* 51, 103.
- Tandberg-Hanssen, E.: 1974, *Solar Prominences*, D. Reidel Publ. Co., Dordrecht, Holland.
- Vernazza, J. E. and Reeves, E. M.: 1978, *Astrophys. J., Supplement Series* 37, 485.
- Vial, J. C., Gouttebroze, P., Artzner, G., and Lemaire, P.: 1979, *Solar Phys.* 61, 39.

Article VI

Optically thick lines in a quiescent prominence :
profiles of $L\alpha$, $L\beta$ (H I), k and h (Mg II), K and H (Ca II) lines
with the OSO-8 LPSP instrument

VIAL, J.C.

OPTICALLY THICK LINES IN A QUIESCENT PROMINENCE :
PROFILES OF $L \alpha$, $L \beta$ (H I) , k AND h (Mg II), K AND H (Ca II) LINES
WITH THE OSO-8 L.P.S.P. INSTRUMENT

VIAL, J.C.

Laboratoire de Physique Stellaire et Planétaire
(C.N.R.S.)

B.P. N° 10 91370 VERRIERES LE BUISSON FRANCE

Received 1981 March 4 :

Running title : Optically thick lines in a quiescent prominence

To be published in Astrophysical Journal, February 1982.

ABSTRACT

A full set of observations in the resonance lines of Mg II, Ca II, H I (and O VI) and in the $L\beta$ (H I) line has been obtained with the LPSP instrument on OSO-8. The observing modes (images, profiles) and the procedures of analysis are described and a special attention is paid to the intensity calibrations.

Typical lines profiles parameters (widths, intensities) are summarized in Table I. The Ca II lines have a low opacity : in the K line center it varies from 1.4 to 3.2. Non Thermal Velocities range from 5 to 9 km s⁻¹ and line shifts are small but reach 8 km s⁻¹ at the edges. Intensities are lower than the incident chromospheric intensities multiplied by the dilution factor. The ratio of K_3 and H_3 intensities (K_3/H_3) is about 1.4.

The Mg II lines are measured in the whole prominence only. Departures from Gaussian profiles may result from the integration of many elements with different velocities along the line of sight and also from line saturation. However, we observe an intensity ratio k/h of about 1.6, higher than the K/H ratio (as it is in the chromosphere). This result can be understood if the source function of resonance lines of Mg II and Ca II is dominated by the incident radiation. But the important width of Mg II lines, as compared to Ca II lines, is not explained.

The full profiles of $L\alpha$ and $L\beta$ (H I) lines are observed for the first time in a quiescent prominence. Both are reversed, with a separation of 0.35-0.40 Å for $L\alpha$ and 0.33 Å for $L\beta$. Intensities are about equal to the incident chromospheric intensities multiplied by the dilution factor. Opacities are very high and the radiation transfer is dominated

by the scattering of chromospheric $L \alpha$ and $L \beta$ photons. The $L \alpha / L \beta$ ratio is lower than the chromospheric one.

The ratio of $L \alpha$ to Ca K intensities does not vary much (less than a 1.6 factor) and indicates a ionization degree of about 3. Both features indicate that the ionizing Lyman continuum penetrates fully in the prominence.

INTRODUCTION

Because of the changing properties (with time and space) of prominences, simultaneous scans in different lines (with good spatial resolution) are of great interest. This is exemplified by the observations of Illing et al. (1975), of Landman and Illing (1977), of Landman et al. (1977) who discovered intensity oscillations, and Landman et al. (1978) who observed as many as 9 lines simultaneously. These results were compared by Heasley and Milkey (1978) with their computations of line intensity ratios (e.g., Ca II H/K, Ca II (8542)/H β , ...). A good agreement was found, except for the pressure, derived from models, that is too low and implies a large geometrical extent of the prominence. The inferred kinetic temperature and non thermal velocities were 7500 to 10 000 K and 4.5 to 7 km s⁻¹ (Landman et al., 1977). From line width analysis also, other authors found lower temperature (4500 to 8500 K) (see Hirayama's review in Physics of Solar Prominences, 1978). Because of the shape of the D₃ wings, Landman et al. (1977) proposed to add a high temperature component, a result confirmed by Kureizumi et al. (1977) and Landman (1980).

More recently, Kanno et al. (1980) and Orrall and Schmahl (1980) found a low ionization from their study of e.u.v. lines that are formed in the Prominence-Corona (P.C.) transition region. Their ratio of proton to neutral hydrogen populations ($\frac{n_p}{n_1}$) is lower than 2. It is certainly smaller in cooler regions of the prominence. Such a result does not agree very well with the large range ($1 < \frac{n_p}{n_1} < 10$) found by Hirayama (1978).

Thus it appears that the large-scale thermal conditions within prominences are still not well known. Some authors (Engvold et al., 1980)

noticed that the observed line profiles (K of Ca II, for instance) changed when the spatial resolution improved from about 15 arcsec to 2 arcsec : for instance, line widths exceeded the thermal values by a factor 2 only. One could quickly conclude that no useful information can be obtained unless the spatial resolution reaches the size of structures known to exist ($H\alpha$ vertical threads (Engvold, 1976), $L\alpha$ threads or loops (Bonnet et al., 1980)). However, except for the SMM-UVSP experiment, no instrument now is capable of resolving these structures from a spectroscopic point of view, and the same remark applies for all solar features. Moreover, in spite of recent advances (Mihalas et al., 1978) the theory of radiation transfer has no clues for such complex observations. We think that medium resolution observations are still a valid approach, provided that they are performed simultaneously in many different lines (or continua), through the same slit.

The LPSP instrument on board OSO-8 gives such a capability of simultaneously scanning lines of different opacities and temperatures of formation. The observed lines ($L\alpha$ (and $L\beta$) of H I, k and h of Mg II, K and H of Ca II) allow a probing of different regions from the central (cool) to the outer (hot) part of prominences. The rastering device on board OSO-8 also allows a mapping of the structures. Observations of an active region prominence are reported by Vial et al. (1979) (Paper I) and preliminary results from a quiescent prominence are given in Paper III (Vial et al., 1981). We now have a full set of observations in all six lines : the Ca II (H and K) lines observed from spacecraft are free from atmospheric contamination ; moreover, they can be used as a reference, when we compare u.v. lines with other lines

observed from the ground. The Mg II lines can be recorded for a long time only from satellite. They should have a higher opacity than the Ca II lines and photons should originate from outer regions. The hydrogen lines should be formed in the transition region between the prominence and the corona. The $L \alpha$ and $L \beta$ profiles reported here are the first measured ones in a quiescent prominence.

The instrumental configuration and data processing are described in Section I. The morphology of the observed prominence is discussed in Section II. Typical profiles are presented in Section III. The spatial variations of the profiles are given in Section IV. Section V is devoted to a discussion of the results.

I. INSTRUMENTAL CONFIGURATIONS, OBSERVING SEQUENCES AND DATA PROCESSING

a. INSTRUMENTAL CONFIGURATIONS

The instrument is described in Artzner et al. (1977) and Bonnet et al. (1978), (see also, Bonnet (1981)). It consists in a multichannel spectrometer fed by a 16 cm diameter Cassegrainian telescope.

$L \alpha$ and $L \beta$ lines of H I, h and k of Mg II, H and K of Ca II can be simultaneously scanned when rotating the grating with a basic spectral resolution of $20 \text{ m}\overset{\circ}{\text{A}}$. With a full rotation of the grating, the O VI line ($\lambda = 1032 \overset{\circ}{\text{A}}$) can also be reached in the $L \beta$ channel while the Ca II and Mg II channels then record the Fraunhofer spectrum at $\lambda = 3982, 3949, 2822, 2815 \overset{\circ}{\text{A}}$. The secondary mirror of the telescope can be moved with 1 arcsec step within a $64 \times 64 (\text{arcsec})^2$ field.

At any spatial position, a spectral scan can be performed with a basic integration time of 0.16 s for each grating position. For a given grating position, spatial information can also be obtained with spacecraft rasters. The grating position may be incremented between rasters allowing for a line profile scanning. The most frequently used rasters have a size of 2.7×2.5 (arcmin)², a spatial resolution of 10×5 (arcsec)², and need 82 s to be achieved. These different capabilities were used in the observations described below.

b. OBSERVING SEQUENCES

The set of observations consists of 7 consecutive orbits. We distinguish 4 observing modes :

1) Images at variable wavelengths (orbits 5018, 5022) : the spectral resolution is $20 \text{ m}\text{\AA}$ in Mg II and Ca II resonance lines, 0.2 \AA in L α and 1 \AA in L β . At the end of each raster, the wavelength is changed by steps of 0.120 , 0.135 , 0.18 \AA , 0.07 \AA for H, K, h and k, L α respectively. Because of the orbital velocity, wavelengths are shifted during one orbit. Moreover, a pointing drift occurs during the whole orbit (10 arcsec) (Lemaire, 1978) and is corrected for.

2) Profiles at different positions (orbits : 5019, 5021) : the slit was parallel to the limb and was moved radially by steps of 1 arcsec : the scan included 8 positions but because of a horizontal drift in the pointing system, the overall scan was 17" long. The length of the slit was 20". A vertical drift is known to exist also (Lemaire, 1978) but it is sufficiently small that we have not taken

it into account here. The spectral resolution is $20 \text{ m}\text{\AA}$ for all lines, except for $L \alpha$ (0.2 \AA) and $L \beta$ (1 \AA). The wavelength steps are half of that in (2).

3) Profiles at a given position : (orbit 5020) because of the drift mentioned above, they refer to an averaging over about $4''$; the slit length was $40''$. The spectral resolution is the same for Ca II and Mg II lines but it is now $20 \text{ m}\text{\AA}$ for $L \alpha$ and $60 \text{ m}\text{\AA}$ for $L \beta$.

4) Monochromatic images, obtained in the whole O VI line ($\lambda = 1032 \text{ \AA}$) during 2 orbits (5016, 5017).

C. DATA PROCESSING AND CALIBRATION

i. Stray light

Because of the low signal levels, much care was paid to the determination of the noise and the stray light. In modes 1 and 4, both quantities could not be separated, and their sum was measured at different locations of the image free of emission in any wavelength. For the Ca II channels, the stray light is time dependent within one orbit (Lemaire, 1978) and a correction was necessary for these modes. In modes 2 and 3, the correction was simply made by considering that the signal in excess of the signal measured in the wings corresponds to the emission in Ca II and Mg II lines. Such a scheme was impossible for the $L \alpha$ and $L \beta$ lines. For these lines, we considered that the minimum signal averaged in an above-the-limb region free of Ca II emission was representative of the sum of the noise and the stray light. For typical profiles (see III), disk profiles were subtracted with the appropriate scattered light factor.

ii. Wavelength calibration

For the whole lifetime of the instrument, the position of selected absorption lines in the wings of Ca II and Mg II lines, was systematically recorded at Sun center. The observing time of these lines usually extended over more than 5 minutes. A 3rd order polynomial fit proved to be sufficient for the determination of reference wavelengths and local dispersions. Moreover, the variations of dispersion were proven to be strongly correlated to the temperature of the grating. As a further check, profiles obtained at the extreme limb but on the solar disk, were also used and the solar rotation taken into account. As a result of these different determinations, an accuracy better than ± 0.5 grating step (i.e. about 1.1. km/s) was achieved for Ca II lines. It is ± 1 grating step for Mg II lines, corresponding to ± 2.4 km/s. The L α and L β wings do not have absorption lines that may be used as references. The only reference is the geocoronal absorption, 30 to 40 mÅ wide, at the center of the L α line. The accuracy of this positioning is about ± 10 mÅ. The dispersion is computed from the measured properties of the spectrometer in Mg II and Ca II lines. A comparison between computed and measured values (in the laboratory) has shown that the procedure is accurate within $3 \cdot 10^{-3}$.

3.i. Intensity calibration

We follow the procedure described in previous papers (Papers I and III) : Long term average profiles measured in a quiet region at

Sun center at the approximate time of the prominence measurements, serve for a relative intensity calibration.

The Ca II lines minima K_{1V} and H_{1V} are not very sensitive to the local activity (network/cell) in addition to which, we average over (10×10) arcsec² regions for the disk center measurements. Absolute intensities in H_{1V} and K_{1V} are taken as 0.0751 and 0.0687 respectively in units of the continuum intensity at 4000 Å (Linsky, 1970). The variation of these quantities from one solar cycle to another is much lower than the variations of K_3 and H_3 . At Sun center, White and Livingston (1978) did not measure any variation of K_3 between 1974, 1975 and 1977 (this time period covers the observations reported here). And very recent measurements of White and Livingston (1981) above quiet Sun center regions, indicate a constancy of the K_3 intensity (within 5 percent) and of the K index (within 0.3 per cent) from minimum to maximum of solar cycle 21. We conclude that the variation of K_{1V} and H_{1V} between 1975 to 1976 is less than 3% but may depart from Linsky's absolute values by a factor that only more statistical studies of solar cycles will determine.

At the time of our prominence observations, the standard deviation for K_{1V} , H_{1V} measurements is about 2 and 2.4 per cent of respective average values.

The same procedure holds for the Mg II measurements of k_1 and h_1 . Absolute values are taken from Kohl and Parkinson (1976). We adopt $k_{1r} = 6.5 \cdot 10^4 \text{ erg s}^{-1} \text{ cm}^{-2} \text{ sr}^{-1} \text{ Å}^{-1}$ and $h_{1r} = 5.27 \cdot 10^4 \text{ erg s}^{-1} \text{ cm}^{-2} \text{ sr}^{-1} \text{ Å}^{-1}$. Because of the low transmission of the instrument and a significant contribution of continua at $\lambda = 3500 \text{ Å}$ (4th order) in the Mg II channels at the time of our observations, the (k_1, h_1) procedure

proved to be impossible. In order to avoid both difficulties, we use the integrated intensities of k and h lines measured above the k_1 (h_1) levels. We compare to Kohl and Parkinson values :

$$J_k = 1.45 \times 10^5 \text{ erg s}^{-1} \text{ cm}^{-2} \text{ sr}^{-1}$$

$$J_h = 0.98 \times 10^5 \text{ erg s}^{-1} \text{ cm}^{-2} \text{ sr}^{-1}$$

where :

$$J_k = \int_{\Delta\lambda(k_{1v}, k_{1r})} I_k d\lambda - \frac{k_{1v} + k_{1r}}{2} * \Delta\lambda(k_{1v}, k_{1r})$$

Obviously, this procedure relies on two assumptions :

- 1) Kohl and Parkinson's intensities are representative of an average solar quiet region ;
- 2) the chromospheric emission (measured by J) does not change from 1974 to 1976.

A third assumption, i.e. that our observations at Sun center are made on an average solar region, is satisfied because of a careful selection of Ca II profiles (no active profiles are included), the size of the slit (1"x40") and the computation of an average profile over "cell and network" measurements. The second assumption cannot be checked because no data are available between the Kohl and Parkinson rocket measurements and OSO-8. However, the constancy of K_3 during the same period indicates that no change occurs within 5%. If we interpret any change as a temperature effect, it should also exist in k_3 with a magnification by the ratio of the frequencies (1.4). We can adopt the same scaling factor for k_2 and h_2 versus K_2 and H_2 and we conclude that J_k (or J_h) is constant within 7% from 1974 to 1976.

The first assumption is assessed by Kohl and Parkinson from a careful positioning of their slit within a region free of activity.

However, according to observations of Lemaire et al. (1981), their line measurements may give too much weight to the chromospheric network. The amount of correction needed is unknown, but the overestimation of the reference absolute intensity (in 1974), would compensate a possible overestimation of the measured quiet Sun profile (1976).

When the statistics were good, both methods (k_{1v} and J_k) were compared. We assumed that the first method (k_{1v} , h_{1v}) was quite insensitive to solar conditions and we calibrated the second method versus the first one ; the disagreement between them is a measurement of the deviation from assumptions 1 and 2.

The standard deviation for J_k and J_h is about 5.7 and 10 per cent of respective average values.

The $L \alpha$ line : in this channel, we have no continuum to rely on and the only reference is the $L \alpha$ line itself, measured in a quiet solar region. Different measurements were performed in 1976 with different instruments : a summary is given in Lemaire et al. (1978). The reduction of these data leads to a value of $6.5 \cdot 10^4 \text{ erg s}^{-1} \text{ cm}^{-2} \text{ sr}^{-1}$ for the quiet Sun (Lemaire et al., 1981). The accuracy of the procedure is hardly affected by the time interval between our quiet Sun measurements and the calibrations (a few months only). It is however limited by two factors :

- 1) the low signal to noise ratio,
- 2) the $L \alpha$ line is wide (about 2 \AA) and our reference quiet Sun profiles extend over 1 \AA only.

The only solution to the first problem consists in taking into account as many non active reference profiles as possible and then averaging over them.

As for the second factor we decided to use the reversal of the line as our parameter representative of time variation. From the study of many $L\alpha$ profiles throughout the lifetime of the instrument, we noticed that the intensity at line center, measured with a 0.2 \AA band pass (including the geocoronal absorption dip), represented about 15% of the whole intensity, in quiet solar regions. Published calibrated $L\alpha$ profiles (Lemaire *et al.* (1978), Basri *et al.* (1979)) support our value. However, our method is sensitive to any change of the $L\alpha$ reversal (either solar : coronal hole, filament, ... or geocoronal) that might be unnoticeable in other channels (Vidal-Madjar and Phissamay, 1980). These changes could certainly occur on a time interval short compared to the temporal range of our quiet Sun observations. They result in an increase of the deviation about a mean value.

The standard deviation for the quiet Sun $L\alpha$ profiles recorded at the time of our prominence observations is found to be about 5% of the average value.

The $L\beta$ line : Prominence measurements were compared to systematic quiet Sun center measurements at the same epoch. The reference quiet Sun absolute intensity was taken as $920\text{ erg s}^{-1}\text{ cm}^{-2}\text{ sr}^{-1}$ (Lemaire *et al.*, 1978, Lemaire *et al.*, 1981), and we assumed that it did not change between February 1976 and May 1976. However, this reference value is in the upper part of the range of previous determinations (see for instance, Vernazza and Reeves (1978)).

The standard deviation of the $L\beta$ absolute intensity is about 5 per cent of the average value.

As far as line ratios are concerned, we computed the standard deviations of the measured ratios of transmissions (which are rather

insensitive to solar activity) and obtained 1% for K/H, 5% for k/h, and 3% for $L \alpha/L \beta$ of respective average values.

d. DECONVOLUTION

We follow the procedure given by Brault and White (1971) with no difficulty when the signal to noise ratio is high enough. But for the Lyman lines, we both have a low statistics and the existence of a geocoronal absorption feature at the center of the $L \alpha$ (and $L \beta$) line. In the $L \alpha$ line, the exit slit was either 20 mÅ (about the half-width of the geocorona absorption) or 0.2 Å. It is in principle possible to restore the true profile in both cases up to the Nyquist frequency. It was proved to be difficult in the first case because the absorption profile is very narrow and hence has associated high frequencies : keeping these high frequencies in the restoring process would introduce important "oscillations" in other parts of the profile. The frequency limit is then determined by the noise level. The typical $L \alpha$ profile we give in Section III results from a compromise between the two requirements. In the second case (0.2 Å exit slit), the Nyquist frequency is below the frequency of the absorption feature and the restoration is limited by the noise level anyway. We only performed a "smoothing" restoration on these profiles (Section IV).

II. MORPHOLOGY : INTENSITIES AND VELOCITIES

We first present the results obtained in the six lines (mode number 1) 90 minutes before and after the profiles that will be discussed in § IV.

The filament was observed on the 19th of May 1976 from 0. to 11. U.T. when it appeared at the East limb. Martres and Zlicaric (1976) refer to it as a new filament (latitude 24°N , longitude 45°) in Carrington rotation 1641. At the time of our observations, the position angle was about 60° . Its heading part was about 45° inclined to the solar parallel ; the ending part was lined up on the parallel.

It is a faint structure, hardly visible in $\text{H } \alpha$ (Figure 1.a). The good correlation between ground and OSO-8 K_3 images, in spite of a time difference of -4 and +2 hours, indicates that the prominence is stable (Figures 1.b and 3).

We distinguish 2 structures, a closed one at lower latitude, and a second (and higher) one which seems open, probably because a leg is located behind the disk. We notice that there is no emission between the "loop" and the disk. This is an indication that there is not much material between the plane of sky and the observer. Furthermore, the piece of filament found at the very limb is located a few degrees below the lower leg of our structure : because of the negative value of ϑ_c (heliographic latitude of disk center), its extension to the limb would be located in a still lower position, and is not found. As a consequence, our line of sight is nearly perpendicular to the face-on structure.

We give in Figures 1.c, the images obtained in the Ca K integrated line for orbits 5018 (Figure 1.c.1) and 5022 (Figure 1.c.2). The scale is linear in the prominence intensity range but saturated for disk levels. The morphology is different in the $\text{L } \alpha$ and $\text{L } \beta$ lines

(Figures 1.d.1-1.d.2 ; 1.e.1-1.e.2 respectively). In hydrogen lines, the prominence is brighter and more extended than in Ca II lines. This result is discussed in § V.

We separated the monochromatic images obtained in mode 1, for the Ca II channel, into two sets : a first one (blue) in wavelengths lower than the central wavelength λ_0 of the profile, and a second one (red) in wavelengths higher than λ_0 . For orbits 5018 and 5022 (separated by 6 hours), Figures 2 (a.1-b.1) show the 2 dimensional representation of $\Sigma I(\lambda) - \Sigma I(\lambda)$ for the K line. It is an indication of the velocity fields in the prominence (at least their sign). We easily notice the solar rotation at the limb (line of sight velocity directed to the observer, so blue shift). We also observe some important redshift at the top of the structure (Figure 2.a.1) and a less important redshift at the bottom of it (Figure 2.b.1). So, in order to have the magnitude of velocities, we constructed the profiles at any location of the prominence (a 5"×10" area), fitted Gaussian functions to them, and derived all parameters including full widths at half maximum and line shifts.

Figures 2.a.2 and 2.a.3 are gray scale representations of line-of-sight velocities (orbit 5018) directed away from and towards the observer, respectively. We notice (Figure 2.a.2) high positive velocities (away from the observer) at the top of the filament, especially at the edges. The maximum amplitude is 8 km.s⁻¹. Positive velocities also exist in the lower part of the structure. Negative velocities (Figure 2.a.3) are also present in the lower and upper regions, but in their central part and with a lower amplitude

(3 km s⁻¹). Because of the uncertainty in the determination of the zero velocity, our negative velocities may well be zero. In this case, positive velocities may reach 11 km s⁻¹. Higher velocities certainly exist but cannot be measured with a (5×10) arcsec² resolution.

A few hours before the velocity measurements described above, we also performed O VI ($\lambda=1032 \text{ \AA}$) rasters (mode 4). The statistics was not very good and no correction for stray light was made. However, we notice (Figure 2.c) that the O VI emission coincides with the emission in the chromospheric lines. The brightest region is at the intersection of the 2 structures visible in K₃. The intensity, here, is about 1/3 the intensity of the bright O VI ring.

This ring is not visible in Figure 2.c because we saturated the highest levels in order to make the prominence appear more clearly. This maximum O VI intensity at the limb is about 7-8 times larger than the quiet Sun center intensity (Vial et al., 1980). The brightest point in "the" prominence is therefore about 2.5 times as bright as the quiet Sun. This is probably due to the high number of prominence corona (P.C) interface layers (4 since the line of sight intercepts 2 structures at least). No O VI profile being obtained, we do not discuss O VI data any further.

III. TYPICAL PROFILES

The entrance slit of the spectrometer (1"x40") was positioned along the lower structure mentioned in II. It is shown in Figure 3 in the K₃ intensity image. We indicate the size and the

location of the slit, and also its drift due to a varying mis-alignment between the two pointed instruments on OSO-8. Such a drift perpendicular to the limb, was corrected for in orbit and is not critical since we study time averaged profiles.

However, Ca II profiles showed some change from the beginning to the end of the orbit. So, we divided the observed profiles into 2 classes corresponding to "the first part of the orbit" (FPO) and "the last part of the orbit" (LPO) where averaging is done over two regions $40 \times 2.5 \text{ arcsec}^2$, separated by 2.5 arcsecond. All profiles were corrected from scattered light. They are given in Figures 4.a and b and parameters summarized in Table 1. We give in Table 1 the accuracy of integrated intensities : it takes into account the accuracy of quiet Sun center (see § I.C.3i) and prominence observations. The precision of reference quiet Sun absolute intensity measurements is discussed by Lemaire et al. (1981) and is not taken into account here.

Because the long slit intercepts structures with low emission, we correct the measured intensity with a slit "filling factor" computed as follows: from the monochromatic images obtained in the raster mode with a $5 \times 10 \text{ (arcsec)}^2$ resolution, we derive $C = \frac{I_{\text{max}}}{\langle I \rangle_{\text{slit}}}$ at the location of the long slit where profiles are measured. We assume that the actual prominence emission is the one measured at positions where the intensity is maximum. So the slit "filling factor" is C^{-1} . We obtained 0.8.

$L \beta$ and $L \alpha$ profiles (Figures 4.a-b(5,6)) are reversed : the peak-to-peak distance ranges from 0.35 to 0.37 and 0.30 to 0.33 for $L \alpha$ and $L \beta$ respectively. We notice that LPO profiles are narrower

than FP0. This is observed in other lines. It is also evident from peak to center intensities ratio for $L\beta$: 2(FP0) and 1.7(LP0). We find 1.4 for FP0 and LP0 $L\alpha$ profiles, but it should be stressed that the depth of the reversal is very sensitive to the deconvolution : the peak-to-center intensities ratios should be considered as upper limits. The $L\beta$ integrated intensity is 440 (± 40) and 370 (± 33) $\text{erg s}^{-1} \text{cm}^{-2} \text{sr}^{-1}$ for FP0 and LP0 (mean value 400). The $L\alpha$ intensity on the contrary does not change much (2.8 and 2.9 10^4 (± 0.2) $\text{erg s}^{-1} \text{cm}^{-2} \text{sr}^{-1}$), as it would result from the scattering of the chromospheric radiation (see § V.b). These intensities represent about 0.44 times the quiet Sun $L\beta$ and $L\alpha$ intensities.

With filling factors evaluated as 0.8 for $L\beta$ and $L\alpha$, we obtain 500 (± 45) and 3.6 10^4 (± 0.25) $\text{erg s}^{-1} \text{cm}^{-2} \text{sr}^{-1}$ (0.55 times the quiet Sun intensity). The ratio of $L\alpha$ to $L\beta$ integrated intensities is 71(± 6), exactly the same value measured in the quiet Sun. Vial et al. (1981) found a lower ratio in a quiescent prominence but they scanned only a fraction of the $L\alpha$ profile.

Both h and k lines profiles of Mg II (Figure 4.a-b (3 and 4)) are unreversed, as previously noticed by Vial et al. (1980) in a quiescent prominence. FWHM of k and h profiles are about .53 and .40 Å for FP0 and LP0 respectively. The absolute intensities vary from 2.5 10^4 (FP0) to 2.25 10^4 (± 0.2) (LP0) $\text{erg s}^{-1} \text{cm}^{-2} \text{sr}^{-1}$ for k and 1.55 10^4 (FP0) to 1.4 10^4 (± 0.2) (LP0) $\text{erg s}^{-1} \text{cm}^{-2} \text{sr}^{-1}$ for h. After correction for a filling factor 0.8 the mean values for k and h (2.4 10^4 and 1.5 10^4) become 2.95 10^4 (± 0.25) and 1.8 10^4 (± 0.3) $\text{erg s}^{-1} \text{cm}^{-2} \text{sr}^{-1}$ for k and h respectively. They represent about 0.13 and 0.1 times the k and h

intensities at Sun center. The ratio of k to h intensities is 1.6 (± 0.19). Since the oscillator strengths of k and h lines are in a ratio of 2, the observed value of k/h would indicate a non negligible saturation of both lines, that could explain why both profiles are wide. Neglecting such a possible opacity effect and assuming a temperature of 8000°K, the computed non-thermal velocity (NTV) would be 34 (FPO) and 26 (LPO) km s^{-1} . However Mg II FPO profiles are non-Gaussian contrary to Ca II profiles (see below) : another explanation may be given in terms of unresolved line-of-sight macrovelocities.

H and K lines of Ca II (Figure 4.a-b (3 and 4)) are also unreversed, as previously noticed in most quiescent prominences (Hirayama, 1978 and also Vial *et al.*, 1981). FWHM are smaller in the last part of the orbit ($.23 \text{ \AA}$ instead of $.29$ for K). The absolute intensities are : $1.3 \cdot 10^4$ (FPO), $1.2 \cdot 10^4$ (± 0.3) for K and $9.5 \cdot 10^3$ (FPO), $8.1 \cdot 10^3$ (± 0.2) (LPO) $\text{erg s}^{-1} \text{ cm}^{-2} \text{ sr}^{-1}$ for H. After correction for a 0.8 filling factor, they become $1.6 \cdot 10^4$ (FPO), $1.5 \cdot 10^4$ (LPO) and $1.2 \cdot 10^4$, $1.0 \cdot 10^4$ $\text{erg s}^{-1} \text{ cm}^{-2} \text{ sr}^{-1}$ for K and H. The ratio of K to H intensities varies from 1.3 (FPO) to 1.5 (LPO) (± 0.02). It indicates a rather high saturation of both lines. Neglecting a possible opacity effect, and assuming a temperature of 8000°K, the NTV computed from K and H lines would be about 12.6 km s^{-1} (FPO), and 10 km s^{-1} (LPO). Ca II NTV are lower than Mg II NTV by a factor of 2.5. All metallic lines do not show any significant shift of their profile, which is probably due to the integration of many different elements within the field of view. Line of sight macrovelocities also exist and provide non Gaussian profiles. This is especially clear on Mg profiles (FPO) where two or three components are necessary to fit the observed profile. However Ca II

profiles are rather narrow as compared to the Mg II profiles (see the computed NTV : about 30 km/s for Mg II, 12 km/s for Ca II). But the lines ratio (about 1.6 for Mg II, 1.4 for Ca II) seems to indicate a higher saturation of Ca II lines. Such a result was already noticed by Vial et al. (1980) in an active prominence and Vial et al. (1981) in a quiescent prominence. The ratio of $L \alpha$ to Ca K intensities, representative of the ionization degree (Vial et al., 1981) varies from 2.3 (FPO) to 2.4 (LPO).

IV. SPATIAL VARIATIONS OF PROFILES

In order to study the local variations of profiles, the observing mode 2 mentioned in I.b. was used at the same location where typical profiles were recorded (cf. § III) but the 20 arcsec slit moves along a line 17 arcsec long perpendicular to the limb. For Ca II and $L \alpha$ lines, the 17 profiles are averaged at positions where the number of counts is low : we obtain 13 profiles for which the statistics is roughly the same. For Mg II lines, we only build average profiles for the whole area 20×17 (arcsec)². For the $L \beta$ line we compute the 17 integrated intensities (the only information we have). We first discuss the results obtained during one orbit (5019) located between the first images (5018) and the typical profiles discussed above.

a. FIRST SET OF OBSERVATIONS (ORBIT 5019).

We give, in Figure 5, Ca II H and K profiles and the $L \alpha$ profile for 3 positions in the scan : position 1 to 3 (about 20 arcsec above the limb) (Figure 5.a), position 9 (12 arcsec) (Figure 5.b) and position 17 (at about 3 arcsec above the limb) (Figure 5.c).

4. Ca II and Mg II

For Ca II lines we superimpose Gaussian fits. We notice that both profiles exhibit a similar behavior : they are narrower at both edges of the scan (and particularly close to the limb). In the same time, the width of the $L \alpha$ line does not change much but the reversal is maximum at the central position and nearly disappears close to the limb. Such unexplained features were also observed 2 orbits later (5021).

The Gaussian fits to Ca II profiles allowed us to derive the shift of lines (Figure 6.a), their full widths at half maximum (FWHM) (Figure 6.b) and their maximum intensity (Figure 6.c), for every position in the scan. Both (blue) shift and FWHM are maximum at the center of the scan. The shift corresponds to a line-of-sight approaching velocity of about 4 km s^{-1} . The FWHM range between 0.15 \AA and 0.24 \AA , corresponding to non thermal velocities (NTV) of 7 to 11 km s^{-1} . High values (11 km s^{-1}) are found in the central position where typical profiles were recorded (see § III): NTV measured with a larger aperture ($1 \times 40 \text{ (arcsec)}^2$) ranged from 12.6 to 10 km s^{-1} , in good agreement with the present measurements. The lowest values (0.15 \AA) are intermediate between high and low spatial resolution FWHM (0.125 \AA ; 0.170 \AA) found by Engvold *et al.* (1980). K_3 intensity is also maximum at this location, but H_3 grows quite continuously towards the limb.

As far as the Mg II lines are concerned, average profiles (Figure 7) indicate 0.25 \AA (for h) and 0.34 \AA (for k). Neglecting the thermal contribution, we obtain 16 km s^{-1} (h) and 22 km s^{-1} (k) for the NTV. Mg II NTV are about twice the Ca II NTV.

These values are lower than the ones found in the previous section (26 to 34 km s^{-1}) for Mg II. An effect of integration over very

different elements cannot explain it since the scanned area is more than 3 times larger than the area of § III. Moreover the observed profile here is more Gaussian than the profiles of § III.

The integrated intensities were computed and are plotted in Figure 8.a. versus the position in the scan. We notice a brighter structure around position 8 where FP0 profiles (see section III) were obtained. We also computed the ratio of K and H integrated intensities and the same ratio for central intensities. They are plotted in Figure 8.b. Both ratios don't agree exactly, but vary from about 1.3 to 1.65. The lower value corresponds to the position very close to the limb where K and H intensities are low, a feature that will be discussed later on.

ii. $L\alpha$ and $L\beta$

Although peak disymmetries exist, quite all $L\alpha$ profiles show the same features : a reversal with a peak separation of about 0.40 \AA , a FWHM of 0.73 \AA . The variation of the integrated intensity versus the position in the scan is given in Figure 8.a. We notice a steady increase towards the limb that contrasts with the variation of K and H intensities.

The procedure followed for the correction of stray light (see I.c.i.) ensures us that such an increase is not the result of the vicinity of the solar disk. It is a solar feature, possibly due to the contribution of high spicules for instance, but it contaminates the prominence data obtained at the end of the scan. On the contrary, the $L\beta$ intensity is quite constant (within 10%). The ratio of the $L\alpha$ to $L\beta$ intensities shown in Figure 8.c follows the variation of the $L\alpha$ intensity. The $L\alpha$ intensity varies from $2 \cdot 10^4$ to

$2.9 \cdot 10^4 \text{ erg s}^{-1} \text{ cm}^2 \text{ sr}^{-1}$ (0.31 to 0.45 times the disk value). It is lower or equal to the intensity (not corrected for a filling factor) found in § III ($2.9 \cdot 10^4 \text{ erg s}^{-1} \text{ cm}^2 \text{ sr}^{-1}$). The $L \beta$ average intensity is $550 \text{ erg s}^{-1} \text{ cm}^2 \text{ sr}^{-1}$. It is very close to the value found in § III (500) after correction of the filling factor. The ratio of $L \alpha$ to $L \beta$ intensities varies from 34 to 57. It is lower than the ratio found in section III (71) although the observed structure is the same, the only difference being the time separation (one hour and a half) and the spatial resolution. Such a low ratio was found already by Vial *et al.* (1981) in another prominence. The ratio of $L \alpha$ to Ca K intensities is lower than the one found in section III ; it varies from 1.3 to 2.0, an indication that the ionization degree does not change much within the field of view ($17 \times 20 \text{ arcsec}^2$).

b. SECOND SET OF OBSERVATIONS (ORBIT 5021)

The above observations were repeated 3 hours later (orbit 5021) and the same analysis was performed.

c. Ca II and Mg II

The variations of Ca II lines shifts and FWHM are given in Figure 9.a and 9.b. Both quantities decrease towards the limb : the (blue) shift varies from 0.1 to 0.04 \AA , the derived line-of-sight velocities being 8 to 3 km s^{-1} . The FWHM vary from about 0.25 to 0.1 \AA . As for the previous observations, the maximum shift corresponds

to the maximum FWHM. We give in Figure 9.c, the run of central intensities K_3 , H_3 versus the position. When we compare with Figure 6.c, we notice a larger variation of both quantities (more than a factor 2). Maximum values are quite the same as in Figure 6.c, but minimum values are much lower. They are also found at the beginning of the scan, where now, FWHM and shifts are maximum. In this respect, they remind similar observations by Engvold and Malville (1977).

ii. $L \alpha$ and $L \beta$

The absolute intensities of K, H and $L \alpha$ lines are plotted in Figure 10.a. As in Figure 8.a, the $L \alpha$ intensity increases towards the limb when H and K intensities decrease. As a result, the $L \alpha / Ca K$ ratio increases from 1.6 to 2.6 (close to the limb). The $L \beta$ intensity being quite constant around an average value of $500 \text{ erg s}^{-1} \text{ cm}^{-2} \text{ sr}^{-1}$, the $L \alpha / L \beta$ ratio increases close to the limb (Figure 10.c). The ratio of K and H intensities (K/H) decreases towards the limb : from 1.8 it becomes as low as 1.35 in a region of low H and K emission. The K_3/H_3 ratio has the same behaviour but it is systematically lower than (K/H). The discrepancy is the most noticeable in the region where the emission is minimum, i.e., where line saturation should be negligible.

If we compare results of orbit 5021 with orbit 5019, we immediately notice some differences (Figures 6.c and 9.c, for instance) that result from morphological changes with time (since solar rotation is negligible within 3 hours). But, most other features are quite

similar in both observations, namely : the correlation between FWHM and shift of Ca II lines, the increase of $L \alpha / \text{Ca K}$, $L \alpha / L \beta$ ratios towards the limb, the decrease of K/H towards the limb and some systematic discrepancy between K/H and K_3/H_3 in low emission regions.

V. DISCUSSION

a. METALLIC LINES

In spite of a moderate spatial resolution, our Ca II observations confirm previous results obtained in the same lines :

1) We find no reversed profile. It indicates that the opacity in K (and H) line is low. A rough computation with a simple geometrical model leads to the same conclusion : let us take a layer 5 Mm thick, at low temperature ($\sim 8000^\circ\text{K}$), with a uniform electron density of $2 \cdot 10^{10} \text{ cm}^{-3}$; if we take the ratio $\frac{n_p}{n_1}$ (proton density/neutral hydrogen density) as a parameter varying from 1 to 10 (Hirayama, 1978), we obtain a K_3 opacity in the range (3,16).

2) Our measured FWHM agree with previous measurements with the same spatial resolution (see e.g. Engvold et al., 1980). We corrected the FWHM for the optical opacity in K and H lines (see § V.a.5) with the following formula giving the Doppler width :

$$\Delta\lambda_{D_{\text{true}}} = \frac{1}{2} \times \text{FWHM}_{\text{measured}} \times \left(\log \left(\frac{\tau_o}{\log \frac{2}{1+e^{-\tau_o}}} \right) \right)^{-1/2}$$

where τ_o is the
central line
opacity

The derived NTV (5 to 9 km s⁻¹) are upper limits if we follow the conclusions of Engvold et al. (1980). However, they agree with most values found in quiescent prominences (e.g. Tandberg-Hanssen's "Solar Prominences", p. 16, 1974, and more recently Mouradian and Leroy (1977), Landman (1980)).

3) Line shifts are small, and derived line-of-sight velocities reach only 8 km s⁻¹ at the edges of the prominence (see Section II). Engvold et al. (1978) found much higher velocities (30-40 km s⁻¹) with a better spatial resolution than ours (5x10 arcsec)². We notice for both scans a correlation between shift and FWHM : it may indicate that large FWHM are due to the line of sight integration of macrovelocities larger than the measured shift.

4) Integrated intensities. They account for about 10% of the absolute chromospheric intensity from K_{1v}(H_{1v}) to K_{1r}(H_{1r}). If we examine the central intensities we find about 20% of the chromospheric central intensity for K₃ and 15% for H₃. Both central and absolute intensities are lower than the chromospheric intensities multiplied by the dilution factor (~ 0.3). Such results have been found previously (Mouradian and Leroy (1977)), Landman and Illing (1977), Landman et al. (1978) but our measurements lie (up to a factor 10) above the mentioned intensities. They are close to computations of Ishizawa (1971) and observations of Engvold (1978, 1980).

5) The ratio of K to H integrated intensities varies (with time and position) from 1.8 to 1.3. Typical values are about 1.5 (± 0.02) and indicate some saturation. However, profiles are not reversed. The ratio for K to H central intensities varies from 1.5 to 1.2 and is always lower than the ratio of absolute intensities, which is a further indication of some saturation. The computation of :

$$\frac{\int_0^{\tau_0^K} S(\tau) e^{-\tau} d\tau}{\int_0^{\tau_0^H} S(\tau) e^{-\tau} d\tau} = 1.4, (\pm 0.03) \text{ with the assumption of K and H having quite}$$

the same constant source function (which is valid if the radial opacity is not too high) leads to $\tau_0^K = 1.8 (-0.1, +0.2)$ (and $\tau_0^H = 0.9$).

Computations of Ishizawa (his Figure 5) indicate that the K optical opacity is in the range 3-10 for K/H equal to 1.5 whatever the electron density (in the range $10^{10} - 10^{12} \text{ cm}^{-3}$) and the electron temperatures (4000 to 20 000°K). With typical values of 10^{10} cm^{-3} for the electron density, Ishizawa's computations give $T_K \lesssim 4$, that is $\tau_0^K \lesssim 2.2$, in good agreement with our computation. In any case, we do not find the high opacities quoted in the literature (Morozhenko, 1974).

Our Mg II observations cannot be compared with previous ones, except for an active prominence (Vial et al. 1979), and a quiescent prominence (Vial et al. 1981). We firstly notice some departure of the profile from a Gaussian shape that we could explain by the spatial integration over many structures. However, the Ca II profiles do not show such a strong departure. Lines profiles for both ions are still different, as far as widths are concerned. For all positions in the structure, we have Mg II lines larger than Ca II lines, a result found already in paper III. The FWHM range from 0.25 \AA to 0.50 \AA , instead of 0.40 \AA in the whole prominence of Paper III. The resulting NTV are about twice the NTV derived from Ca II lines. Such a discrepancy could result from a higher opacity of Mg II lines, due essentially to a higher abundance of Mg atoms. However, the ratio of k to h absolute intensities is higher than the same ratio for Ca II resonance lines. The absolute

intensities (2.4 to $3.5 \cdot 10^5 \text{ erg s}^{-1} \text{ cm}^{-2}$ for k , 1.5 to $1.9 \cdot 10^5 \text{ erg s}^{-1} \text{ cm}^{-2}$ for h) are in good agreement with Paper III. But the ratio k/h is about 1.6 , (± 0.19) a value systematically higher than the average value for Ca II (1.4) (± 0.02). For k/h the accuracy of this determination is poor (but better than 12%) and allows for a ratio equal to the Ca II one. However such a result was already found with a better statistics in active (Paper I) and quiescent (Paper III) prominences. We think that $k/h > K/H$ is a typical feature of prominences that needs a physical explanation. Vial *et al.* (1979, 1980) suggested a special temperature distribution (preventing the existence of Mg^+ ions) or radial velocities. However, the ionization potentials of Ca, Mg atoms, and Ca^+ , Mg^+ ions are close enough to rule out a temperature effect. Radial velocities have been investigated (results will be given in a forthcoming paper) but have a negligible effect. We propose below another explanation.

Let us take a simple prominence model (see above). The ratio of the incident radiation (at the line wavelength) to the internal thermal radiation is about 10^3 for Mg II lines and 300 for Ca II lines. Consequently the source function (and the emergent intensity) is fully determined by the incident radiation. It happens that the incident (chromospheric) radiation is about the same for K and H lines, while it is in a ratio 1.3 for k and h lines. Of course, we should take into account the fact that because of the radial opacity, the incident radiation does not penetrate directly. However, the fact that the ratio of incident k and h intensities is higher than the same ratio for Ca II lines contributes to the "inversed" ratio observed in prominences.

$$\text{For Mg II lines, the measured ratio } \frac{k_3}{h_3} = \frac{\int_0^{\tau_0^k} S_k(\tau) e^{-\tau} d\tau}{\int_0^{\tau_0^h} S_h(\tau) e^{-\tau} d\tau} \text{ is } 1.5 (\pm 0.3)$$

We assume $\frac{I_{k3}^{\text{chrom}}}{I_{h3}^{\text{chrom}}} = \frac{S(k)}{S(h)} = 1.135$ (See Kohl and Parkinson (1976) for

chromospheric values). With the same procedure as above (for Ca II), we derive $\tau_o^k = 2.3 (\pm 1)$ (and $\tau_o^h = 1.15$). If we compare τ_o^k with τ_o^K (Ca II K opacity), we can compute the ratio of Mg II to Ca II ions populations in the ground level. We find a value 8 times lower than the ratio of abundances. This result can be compared with the impossibility of matching Mg II and Ca II lines for the establishment of a chromospheric model (Lemaire et al., 1981).

b. HYDROGEN LINES

The $L \alpha$ of hydrogen was observed in an active prominence (Vial et al., 1979) and in a quiescent prominence (Vial et al., 1981). It was found reversed in a quiescent prominence, with a minimum peak to peak distance of about 0.3 \AA . We confirm this observation but we now have the full profiles. The peak distance does not vary much around $0.35\text{--}0.40 \text{ \AA}$ (the chromospheric value). Smaller reversals (or no reversal at all) are observed in low intensity regions, a fact that explains why our typical $L \alpha$ profile (section III) measured with a long slit is narrower than the other ones. The intensity ranges from $2 \cdot 10^4$ to $3 \cdot 10^4 \text{ erg s}^{-1} \text{ cm}^{-2} \text{ sr}^{-1}$, that is 0.3 to 0.5 times the incident chromospheric intensity. It confirms that the radiation transfer is dominated by the scattering of chromospheric $L \alpha$ photons. The radial opacity is certainly very high and the source function will increase beyond the incident intensity. It explains why the intensity may be higher

than 0.4 times the chromospheric intensity (and also the extension of the prominence in the $L\alpha$, $L\beta$ lines). Such features were noticed in $L\alpha$ spectroheliograms of Bonnet et al. (1980). But these spectroheliograms also show low opacity threads within prominences. Such threads cannot be detected with OSO-8 because the large entrance slit allows bright structures to dominate all other ones.

The $L\beta$ line reversal (0.33 \AA) also reflects the chromospheric reversal. The intensity is about 0.6 the chromospheric intensity ; such a high value of the source function is made possible by the large opacity in the line. This is no surprise, since we found a large $L\alpha$ opacity and the ratio of $L\beta$ to $L\alpha$ opacities is about 0.2. The average $L\alpha/L\beta$ ratio is slightly lower than the chromospheric one. Such a ratio may even reach half the chromospheric value, in upper boundary regions. Without detailed computation, we can explain this feature by the importance of the $H\alpha$ radiation in the statistical equilibrium of level 3. Upper edges may receive a lower $L\alpha$ incident radiation, while the $H\alpha$ line is not thick. It can depopulate the $n = 2$ level (which may be a marginal effect in view of the importance of $L\alpha$ radiation) and it overpopulates the $n = 3$ level, which can enhance the $L\beta$ source function. Detailed computations are postponed for a further paper.

c. $L\alpha$ AND $Ca K$ INTENSITIES AND THE IONIZATION

The $L\alpha$ and $Ca II$ intensities give important information on the ionization of the emitting plasma. We demonstrate this result in a crude way in the Appendix where we find $\frac{n_p}{n_1} \approx 3.4$ (within a factor 3). The ionization does not change much because it is dominated by the incident

Lyman continuum (Hirayama, 1963). However, our average value for $\frac{n_p}{n_1}$ (~ 3) although well within the range (1,10) predicted by Hirayama (1978) is larger than the recent results of Orrall and Schmahl (1980) and Kanno et al. (1980). These authors use the Ly continuum intensities to derive the ionization and obtain $\frac{n_p}{n_1} \lesssim 1$ (O.S) and $\frac{n_p}{n_1} \lesssim 1.9$ (K et al.) for electron densities notably higher than ours. It is difficult to interpret such a discrepancy since the observed prominences are all different objects, viewed under different angles. Our method relies on many assumptions including a constant source function in the K line (i.e. a full penetration of the chromospheric radiation), the constancy of $\frac{n_e^2}{n_2}$ (and its value) and the thickness of the layer (see the Appendix). Since $(\frac{n_p}{n_1})^2$ is proportional to the thickness, a reduction of this parameter by a factor 4 leads to a $\frac{n_p}{n_1}$ ratio in the range 1 to 2.

We conclude that our derived ionization degree tends to be higher than the one given by Orrall and Schmahl (1980), Kanno et al. (1980) but the disagreement is well within the uncertainties associated with the observations and the assumptions used in the computation. Another interesting feature is the quite constancy of the ionization degree within our field of view. This was already noticed by Kureizumi et al. (1977) in a loop prominence. This can be interpreted as the result of a complete penetration of the Lyman continuum chromospheric radiation because of an important fragmentation of the prominence into threads or loops. However, in this picture, the $L \alpha$ intensity should be reduced in proportion to the void between the structures, which is not observed since the $L \alpha$ intensity is equal to the incident intensity multiplied by the dilution factor. Only a full treatment of the radiative scattering from small and numerous structures, can give an answer to this question.

VI. CONCLUSION

From the first set of simultaneous measurements of (H I) L α and L β , (Ca II) K and H, (Mg II) k and h lines, in a quiescent prominence we select the main following features :

1) The resonance lines of Ca II have a low opacity : the optical thickness at the center of the K line varies from 1.4 to 3.2. We do not observe reversed profiles as Kubota (1980) did. Non thermal velocities range from 5 to 9 km s⁻¹ in good agreement with Landman et al. (1977). Line shifts are small but significant at the edges (8 km s⁻¹). A good correlation between FWHM and shifts is observed. Intensities are lower than the incident radiation field (corrected by the dilution factor), but are high enough to be in the range of Ishizawa's computations and Engvold's observations.

2) The resonance lines of Mg II, measured in the whole prominence, depart from Gaussian profiles. The profiles are much broader than corresponding Ca II ones, a feature we cannot explain. The observed Mg II and Ca II "inversed" intensity ratios may be a consequence of the different incident intensities ratios.

3) The L α and L β lines of H I have the same reversals as the chromospheric lines, at least in bright regions. Unreversed profiles may be observed in darker regions. The intensities are larger than the diluted incident radiation. The opacity is very high and reaches values of about 10⁵, as in Paper I. The L α /L β ratio is lower than the chromospheric one but we do not confirm the very low limit found in Paper III. The comparison of L α and Ca II intensities leads to a ionization degree $\frac{n_p}{n_1}$ of about 3.4 (with a large uncertainty factor of 3) a value slightly higher than

most recent computations (1 to 2) and quite constant through a region 17×20 (arcsec)². We conclude that it is an indication of a full penetration of the Lyman continuum radiation through a region composed of many small structures.

ACKNOWLEDGEMENTS

The L.P.S.P. experiment on board NASA/OSO-8 spacecraft was funded by CNES (Centre National d'Etudes Spatiales). Computations have been performed on CNES computer in Toulouse.

The author thanks the many L.P.S.P. members involved in the OSO-8 program, Mrs J. SALM-PLATZER for her help in data reduction, Ms A. TALBOT for typing the manuscript. The comments of the anonymous referee were useful for improving the paper.

APPENDIX

Firstly, the monochromatic L α intensity $I(\lambda)$ is a measure of $\frac{n_2}{n_1}$ (where n_1, n_2 are the neutral hydrogen populations in levels 1 and 2) at the depth where $\tau_\lambda = 1$ is verified. For a very large line opacity, the integrated L α intensity is given by :

$$I(L \alpha) (\text{erg s}^{-1} \text{ cm}^{-2} \text{ sr}^{-1} \text{ Hz}^{-1}) = 0.055 < \frac{n_2}{n_1} > \quad (1)$$

where $< \frac{n_2}{n_1} >$ is the value of $\frac{n_2}{n_1}$ averaged on that part of the line-of-sight where the opacity is lower than 1. So we have

$$< \frac{n_2}{n_1} > = 8.9 \cdot 10^{-12} I(L \alpha) (\text{erg s}^{-1} \text{ cm}^{-2} \text{ sr}^{-1} \text{ \AA}^{-1}) \quad (2)$$

Secondly, we establish that the Ca II population is proportional to the neutral hydrogen density. This is typical of metallic ions whose further ionization potential is close to the hydrogen potential. Hirayama (1978) derives :

$$n(\text{Ca II}) = A n(\text{H I}) \quad (3)$$

where A is the Ca abundance relative to hydrogen. But relation (3) is verified only if :

$$\frac{n(\text{Ca II})}{n(\text{Ca III})} = \frac{n_1}{n_p} \quad (4)$$

where n_p is the proton density. Let us compute both sides of relation (4). We assume that Ca is in the first or second ionization states only, which is valid for prominence temperatures. We also assume that the ionization of Ca II and H I is dominated by the incident Lyman continuum which penetrates equally in the prominence at both ionization edges (but not necessarily fully). The balance between photoionization and radiative recombination rates leads to :

$$\frac{n(\text{Ca II})}{n(\text{Ca III})} / \frac{n_1}{n_p} = \left(\frac{n(\text{Ca II})}{n(\text{Ca III})} \right)^* / \left(\frac{n_1}{n_p} \right)^* \frac{B_{1045}(T_e)}{B_{1045}(T_{\text{rad}})} \frac{B_{912}(T_{\text{rad}})}{B_{912}(T_e)} \quad (5)$$

where the subscript (*) refers to L.T.E. values, T_{rad} is the radiation temperature of the incident radiation and 1045,912 note the wavelengths for the Planck functions. We adopt 6500 and 5500 K for T_{rad} at 912 and 1045 Å respectively, and 8.10^3 K for T_e . We obtain :

$$\frac{n(\text{Ca II})}{n(\text{Ca III})} / \frac{n_1}{n_p} \sim 3.2 \quad (6)$$

Instead of (3), we now have :

$$n(\text{Ca II}) = A \times \frac{3 n_H}{2 + \frac{n_H}{n_1}} \quad (7)$$

where n_H is the total hydrogen population. When $\frac{n_H}{n_1}$ varies (from one to infinity), $n(\text{Ca II})$ varies from An_H ($=An_1$) to $3An_1$. The Ca II population is proportional to the neutral hydrogen population and we adopt :

$$n_{\text{Ca II}} = \pi.A.n_1 \quad (8)$$

with $\pi = 2 (\pm 1)$

Thirdly, the Ca II resonance lines intensities are proportional to the level 1 populations (along the line-of-sight). If the K line is optically thin, we have $I(K) = w I_0 \tau_0^K \sqrt{\pi} \Delta\lambda_D$ (9) where w is the dilution factor, I_0 the incident chromospheric intensity and $\Delta\lambda_D$ the Doppler width. Since τ_0^K is proportional to the Ca II population related to n_1 by (8), we have established that K(and H) intensities are proportional to the neutral hydrogen population.

Fourthly, we now admit that the quantity $\frac{n_e^2}{n_2}$ (the ratio of the emission measure to the Balmer continuum) does not change much with the temperature, the pressure and the total mass in the line-of-sight (Hirayama, 1978).

Poland et al. (1974) give $\frac{n_e^2}{n_2} \sim 1.6 \cdot 10^{17} \text{ (cm}^{-3}\text{)}$. Heasley and Mihalas computations (1976) vary from 1 to $3 \cdot 10^{17} \text{ (cm}^{-3}\text{)}$. We adopt recent values of Landman and Mongillo (1979) : $0.3 \cdot 10^{17} \text{ (cm}^{-3}\text{)}$ at $8 \cdot 10^3 \text{ K}$. Assuming $\langle \frac{n_2}{n_1} \rangle = \frac{\langle n_2 \rangle}{\langle n_1 \rangle}$ and $\langle n_1 \rangle^2 = \langle n_1^2 \rangle$ (where brackets indicate an average along the line-of-sight) we get :

$$\frac{\langle n_2 \rangle}{\langle n_1 \rangle} = \frac{\langle n_e^2 \rangle}{0.3 \cdot 10^{17} \langle n_1 \rangle} \quad \text{and taking account of (2), (8) and (9),}$$

$\frac{\langle n_e^2 \rangle}{\langle n_1^2 \rangle} \sim \frac{I(L \alpha)}{I(Ca K)}$: At this step, we have justified that the ratio of $L \alpha$ to $Ca K$ intensities is proportional to the square of the ionization degree.

For the actual computation, we rely on the K_3/H_3 ratio from which we derive τ_o^K (~ 1.8) with the only assumption that both K and H source functions are constant and equal. We have $\tau_o^K = \langle n_1(Ca II) \rangle k_o X$ (10)

$$\text{where } k_o = \frac{g_2}{g_1} \frac{\lambda^2}{8\pi\sqrt{\pi}} A_{21} \frac{1}{\Delta\nu_D} \quad (11)$$

with all quantities with the usual meaning.

The corrected Doppler width $\Delta\lambda_D$ is 90 m\AA , so $\Delta\nu_D = 1.7 \cdot 10^{10} \text{ s}^{-1}$. From (10) and (11), we derive $\langle n_1(Ca II) \rangle X = 1.6 \cdot 10^{12} \text{ cm}^{-2}$. If we assume a typical thickness of 5 Mm , we get $\langle n_1(Ca II) \rangle = 3.2 \cdot 10^3 \text{ cm}^{-3}$. With an average measured $L \alpha$ intensity of $3.0 \cdot 10^4 \text{ erg s}^{-1} \text{ cm}^{-1} \text{ sr}^{-1} \text{ \AA}^{-1}$, we obtain $n_1 = 1.25 \cdot 10^{-10} n_e^2$. We rearrange (7) with the computed value of $n_1(Ca II)$ and $n_H = n_1 + n_e$, the resulting equation is of degree 3 in n_e . It has only one positive solution : $n_e = 2.3 \cdot 10^9 \text{ cm}^{-3}$. So we have $n_1 = 6.7 \cdot 10^8 \text{ cm}^{-3}$ and $n_e/n_1 = 3.4$. With these values, the n factor in (8) is 2.08, which justifies our derivation.

It is necessary to evaluate the weight of the many assumptions made in our calculations.

We first have uncertainties deriving from our measurements : about 7% for the L α intensity, 2.2% for the Ca K intensity, 2% for K_3/H_3 , and a few percent for $\Delta\lambda_D$. We also have simplifications made in our computations : relation (5) derives from the balance between photoionization and radiative recombination rates, computed at the head of the continuum. A more detailed computation, taking into account the ν^{-3} dependance of the absorption coefficient, leads to the same relation (5) modified by a factor equal to $T_{\text{rad}}(912 \text{ \AA})/T_{\text{rad}}(1045 \text{ \AA})$, less than 1.2. But the main uncertainties derive from the external parameters : the thickness X of the layer and the ratio n_e^2/n_2 . Our adopted value of $n_e^2/n_2 (0.3 \cdot 10^{17} \text{ cm}^{-3})$ is low as compared to previous determinations : if we multiply it by 5 we obtain $n_e/n_1 = 8.5$. If we also multiply the thickness of the layer by a factor 10 ($X : 50\,000 \text{ km}$) we get $n_e/n_1 = 12$. Dividing it by 10 ($X = 500 \text{ km}$) leads to $n_e/n_1 = 0.9$. So, the ionization degree roughly behaves as the square root of the two unknown parameters (X and n_e^2/n_2). As a consequence, our derivation of the ionization degree (3.4) is valid within a large factor (about 3). But it is interesting to note that the possible range (about 0.9 to 12) is very comparable to the range of values given by Hirayama (1978).

Moreover from the variations of the ratio L α /Ca K, we can derive the (relative) variations of the ionization degree. The spatial scans obtained at orbits 5019 and 5021 show that the overall variation of L α /Ca K is within a factor 2 : consequently, the variation of the ionization degree is smaller than a factor 1.4.

TABLE 1

Parameters of typical prominence profiles
of L β , L α , Mg II and Ca II lines.

	Ca H	Ca K	Mg h	Mg k	L α	L β
<u>F.P.O.</u> (First Part of Orbit)						
FWHM (\AA)	0.27	0.29	0.53	0.53	0.72	0.61
Peak to peak distance (\AA)					0.37	0.33
Intensity ($\times 10^3$) ($\text{erg s}^{-1} \text{cm}^{-2} \text{sr}^{-1}$)	9.5 (± 0.25)	12.6 (± 0.3)	15.5 (± 2.2)	24.6 (± 2.1)	28.4 ($\pm 2.$)	0.44 (± 0.04)
I (corrected for filling factor) ($\times 10^3$)	11.8 (± 0.3)	15.7 (± 0.35)	19.3 (± 2.8)	30.8 (± 2.6)	35.5 (± 2.5)	0.55 (± 0.05)
<u>L.P.O.</u> (Last Part of Orbit)						
FWHM (\AA)	0.21	0.23	0.40	0.39	0.70	0.56
Peak to peak distance (\AA)					0.35	0.30
Intensity ($\times 10^3$) ($\text{erg s}^{-1} \text{cm}^{-2} \text{sr}^{-1}$)	8.1 (± 0.2)	11.9 (± 0.25)	14.0 ($\pm 2.$)	22.5 (± 1.9)	28.8 ($\pm 2.$)	0.37 (± 0.03)
I (corrected for filling factor) ($\times 10^3$)	10.1 (± 0.3)	14.9 (± 0.3)	17.6 (± 2.6)	28.1 (± 2.4)	36.0 (± 2.5)	0.46 (± 0.04)

REFERENCES

- Artzner, G., Bonnet, R.M., Lemaire, P., Vial, J.C., Jouchoux, A., Leibacher, J., Vidal-Madjar, A., and Vite, M., 1977, *Space Science Instrumentation*, 3, 131.
- Basri, G.B., Linsky, J.L., Bartoe, J.-D.F., Brueckner, G., and Van Hoosier M.E., 1979, *Ap. J.*, 230, 924.
- Bonnet, R.M., 1981, *Space Science Instrumentation*, in preparation.
- Bonnet, R.M., Lemaire, P., Vial, J.C., Artzner, G., Gouttebroze, P., Jouchoux, A., Leibacher, J., Skumanich, A., and Vidal-Madjar, A., 1978, *Ap. J.*, 221, 1032.
- Bonnet, R.M., Bruner, E.C., Jr., Acton, L.W., Brown, W.A., and Decaudin, M., 1980, *Ap.J.*, 237, L 47.
- Brault, J. and White, O.R., : 1971, *Astron. Astrophys.*, 13, 169.
- Engvold, O., : 1976, *Solar Phys.* 49, 283.
- Engvold, O., : 1978, *Solar Phys.* 56, 87.
- Engvold, O., : 1980, private communication.
- Engvold, O., and Malville, J.M., 1977, *Solar Phys.*, 52, 369.
- Engvold, O., Malville, J.M., and Livingston, W., 1978, *Solar Phys.*, 60, 57.
- Engvold, O., Wiehr, E. and Wittmann, A., 1980, *Astron. Astrophys.*, 85, 326.

- Heasley, J.N. and Milkey, R.W. : 1978, *Ap. J.*, 221, 677.
- Hirayama, T., 1963, *Publ. Astron. Soc. Japan*, 15, 122.
- Hirayama, T., 1978, in "*Physics of Solar Prominences*" (I.A.U. Colloquium 44). Jensen, Maltby, Orrall, eds, D. Reidel. Publ. Co, Dordrecht, p. 4.
- Illing, R.M.E., Landman, D.A., and Mickey, D.L., : 1975, *Solar Phys.*, 45, 339.
- Ishizawa, T., : 1971, *Publ. A.S. Japan*, 23, 75.
- Kanno, M., Withbroe, G.L., and Noyes, R.W., 1981, *Solar Phys.*, 69, 313.
- Kohl, J.L. and Parkinson, W.H., : 1976, *Ap. J.*, 205, 599.
- Kubota, J., 1980, *Publ. Astron. Soc. Japan*, 32, 359.
- Kureizumi, T., Kubota, J., Tamenaga, T., Maeda, K., Kawaguchi, I., and Kitai, R., 1977, *Publ. Astron. Soc. Japan*, 29, 129.
- Landman, D.A., 1980, *Ap. J.*, 237, 988.
- Landman, D.A. and Illing, R.M.E., : 1977, *Astron. Astrophys.*, 55, 103.
- Landman, D.A., Edberg, S.J. and Laney, C.D., : 1977, *Ap. J.*, 218, 888.
- Landman, D.A., Illing, R.M.E. and Mongillo, M., : 1978, *Ap. J.*, 220, 666.
- Landman, D.A., and Mongillo, M., 1979, *Solar Phys.*, 63, 87.
- Lemaire, P., : 1978, *Orbital Technical Handbook*, Rapport Interne L.P.S.P. T 60.
- Lemaire, P., Gouttebroze, P., Vial, J.C., and Artzner, G.E., 1981, *Astron. Astrophys.*, 103, 160.
- Lemaire, P., Charra, J., Jouchoux, A., Vidal-Madjar, A., Artzner, G.E., Vial, J.C., Bonnet, R.M., and Skumanich, A., 1978, *Ap. J. (Letters)*, 223, L 55.

- Linsky, J.L., 1970, *Solar Phys.*, 11, 355.
- Martres, M.J. and Zlicaric, G., 1976, "Les Cartes synoptiques de la chromosphère solaire et Catalogues de filaments et centres d'activité". (Volume VI, Fascicule 2).
- Mihalas, D., Auer, L.H. and Mihalas, B.R., 1978, *Ap. J.*, 220, 1001.
- Morozhenko, N. : 1974, *Solar Phys.*, 35, 395.
- Mouradian, Z. and Leroy, J.L. : 1977, *Solar Phys.*, 51, 103. .
- Orrall, F.Q., and Schmahl, E.J., 1980, *Ap. J.*, 240, 908.
- Poland, A.I., Skumanich, A., Athay, R.G., Tandberg-Hanssen, E., : 1971, *Solar Phys.*, 18, 391.
- Tandberg-Hanssen, E., 1974, *Solar Prominences*, D. Reidel Publ., Co. Dordrecht, Holland.
- Vernazza, J.E., and Reeves, E.M. : 1978, *Ap. J. Suppl. Ser.* 37, 485.
- Vial, J.C., Gouttebroze, P., Artzner, G., and Lemaire, P., 1979, *Solar Phys.*, 61, 39 (Paper I).
- Vial, J.C., Lemaire, P., Artzner, G., and Gouttebroze, P., 1980, *Solar Phys.*, 68, 187 (Paper II).
- Vial, J.C., Martres, M.J., and Salm-Platzer, J., 1981, *Solar Physics*, 70 , 325 (Paper III).
- Vidal-Madjar, A., and Phissamay, B., 1980, *Solar Phys.*, 66, 259.
- White, O.R., and Livingston, W., 1978, *Ap. J.*, 226, 679.
- White, O.R., and Livingston, W., 1981, *Ap. J.*, 249, 798

FIGURE CAPTIONS

Figure 1.a. : Part of H α spectroheliogram from Culgoora Observatory
(Courtesy, R.A. Duncan, Australian Ionospheric Prediction
Service and Division of Radiophysics, CSIRO) 18 May 1975,
18.58 U.T.

Figure 1.b. : Part of Ca K spectroheliogram from Meudon Observatory
(Courtesy M.J. Martres) 19 May 1975 - 8.10 U.T.

Figure 1.c. : Ca K picture (bandpass = 1 Å) from OSO-8.
Size 2.7 x 2.5 (arcmin)².

Figure 1.c.1. : at 4.00 U.T. (orbit 5018)

Figure 1.c.2. : at 10.00 U.T. (orbit 5022)

Figure 1.d. : L α picture from OSO-8. Same size and observing hours as
Figures 1.c.

Figure 1.d.1. : orbit 5018

Figure 1.d.2. : orbit 5021

Figure 1.e. : L β picture from OSO-8. Same size and observing hours as
Figures 1.c.

Figure 1.e.1. : orbit 5018

Figure 1.e.2. : orbit 5022

Figure 2.a. : Ca K Dopplergram (same size as Figure 1.c).

Figure 2.b.

Figure 2.a.1. (orbit 5018) : The Dopplergram is obtained in subtracting the blue and red parts of the line. Bright regions correspond to a blue shift of the emission line.

Figure 2.b.1. (orbit 5022)

Figure 2.a.2. : For orbit 5018, the Dopplergram represents the shift of the Gaussian fit (for the prominence only); the line represents the position of the K_3 limb (solar disk is on the right).

Figure 2.a.3.



Figure 2.a.2. Dark regions correspond to receding velocities (maximum value 8 km s^{-1}).

Figure 2.a.3. Dark regions correspond to approaching velocities (maximum value 3 km s^{-1})

Figure 2.c. : Spectroheliogram in the O VI line ($\lambda = 1032 \text{ \AA}$).
Orbit 5017 (1.45 to 2.40 U.T.).

Figure 3 : Position size of the entrance slit, in a K_3 (bandpass 0.1 \AA) image.

Hatched box : drift of the $(1 \times 40) \text{ arcsec}^2$ slit

( F.P.O.,  L.P.O.) - Orbit 5022.

White box : area scanned by the $(1 \times 20) \text{ arcsec}^2$ slit - orbit 5022.

- Figure 4 : Typical profiles in the 6 lines (orbit 5020).
Figure 4.a. : corresponds to First Part of Orbit (FPO) profiles.
Figure 4.b. : corresponds to Last Part of Orbit (LPO) profiles. 1,2,...6 are labels for Ca K, Ca H, Mg k, Mg h, L α , L β lines.
- Figure 5 : Profiles of Ca H, Ca K and L α obtained in 3 positions of the spatial scan of orbit 5019 :
Figure 5.a. : 20 arcsec above the limb.
Figure 5.b. : 12 arcsec above the limb.
Figure 5.c. : 3 arcsec above the limb.
 For Ca II profiles, Gaussian fits have been superimposed.
- Figures 6 : Parameters of Ca K and H lines are plotted as functions of the position in the spatial scan (position 1 corresponds to a distance of about 20 arcsec above the limb ; step of one arcsec) - orbit 5019. Ca K (.), Ca H (+).
Figure 6.a. : Shift of the line (\AA).
Figure 6.b. : FWHM (\AA).
Figure 6.c. : Central intensity ($\text{erg s}^{-1} \text{cm}^{-2} \text{sr}^{-1} \text{\AA}^{-1}$)
- Figure 7 : Mg k (Fig. 7.a) and h (Fig. 7.b) profiles averaged over the spatial scan of orbit 5019.

Figure 8 : Variations of different parameters in the spatial scan of orbit 5019.

Figure 8.a. : absolute intensities ($\text{erg s}^{-1} \text{cm}^{-2} \text{sr}^{-1}$) of $L \alpha$ (x), Ca K (.), Ca H (+).

Figure 8.b. : ratio of absolute intensities (K/H : +) and central intensities (K_3/H_3 : x) of Ca II K and H lines.

Figure 8.c. : ratio of $L \alpha$ to $L \beta$ intensities.

Figure 9 : Same parameters as in Figure 6, for orbit 5021.

Figure 10 : Same parameters as in Figure 8, for orbit 5021.



Fig. 1.a.

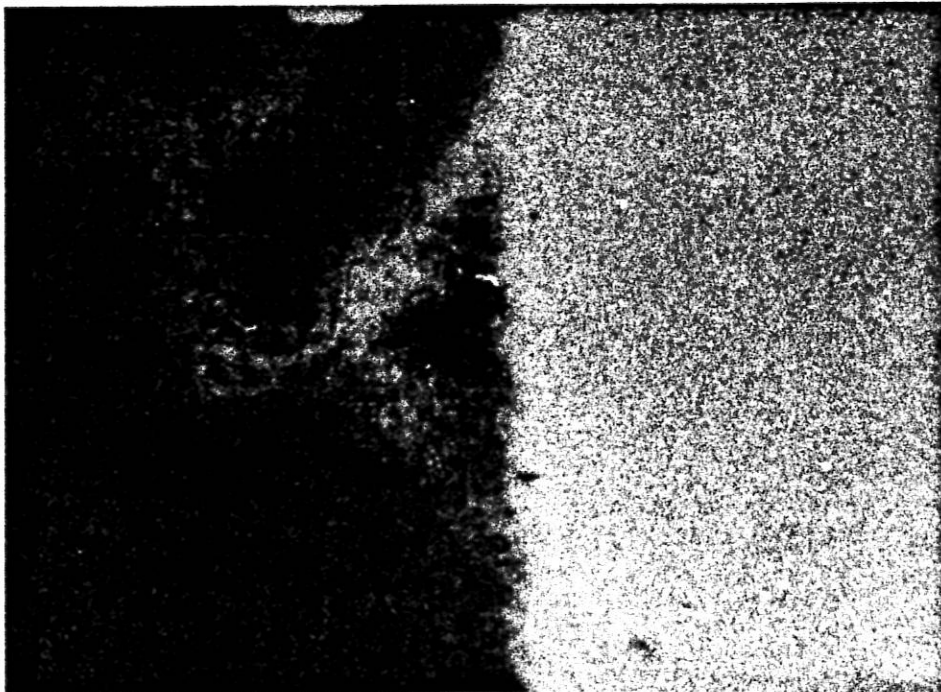


Fig. 1. b.



Fig. 1.c.1.



Fig. 1.c.2.



Fig. 1.d.1.



Fig. 1.d.2.



Fig. 1.e.1.



Fig. 1. e.2.

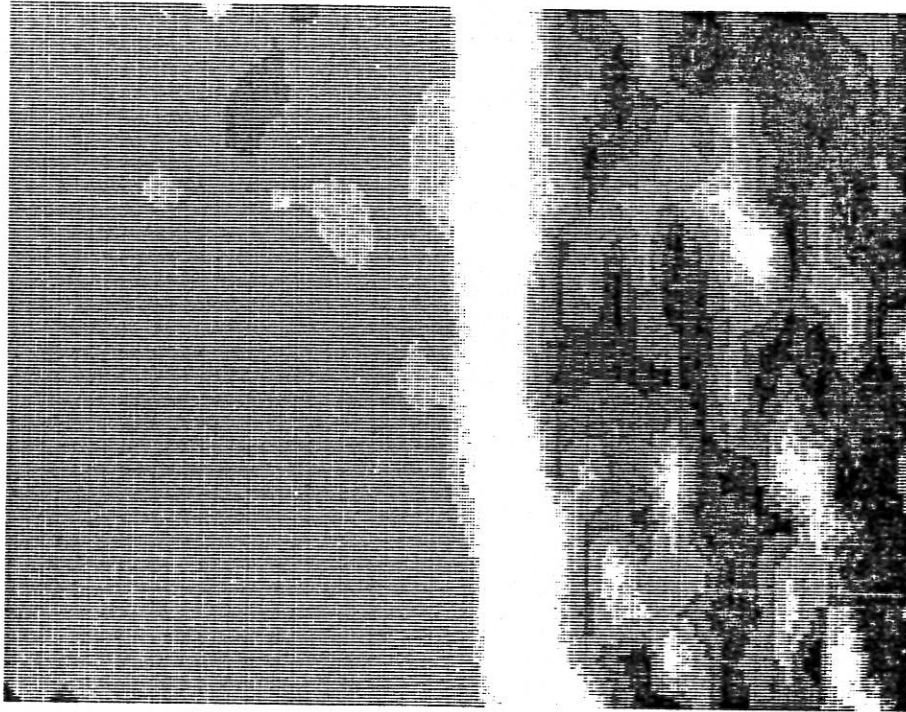


Fig. 2.a.1.

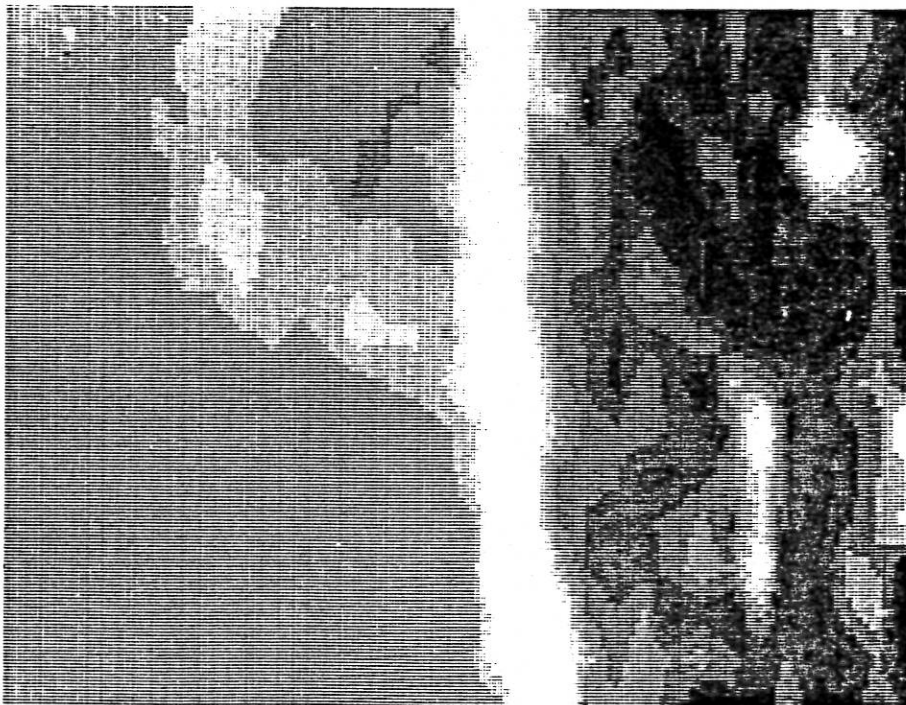


Fig. 2. b.1.

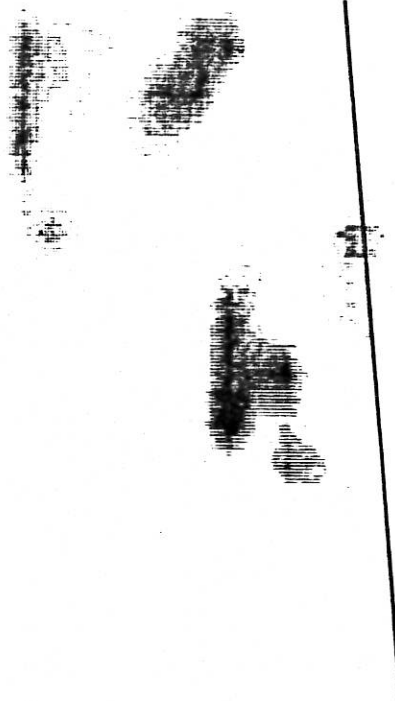


Fig. 2. a.2.

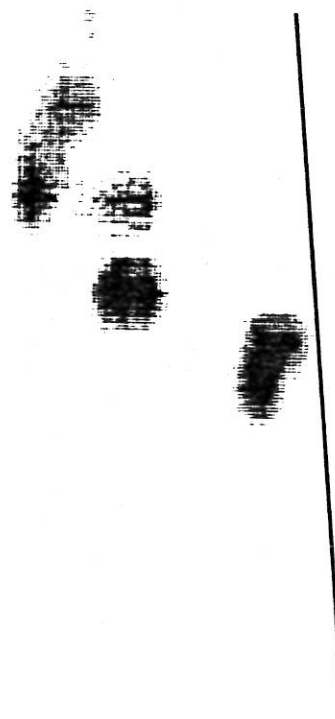


Fig. 2.a.3.

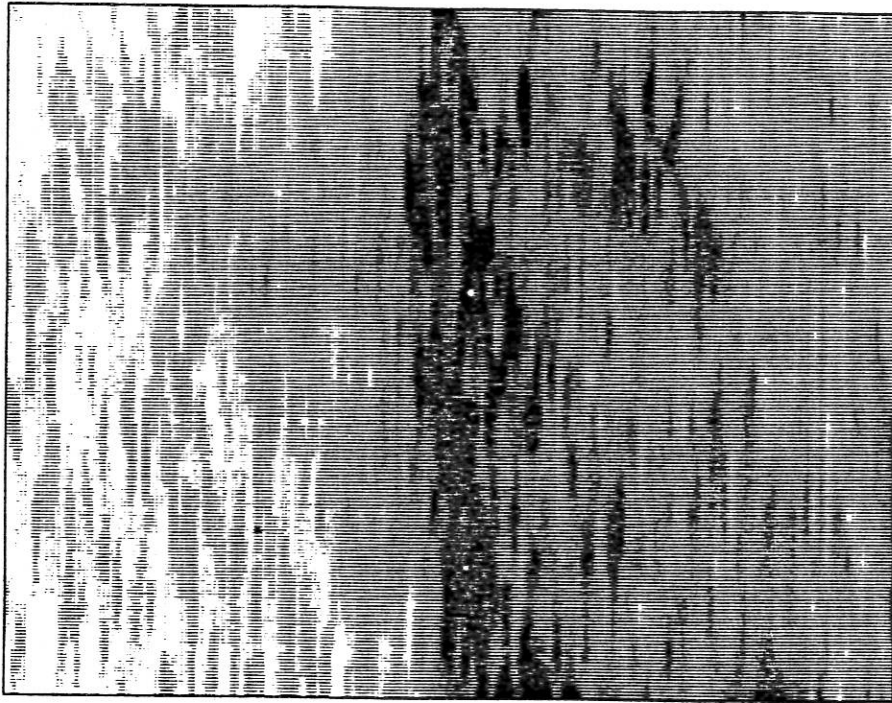


Fig. 2. c.

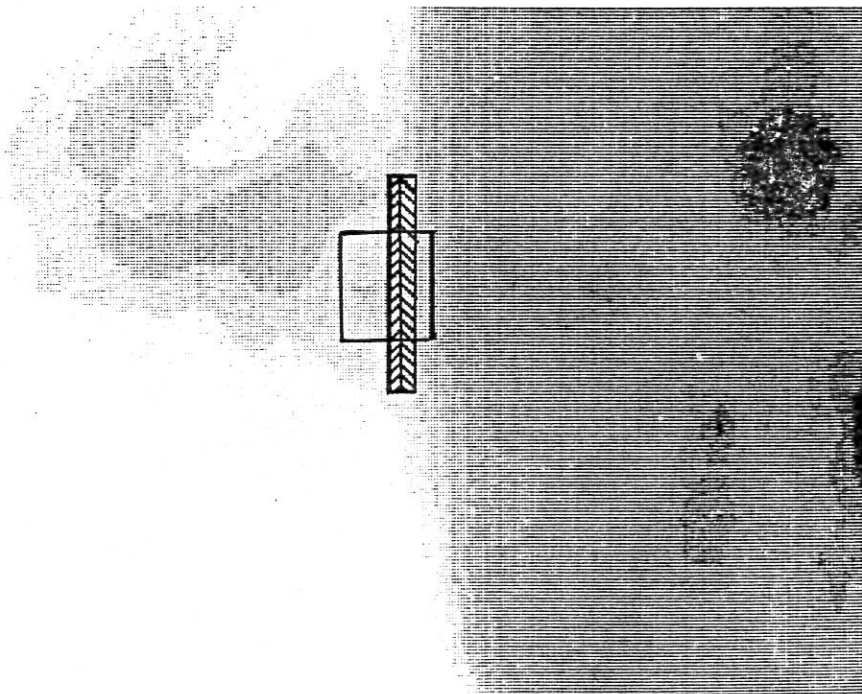
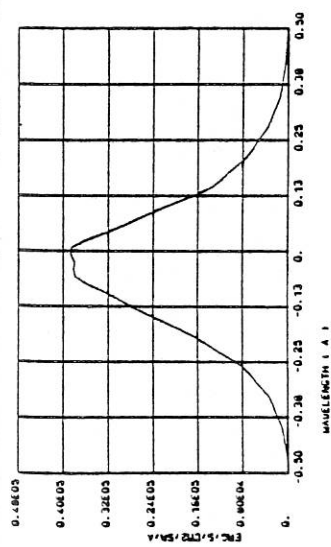
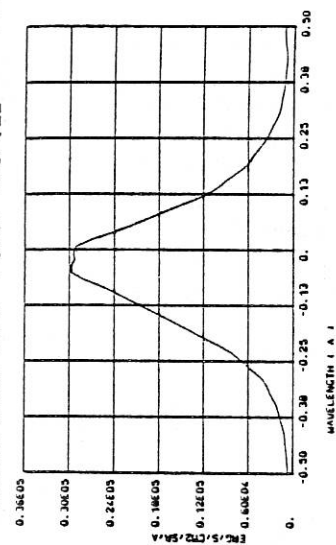


Fig. 3.

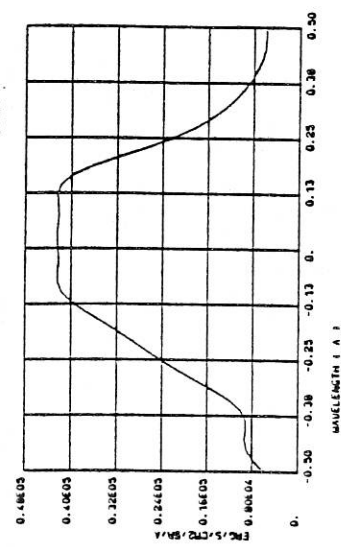
CYCLE 5020 CA K FIRST PROFILE 4.a.1.



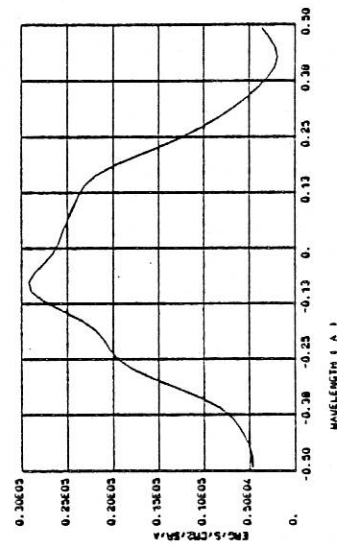
CYCLE 5020 CA H FIRST PROFILE 4.a.2.



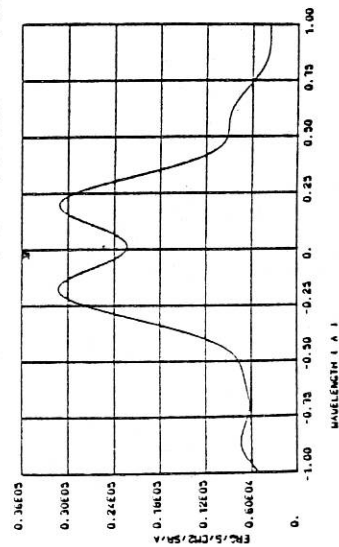
CYCLE 5020 MG K FIRST PROFILE 4.a.3.



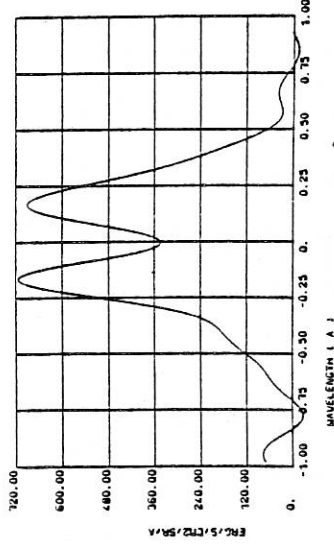
CYCLE 5020 MG H FIRST PROFILE 4.a.4.



CYCLE 5020 LY A FIRST PROFILE 4.a.5.

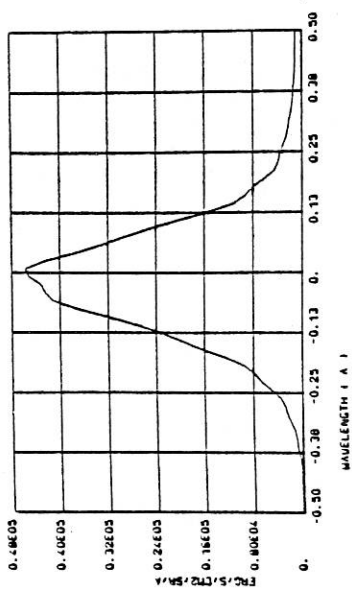


CYCLE 5020 LY B FIRST PROFILE 4.a.6.



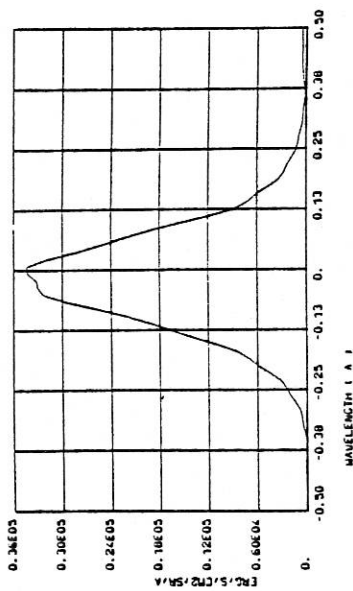
4.b.1.

CYCLE 5020 CA K LAST PROFILE



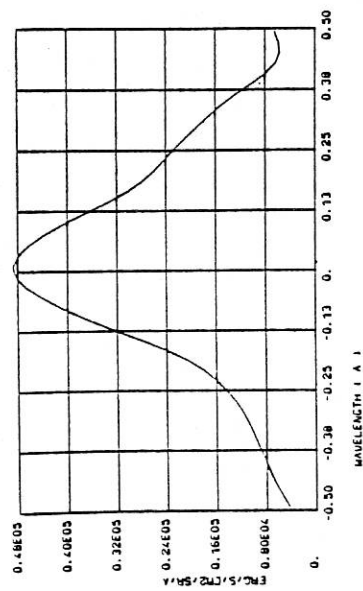
4.b.2.

CYCLE 5020 CA H LAST PROFILE



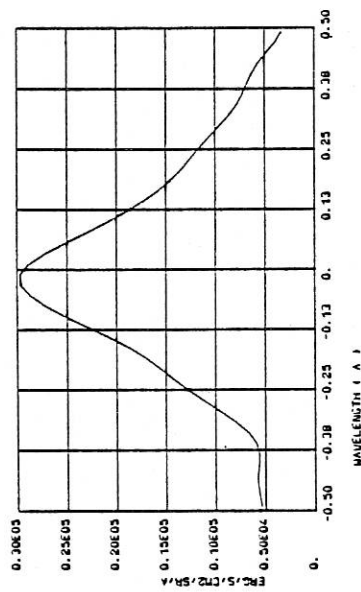
4.b.3.

CYCLE 5020 MG K LAST PROFILE



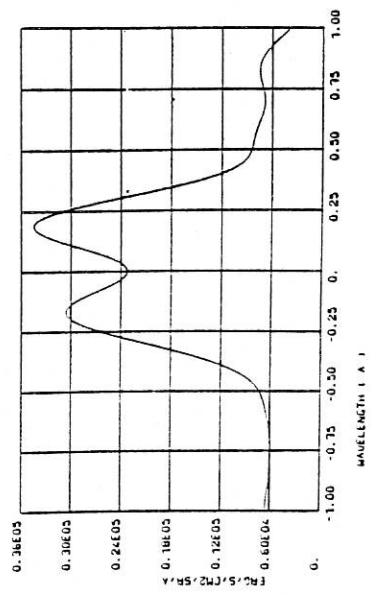
4.b.4.

CYCLE 5020 MG H LAST PROFILE



4.b.5.

CYCLE 5020 LY A LAST PROFILE



4.b.6.

CYCLE 5020 LY B LAST PROFILE

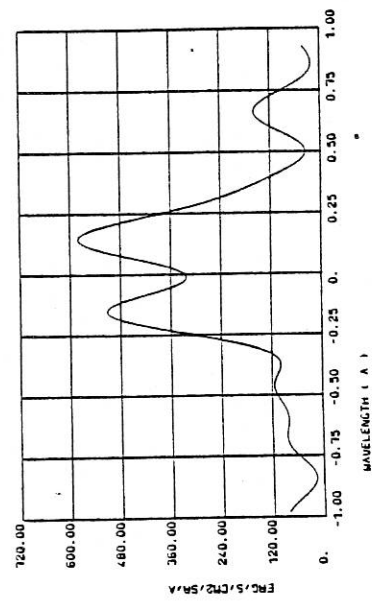


FIG. 5.a.

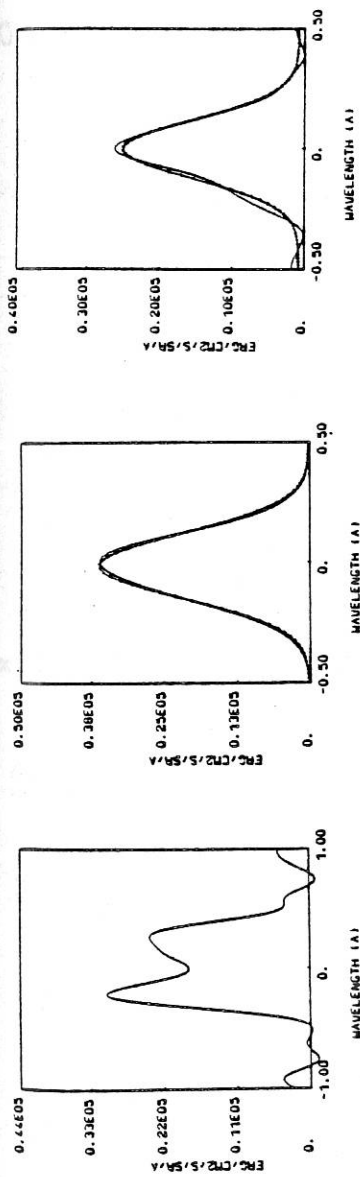


FIG. 5.b.

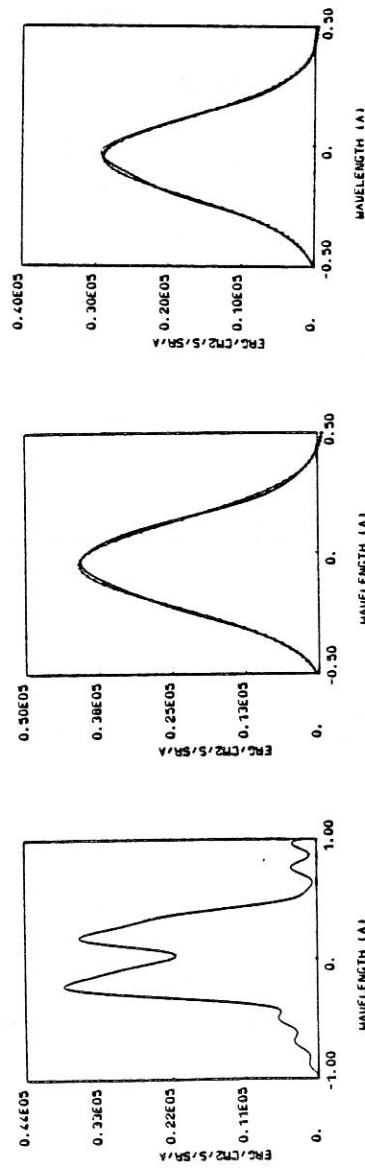
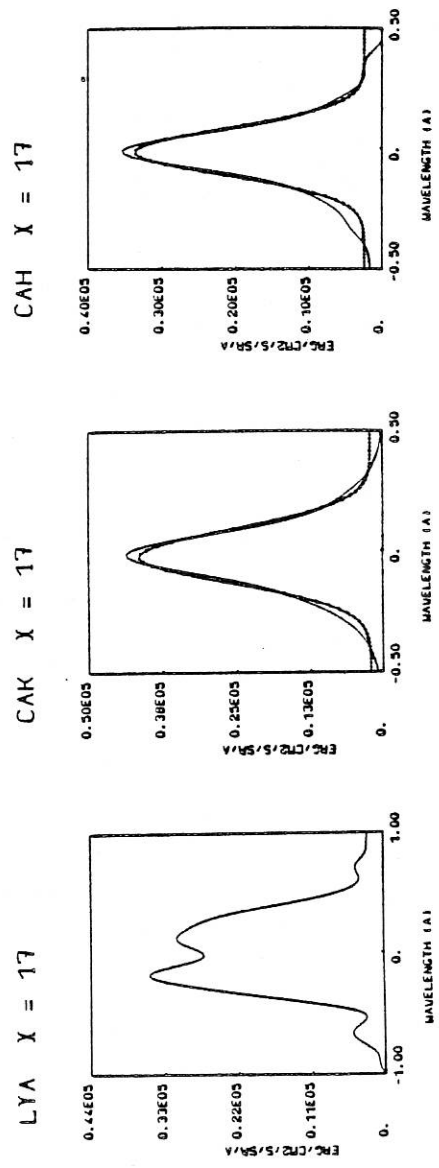


FIG. 5.c.



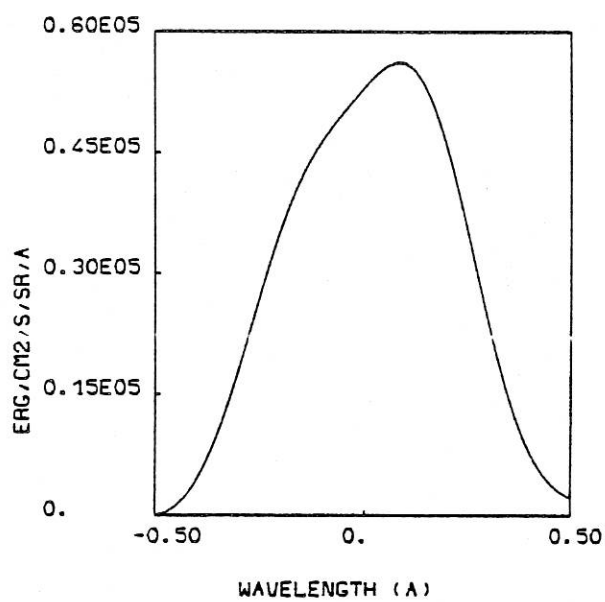
MGK $\chi = 4$ TO 16

Fig. 7. a.

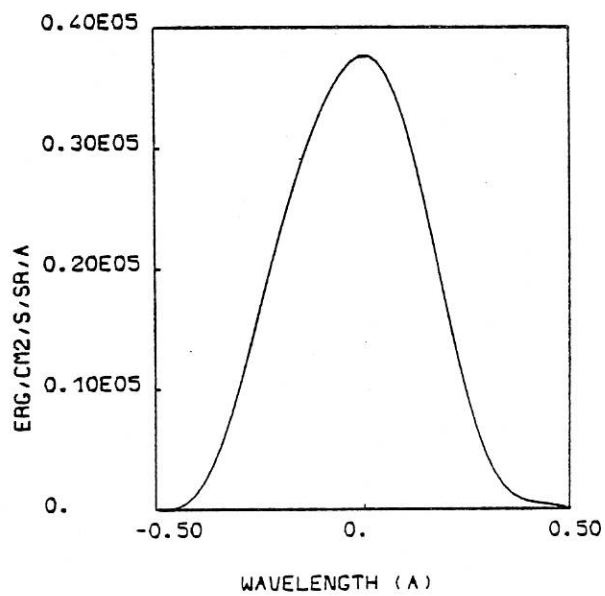
MGH $\chi = 4$ TO 16

Fig. 7. b.

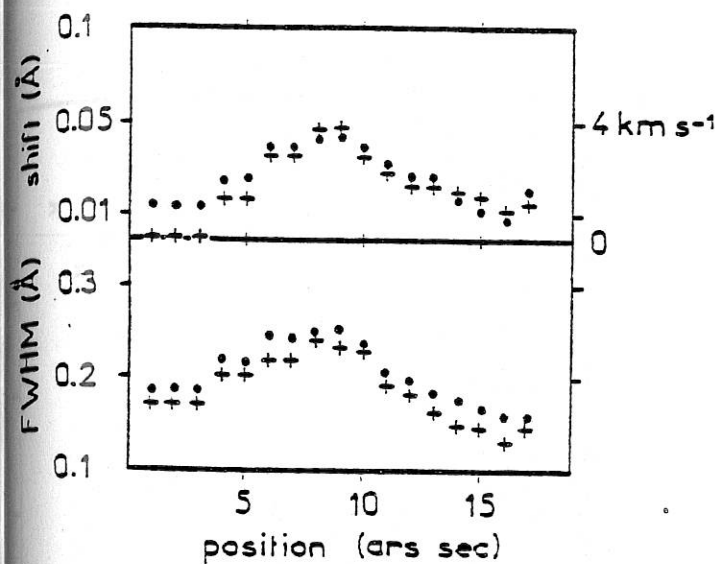


Fig. 6. a et b

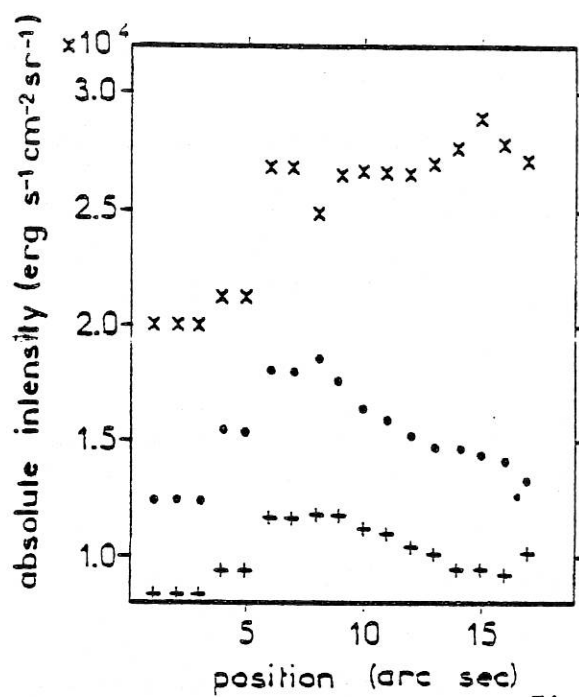


Fig. 8. a.

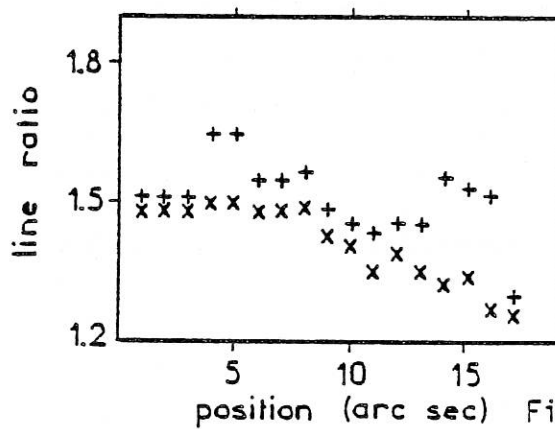


Fig. 8. b.

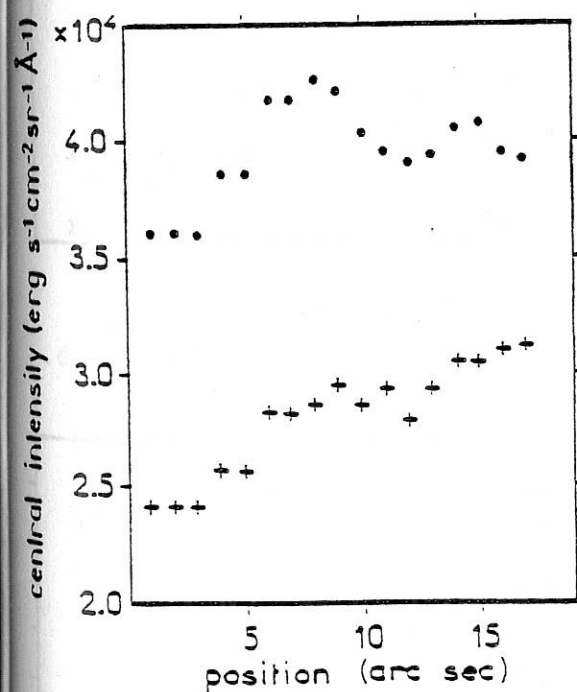


Fig. 6. c.

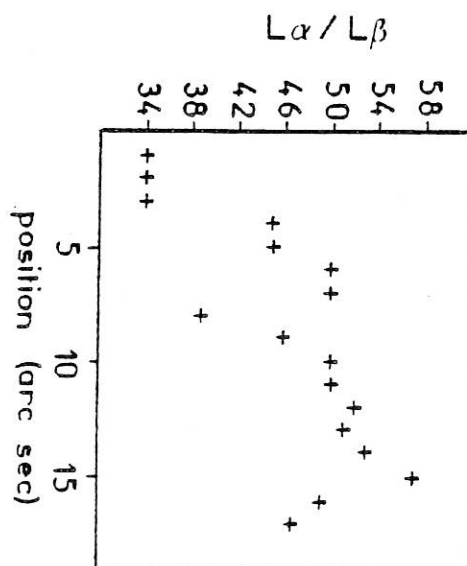


Fig. 8. c.

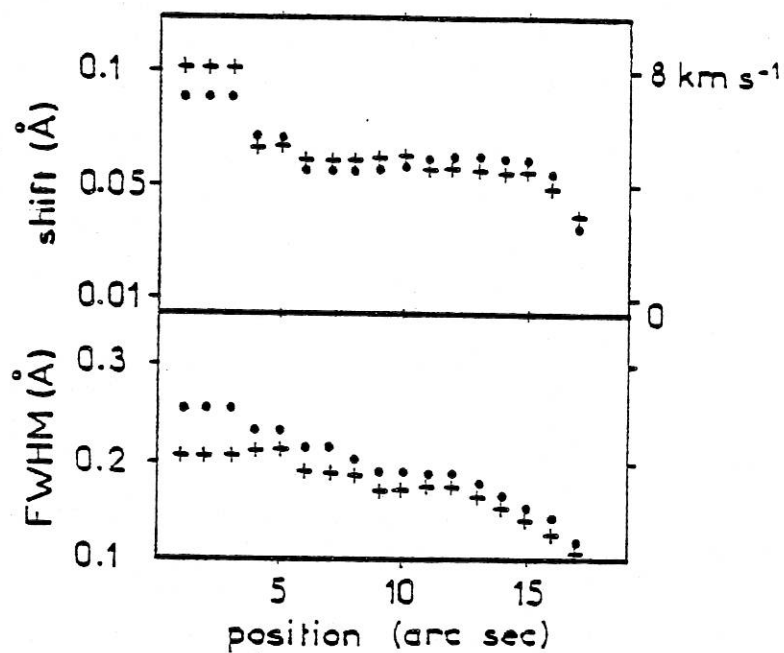


Fig. 9. a et b

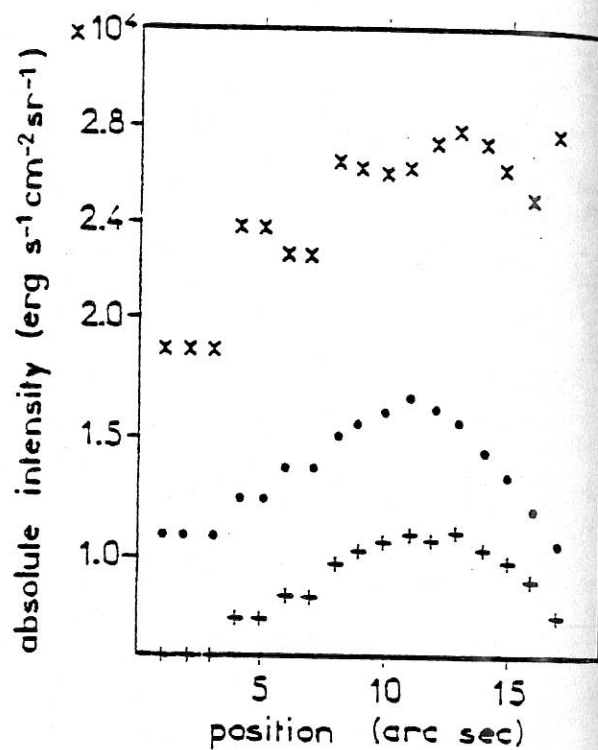


Fig. 10. a.

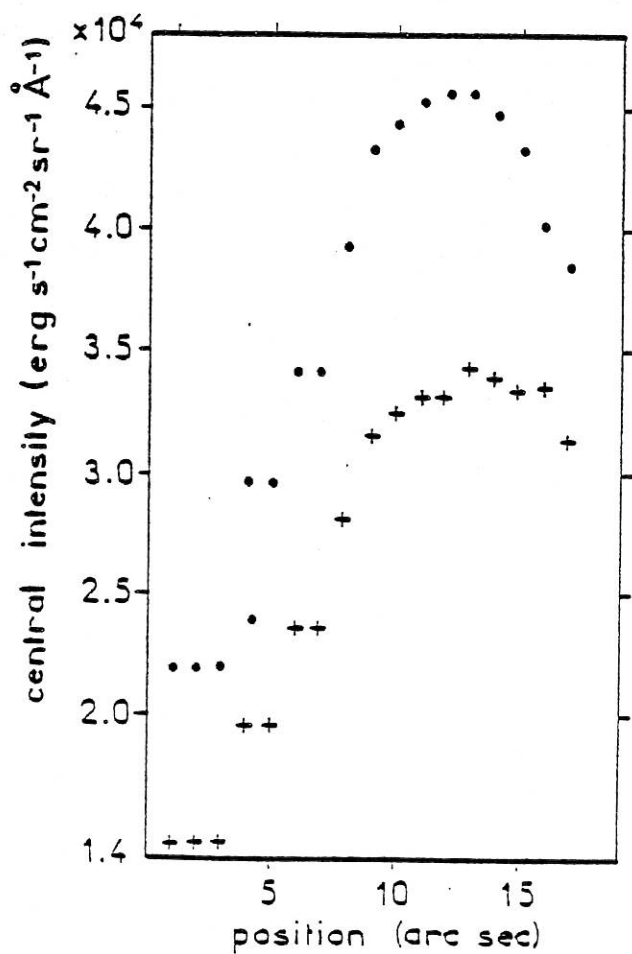


Fig. 9. c.

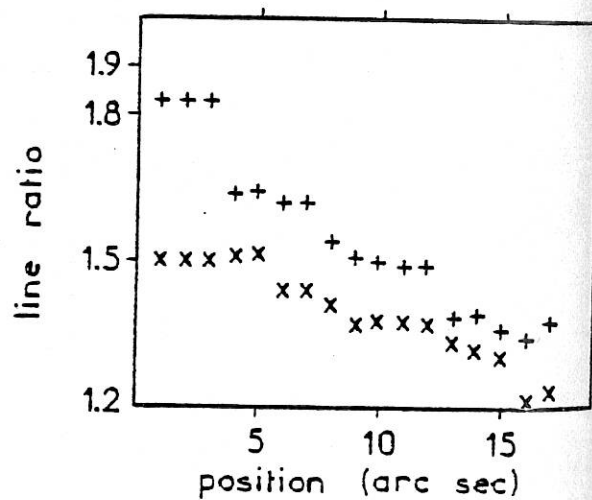


Fig. 10. b.

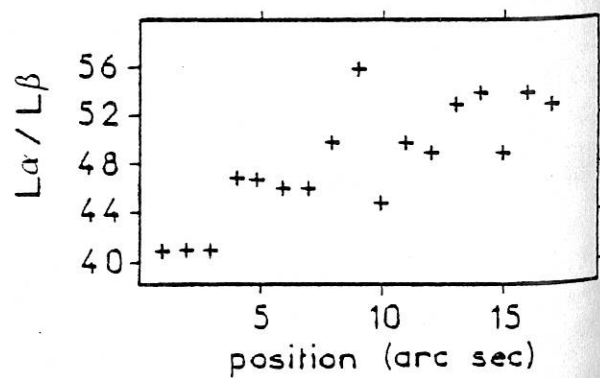


Fig. 10. c.

III. CALCUL DU TRANSFERT (A DEUX DIMENSIONS ET HORS E.T.L.) DANS LES
CINQ RAIES DE RESONANCE (H $L\alpha$, Mg II h et k, Ca II H et K).
COMPARAISON AVEC LES OBSERVATIONS OSO-8.

Article VII.

Two-dimensional non l.t.e. transfer computations of resonance lines
in quiescent prominences.

We use the two-dimensional (2D) transfer code of Mihalas et al (1978) to compute emergent profiles of resonance lines of H I, Mg II, $\overline{\text{Ca II}}$. The model (a uniform slab limited in two directions) and the thermodynamic and radiative quantities are described. Metallic line profiles are sensitive to the ionization degree (n_p/n_1 varying from 1 to 10). The ionization degree is fixed at ($n_p/n_1 = 10$). Some modifications are implemented in the code (especially, the true incident profiles of chromospheric lines). 2D and 1D profiles are compared. A good agreement between computed and observed profiles is found for $L\alpha$ and Ca II, but not for Mg II lines. Radial velocities improve the agreement. We discuss necessary improvements in the computations and the observations of resonance lines in prominences.

TWO DIMENSIONAL NON L.T.E. TRANSFER
COMPUTATIONS OF RESONANCE LINES
IN QUIESCENT PROMINENCES

Running title : computations of resonance lines in quiescent
prominences

VIAL, J.C.(1)

Laboratoire de Physique Stellaire et Planétaire

Received - 1981 July 16 ;

- (1) The major part of this work has been done in 1979 as a Summer Visitor at High Altitude Observatory, N.C.A.R., Boulder, Colorado, U.S.A. (The National Center for Atmospheric Research is sponsored by the National Science Fondation).

ABSTRACT

We use the two-dimensional (2D) transfer code of Mihalas et al (1978) to compute emergent profiles of resonance lines of H I, Mg II, Ca II. The model (a uniform slab limited in two directions) and the thermodynamic and radiative quantities are described. Metallic line profiles are sensitive to the ionization degree (n_p/n_1 varying from 1 to 10). The ionization degree is fixed at ($n_p/n_1 = 10$). Some modifications are implemented in the code (especially, the true incident profiles of chromospheric lines). 2D and 1D profiles are compared. A good agreement between computed and observed profiles is found for L α and Ca II, but not for Mg II lines. Radial velocities improve the agreement. We discuss necessary improvements in the computations and the observations of resonance lines in prominences.

INTRODUCTION

The observations of $L \alpha$ (H I), k and h (Mg II), K and H (Ca II) lines in solar prominences with OSO-8 give the possibility to test the few existing models ; the OSO-8 spatial resolution being better than the scales of models (usually infinite). First attempts to compute Non L.T.E. populations were made by Hirayama (1964), Kawaguchi (1964), Giovanelli (1967) and Yakovkin and Zeldina (1964). Poland et al (1971) computed the ionization consistently and Yakovkin and Zeldina (1968) treated the problem of the $L \alpha$ scattering. Complete Non L.T.E. computations have been performed on prominence models by Ishizawa (1971), Heasley and Mihalas (1976), Heasley and Milkey (1976, 1978).

But no emergent profile was computed for all lines ; in the absence of any observation, no attention was paid to the computation of the Mg II lines in prominences. We present the results of N.L.T.E. computations in the 5 lines performed with the code of Mihalas et al. (1978), called hereafter MAM. We discuss the results in connection with the involved hypotheses. We compare with the OSO-8 observations (Vial, 1981). We finally indicate some possible improvements in terms of computations (and observations).

I. TWO DIMENSIONAL TRANSFER COMPUTATIONS WITH THE MAM CODE.

The MAM code allows for 2 dimensional (2D) non L.T.E. transfer in periodic media or free standing slabs. In the case of free standing slabs illuminated by an incident radiation, it takes into account 2D effects that previous codes (Heasley and Mihalas, 1976) did not. It is

fast and flexible enough to study the influence of the geometry, the ray orientation, the incident radiation, and velocity fields. However, it oversimplifies the atom (2 levels) which means that the ionization must be known in some way ; the frequency redistribution is assumed complete.

We got rid of other simplifications with the following changes in the code :

- a) the Doppler profile was replaced by a Voigt profile ;
- b) instead of a "continuum" (frequency independent) for the incident radiation, we implemented the true profiles (those observed with OSO-8) ;
- c) we considered the dilution factor as a parameter depending on the line.

a) Method

The geometry of the model is shown in Figure 1. We use the notation of MAM (Mihalas et al., 1978). The (xy) plane is parallel to the solar surface. The slab is standing above it and its height above the surface is specified by the value of the dilution factor. The slab is infinite along the y axis ; its thickness along x is X, its height is Z. The transfer equation along a ray is :

$$(1) \quad \frac{\mu}{X} \cdot \frac{\partial I}{\partial Z} + \frac{\gamma}{X} \frac{\partial I}{\partial X} = S - I$$

where $\mu = \cos \theta$ (θ angle to the z axis)

$\gamma = \sin \theta \cos \phi$ (ϕ angle of the projection on (xy) to the x axis)

$I = I(x, z, \nu, \theta, \phi)$ specific intensity

$$(2) \quad \chi = \text{opacity given by } \chi(x, z, \nu, \theta, \phi) = \chi_L(x, z) \Phi(x, z, \nu, \theta, \phi) + \chi_C(x, z) \equiv \chi_C(x, z) [(1 + \beta(x, z) \Phi)]$$

χ_L and χ_C are line and continuum opacities (we mean here the opacity per length unit),

ϕ is the line profile function, $\beta = \chi_L/\chi_C$

With a two-level atom, with complete redistribution, the source function is :

$$(3) \quad S(x, z, \nu, \theta, \phi) = [1 - \xi(x, z, \nu, \theta, \phi)] \bar{J}(x, z) + \xi(x, z, \nu, \theta, \phi) B(x, z)$$

where ξ is the total destruction probability of a photon given by :

$$(4) \quad \xi(x, y, \nu, \theta, \phi) = \frac{1 + \epsilon(x, z) B(x, z) \phi(x, z, \nu, \theta, \phi)}{1 + \beta(x, z) \phi(x, z, \nu, \theta, \phi)}$$

B is the thermal source term, ϵ the collisional destruction probability (C_{21}/A_{21}).

\bar{J} is the mean intensity given by :

$$(5) \quad \bar{J}(x, z) = \iint I(x, z, \nu, \theta, \phi) \phi(x, z, \nu, \theta, \phi) \, d\nu \frac{d\omega}{4\pi}$$

All details about the computation method are given in MAM.

b) The model atmosphere

We take $X = 5.10^3$ Km, $Z = 3.10^4$ Km. Thermal quantities are uniform :

$T_e = 8.10^3$ K, $n_e = 2.10^{10}$ cm⁻³ and the microturbulent velocity is 8 km s⁻¹.

The ionization degree (ratio of proton to neutral hydrogen populations) is a free parameter ranging from 1 to 10 (Hirayama, 1978) but most computations have been made with $n_p/n_1 = 10$. This is discussed in § c.

With such values, the gas pressure varies from 0.066 to 0.046 dyne.cm⁻².

The grid for x and z is chosen in order to have a linear scale in $\log \tau$. We took 37 points in x and 10 points in z . The frequency grid is linear, with 25 points. The angle grid takes into account only one point per octant.

In the case of the free standing slab, the incident radiation appears as a boundary condition to be specified. We assume no incident line radiation, no enhanced radiation scattered from "above" ($\mu < 0$) i.e. from the corona.

c) Determination of parameters entering the transfer equation, for the OSO-8 lines.

The computations are performed for the L α , k and h (Mg II), K and H (Ca II) lines.

Given T_e and the microturbulence, we compute the Doppler width Δv_D .

1) Line opacity

In $\chi_L = g_2/g_1 \lambda^2/8\pi\nu\pi A_{21} 1/\Delta v_D n_1$, we need the ground state populations.

For H, it is given immediately through n_e and n_p/n_1 since we assume $n_p = n_e$ and n_H^0 (neutral) $\sim n_1$.

For Ca II and Mg II lines, we need ground state populations of Mg^+ and Ca^+ .

We have :

$$(6) \quad n_{M II}^1 = A \frac{n_{M II}^0}{n_M} n_H$$

where M may be Ca or Mg, A is the abundance of the element, n_H the total hydrogen population and $n_{M II}/n_M$ the ratio of populations of the ionized metal to the total one. For Ca, we adopted Holweger (1973) photospheric abundance ($2.3 \cdot 10^{-6}$). Our Mg abundance ($3.5 \cdot 10^{-5}$) lies between Shine (1973) value ($3 \cdot 10^{-5}$) and a more recent value of Lambert and Luck (1978) from which it differs by less than 20%.

We have assumed $n_{M II} \sim n_{I M II}$

With $n_M = n_{M II} + n_{M III}$ (no neutral metal) and $n_H = n_e + n_H^0 \approx n_e(1 + (n_p/n_1)^{-1})$ we obtain :

$$(7) \quad n_{M II}^1 = A \cdot n_e \frac{1}{1 + \frac{n_{M III}}{n_{M II}}} \left(1 + \left(\frac{n_p}{n_1}\right)^{-1}\right)$$

The ratio $n_{M III}/n_{M II}$ is derived from the ionization equilibrium equation between M II and M III.

The ionization of M II is dominated by photoionizations. Continuum edges of Ca II and Mg II are located at 1045 and 824 Å respectively. Consequently, photoionizations are dominated by the Lyman continuum, which fully determines the H ionization itself. For all elements (H, Ca II, Mg II) we have a balance between the photoionization and radiative recombination rates. After Mihalas (1978), we write :

$$N_{jc} = N_j \int_{\nu_j}^{\infty} J_{\nu} \frac{4\pi\alpha_{\nu}}{h\nu} d\nu \text{ number of photoionizations/cm}^3/\text{s}$$

and

$$N_{cj} = N_p \left(\frac{N_j}{N_p}\right)^* \int_{\nu_j}^{\infty} \frac{2h\nu^3}{c^2} \exp\left(-\frac{h\nu}{kT_e}\right) \frac{4\pi\alpha_{\nu}}{h\nu} d\nu \text{ number of spontaneous}$$

recombinations/cm³/s.

where symbols have their usual meaning :

n_p proton density

J_ν mean monochromatic intensity

α_ν photoionization cross-section

The (*) means "L.T.E. values".

We write $J_\nu = B_\nu(T_{\text{rad}}) w_\nu$,

T_{rad} being the radiation temperature of the chromosphere at frequency ν . w_ν is a factor that takes into account the geometrical dilution and the degree of penetration of the Lyman continuum. We further assume that this factor is frequency independent below 1045 Å ($w_\nu = w$). So $N_{jc} = N_{cj}$ for the ground level ($j=1$) implies :

$$(8) \quad N_1 w \int_{\nu_1}^{\infty} B_\nu(T_{\text{rad}}) \frac{4\pi\alpha_\nu}{h\nu} d\nu = N_{\text{ion}}^+ \left(\frac{N_1}{N_{\text{ion}}}\right)^* \int_{\nu_1}^{\infty} B_\nu(T_e) \frac{4\pi\alpha_\nu}{h\nu} d\nu$$

We have :

$$B_\nu \sim (\)^3 \exp\left(-\frac{h\nu}{kT}\right) \text{ and } \alpha_\nu \sim (\)\nu^{-3} \text{ (Mihalas, 1978)}$$

$$\text{so} \quad N_1 w \int_{\nu_1}^{\infty} e^{-\frac{h\nu}{kT_{\text{rad}}}} \frac{d\nu}{\nu} = N_{\text{ion}}^* \left(\frac{N_1}{N_{\text{ion}}}\right)^* \int_{\nu_1}^{\infty} e^{-\frac{h\nu}{kT_e}} \frac{d\nu}{\nu}$$

$$\text{or} \quad N_1 w E_1(t_1) = N_{\text{ion}}^+ \left(\frac{n_1}{N_{\text{ion}}}\right)^* E_1(t_2)$$

$$\text{where} \quad t_1 = \frac{h\nu_1}{kT_{\text{rad}}} \quad \text{and} \quad t_2 = \frac{h\nu_1}{kT_e}$$

Quantities t_1 and t_2 being very large, the integro-exponential function $E_1(t)$ is close to $1/(te^t)$.

We finally obtain :

$$(9) \quad \frac{N_1}{N_{\text{ion}^+}} = \frac{1}{w} \left(\frac{N_1}{N_{\text{ion}}} \right)^* \exp \left[\frac{h\nu_1}{k} \left(\frac{1}{T_{\text{rad}}} - \frac{1}{T_e} \right) \right] \frac{T_e}{T_{\text{rad}}}$$

where the exponential may be replaced by the ratio of the Planck functions.

If we call $R_{\text{Mg}} = N_{\text{Mg II}}/N_{\text{Mg III}}$, $R_{\text{Ca}} = N_{\text{Ca II}}/N_{\text{Ca III}}$, $R_{\text{H}} = N_1/N_p$ we obtain :

$$(10) \quad R_{\text{Mg}}/R_{\text{H}} = \left(\frac{N_1^{\text{Mg II}}}{N_{\text{Mg III}}} \right)^* / \left(\frac{N_1}{N_p} \right)^* \frac{B_{824}(T_e)}{B_{824}(T_{\text{rad}}^{\text{Mg}})} \frac{B_{912}(T_{\text{rad}}^{\text{H}})}{B_{912}(T_e)} \times \frac{T_{\text{rad}}(\text{H})}{T_{\text{rad}}(\text{Mg})}$$

$$(11) \quad R_{\text{Ca}}/R_{\text{H}} = \left(\frac{N_1^{\text{Ca II}}}{N_{\text{Ca III}}} \right)^* / \left(\frac{N_1}{N_p} \right)^* \frac{B_{1045}(T_e)}{B_{1045}(T_{\text{rad}}^{\text{Ca}})} \frac{B_{912}(T_{\text{rad}}^{\text{H}})}{B_{912}(T_e)} \times \frac{T_{\text{rad}}(\text{H})}{T_{\text{rad}}(\text{Ca})}$$

where we replaced the frequency subscript by the wavelength of the continuum edge. We adopt radiation temperatures given in Table 1.

L.T.E. populations are derived from Saha equations.

After some computations we obtain :

$$R_{\text{Mg}}/R_{\text{H}} \sim 8.8 \text{ and } R_{\text{Ca}}/R_{\text{H}} \sim 3.8$$

These relations represent the scaling of the Ca II and Mg II ionizations versus the hydrogen ionization.

$$\text{For } \frac{n_p}{n_1} < 3, \text{ we have } n_{\text{Mg II}} > n_{\text{Mg III}}$$

and

$$n_{\text{Ca II}} \sim n_{\text{Ca III}}$$

We adopted : $n_{\text{Mg}} = n_{\text{Mg II}}$ and $n_{\text{Ca}} = 2 \cdot n_{\text{Ca II}}$ even in the case $n_p/n_1 = 10$. We know that we overestimate Mg II and especially Ca II populations, but these fixed values will be sufficient for our computations that aim at an evaluation of emergent profiles.

Line opacities (in cm^{-1}) appear in table 2 in the case $n_p/n_1 = 3$ only. We also give the total line center opacity τ_0 .

2) Continuum opacities

They depend very much on the wavelength. We computed all known possible contributions : -Rayleigh scattering - H^+ , H^- - C I continuous absorption (for L α only) -H bound-free (free-free is negligible) : Balmer for L α and Mg II, Paschen for L α , Mg II, Ca II. - e^- scattering and metal absorptions.

Lyman α : The continuum opacity is dominated by the C I photoionization at 1242 \AA from the $2D^1$ level. The C I and C II populations were derived from chromospheric computations for similar temperatures and densities (Lites, 1979). We obtained :

$$n(2D^1)/n_{\text{C}} = 0.08. \text{ The abundance of C was taken as } 3.47 \cdot 10^{-4}.$$

Mg II lines : The continuum opacity is dominated by the H bound-free (Balmer) and the electron scattering.

Ca II lines : The electron scattering is the main contributor to the opacity.

Values of x_c (and $\beta = x_L/x_c$) are given in Table 2.

We notice that the line opacity dominates the continuum for all lines.

3) Other parameters

The computations of ϵ follows from $\epsilon = n_e L_{21}/A_{21}$ where L_{21} are given by Allen (1973).

Other entries in Table 2 include the chromospheric incident intensity $\langle I_0 \rangle$ around line center. The ratio $\langle I_0 \rangle / \epsilon B$ is higher than 300, which indicates the domination of the scattering term, for the Doppler core, in equation (3) of the source function. We also give the damping parameter a and the thermalization lengths (Λ) in the Doppler and Voigt approximations (Mihalas, 1978). We notice that the thermalization lengths are larger than half the optical thickness of the layer (effectively thin atmosphere).

The last column gives the value of the Doppler width (in $m \text{ \AA}$) throughout our uniform medium, that serves as a "fiducial" width. In many plots, wavelength will be replaced by the frequency distance to the line center, divided by this fiducial Doppler width.

II. RESULTS OF COMPUTATIONS

II.1. Variations of profiles with the ionization degree

We first used the code in its initial status and we let the ionization degree vary in order to evaluate its influence. The emergent

radiation is computed along the x axis. The incident radiation (wavelength independent, here) is the one given in table 2 (for metallic lines, we took the mean of central and peak values).

L α line : the emergent profile is shown in Figure 2.a., for $n_p/n_1 = 3$. It is quite unreversed since, in the Doppler core, it follows the incident "profile". The FWHM (full width at half maximum) is about 0.39 \AA ; the central intensity is one half the incident intensity since the dilution factor is assumed to be 0.5. The profile does not change much when n_p/n_1 varies. 2D (two dimensional) solutions are identical to 1D (one dimensional) solutions.

Mg II lines : k profile is shown in Figure 2b for $n_p/n_1 = 3$. It is reversed and the FWHM is 0.34 \AA .

The intensity is low because the dilution factor was (wrongly) taken as 0.15. The reversal disappears with $n_p/n_1 = 10$.

The 2D profile is lower than the 1D : we notice that the 2D transfer gives significant differences with the 1D, for Mg II lines.

Ca II lines : K profile is shown in Figure 2.c for $n_p/n_1 = 3$. It is not reversed and the FWHM is 0.29 \AA . The central intensity is equal to the chromospheric intensity multiplied by the dilution factor (0.3). FWHM and central intensities are lower for increasing n_p/n_1 . No 2D effect is detected.

L α , Mg II and Ca II results are summarized in Table 3.

Let us notice that these results already evidence some features observed by Vial (1981) in a quiescent prominence :

$k_3/h_3 > K_3/H_3$, $\text{FWHM}(\text{Mg II}) > \text{FWHM}(\text{Ca II})$ (when converted in velocities) and a relative insensitivity of the $L \alpha$ profiles to the ionization conditions.

Before turning to a more complete treatment, and in order to minimize computing time, we decided to fix the ionization degree. We chose the ratio n_p/n_1 that did not "reverse" the Mg II lines : $n_p/n_1 = 10$. (1).

(1)

However, $n_p/n_1 = 3$ (the value derived from observations by Vial (1981)) would have given a ratio of K/H to k/h , close to the observed one. Further computations should investigate the profiles obtained with this value of the ionization degrees.

II.2. Final results with a static atmosphere

We replace Doppler absorption (and emission) profiles by Voigt profiles. The incident radiation is now given by the chromospheric line profiles measured on OSO-8 (Figure 3) multiplied by a dilution factor. The dilution factor w_λ is given by :

$$(12) \quad w_\lambda = \frac{1}{2} \frac{\int_{\mu_0}^1 I_\lambda(\mu) d\mu}{\int_0^1 I_\lambda(\mu) d\mu}$$

where $\mu_0 = \cos \theta_0$

θ_0 being half the angle under which the Sun is seen

w_λ depends on the wavelength because of the limb darkening.

We compute a "mean" dilution factor :

$$w = \frac{1}{2} \frac{\int_{\mu_0}^1 \bar{I}(\mu) d\mu}{\int_0^1 \bar{I}(\mu) d\mu}$$

where $\bar{I}(\mu) = \int I_{\lambda}(\mu) d\lambda$

We consider this factor as a constant from the bottom to the top of the atmosphere. We took Ca II and Mg II data from Linsky (1968) and Kohl and Parkinson (1976) respectively. As for the L α line, we assumed no center to limb variation of the integrated intensity (see, for instance, Bonnet *et al.*, 1980). At a height of 13.10^3 km (18 arc second) above the Sun, we obtain 0.4 for L α and 0.3 for Ca II and Mg II lines.

We computed average profiles emergent from the whole atmosphere along the x axis, in order to compare to observations. The profiles of the 5 lines are shown in Figures 4 (thick line corresponds to 2 D results, thin line to 1D). Line parameters are given in Table 4.

1- We first discuss the changes in the emergent profiles that result from the 3 modifications mentioned above. For the L α line, we now have a reversed profile with a peak-to-peak distance of 0.32 \AA instead of a flat -topped one. It mimics the chromospheric profile but it is slightly narrower because peaks of the incident profile are located at a frequency out of the Doppler core. Because of the Voigt profile, wings are somewhat more extended (since we have $\alpha\tau_0 > 1$). For the same reasons, the Mg II profiles are now reversed.

Ca II profiles are not reversed : because of the low opacity, the emergent intensity is quickly smaller than the source function at increasing distance from the central frequency.

2- Now we compare the 2D to 1D profiles.

The 2D L α profile (Figure 4.a.) is reversed, contrary to the 1D profile. This is due to the weight of bottom regions (close to the Sun) where the reversal is very important. We show in Figure 5.a the

emergent profile from the top of the atmosphere (along x) : it is not reversed and (slightly) fainter than the average profile. On the contrary, the emergent profile at the bottom (along x) is high and deeply reversed (with $I(\text{peak})/I(\text{center}) \sim 2$).

We observe , here, "edge" effects that do not balance each other because the 2D computations take into account the direct illumination of the lower (xy) surface. The way the emergent profile changes with altitude is illustrated in Figure 5.c where we plot the emergent intensity (multiplied by 10^8) as halftones as a function of the frequency and the vertical position in the slab (Z axis ; position 1 corresponds to the top).

The 2D integrated intensity is 20% lower than the 1D integrated intensity.

The 2D Ca II profiles (Figures 4.d, e) are lower than 1D profiles. We interpret this result as a consequence of the low opacity in the line : with the illumination of the bottom surface, we allow for more many incident photons, but also for the possibility that photons from the whole atmosphere escape across this surface. The source function may be lower. This is illustrated in Figure 5.d where we plot the emergent intensity as halftones as a function of the frequency and the vertical position in the slab.

The last two results ($S(2D) < S(1D)$) are very similar to the conclusion of Morozhenko (1978) who computed the transfer of radiation in filamentary structures (vertical helical spires). For a large range of opacities (10 to 100) in a resonance line (2 level atom), he found that the "source function is the less, the greater the degree of filamentation".

On the contrary, 2D profiles of Mg II lines are about 2 times higher than 1D (Figures 4.b, c), a result also found in the integrated intensity. The 2D influence extends throughout the whole atmosphere, contrary to Jones and Skumanich's prediction (1980). However, we should point out that the incident radiation implemented here is not a "continuum background" for which scaling laws can be applied.

The emergent intensity is plotted in Figure 5.e as halftones as a function of the frequency and the vertical position in the slab.

II.3. Comparison with observations

It is made possible through Table 4, where observations are taken from Vial (1981). We warn the reader that the chromospheric incident profiles used in computations may depart from the quiet Sun profiles used for the calibrations of the observed profiles. Consequently, the comparison of computed and observed intensities is valid within a maximum departure of 15% in $L \alpha$ and better for other lines.

We notice a good agreement for the widths of $L \alpha$ and Ca II lines. The computed depth of the $L \alpha$ reversal is close to the observed one. Observed central intensities are lower than computed ones. This is also true for Ca II (and Mg II) integrated intensities, but not for $L \alpha$.

The Mg II lines show definite differences : the observed profiles are not reversed, contrary to the computed ones. Observed central and integrated intensities are lower than computed 2D ones.

Other features such as ($k_3/h_3 \sim 1.3$; $K_3/H_3 \sim 1$) that we already noticed are still present in the computations and agree with observations.

However, we do not explain some observations mentioned in Vial (1981) ;

a) The fact that close to the limb, we both had K and H decreasing intensities while K/H was about 1.

b) Some larger $L \alpha$ profiles (peak-to-peak distance up to 0.37 \AA).

There is no obvious explanation for the first feature : at low K and H intensities, we should have K/H close to the ratio of oscillator strengths. We notice that far wings are steeper in H than in K ; Engvold's observations (1976) show downwards radial velocities ; moreover Hyder and Lites (1970) already introduced radial velocities in (eruptive) prominences in order to explain H α Doppler brightening (and $L \alpha$ "Dimming").

Consequently, we implemented in the code a set of radial velocities V_z ranging from -56 to $+56 \text{ km s}^{-1}$.

II.4 Moving atmosphere

For the $L \alpha$ line, the profile becomes unreversed at velocities higher than 40 km s^{-1} . The integrated intensity decreases when the velocity increases (because we are "losing" photons from a peak of the incident profile).

For the Mg II lines, the profile is no longer reversed for $|V_z| \gtrsim 25 \text{ km s}^{-1}$, with no important changes in the integrated intensity.

It is interesting to notice that Ca II intensities increase with increasing velocities, probably because of the shape of the incident line profiles. As a consequence, we cannot explain our Ca II observations since large velocities provide with larger intensities. However, the Mg II profiles are closer to observed ones.

Because of the small number of points in the angular grid these results should not be taken too literally.

We give in Figures 6.a,b,c the profiles of $L\alpha$, $Mg\ k$, $Ca\ K$ with $V_z = 42, 25, 33\text{ km s}^{-1}$ respectively.

In order to explain some wide observed $L\alpha$ profiles, we also computed emergent profiles at an angle ϕ of 60° from the x axis in the xy plane. The profile (Figure 7) is slightly larger (peak to peak distance is 0.35 \AA) and the intensity is higher (which is closer to observations).

III. CONCLUSION

The 2D computations with the MAM code, basically explain many features of the observed OSO-8 line profiles, at the exception of $Mg\ II$.

We show that some discrepancies can be reduced when radial velocities, emergence angle variations are included. Some observed edge effects (in $L\alpha$, see Vial, 1981) are comparable to computations. Other discrepancies could be solved with further improvements in the model : for instance, we could obtain a larger $L\alpha$ computed profile with a higher temperature (physically more correct since $L\alpha$ photons are probably emitted in the transition region between the prominence and the corona). We could also compute $L\alpha$ profiles more extended in the wings. We could have a dilution factor dependent on the height in the slab.

The improvements cannot be pushed too far because we meet two different basic limitations :

1) Code limitations

The two level atom may be valid for $Mg\ II$, but not for $Ca\ II$ and $L\alpha$. We attempted a comparison with 1D multilevel atom computations

of Heasley and Milkey (1976) : our integrated $L \alpha$ intensity is very close to their value when we take into account the different dilution factors, ionization degrees.

As for the Ca II lines, Ishizawa (1971) evaluated the importance of the $3d^2D$ levels : he found that K and H intensities for an atom with D levels are higher than intensities without D levels (his table 4).

We also should have in mind that the frequency redistribution is complete in the MAM, which provides with broader profiles than the true redistribution (Milkey et al. 1978)

Finally, the ionization should be computed with a multilevel H atom. Then, putting together all correcting factors mentioned above, it may be possible to reach a good agreement for all parameters of the five lines : a higher (transition) temperature would improve FWHM and intensities of $L \alpha$ profiles ; a more detailed calculation of Mg II and Ca II ionization can provide with smaller populations and consequently narrower Mg II profiles and lower intensities (compensated by the inclusion of D levels in the case of Ca II).

However we also meet :

2) Observations limitations

Prominences are very complex structures, less simple than any 1D, 2D (or 3D) slab. A single line of sight intercepts different loops at different angles. According to Engvold (1980) the plasma could not be in a stationary radiative state. We know velocity fields to exist, even when observed at medium resolution (Vial, 1981). The magnetic field should also be taken into account as determining the morphology

and as an important pressure term.

We think that these fine and complex structures need improved 2D (and 3D) treatments of the transfer equation (even at the cost of atomic simplifications). The results presented here, obtained in 5 resonance lines, seem to be promising when compared with OSO-8 observations. In this respect, the MAM computations can be considered as a first step towards a better modelling of prominences with the help of better new observations.

ACKNOWLEDGEMENTS

Computations have been performed at High Altitude Observatory (operated by National Center for Atmospheric Research, Boulder, Colorado). The author expresses his deepest thanks to Dr. D. Mihalas for his help and encouragement during this work, and to H.A.O. members for their kind hospitality. The manuscript was typed by Ms. Talbot at L.P.S.P.

Table 1Adopted chromospheric radiation temperatures

$\lambda(\text{\AA})$	$T_{\text{rad}}(^{\circ}\text{K})$
824	6600
912	6500
1045	5500

Table 2

Model parameters

	ϵ	B_v (1)	$\langle I_o \rangle^* (1)$	$\langle I_o \rangle / \epsilon B$	$\chi_L (cm^{-1})$	$\chi_C (cm^{-1})$	β	τ_o	$a^{(2)}$	Λ Doppler ⁽³⁾	Λ Voigt ⁽³⁾	$\Delta\lambda_D$ (mÅ)
L α	$1.4 \cdot 10^{-7}$	$8.3 \cdot 10^{-8}$	$4 \cdot 10^{-8}$	$3 \cdot 10^6$	$3.7 \cdot 10^{-4}$	$6.7 \cdot 10^{-13}$	$5.5 \cdot 10^8$	$1.9 \cdot 10^5$	$3.25 \cdot 10^{-4}$	$6.9 \cdot 10^6$	$1.4 \cdot 10^{10}$	57
Mg II k	$2.1 \cdot 10^{-5}$	$2.9 \cdot 10^{-5}$	$8 \cdot 10^{-7}$	$1.3 \cdot 10^3$	$3.0 \cdot 10^{-7}$	$2.5 \cdot 10^{-14}$	$1.2 \cdot 10^7$	150	$7.1 \cdot 10^{-4}$	$4.8 \cdot 10^4$	$1.4 \cdot 10^6$	78
Mg II h	$2.1 \cdot 10^{-5}$	$2.9 \cdot 10^{-5}$	$5.5 \cdot 10^{-7}$	$9 \cdot 10^2$	$1.5 \cdot 10^{-7}$	$2.5 \cdot 10^{-14}$	$6 \cdot 10^6$	75	$7.1 \cdot 10^{-4}$	$4.8 \cdot 10^4$	$1.4 \cdot 10^6$	78
Ca II K	$5.9 \cdot 10^{-5}$	$6.8 \cdot 10^{-5}$	$1.35 \cdot 10^{-6}$	$3 \cdot 10^2$	$1.5 \cdot 10^{-8}$	$1.4 \cdot 10^{-14}$	10^6	7.5	$5.4 \cdot 10^{-4}$	$1.7 \cdot 10^4$	$1.4 \cdot 10^5$	107
Ca II H	$5.9 \cdot 10^{-5}$	$6.9 \cdot 10^{-5}$	$1.35 \cdot 10^{-6}$	$3 \cdot 10^2$	$7.5 \cdot 10^{-9}$	$1.4 \cdot 10^{-14}$	$5 \cdot 10^5$	3.8	$5.5 \cdot 10^{-4}$	$1.7 \cdot 10^4$	$1.4 \cdot 10^5$	108

* chromospheric intensity with no dilution

(1) $erg \cdot s^{-1} \cdot cm^{-2} \cdot sr^{-1} \cdot Hz^{-1}$

(2) damping parameter

(3) thermalization length

Table 3

Variations of lines parameters with the ionization degree.

n_p/n_1	FWHM(\AA) L α	FWHM(\AA) k	FWHM(\AA) h	k_3/h_3	FWHM(\AA) K	FWHM(\AA) H	K_3/H_3
1	0.42	0.36	0.34	1.3	0.35	0.30	1.05
3	0.39	0.335	0.32	1.45	0.29	0.25	1.1
10	0.38	0.32	0.29	1.45	0.225	0.205	1.5



Table 4

Comparison of computed and observed line profiles parameters

	L α		Mg k		Mg h		Ca K		Ca H	
	Comp.	Obs (1)	Comp.	Obs (1)	Comp.	Obs (1)	Comp.	Obs (1)	Comp.	Obs (1)
FWHM (\AA)										
Peak-to-peak distance (if reversal) (\AA)	0.32	0.35-0.37	0.28	0.35-0.53	0.25	0.25-0.53	0.29	0.21-0.27	0.245	0.23-0.29
$I(\text{peak})/I_0$ (central) (reversal depth)	1.3	1.4	1.3	1	1.2	1	1	1	1	1
I_0 (central intensity)	0.46	0.39	0.41	0.24-0.27	0.42	0.24	0.38	0.24-0.28	0.35	0.19-0.22
I_0 (center chromos- pheric intensity)										
Integrated intensity (1D solution) ($\text{erg s}^{-1} \text{ cm}^{-2} \text{ sr}^{-1}$) (10^4)	1.94		1.97		1.22		3.14		3.1	
Integrated intensity (2D solution) ($\text{erg s}^{-1} \text{ cm}^{-2} \text{ sr}^{-1}$) (10^4)	1.61	3.6	3.97	2.8-3.1 (1) (2)	2.60	1.8-1.9 (1) (2)	2.26	1.5-1.6	1.76	1.0-1.2

(1) Observations are taken from typical profiles of Vial (1981) : they take into account
a slit "filling" factor of 0.8. We added the Mg II profile of Figure 7 of this paper.

$$\frac{2.8}{1.8} = \frac{1.4}{0.9} = 1.55$$

$$\frac{3.1}{1.9} = 1.63$$

$$\frac{1.4}{0.9} = 1.55$$

$$\frac{3.1}{1.9} = 1.63$$

REFERENCES

- Allen, C.W., 1973, *Astrophysical Quantities*, The Athlone Press, p. 43.
- Bonnet, R.M., Bruner, E.C., Jr., Acton, L.W., Brown, W.A., and
Decaudin, M., 1980, *Ap. J.*, 237, L 47.
- Engvold, O., 1976, *Solar Phys.* 49, 283.
- Engvold, O., 1980, *Solar Phys.* 67, 351.
- Giovanelli, R.G., 1967, *Australian J. Phys.* 20, 81.
- Heasley, J.N. and Mihalas, D., 1976, *Ap. J.*, 205, 273.
- Heasley, J.N., and Milkey, R.W., 1976, *Ap. J.*, 210, 827.
- Heasley, J.N. and Milkey, R.W., 1978, *Ap. J.*, 221, 677.
- Hirayama, T., 1964, *Publ. Astron. Soc. Japan*, 16, 104.
- Hirayama, T., 1978, in "Physics of Solar Prominences" (IAU Colloquium
44), Jensen, Maltby, Orrall eds, D. Reidel Publ. Co, Dordrecht.
- Holweger, H., 1973, *Astron. Astrophys.*, 26, 275.
- Hyder, C.L. and Lites, B.W., 1970, *Solar Phys.*, 14, 147.
- Ishizawa, T., 1971, *Publ. Astron. Soc. Japan*, 23, 75.
- Jones, H.P. and Skumanich, A., 1980, *Ap. J. Suppl. Series*, 42, 221.
- Kawaguchi, I., 1964, *Publ. Astron. Soc. Japan*, 16, 86.
- Lambert, D.L., and Luck, R.E., 1978, *M.N.R.A.S.*, 183, 79.
- Linsky, 1968, Ph. D. Thesis, Smithsonian Astrophysical Observatory,
Cambridge Report # 274.
- Lites, B.W., 1979, private communication.
- Mihalas, D., *Stellar Atmospheres*, 2nd ed., W.H. Freeman, San Francisco
(1978).
- Mihalas, D., and Auer L.H., and Mihalas, B.R., 1978, *Ap. J.*, 220,
1001.

- Milkey, R.W., Heasley, J.N., Schmahl, E.J., and Engvold, O., 1978, in "Physics of Solar Prominences" (IAU Colloquium 44), Jensen, Maltby, Orrall, eds, D. Reidel Publ. Co, Dordrecht.
- Morozhenko, N.N., 1978, Solar Phys., 58, 47.
- Poland, A.I., Skumanich, A., Athay, R.G. and Tandberg-Hanssen, E., 1971, Solar Phys., 18, 391.
- Shine, R., 1973, Thesis, University of Colorado.
- Vial, J.C, 1982, "Optically thick lines in a quiescent prominence : Profiles of $L\alpha$, $L\beta$ (H I), K and h (Mg II), K and H (Ca II) lines with the OSO-8 L.P.S.P. instrument", to be published in Ap. J. (Feb. issue).
- Yakovkin, N.A. and Zel'Dina, M. Yu, 1964, Soviet Astron., 8, 262.
- Yakovkin, N.A. and Zel'Dina, M. Yu, 1968, Soviet Astron., 12, 40.

FIGURE CAPTIONS

Figure 1 : Geometry of the prominence model. The plane represents the solar chromosphere ; the bar corresponds to the prominence.

Figure 2 : Lines half-profiles computed with the initial MAM configuration. $n_p/n_1 = 3$. (Thick and long dashes : two-dimensional (2D) computations ; thin and short dashes : one-dimensional (1D) computations).

abscissae : frequency distance from line center (measured in units of the line Doppler width).

ordinates : emergent specific intensity along the x axis.

Fig.2.a. : L α

Fig.2.b. : Mg II k

Fig.2.c. : Ca II K

Figure 3 : OSO-8 chromospheric line profiles adopted in our computations.

ordinates : specific intensity in $\text{erg s}^{-1} \text{cm}^{-2} \text{sr}^{-1} \text{Hz}^{-1}$; in abscissae, we have wavelength distance from line center (in \AA) to make it easier to compare with other published data.

Fig.3.a. : L α

Fig.3.b. : Mg k

Fig.3.c. : Mg h

Fig.3.d. : Ca K

Fig.3.e. : Ca H

Figure 4 : Lines profiles computed with the modified MAM. $n_p/n_1 = 10$; static atmosphere (same captions as Fig. 2).

Fig.4.a. : L α

Fig.4.b. : Mg k

Fig.4.c. : Mg h

Fig.4.d. : Ca K

Fig.4.e. : Ca H

Figure 5 : Evidence for edge effects in the 2D computation of the L α line.

Fig.5.a.b. : emergent L α profile along the x axis, at the top (5.a) and at the bottom of the atmosphere (5.b).

ordinates : specific intensity ($\text{erg s}^{-1} \text{cm}^{-2} \text{sr}^{-1} \text{Hz}^{-1}$)

abscissae : wavelength distance from line center (\AA)

Fig.5.c. : emergent intensity plotted as half tone as a function of the frequency distance from line center ($\Delta\nu/\Delta\nu_D$) and vertical position (Z : index 1 corresponds to the top).

Figures 5.d. and 5.e. : represent the same quantities as Figure 5.c., for Ca K and Mg k lines, respectively.

Figure 6 : Lines profiles computed with the modified MAM. $n_p/n_1 = 10$, moving atmosphere (same caption as Fig.2).

Fig.6.a. : L α ($V_z = 42 \text{ km s}^{-1}$)

Fig.6.b. : Mg k ($V_z = 25 \text{ km s}^{-1}$)

Fig.6.c. : Ca K ($V_z = 33 \text{ km s}^{-1}$)

Figure 7 : $L \propto$ profile emergent at 60° from the x axis in the xy plane. $n_p/n_1 = 10$, static atmosphere (same captions as Fig.2).

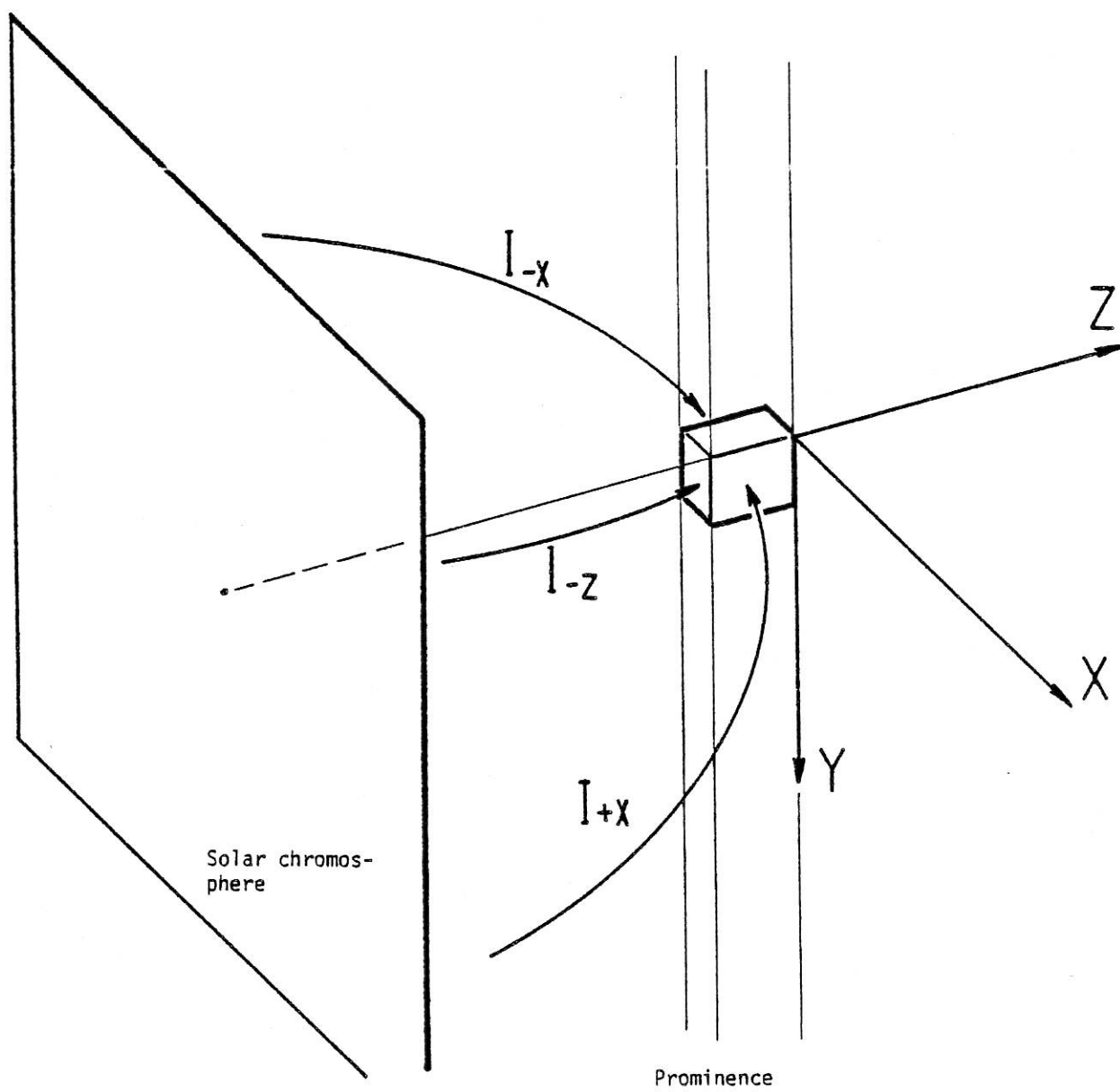


FIG.1. : Geometry of the prominence model.

128597 VIAL 7008 29152061

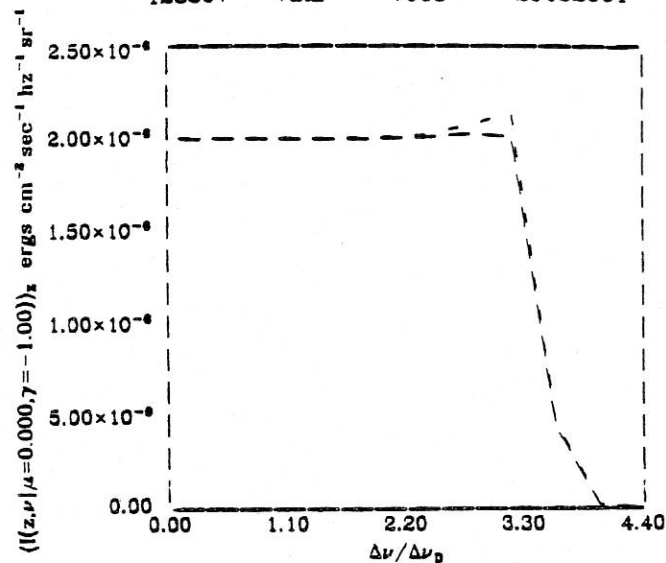


FIG.2.a.

129751 VIAL 7008 29152061

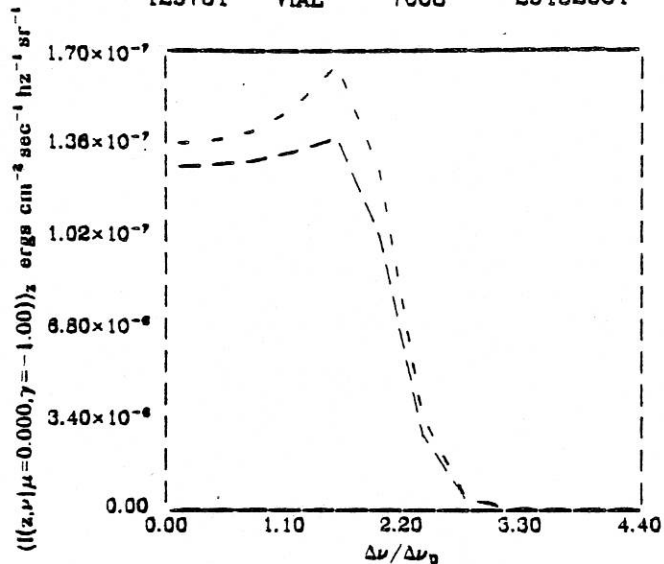


FIG.2.b.

120819 VIAL 7008 29152061

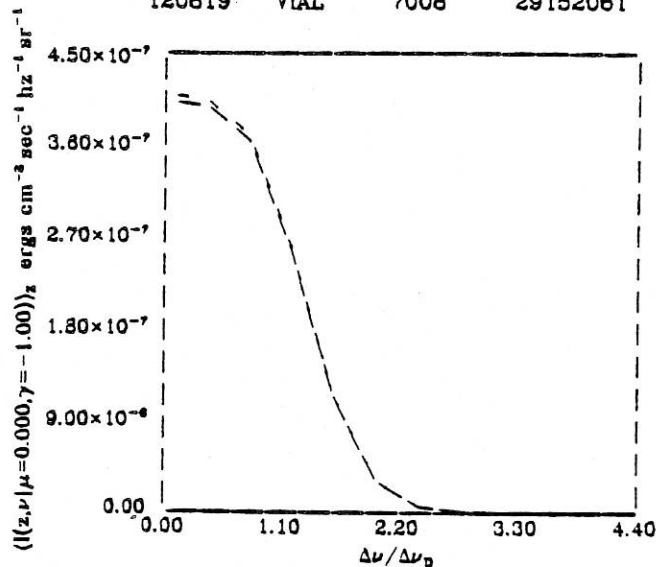


FIG.2.c.

FIG. 2. : Lines profiles computed with the initial MAM configuration.
 $\frac{n_p}{n_1} = 3$. (Thick and long dashes : two-dimensional (2D) computations ;
 thin and short dashes : one-dimensional (1D) computations).

abscissae : frequency distance from line center (measured in units
 of the line Doppler width).

ordinates : emergent specific intensity along the x axis.

Fig.2.a. : L α

Fig.2.b. : Mg II k

Fig.2.c. : Ca II K

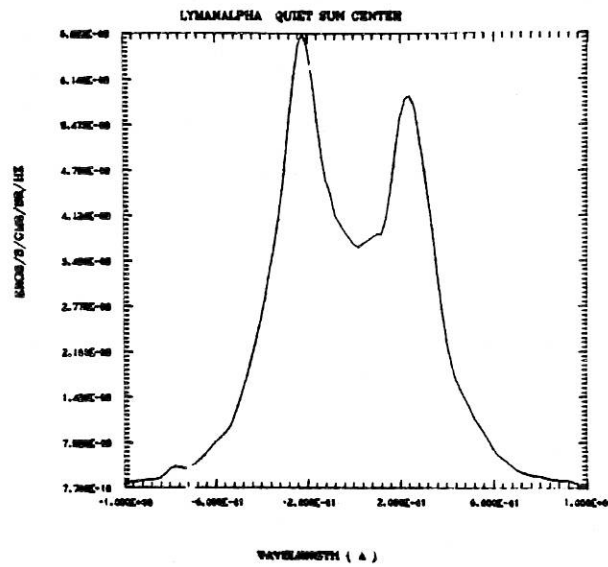


FIG.3.a.

FIG.3.b.

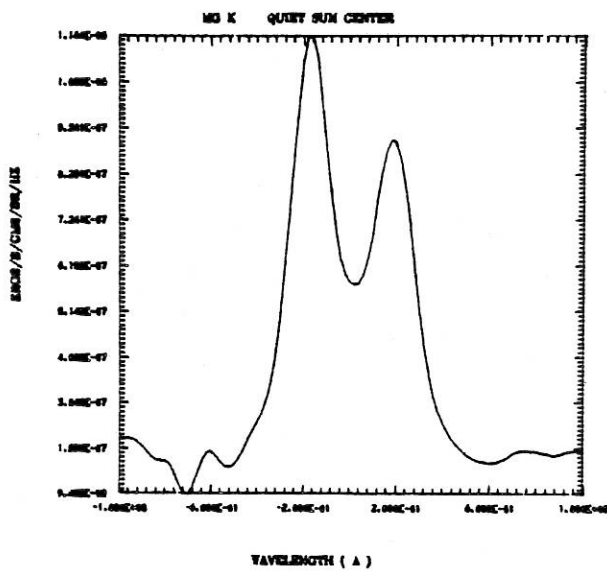


FIG.3.c.

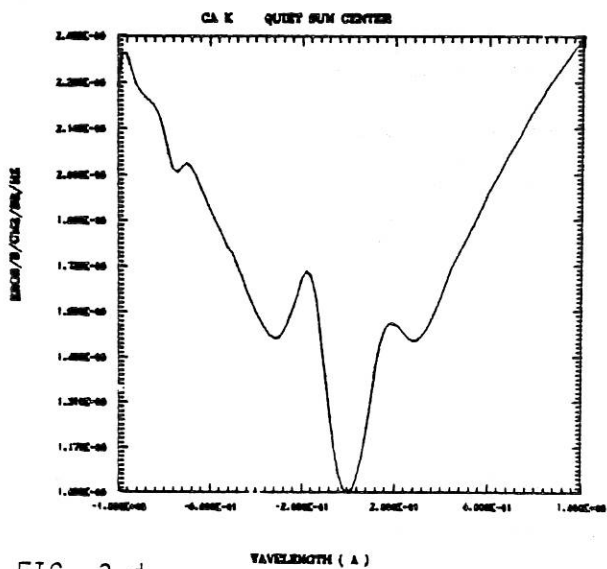
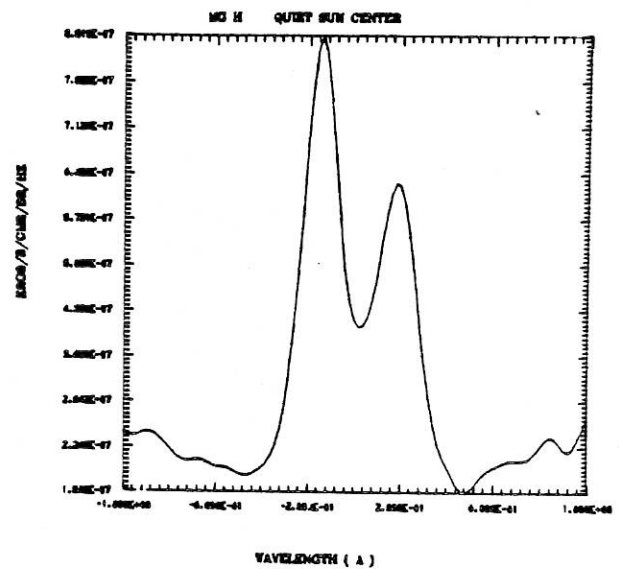


FIG. 3.d

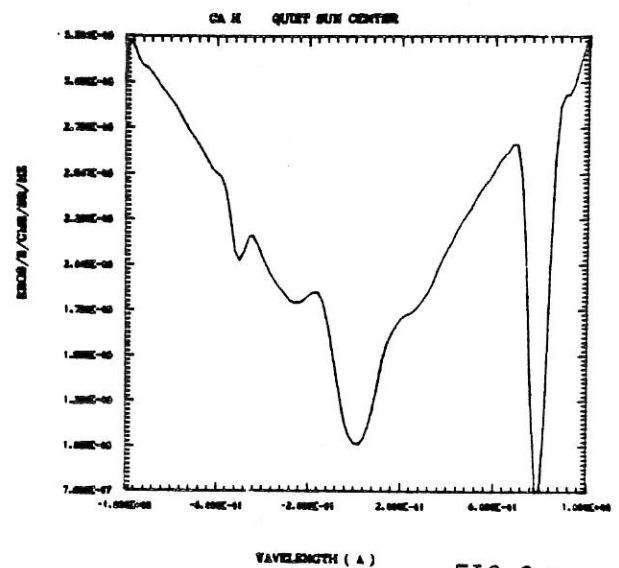


FIG.3.e.

FIG. 3. : OSO-8 chromospheric line profiles adopted in our computations.

ordinates : specific intensity in $\text{erg s}^{-1} \text{cm}^{-2} \text{sr}^{-1} \text{Hz}^{-1}$; in abscissae, we have wavelength distance from line center (in Å) to make it easier to compare with other published data.

Fig.3.a. : L α

Fig.3.b. : Mg k

Fig.3.c. : Mg h

Fig.3.d. : Ca K

Fig.3.e. : Ca H

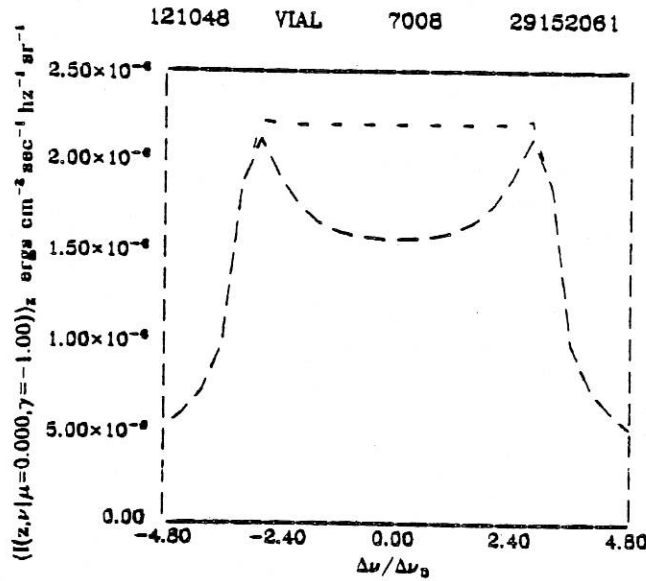


FIG.4.a.

FIG. 4.b

FIG. 4.c

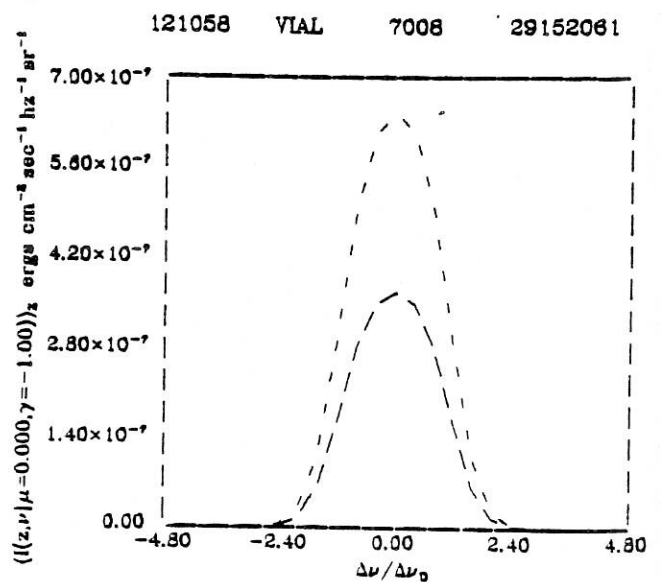
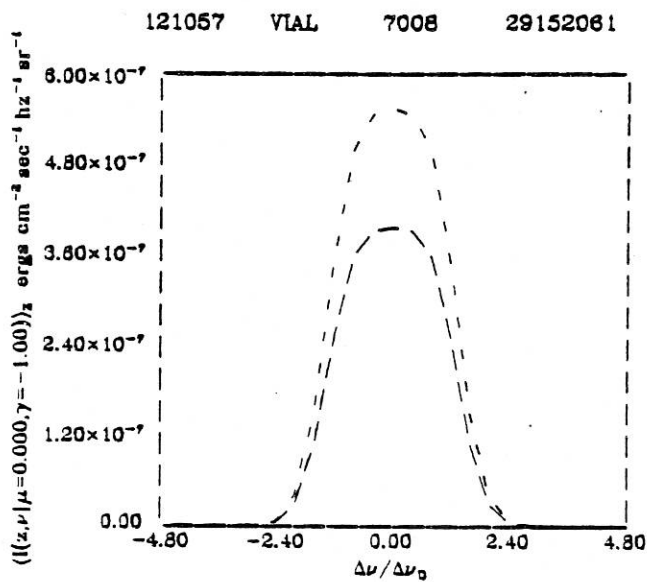
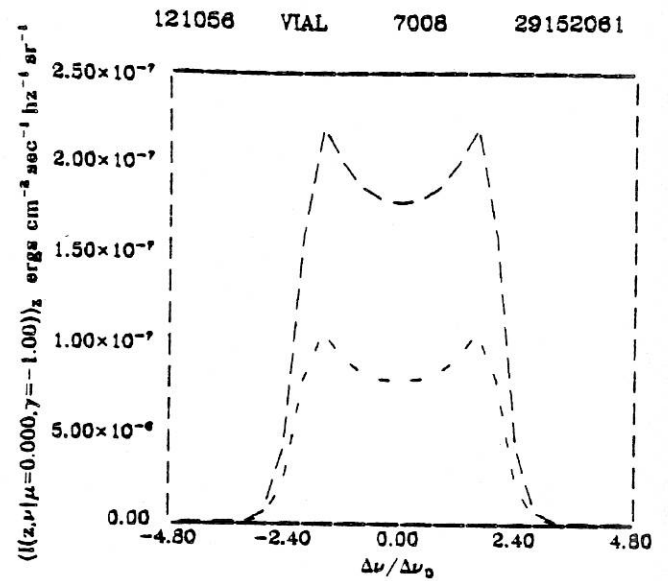
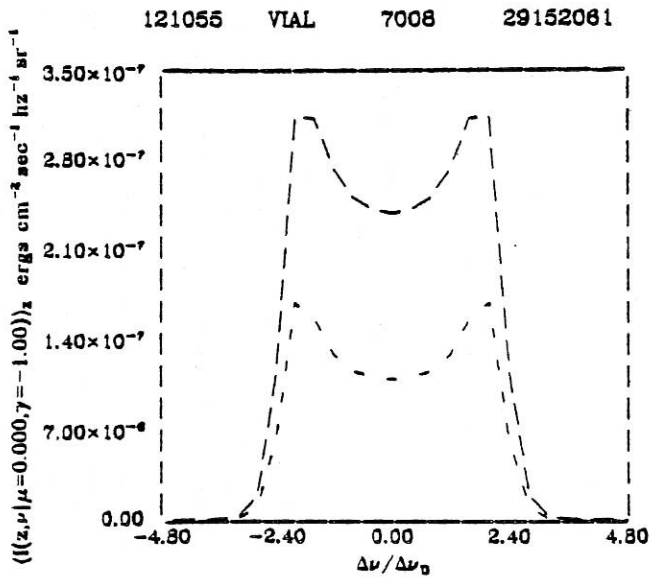
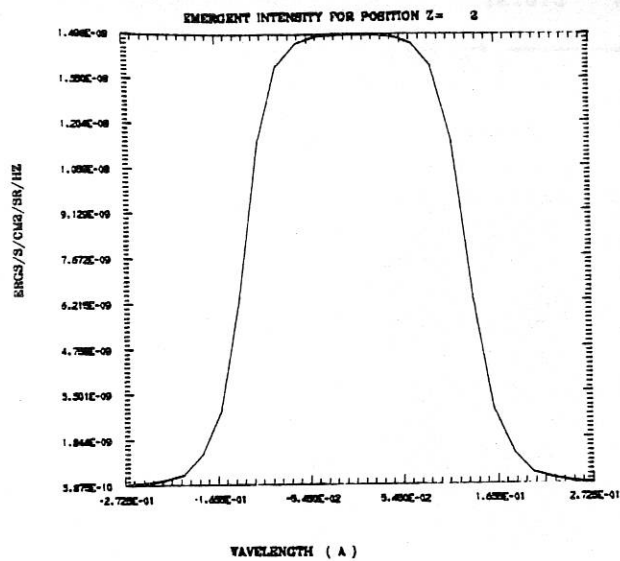


FIG. 4.d

FIG.4.e.

FIG. 4. : Lines profiles computed with the modified MAM. $n_p/n_1 = 10$;
static atmosphere (same captions as Fig.2)

Fig.4.a. : L α Fig.4.b. : Mg k Fig.4.c. : Mg h Fig.4.d. : Ca K Fig.4.e. : Ca H



229

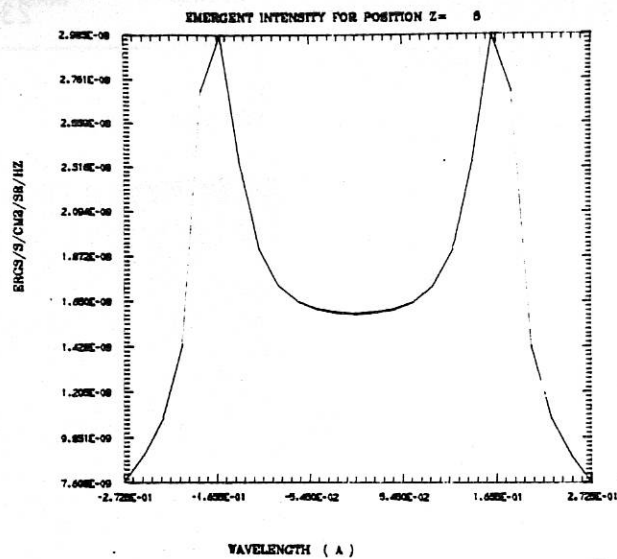


FIG.5.a.

FIG.5.b.

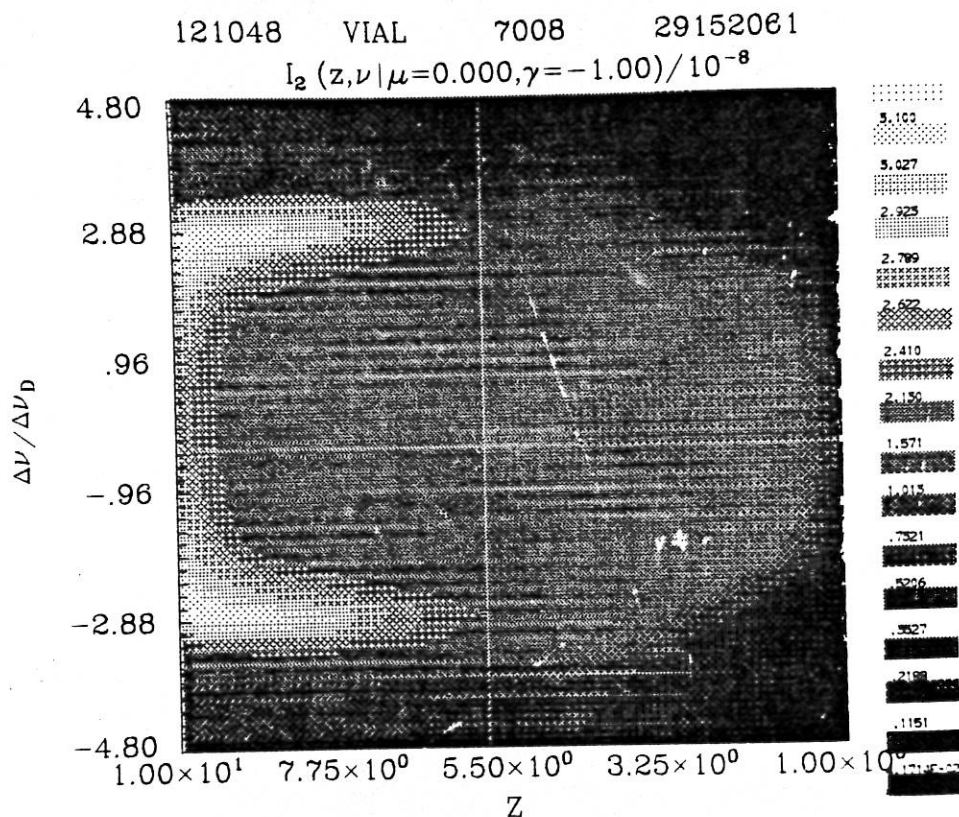


FIG.5.c.

FIG. 5. : Evidence for edge effects in the 2D computation of the L α line.

Fig.5.a.b. : Emergent L α profile along the x axis, at the top (5.a) and at the bottom of the atmosphere (5.b).

ordinates : specific intensity ($\text{erg s}^{-1} \text{cm}^{-2} \text{sr}^{-1} \text{Hz}^{-1}$)
 abscissae : wavelength distance from line center (\AA)

Fig.5.c. : Emergent intensity plotted as half tone as a function of the frequency distance from line center ($\Delta\nu/\Delta\nu_D$) and vertical position (Z : index 1 corresponds to the top).

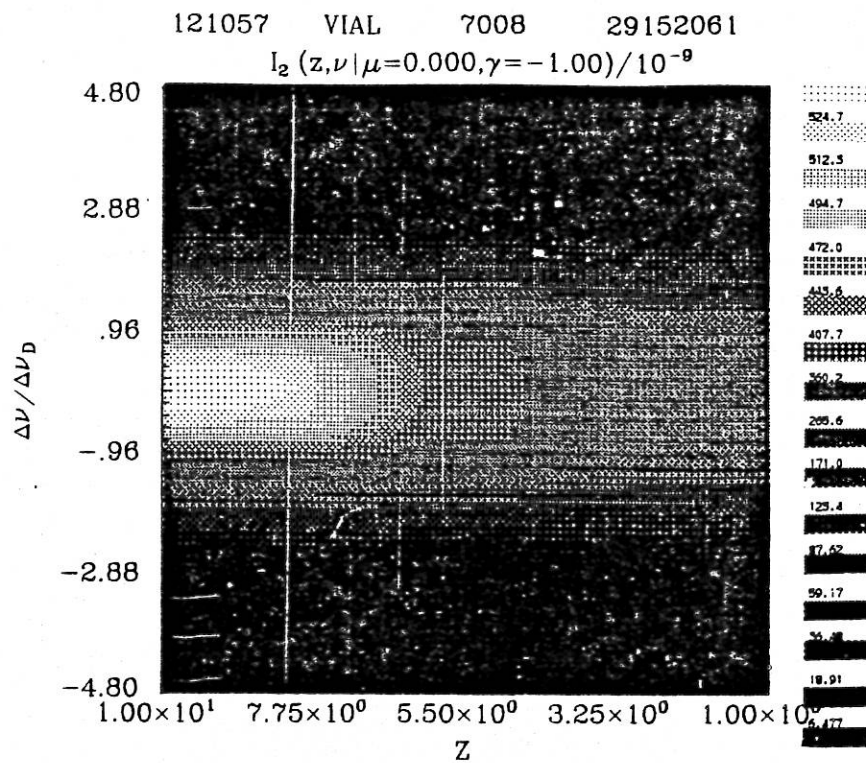
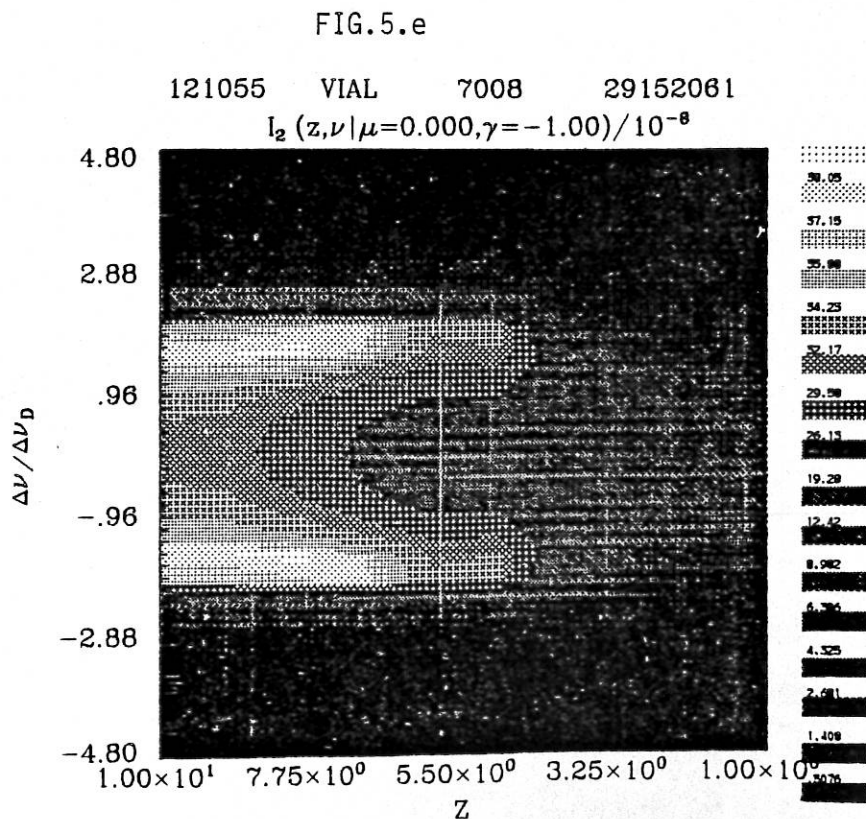


FIG.5.d



The FIG.5.d. and 5.e. represent the same quantities as Fig.5.c., for Ca K (5.d) and Mg k (5.e).

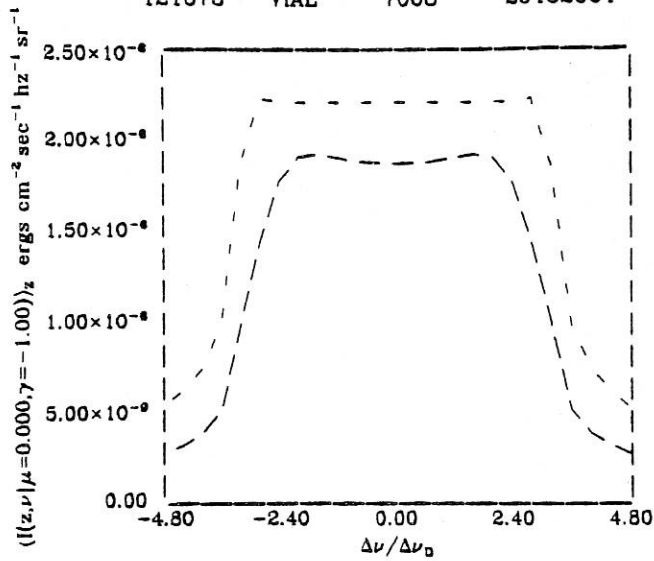
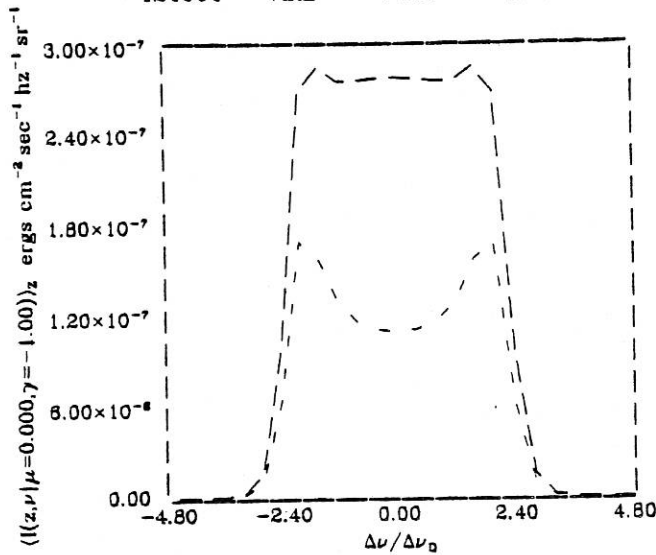


FIG.6.a.

FIG.6.b.

121661 VIAL 7008 29152061



121681 VIAL 7008 29152061

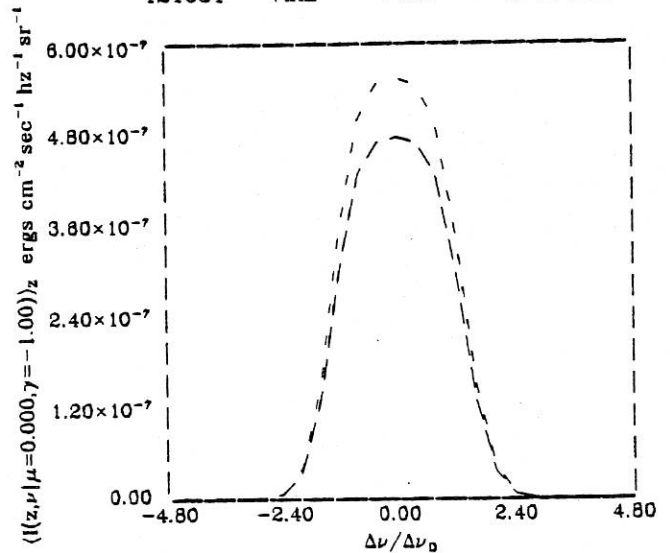


FIG. 6. : Lines profiles computed with the modified MAM, $n_p/n_1 = 10$, moving atmosphere (same caption as Fig. 2).

Fig.6.a. : L α ($V_z = 42 \text{ km s}^{-1}$) Fig.6.b. : Mg k ($V_z = 25 \text{ km s}^{-1}$)

Fig.6.c. : Ca K ($V_z = 33 \text{ km s}^{-1}$)

120994 VIAL 7008 29152061

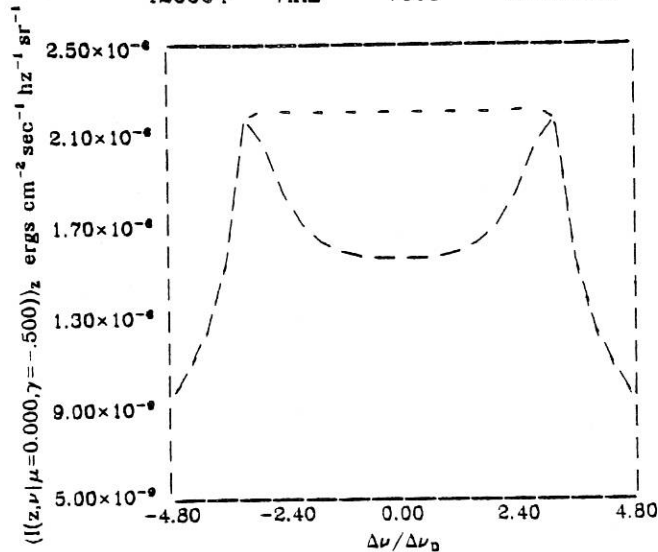


FIG.7. : L α profile emergent at 60° from the x axis. $n_p/n_1 = 10$, static atmosphere (same captions as Fig.2).

CONCLUSION

Malgré les limitations propres à l'instrument OSO-8 (du point de vue résolution spatiale, spectrale, temporelle, taux de lumière diffusée etc...) et le faible nombre d'objets étudiés, nous avons pu mettre en évidence quelques propriétés des protubérances.

1 - Protubérance active

Nous confirmons une observation de P. Mein (1977) faite au centre du disque : l'existence de vitesses le long de la ligne de visée importantes au-dessus de l'objet et croissantes vers la périphérie. Nous mettons en évidence des rapports de raies des doublets Mg II, Ca II qui semblent en contradiction avec les abondances (résultat que nous retrouvons sur les protubérances quiescentes). La frontière extérieure est le lieu du minimum de largeur et du maximum de déplacement de la raie O VI. Nous observons une grande "excitation" au-dessus de la protubérance dans la couronne : probablement une température élevée (supérieure à 10^5 K) et des vitesses non thermiques de l'ordre de 50 km s^{-1} . Il est possible de réduire les vitesses turbulentes si on admet l'existence de vitesses organisées et de signes opposés dans des boucles. Il est certain toutefois que les profils s'élargissent avec la hauteur : s'agit-il de boucles de même densité à températures de plus en plus élevées contrairement à la conclusion de Golub et al. (1980) ou de boucles de densité décroissante qui sont le siège de vitesses (organisées ou non) croissantes avec l'altitude ? Plus d'observations sont nécessaires pour trancher cette question.

2 - Protubérance quiescente

Nous avons fourni des profils typiques calibrés des 6 raies, leurs variations d'une protubérance à l'autre et à l'intérieur même d'une protubérance. Les résultats sont résumés dans le tableau II ci-joint. Inédits, ils nous paraissent être utiles pour les futures observations.

Nous confirmons par une observation directe l'importante opacité des raies $L \alpha$ (et $L \beta$). Nous établissons un résultat déjà trouvé sur protubérance active :

$$(I_k/I_h)_{\text{Mg II}} > (I_k/I_h)_{\text{Ca II}}$$

Nous suggérons l'idée (confirmée par nos calculs) que ces rapports reflètent les intensités des raies chromosphériques. Ils confirment la domination du rayonnement incident pour le transfert dans les raies u.v. optiquement épaisses. Les opacités aux centres des raies K et k sont de l'ordre de 2.

Nous trouvons de faibles variations du rapport $I L \alpha / \text{Ca K}$ ce qui, indique une ionisation à peu près constante. Les valeurs trouvées du rapport nous permettent, moyennant de nombreuses simplifications de calculer le rapport n_0/n_1 . Nous obtenons une valeur voisine de 2 à 3. Ceci est une confirmation supplémentaire de la forte ionisation, due à une pénétration, à peu près complète, du continu de Lyman. Ceci justifie l'introduction du paramètre de pénétration de $\text{Ly} \infty$ par Heasley et Milkey (1976).

TABLE II Caractéristiques des raies observées sur 2 protubérances quiescentes

	L β	L α	k	h	K	H
Intensités absolues (10^4) ($\text{erg s}^{-1} \text{ cm}^{-2} \text{ sr}^{-1}$)	0.05 0.05 (0.045-0.06)	>1.9 3.6 (2.0-3.6)	2.4 2.95 (2.4-3.5)	1.4 1.85 (1.5-1.9)	1.1 1.5 (1.2-2.0)	1.0 1.1 (0.6-1.2)
Intensité (protubérance) Intensité (soleil absolu)	0.5 0.5	>0.3 0.55	0.11 0.13	0.08 0.1	0.16 0.22	0.15 0.16
Largeur à mi-hauteur (convertie en km s^{-1})			28 30	27 30	15 12 (5-13)	17 11 (5-12)
Séparation des pics (\AA)	$\frac{0.33}{0.33}$	>0.30 0.35				
$\frac{I(\text{pic})}{I(\text{centrale})}$	$\frac{1.85}{1.7-2}$	>1.2 1.4 (1-1.5)				

1ère ligne : 17 octobre 1975 (article V)

2ème ligne : 19 mai 1976 (article VI)

Les nombres () indiquent la plage des variations observées.

Nos calculs (transfert à 2 dimensions) effectués avec le programme MAM modifié et adapté au problème protubérance nous permettent une comparaison directe des profils calculés et observés (pour la première fois pour les uns et les autres). Un modèle géométrique très simple, un atome à 2 niveaux, nous permettent toutefois de trouver un accord à peu près satisfaisant avec nos profils typiques : largeurs des raies, intensités, renversements, etc... Le profil $L\alpha$ calculé est plus étroit que le profil observé : sans doute la raie se "forme"-t-elle à plus haute température que celle du modèle.

Nos calculs donnent une largeur des raies Mg II (traduite en vitesse) bien plus grande que la largeur des raies Ca II. Toutefois, les profils calculés Mg II ne deviennent non renversés que pour des vitesses radiales élevées (de l'ordre de 25 km s^{-1}). Les calculs effectués confirment la domination du rayonnement incident dans la raie elle-même. Ils mettent en évidence des "effets de bord" importants qui peuvent expliquer certaines observations en $L\alpha$, de résolution malheureusement insuffisante. Du point de vue théorique, les calculs à 2 dimensions donnent des profils émergents différents des profils à 1 dimension : les effets sont d'ailleurs différents sur Mg II et Ca II. Cela montre, une fois de plus, l'importance de la géométrie, donc du rayonnement incident.

Il nous apparaît que les résultats présentés constituent une étape vers :

a) Des calculs sur des modèles moins rudimentaires.

b) Le dépouillement d'autres observations : un programme d'observations coordonnées avec Meudon (DPSM), Oslo (coronographe) et le Pic du Midi (champ magnétique) a pu être réalisé en mai-juin-juillet 1978, 2 mois avant l'arrêt des opérations. Nous confirmons nos résultats relatifs aux rapports k/h , K/H . Une comparaison des vitesses Ca II et $H\alpha$ est en cours. Nous espérons également travailler sur les objets visés simultanément par le Pic et OSO-8, calculer la pression en différents points et mesurer ainsi le paramètre $\beta = p_G/p_M$. Des profils sur filaments ont également été obtenus. Les profils $L\alpha$ notamment pourront être comparés aux calculs et aux mesures (intégrées) de TRC (Bonnet et al. 1980).

c) De nouvelles observations : avec SMM (et nous l'espérons, avec l'instrument à haute résolution placé au foyer du Solar Optical Telescope).

REFERENCES GENERALES

- ARTZNER, G., BONNET, R.M., LEMAIRE, P., VIAL, J.C., JOUCHOUX, A.,
LEIBACHER, J., VIDAL-MADJAR, A., and VITE, M., 1977, Space Science
Instrumentation, 3, 131. (Article I).
- BONNET, R.M., LEMAIRE, P., VIAL, J.C., ARTZNER, G., GOUTTEBROZE, P.,
JOUCHOUX, A., LEIBACHER, J., SKUMANICH, A., and VIDAL-MADJAR, A.,
1978, Ap. J., 221, 1032 (Article II).
- BONNET, R.M., BRUNER, E.C., Jr., ACTON, L.W., BROWN, W.A., and DECAUDIN, M.,
1980, Ap. J., 237, L 47.
- D'AZAMBUJA, L., et D'AZAMBUJA, M., 1948, Ann. Obs. Paris-Meudon, 6, 7.
- DUNN, R.B., 1960, Thesis, Harvard University.
- ENGVOLD, O., and MALVILLE, J.M., 1977, Solar Phys., 52, 369.
- ENGVOLD, O., MALVILLE, J.M., and LIVINGSTON, W., 1978, Solar Phys., 60, 57.
- ENGVOLD, O., 1980, Solar Phys. 67, 351.
- ENGVOLD, O., WIEHR, E. and WITTMANN, A., 1980, Astron. Astrophys., 85, 326.
- GOLUB, L., MAXSON, C., ROSNER, R., SERIO, S., and VAIANA, G.S., 1980,
Ap. J., 238, 343.
- HEASLEY, J.N., and MIHALAS, D. : 1976, Ap. J. 205, 273.
- HEASLEY, J.N., and MILKEY, R.W., 1976, Ap. J., 210, 827.
- HEASLEY, J.N. and MILKEY, R.W. : 1978, Ap. J., 221, 677.
- HIRAYAMA, T., 1963, Publ. Astron. Soc. Japan, 15, 122.
- HIRAYAMA, T., 1978, in Physics of Solar Prominences (I.A.U. Colloquium 44)
Jensen, Maltby, Orrall, eds, D. Reidel Publ. Co, Dordrecht, p. 4. (P.S.P).
- ISHIZAWA, T. : 1971, Publ. A.S. Japan, 23, 75.
- KANNO, M., WITHBROE, G.L. and NOYES, R.W., 1981, Solar Phys., 69, 313.
- KIPPENHAHN, R., and SCHLUTER, A., 1957, Z. Aph., 43, 36.
- KUBOTA, J., 1980, Publ. Astron. Soc. Japan, 32, 359.
- KUPERUS, M. and TANDBERG-HANSEN, E., 1967, Solar Phys., 2, 39.
- LANDMAN, D.A. and ILLING, R.M.E. : 1977, Astron. Astrophys., 55, 103.
- LANDMAN, D.A., EDGERG, S.J. and LANEY, C.D. : 1977, Ap. J., 218, 888.
- LANDMAN, D.A., ILLING, R.M.E. and MONGILLO, M., 1978, Ap. J. 220, 666.
- LANDMAN, D.A., 1980, Ap. J., 237, 988.
- LANTOS, P., and RAOULT, A., 1980, Solar Phys., 66, 275.

- LEMAIRE, P., CHARRA, J., JOUCHOUX, A., VIDAL-MADJAR, A., ARTZNER, G.E., VIAL, J.C., BONNET, R.M., and SKUMANICH, A., 1978, Ap. J. (Letters), 223, L 55.
- LEMAIRE, P., GOUTTEBROZE, P., VIAL, J.C. and ARTZNER, G.E., 1981, Astron. Astrophys. 103, 160.
- LEROY, J.L., 1981, in Proceedings of the Japan-France Seminar on Solar Physics, Moriyama and Heroux eds.
- MARTRES, M.J., MEIN, P., SCHMEIDER, B., and SORU-ESCAUT, I., Solar Phys., 69, 301.
- MEIN, P., 1977, Solar Phys. 54, 45.
- MERCIER, C. and HEYVAERTS, J., 1977, Astron. Astrophys., 61, 685.
- MIHALAS, D., AUER, L.H., and MIHALAS, B.R., 1978, Ap. J., 220, 1001.
- ORRALL, F.Q., and SCHMAHL, E.J., 1976, Solar Phys. 50, 365.
- ORRALL, F.Q., and SCHMAHL, E.J., 1980, Ap.J., 240, 908.
- PIKELNER, S.B., 1971, Solar Phys. 17, 44.
- POLAND, A.I., SKUMANICH, A., ATHAY, R.G., TANDBERG-HANSEN, E. : 1971, Solar Phys., 18, 391.
- RIBES, E., and UNNO, W., 1980, Astron. Astrophys., 91, 129.
- SECCHI, A., 1877, Le Soleil, Gauthier-Villars, Paris.
- STELLMACHER, G., 1979, Solar Phys., 61, 61.
- TANDBERG-HANSEN, E., 1974, Solar Prominences, D. Reidel Publ. Co. Dordrecht, Holland.
- VERNAZZA, J.E., AVRETT, E.H. and LOESER, R., 1973, Ap. J. 184, 605.
- VERNAZZA, J.E., AVRETT, E.H., LOESER, R., 1976, Ap.J. Supp., 30, 1.
- VIAL, J.C., and BRUSTON, P., 1977, Proceedings of the OSO-8 Workshop, Boulder Nov. 1977, E. Hansen editor, University of Colorado, p. 136.
- VIAL, J.C., GOUTTEBROZE, P., ARTZNER, G., and LEMAIER, P., 1979, Solar Phys., 61, 39 (Article III).
- VIAL, J.C., LEMAIER, P., ARTZNER, G., and GOUTTEBROZE, P., 1980, Solar Phys. 68, 187 (Article IV).
- VIAL, J.C., MARTRES, M.J., and SALM-PLATZER, J., 1981, Solar Phys., 70, 325.
- VIAL, J.C., 1982, Optically thick lines in a quiescent prominence : Profiles of $L\alpha$, $L\beta$ (H I), k and h (Mg II) K and H (Ca II) lines with the OSO-8 LPSP instrument. A paraître dans Ap. J. (Article VI).

Articles OSO-8 non mentionnés dans la thèse.

- ARTZNER, G., LEIBACHER, J., VIAL, J.C., LEMAIRE, P., and GOUTTEBROZE, P. : 1978, *Astrophys. J.* 224, L83.
- ARTZNER, G., CAZES, S., EMERICH, C., VIAL, J.C., and LEMAIRE, P. : 1981, *Astron. and Astrophys.*, 100, 205
- DUMONT, S., MOURADIAN, Z., PECKER, J.C., CHIPMAN, E.G., ARTZNER, G., and VIAL, J.C. : 1980-a, *C.R. Acad. Sci. Paris* 290, B, 317.
- DUMONT, S., MOURADIAN, Z., PECKER, J.C., SIMON, G., ARTZNER, G., and VIAL, J.C. : 1980-b, *C.R. Acad. Sci. Paris* 290, B, 365.
- MOURADIAN, Z., DUMONT, S., PECKER, J.C., CHIPMAN, E.G., ARTZNER, G., and VIAL, J.C., : 1982, à paraître dans *Solar Physics*.
- GOUTTEBROZE, P., LEMAIRE, P., VIAL, J.C., and ARTZNER, G. : 1978, *Astrophys. J.* 225, 655.
- GROSSMANN-DOERTH, U., KNEER, F., and VON UEXKULL, M., ARTZNER, G., and VIAL, J.C. : 1980, *Solar Phys.* 66, 3.
- JOUCHOUX, A., VIAL, J.C., ARTZNER, G., GOUTTEBROZE, P., and LEMAIRE, P., : 1981, *Astron. and Astrophys.* 93, 415.
- KNEER, F., SCHARMER, G., MATTIG, W., WYLLER, A., ARTZNER, G., LEMAIRE, P., and VIAL, J.C. : 1981, *Solar Phys.*, 69, 289.
- LEMAIRE, P. : 1978, "OSO-8/CNRS Multichannel High Resolution UV and Visible Spectrometer", *Orbital Technical Handbook, LPSP Internal Report T60*.
- SIMON, G., DUMONT, S., MOURADIAN, Z., PECKER, J.C., ARTZNER, G., and VIAL, J.C. : 1980, *Astron. and Astrophys.* 89, L8.